UNIVERSITÀ DEGLI STUDI DI TRIESTE

UNIVERSITÀ DEGLI STUDI DI TRIESTE

XXXVIII CICLO DEL DOTTORATO DI RICERCA IN FISICA

Finanziato dall'Unione europea - NextGenerationEU
Funded by the European Union - NextGenerationEU

Structure and reactivity of biomimetic iron-centered 2D materials from ultra-high vacuum to near-ambient pressure

Settore scientifico-disciplinare: **FIS/03**

DOTTORANDO

Alessandro Namar

COORDINATORE

PROF. Angelo Bassi

SUPERVISORE DI TESI

PROF. Erik Vesselli

CO-SUPERVISORE DI TESI

DR. Mattia Scardamaglia

ANNO ACCADEMICO 2024/2025

Finanziato dall'Unione europea NextGenerationEU
Ministero dell'Università e della Ricerca
Italiadomani
UNIVERSITÀ DEGLI STUDI DI TRIESTE

ABSTRACT

It is curious how life can seem obvious, and how easily we take it for granted, while billions of complex biological processes unfold every second within and around us. From plants capturing sunlight and converting it into chemical energy while releasing oxygen into the atmosphere, to microorganisms in the soil performing, under ambient conditions, one of the most challenging chemical reactions known to humankind: the conversion of dinitrogen gas into ammonia, which provides essential building blocks for life. Many, but not all, of these biological processes are catalyzed by metalloproteins whose reactive centers consist of an isolated metal atom embedded in tetrapyrrolic macrocycles, such as porphyrins. The exceptional selectivity and efficiency of these natural systems have inspired biomimetic approaches to stabilize single metal atoms in well-defined coordination environments for heterogeneous catalysis. In this context, 2D metalorganic architectures based on metalated porphyrins represent a promising platform, as they can self-assemble on suitable supports where the intrinsic properties of the metal center can be tuned through surface trans-effect and lateral coordination. This thesis investigates the structural, electronic and reactive properties of mono- and bi-metallic porphyrin-based layers and networks under UHV and NAP conditions, with a focus on the interaction with CO and O_2.

Two porphyrins featuring the same Fe-based macrocycle but distinct peripheral functionalization residues were selected as molecular building blocks: FeTPyP deposited on Gr/Ir(111), and hemin deposited on Au(111). In both systems, cobalt atoms were introduced as a second metal to generate bimetallic structures.

Structural characterization of both assemblies was performed by STM, complemented, depending on the system, by NAP-XPS, IR-Vis SFG, NEXAFS spectroscopies and DFT calculations.

FeTPyP molecules self-assemble into a close-packed structure with Fe in +2 oxidation state. Upon Co post-deposition, the molecular layer undergoes a complete structural reorganization, yielding a bimetallic network in which Co atoms coordinate to the pyridinic termination, forming a macrocycle-like arrangement. This restructuring is accompanied by a significant electronic rearrangement: Co is stabilized in the +1 oxidation state, while the central Fe gets unexpectedly reduced to Fe(I), a highly reactive species capable of activating O_2 even under UHV conditions at room temperature.

While Fe in the monometallic system is inert toward CO and O_2, Co addition induces an electronic reorganization that activates Fe, leading both metals to participate in the reactions. CO adsorption was probed as a function of Co loading, revealing site-dependent cooperativity and changes in adsorption energies, while O_2 exposure yields ligation and activation at both metal centers, highlighting the potential applicative approaches of such monophasic bifunctional catalysts.

Hemin on Au(111) forms a close-packed structure composed of both Fe-free and Fe-filled (heme) units, limited by the purity of the biological precursor. The molecules lie flat, with peripheral carboxyl groups predominantly tilted with respect to the macrocycle plane and, in some cases, overlapping the macrocycle of neighboring molecules. While CO shows negligible interaction with this system, O_2 is stabilized at the Fe centers by the additional coordination offered by the nearby carboxyl groups, mimicking the distal histidine in oxyhemoglobin and oxymioglobin, effectively reproducing the second coordination sphere observed in biological environments. To fill the vacant centers, Co was deposited onto the monolayer. Rather than simply occupying the empty sites, Co induces trans-metalation, also producing intermediate states in which both Co and Fe are present within the macrocycles. Upon O_2 exposure, dioxygen activation takes place, further promoting trans-metalation.

Overall, this work grounds on the concept that even when the reactive centers are identical, variations in peripheral functional groups profoundly influence lateral coordination and reactivity, highlighting how subtle structural tuning can be strategically exploited to tailor the properties of bio-inspired heterogeneous catalysts.

TABLE OF CONTENTS

LIST OF ACRONYMS

AES Auger Electron Spectroscopy

Au Gold

BE Binding Energy

DFT Density Functional Theory

Gr Graphene

GS Gunnarsson-Schönhammer

HOMO Highest Occupied Molecular Orbital

IR Infrared

Ir Iridium

LEED Low Energy Electron Diffraction

LUMO Lowest Unoccupied Molecular Orbital

ML Monolayer

MS Multiplet Splitting

MOF Metalorganic Framework

MON Metalorganic Network

NAP Near-Ambient Pressure

NEXAFS Near-Edge X-ray Absorption Spectroscopy

OER Oxygen Evolution Reaction

ORR Oxygen Reduction Reaction

PEY Partial Electron Yield

RT Room Temperature

SAC Single Atom Catalyst

SFG Sum Frequency Generation

STM Scanning Tunneling Microscopy

STS Scanning Tunneling Spectroscopy

TPyP Tetra-Pyridyl Porphyrin

UHV Ultra High Vacuum

VIS Visible

XPS X-ray Photoelectron Spectroscopy

1 | General Introduction

Catalysts represent one of the most significant discoveries in human history. Nearly 90% of all industrial chemical processes rely on catalytic reactions, underscoring their essential role in sectors such as energy conversion, chemical production and oil refining [1,2]. But, what is a catalyst, and why is it so crucial? In general terms, a catalyst is a substance that facilitates a chemical reaction (A + B → C) by lowering its activation energy, thereby accelerating the reaction rate without altering its thermodynamics and without being consumed in the process [3]. Catalytic processes are typically classified as homogeneous or heterogeneous. In homogeneous catalysis, both catalyst and reactants are in the same phase (gas or liquid). These systems often exhibit high activity and selectivity, however, their recovery and reuse are challenging because catalyst and products coexist in the same phase, limiting the applicability in continuous industrial processes. In heterogeneous catalysis, the active phase is solid while the reactants are gaseous or liquid. This phase separation facilitates catalyst recovery and generally enhances robustness and long-term stability, making heterogeneous catalysts the preferred choice for large-scale industrial applications [1,3].

Among heterogeneous catalytic processes, the Haber-Bosch process is the most impactful. It converts abundant but chemically inert atmospheric nitrogen (N_2), whose N≡N triple bond is extremely strong, together with hydrogen (H_2) into ammonia (NH_3) under elevated temperature and pressure conditions. Fritz Haber's pioneering experiments employed osmium as a catalyst, demonstrating remarkable activity for ammonia synthesis, however, its high cost and low availability prevented industrial application [3]. To overcome this limitation, Alwin Mittasch, working at BASF under Carl Bosch, tested thousands of materials and identified an iron-based catalyst with the activity and stability required for large-scale ammonia synthesis. This breakthrough resolved the global nitrogen crisis of the 20th century, revolutionizing agriculture by enabling the mass production of fertilizers needed to sustain a rapidly growing population [3]. Just as the Haber-Bosch process addressed one of the biggest challenges of the 20th century, heterogeneous catalysis continues to play a central role in the 21st.

Today, climate change driven by greenhouse gas emissions presents another global crisis. Catalysis is central to many emerging sustainable technologies such as: CO_2 conversion into fuels and energy vectors [4], water splitting for renewable hydrogen production [5], biomass valorization [6], sustainable ammonia synthesis powered by renewable energy sources [7] and the development of efficient energy-storage devices [8]. Thus, catalysis remains central not only for industrial productivity but also for achieving a carbon-neutral future.

Meeting these modern challenges requires catalysts with enhanced performance and precisely defined active sites. Supported metal catalysts typically consist of nanoparticles with broad size distributions and irregular morphologies [9]. Each particle exposes multiple active sites with distinct reactivity, often compromising the overall selectivity toward the desired products. Consequently, metal particle size is a key parameter governing the catalytic behavior [9]. Reducing particle size can enhance performance through: (i) low-coordination environments, which expose highly reactive unsaturated metal atoms [10,11]; (ii) quantum size effects, where electron confinement leads to discrete energy levels and a tunable HOMO-LUMO (highest occupied-lowest unoccupied molecular orbital) gap [12] and (iii) metal-support interactions, which influence the catalytic behavior through charge transfer [13]. A well-known example of these size effects is gold: while bulk gold is chemically inert, reducing it to sub-nanoclusters transforms it into a highly active catalytic material [10].

However, even nanocluster size still contains several atoms and therefore a variety of active sites. A straightforward strategy, to ensure that every metal atom participates in catalysis is to further reduce them to isolated metal centers, giving rise to single-atom catalysts (SACs) [9].

Nevertheless, decreasing the size of the metal structures increases the surface free energy (which reaches its maximum for isolated atoms). These highly unsaturated species tend to aggregate when deposited on supports, leading to the loss of their unique properties. A workaround to stabilize single

metal atoms on surfaces is therefore essential [9]. One promising strategy draws inspiration from nature, where metalloproteins stabilize isolated metal centers within well-defined organic matrices. To mimic these active sites, metal atoms and simple organic ligands can be co-deposited onto suitable substrates, where they self-assemble into two-dimensional (2D) metalorganic networks (MONs). These structures can be considered the 2D analogues of metalorganic frameworks (MOFs), which are highly porous three-dimensional (3D) architectures composed of metal nodes coordinated by organic linkers arranged in highly ordered structures [14]. The remarkable versatility and broad application potential of MOFs, including gas storage, separations and catalysis, were recognized this year with the awarding of the Nobel Prize in Chemistry to Kitagawa, Robson and Yaghi.

The formation of MONs on surfaces enables direct investigation using surface-science techniques under controlled ultra high vacuum (UHV) conditions, which are essential to elucidate the intrinsic properties of the metal centers, the influence of the supporting surface and ligand interactions [15]. However, catalytic processes can be sluggish under UHV conditions due to the missing contribution of the gas or liquid phase chemical potential. To bridge this gap, the development of *in situ* and *operando* techniques allows to extend these studies to near-ambient pressure (NAP) [16], crucial to explore these systems under realistic conditions.

In this work, to emulate the active sites of metalloproteins, we focus on porphyrins, which constitute the reactive cores of several biological catalysts, investigating their properties in UHV and NAP conditions. When deposited on suitable substrates, these molecules can self-assemble into ordered structures providing multiple ways to tune the electronic properties of the coordinated metal center, as will be described in the next chapter.

2 | Scientific Background and Research Aim

This chapter provides the fundamental concepts for the results presented in this PhD work. An introduction to the motivation for studying tetrapyrroles, and specifically porphyrins on surfaces, is presented. Emphasis is placed on tetra-pyridyl porphyrin (TPyP), highlighting its potential for the development of bifunctional catalysts. Two selected examples of recently investigated bimetallic structures are discussed to illustrate how the deposition of a second metal can modify the structural and electronic properties of the pristine monometallic layer. Finally, the aim of the thesis is outlined.

2.1 From Nature to Supported 2D Materials

Metalloproteins represent nearly half of all proteins in nature, and their metal-binding sites catalyze essential biological processes such as photosynthesis, respiration, water oxidation, oxygen reduction and nitrogen fixation [17].

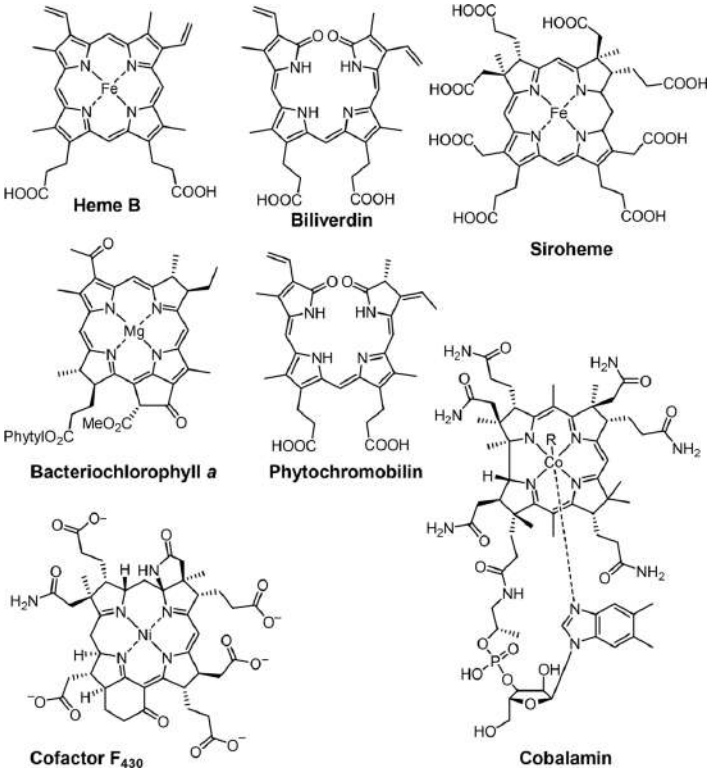

Figure 2.1 Chemical structures of several natural tetrapyrroles. Image taken from [18].

The protein environment surrounding the active site is typically divided into a first coordination sphere, composed of ligands directly bonded to the metal ion (interactions largely dominated by covalent bonding), and a second coordination sphere, which includes nearby residues that do not form direct metal-ligand bonds but interact through non-covalent interactions such as hydrogen bonding, electrostatic interactions, hydrophobic effects and Van der Waals forces [19]. Both spheres play a crucial role in the catalytic processes: the first sphere tunes the electronic structure and chemical reactivity of the metal center, whereas the second sphere influences the kinetics and thermodynamics of enzymatic catalysis [20,21]. A classic example of this interplay is provided by hemoglobin and myoglobin. Although they both rely on the same heme cofactor, differences in their surrounding protein environments allow

them to carry out distinct biological functions: oxygen transport in blood by hemoglobin and oxygen storage in muscle by myoglobin [18].
Tetrapyrroles represent one of the most widely employed macrocyclic architectures in metalloproteins, as illustrated in Figure 2.1. Structurally, tetrapyrrolic macrocycles consist of four pyrrole rings connected by methine (-CH=) bridges, except for the corrin ring in cobalamin, which lacks one methine bridge. The macrocycle can accommodate a central metal atom, typically a transition metal such as Fe, Co, Mn or Ni and its planar geometry allows for axial ligand coordination above and below the ring. Binding of one axial ligand can be influenced by the presence of a second ligand in the trans position, as both compete for charge transfer with the metal center [15]. This phenomenon, known as the molecular trans-effect, provides fine control of the electronic and chemical properties of the metal site and enables structural and electronic information to be transmitted through the protein scaffold. A well-studied example is hemoglobin: upon O_2 binding, the Fe atom shifts from a slightly out-of-plane position into the macrocycle plane, transmitting this displacement to the proximal histidine ligand coordinated to the Fe center. This local structural rearrangement at the Fe center in one subunit is propagated to the remaining three subunits, giving rise to hemoglobin's nonlinear, cooperative oxygen-binding behavior. In contrast, in cytochrome P450, the same Fe macrocycle is coordinated by the anionic thiolate head of cysteine, which plays the role of the proximal histidine in hemoglobin and myoglobin, enabling O_2 activation [16].
The remarkable catalytic efficiency of metalloproteins has inspired surface scientists to reproduce key structural and functional features of biological active sites. One approach involves deposition of metal atoms coordinated by organic ligands onto suitable substrates to mimic the coordination geometry and electronic environment of natural systems [22]. Among these ligands, tetrapyrroles and in particular porphyrins, have proven exceptionally well suited due to their structural rigidity, tunable coordination chemistry and ability to form ordered assemblies on surfaces [15,16].

2.2 Porphyrins at Surfaces

Porphyrins belong to the broader family of tetrapyrroles, often referred to as the "pigments of life" due to their essential roles in biological systems, where they often act as the prosthetic groups of proteins. Hemoproteins, for example, contain a heme cofactor in which an Fe atom is coordinated within a porphyrinic macrocycle, while chlorophyll incorporates a Mg-porphyrin complex responsible for light harvesting in photosynthesis. The study of porphyrins dates back to the earliest investigations of natural pigments, which sought to explain the origin of the characteristic colours of leaves and blood [22]. Porphyrins share the same macrocyclic structure as porphin, which can host and stabilize a single metal atom, with the possibility of coordinating functional substituents at the meso-positions (C_m), as illustrated in Figure 2.2 a).

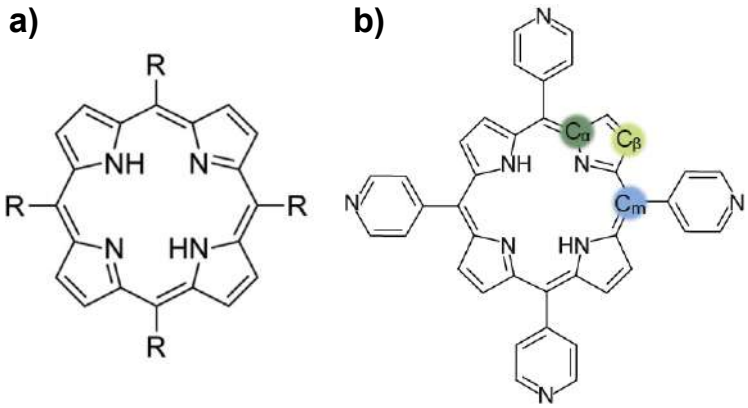

Figure 2.2 Structure of: a) meso-substituted porphyrin and b) four pyridinic groups at the meso positions forming tetra-pyridyl porphyrin. Image adapted from [15,23].

In a surface-science context, porphyrins exhibit particularly favourable properties: their planar geometry promotes 2D adsorption on well-defined substrates, where they arrange into ordered or disordered layers. The formation of ordered heretostructures requires sufficient surface mobility which is promoted on weakly interacting substrates, where intermolecular interactions dominate, and hindered on strongly interacting supports [15]. Upon adsorption, one of the two axial coordination sites of the macrocycle is in direct contact with the surface. The substrate can therefore act as a proximal ligand, mimicking the trans-effect observed in natural molecular coordination. This axial interaction, called surface trans-effect, influences both the spin and oxidation state of the metal center [24] and the geometric configuration of the macrocycle, thereby affecting the molecule's reactivity and its ability to bind additional ligands. A representative example is provided by cobalt-tetraphenyl-porphyrin (CoTPP) on Cu(111): CO adsorption leads to mono and di-carbonylation, which compete with the Co-Cu interaction and induce a pronounced distortion of the organic backbone [25]. In contrast, O_2 ligation to CoTPyP supported on Au(111) results in charge injection from the substrate into the ligand, weakening the O-O bond [26].

Porphyrins are commonly synthesized in solution through complex chemical routes that often allow direct metal incorporation [27]. However, when metalation in solution is not achievable or when heretometallic structures are desired to be investigated, on-surface functionalization provides a versatile strategy to insert a metal atom into a free-base macrocycle (self-metalation) or to replace an existing metal center with a different metal species (trans-metalation). Self-metalation has been widely investigated in surface science and its mechanism is well established. Metal insertion can occur through incorporation of metal adatoms available on the metallic substrate or through metal atoms supplied by co-evaporation [28]. Depending on substrate reactivity, upon deposition of the molecules on a surface, self-metalation may occur at room temperature or it may require thermal activation. In all cases, the reaction involves deprotonation of the two pyrrolic H atoms, followed by coordination of the incoming metal ion at the macrocycle center [28,29]. Recently, it has been demonstrated that self-metalation of 2HTPP on Pd(100) can be promoted even at room temperature (RT) under NAP conditions, where gas-phase O_2 drives metal insertion via an Eley-Rideal mechanism [30].

In contrast, the metal exchange is rare and poorly explored in surface-supported porphyrins. Trans-metalation proceeds via a redox mechanism in which the original metal center is ejected from the macrocycle, reduced, and replaced by a second metal atom originating either from the substrate adatoms or from deposited atoms, which become the oxidized species. Among the few reported cases, two studies describe the replacement of Ni- and Co-porphyrins grown on Cu(111) by Cu adatoms, promoted by the high substrate reactivity under UHV conditions [31,32]. Hötger *et al.* demonstrated that deposition of Co atoms induces trans-metalation of Fe- and Cu- porphyrins supported on Au(111). Conversely, deposition of Fe atoms onto a monolayer of CoTPyP does not lead to metal exchange [33]. Although the identity of the incoming and outgoing metal species can be controlled, achieving high and tunable reaction yields remains challenging, highlighting the need for a detailed understanding of the factors governing trans-metalation on surfaces.

2.3 Bimetallic Organic Network

Focusing on TPyPs, molecules extensively investigated in this work, each macrocycle is functionalized with four peripheral pyridinic terminations, as shown in Figure 2.2 b). When deposited on weakly interacting substrates, these molecules typically exhibit attractive lateral interactions, self-assembling into large ordered islands [34,35]. As recently investigated in our group in the case of CoTPyP grown on graphene (Gr) on Ir(111), molecules form a close-packed arrangement driven by the optimization of intermolecular interactions between the nitrogen atoms in the pyridinic groups and peripheral hydrogen atoms of neighboring macrocycles, as confirmed by DFT calculations [36]. The advantage of these molecular tectons lies in the possibility of creating bimetallic structures, allowing further tuning of the metal center through lateral coordination.

Specifically, the pyridinic groups can coordinate a second metal atom (M_2) when it is deposited onto the monometallic M_1TPyP layer, yielding a bimetallic M_1TPyP-M_2 structure, as illustrated in Figure 2.3 a), with the additional metal bound at the pyridinic terminations [34–37]. This process effectively generates a macrocycle-like coordination environment at the periphery of the molecule, enabling the design of bifunctional systems in which the central metal (M_1) and the peripheral metal (M_2) can perform complementary catalytic roles. Such heterometallic architectures are particularly relevant for the development of next-generation energy-storage technologies.

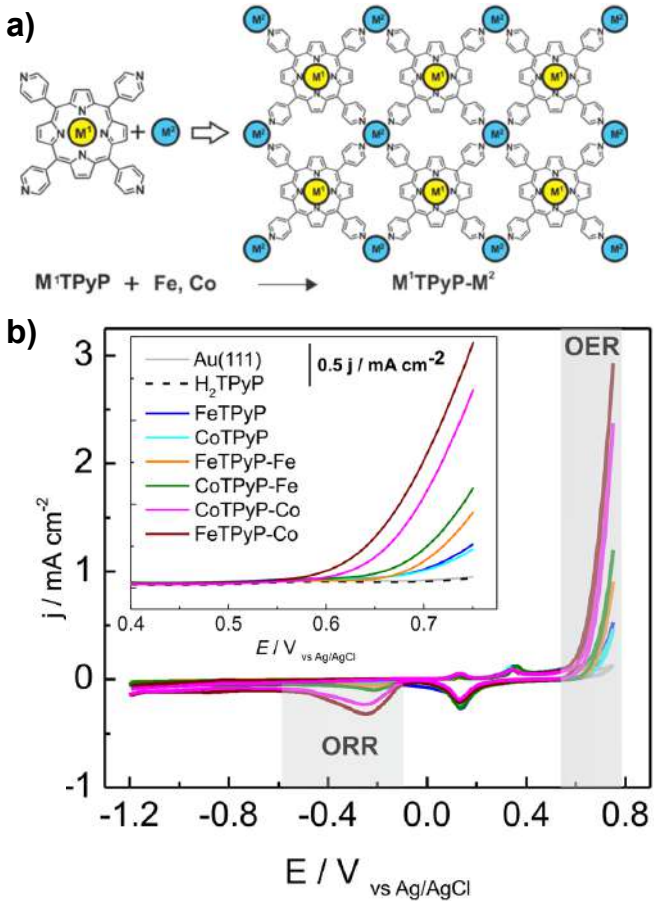

Figure 2.3 a) Representation of a bimetallic 2D network based on TPyP self-assembled on Au(111). b) Cyclic voltammetry at 0.05 Vs^{-1} in NaOH 0.1 M Ar saturated solution for all combinations of the molecular catalysts. The bimetallic compounds exhibit enhanced catalytic performance. Images adapted from [38].

The intermittent nature of renewable sources, such as wind and sun, necessitates the development of efficient, low-cost energy-storage solutions. In this context, metal-air rechargeable batteries are especially promising, as they can be based on earth-abundant materials like Zn, offering a safer, more environmentally friendly and potentially lower-cost alternative to conventional Li-based technologies [8,39,40]. The charge and discharge processes in metal-air batteries are governed by the oxygen evolution (OER) and oxygen reduction (ORR) reactions, respectively [41], described by the equilibrium equation:

$$2H_2O \rightleftarrows O_2 + 4H^+ + 4e^-, \tag{2.1}$$

where the forward reaction corresponds to OER and the reverse to ORR. A major challenge in this framework is defined by the theoretical prediction that the best materials for OER and ORR cannot

coincide [42]. A promising strategy to overcome this limitation involves the design of monophasic bifunctional materials, in which non-equivalent reactive centers are embedded in 2D organic crystals grown on functional templates. In this context, Wurster *et al.* investigated ORR and OER reactions using all combinations of M_1TPyP-M_2 grown on Au(111) ($M_{1,2}$=Fe, Co) where M_2 is co-deposited in UHV and coordinates to the pyridinic nitrogen atoms of four adjacent molecules, as shown in Figure 2.3 a). Electrochemical measurements reveal non-linear enhancement of catalytic activity: the bimetallic systems exhibit conversion rates approximately two orders of magnitude higher than the monometallic counterparts, with FeTPyP-Co displaying the highest activity, Figure 2.3 b), corresponding to an 86-fold increase in O_2 production compared to the monometallic system [38]. These results indicate that the observed cooperative effect arises not from the growth in the number of the active sites but from synergistic modifications of the electronic structure induced by the introduction of the second metal, enabling exploitation of chemically inequivalent reactive centers within the layer.
In our laboratory, we have recently investigated the electronic effects induced by deposition of a second metal onto CoTPyP and MnTPyP monolayers grown on Gr/Ir(111) [35,37]. Both systems undergo similar structural reorganisation upon Co coordination. Focusing on the CoTPyP, the initial monolayer forms a close-packed arrangement, which is subsequently reordered after Co deposition [36]. STM images of the bimetallic CoTPyP-Co layer at partial Co coverage and at saturation (CoTPyP:Co 1:1) are shown in panels a) and b) of Figure 2.4.

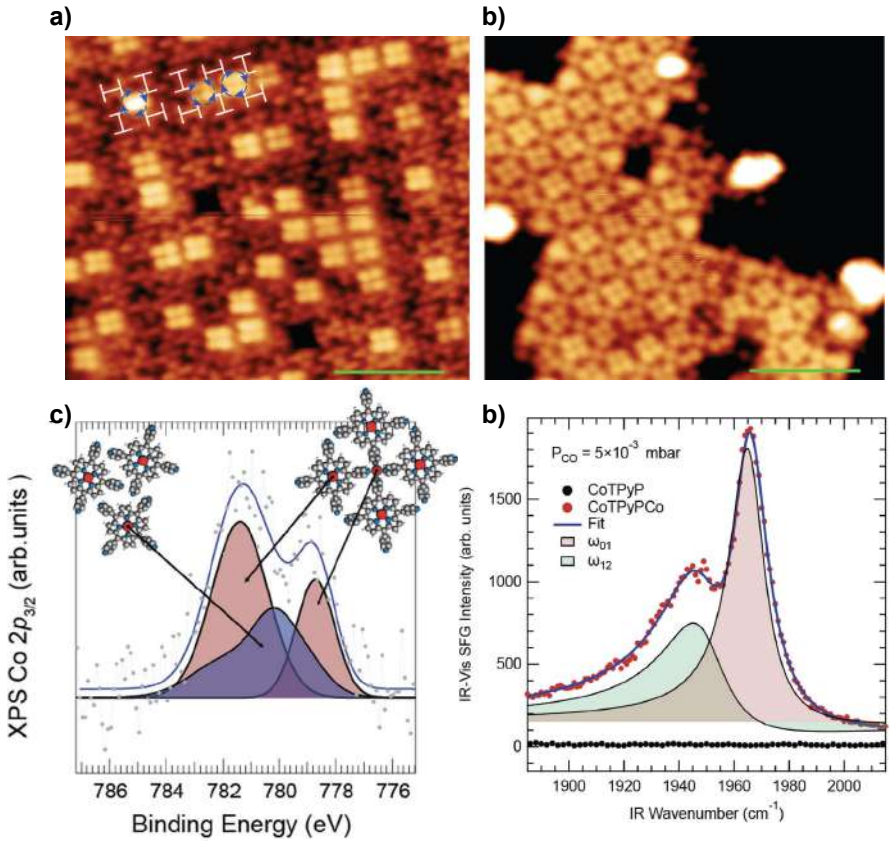

Figure 2.4 a) and b) STM images of CoTPyP-Co molecular layer at partial and full peripheral Co coverage (CoTPyP:Co 1:1), respectively. H-model shapes are superimposed in panel a) to highlight the molecular orientation. Applied bias and tunneling current: V = 2.5 V, I = 60 pA and V = 2.2 V, I= 50 pA, respectively, scale bar: 5 nm. c) Co $2p_{3/2}$ XPS spectra of the CoTPyP-Co monolayer: experimental data (grey dots), best fit (blue solid line) and individual spectral components (red profiles). The blue-filled component corresponds to the contribution of the uncoordinated CoTPyP monolayer. d) Normalized IR-Vis SFG spectra of the internal C–O stretching region, collected in situ in 5 × 10^{-3} mbar CO at room temperature (corresponding to saturation of the Co sites) for the CoTPyP and CoTPyPCo monolayers. Images adapted from [35,36].

In Figure 2.4 a), the layer displays a mixture of uncoordinated molecules and molecules sharing a pyridinic termination, with the different molecular orientations highlighted by the superimposed H-model shape, giving rise to square motifs. DFT calculations indicate that each square represents the pyridinic terminations of four different molecules, with a Co atom tetra-coordinated at the center.
At Co saturation, the layer undergoes further reorganization, as shown in Figure 2.4 b), in which each molecule shares a Co atom. Upon Co coordination, the structural evolution is also accompanied by distinct electronic modifications, as revealed by Co $2p_{3/2}$ core level spectrum shown in Figure 2.4 c). The blue-filled profile corresponds to the monometallic contribution, whereas the Voigt components outlined in red describe the contributions of the bimetallic layer. Upon the formation of the CoTPyP-Co layer, the contribution from the central Co atom shifts to higher binding energy, indicating a change in the oxidation state from +2 to +3. Simultaneously, a new low-binding-energy component emerges attributed to peripheral Co atoms stabilized in the +1 oxidation state, as supported by density functional theory (DFT) simulations. The implications of this electronic reorganization were probed by exposing both systems to carbon monoxide (CO) up to 5×10^{-3} *mbar*. While Co in the monometallic system (**Co**TPyP) is inert toward CO, the bimetallic layer exhibits two vibrational features corresponding to CO adsorbed on peripheral Co atoms: the fundamental 0->1 transition (red) and the hot-band 1->2 transition (green), as evidenced in Figure 2.4 d). DFT calculations attribute this behavior to the fully occupied $3d_{zx,zy}$ orbitals of peripheral Co, capable of π^* bonding with the LUMO of the CO, whereas no contribution arises from Co located in the macrocycle because the Co-N bond length leads to hybridization of the same $3d_{zx,zy}$ orbitals with the surrounding N $2p_z$, thereby hindering CO ligation [35]. Notably, the introduction of the second metal atom also modifies the oxidation state of the center metal. This electronic interaction driven by the organic backbone has been observed for the MnTPyP-Co system as well: the peripheral Co atoms are stabilized in the +1 oxidation state while the central Mn atom undergoes an oxidation from +2 to +3. Consistently, N 1*s* core level displays pronounced shifts of both the pyridinic and iminic components (+1.7 *eV* and +0.9 *eV*, respectively). Upon O_2 exposure, Mn remains inert with Co atoms the only active species in the network. Below 10^{-6} *mbar*, O_2 binds reversibly to Co in a lying-down configuration, identified as the most stable adsorption geometry. This interaction proceeds through a charge transfer mechanism involving the pyridinic moieties and Co atoms, promoting the formation of a metastable superoxo species that can undergo dissociation. Consistently, as the oxygen pressure increases toward the near-ambient pressure regime, O_2 dissociation occurs at room temperature, leading to the accumulation of atomic oxygen at the Co sites with the corresponding oxidation states changed from +1 to +2 [23].
Overall, these results demonstrate that modifications introduced at the peripheral pyridinic terminations are transmitted through the organic backbone, altering the structural and electronic configuration of the pristine layer as well as the oxidation state of the metal centers. These long-range interactions within the bimetallic network give rise to properties that differ fundamentally from those of the corresponding monometallic layer.

2.4 Aim of the Thesis

The aim of this PhD work is to investigate two different porphyrins that share the same Fe-containing macrocycle but functionalized with distinct peripheral groups. Iron was chosen because Fe-containing porphyrins constitute biologically relevant O_2-binding and O_2-activation centers, providing an ideal platform to study fundamental reactivity. Cobalt was selected as the second metal because its coordination at the pyridinic terminations can induce strong structural and electronic modifications, enabling the formation of cooperative bimetallic architectures with enhanced catalytic activity. Specifically, this work aims to elucidate how chemical modifications at the peripheral terminations, together with the effects induced by the deposition of a second metal atom, influence lateral coordinations, as well as the electronic and reactive properties of the resulting metalorganic layers formed on suitable substrates. Panels a) and b) of Figure 2.5 show the two molecular tectons studied: iron tetra-pyridyl-porphyrin (FeTPyP) and ferriprotoporphyrin IX (heme). Both species were deposited

on weakly interacting substrates to probe their intrinsic molecular properties and intermolecular interactions with minimal perturbation from the support.

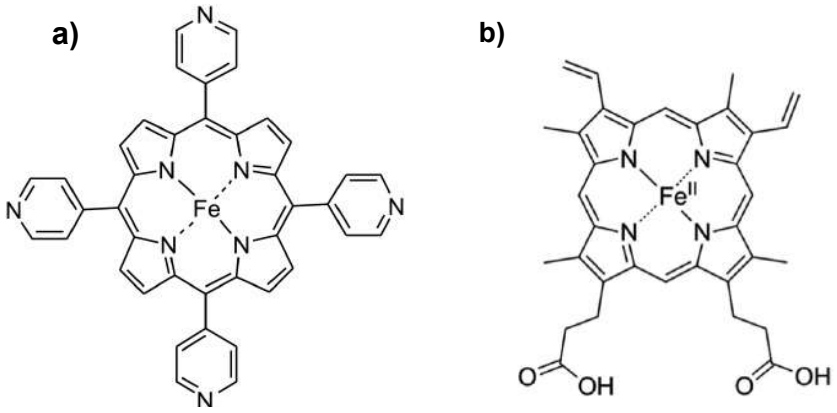

Figure 2.5 Molecules investigated in this PhD work: a) FeTPyP and b) heme.

The first part of the thesis focuses on FeTPyP monolayers grown on Gr/Ir(111). The goal was to characterize the monometallic layer and the modifications induced by cobalt coordination at the pyridinic terminations. To this aim, the structural, electronic and vibrational properties of both systems were examined under UHV conditions as well as under CO and O_2 exposures up to NAP. This approach allows us to determine how the introduction of a second metal atom modifies the local coordination environment, oxidation states and electronic structure of the pristine layer, and how these changes affect the reactivity toward CO and O_2.

CO is widely employed in surface science as a test molecule for identifying reactive metal sites and, in biochemistry, for probing ligand-binding properties and cooperative effects among distinct reactive centers. The interaction with O_2, instead, is a key step for evaluating the potential relevance of these materials in the development of electrodes for emerging metal-air batteries.

To address these aspects, complementary experimental techniques such as scanning tunneling microscopy (STM), infrared-visible sum frequency generation (IR-Vis SFG) and NAP-x-ray photoelectron spectroscopy (XPS) were combined with DFT calculations, providing a comprehensive picture of the properties of the system in UHV (Chapter 4) and under reactive conditions (Chapter 5), both before and after Co deposition. In the results chapter, the characterization under O_2 exposure is presented before CO adsorption. This order facilitates a clearer interpretation of the core-level spectra in both cases, even though, experimentally, CO adsorption was investigated prior to O_2 exposure.

The second part of the thesis focuses on heme monolayers grown on Au(111). To prepare these monolayers, hemin, the commercially available form of heme, was deposited on Au(111). Hemin is the active prosthetic group found in hemoglobin and other heme proteins, in which a chloride ligand stabilizes the Fe centers under ambient conditions. It shares the same porphyrinic macrocycle as FeTPyP but differs in its peripheral substituents, which include carboxylic groups and other substituents rather than pyridinic terminations. The properties of the resulting monolayer were investigated both in UHV (Chapter 6) and under reactive conditions toward CO and O_2 (Chapter 7), with the aim of understanding how the different lateral interactions, and therefore the resulting structural organization, influence the reactivity of the system. Finally, as will be shown, due to the limited purity of the biological starting material from which hemin is obtained, Fe-free molecules were detected in the monometallic layer. This observation motivated the attempt to fill these empty sites by depositing Co atoms, thereby creating a bimetallic structure (Chapter 8). The resulting Co-modified heme layer was characterized in UHV and under O_2 exposure to explore its potential for catalytic processes and energy-storage applications. These studies were carried out using STM, near-edge x-ray absorption fine structure (NEXAFS) and NAP-XPS which provided detailed insights into the structural and electronic properties of the systems.

3 | Experimental Methods

In this thesis, complementary techniques are employed to characterize biomimetic iron-based 2D materials under UHV conditions and to investigate their reactivity under NAP conditions. The principal experimental methods used are IR-Vis SFG, NAP-XPS, and STM, while additional insight is provided by NEXAFS spectroscopy, which is briefly described in this chapter. Although many relevant computational results are reported herein, the underlying methods are not described, as they were developed within the framework of an external collaboration and are therefore not a direct subject of this thesis.

3.1 IR-Vis Sum Frequency Generation Spectroscopy

IR-Vis SFG is a photon-in photon-out surface sensitive technique which provides both vibrational and electronic information about interfaces. As a second-order optical process, it generates a signal only from non-centrosymmetric materials, making it intrinsically sensitive to interfaces [43].
The combination of surface-sensitivity with the long mean free path of IR and Vis photons in the gas phase, makes this technique suitable to study solid-vacuum, solid-liquid, solid-gas and liquid-gas interfaces under both UHV and AP conditions [44,45]. Due to the low cross-section of second-order optical processes, two pulsed laser beams are required to generate a detectable SFG signal: one in the visible range and one in the infrared range, respectively [46]. To produce SFG radiation, these beams must be overlapped both temporally and spatially at the surface. The infrared beam can excite vibrational transitions when its frequency matches a vibrational resonance of the system, while the visible beam induces an electronic transition to an excited virtual state (when non-resonant to an electronic transition). When the system relaxes it emits a photon which has the energy equal to the sum of the energy of the IR and Vis beams:

$$\omega_{SFG} = \omega_{IR} + \omega_{VIS} \tag{3.1}$$

A schematic of this process is shown in Figure 3.1. In our setup, a narrowband visible beam at a fixed wavelength, 532 *nm*, is coupled with a tuneable IR beam 2300 - 10000 *nm*. SFG intensity is then measured as a function of the IR energy using a one-dimensional scanning acquisition mode, allowing identification of molecules and gas adsorbates through their specific vibrational energies.

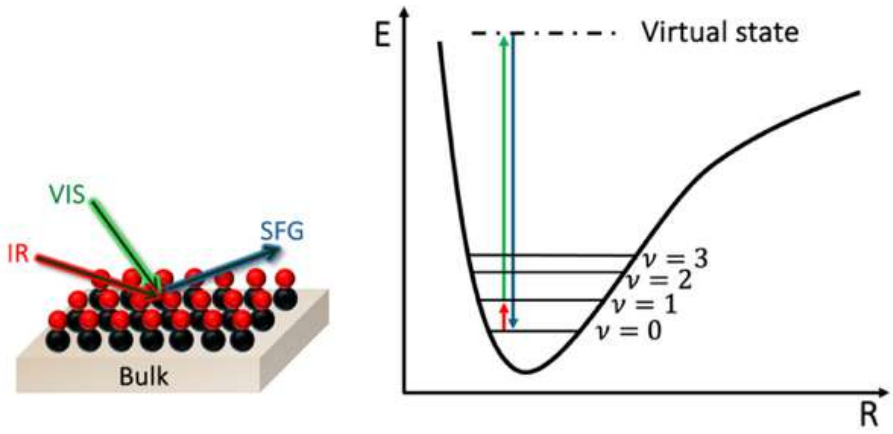

Figure 3.1 Left) SFG signal generated from two laser beams, IR and visible, impinging on a surface. Right) Schematic representation of SFG transitions.

3.1.1 Theoretical Description

Under the electric dipole approximation, the response of atoms, molecules, nanoparticles, and solid-state materials to a weak electromagnetic field is primarily characterized by their electric dipole moments [43].
When an oscillating electric field *E(t)* interacts with matter, it induces a change in the material's dipole moment per unit volume, known as the polarization *P(t)*. *P* depends on the strength of the incident optical electric field. In the regime of linear optics, where the electric field is sufficiently weak, polarization as a function of time is typically expressed by the following equation:

$$P(t) = \varepsilon_0 \chi^{(1)} E(t), \tag{3.2}$$

where ε_0 is the vacuum dielectric constant and $\chi^{(1)}$ is the first order susceptibility of the material [47]. In the presence of strong electric fields ($E \sim 10^6$ *V/m*), light can excite the system into an anharmonic regime and therefore the relation above is no longer valid. It is necessary to expand the polarization as a power series in *E(t)*:

$$\begin{aligned} P(t) = \ & \varepsilon_0 [\chi^{(1)} E(t) + \chi^{(2)} E^2(t) + \chi^{(3)} E^3(t) + \cdots] \\ \equiv \ & P^1(t) + P^2(t) + P^3(t) + \cdots, \end{aligned} \tag{3.3}$$

where the coefficients correspond to higher order susceptibilities [47,48]. It is possible to generalize this description considering the vectorial nature of $\boldsymbol{E}(t)$ and $\boldsymbol{P}(t)$ using tensorial notation for the susceptibilities: $\chi^{(1)}$ becomes a second order tensor and $\chi^{(2)}$ a third order tensor.
If the external impinging electric field is given by the sum of two different components, oscillating at different frequencies, it can be written in the form:

$$\boldsymbol{E}(\boldsymbol{r}, t) = \boldsymbol{E_1}(\omega_1) e^{-i(\omega_1 t + \varphi_1)} + \boldsymbol{E_2}(\omega_2) e^{-i(\omega_2 t + \varphi_2)} + c.c, \tag{3.4}$$

where $\boldsymbol{E}_n(\omega_n) = \frac{1}{2} \boldsymbol{E}_n e^{i \boldsymbol{k}_n \cdot \boldsymbol{r}}$ and $\boldsymbol{E}_n$ is the product of the amplitude and the polarization vector [47].
Using the relation $\boldsymbol{E}_n(-\omega_n) = \boldsymbol{E}_n{}^*(\omega_n)$ a more compact form of (3.4) can be written:

$$\boldsymbol{E}(\boldsymbol{r}, t) = \sum_n \boldsymbol{E}_n(\omega_n) \, e^{-i(\omega_n t - \varphi_n)}, \quad n = -2, -1, 1, 2 \tag{3.5}$$

where the sum extends over positive and negative frequencies, with $\omega_{-n} = -\omega_n$, considering the complex conjugate [47]. It is now possible to write a cartesian component of the second order polarization as:

$$P_i^{(2)}(\boldsymbol{r}, t) = \varepsilon_0 \sum_{jk} \sum_{nm} \chi_{ijk}{}^{(2)}(\omega_n + \omega_m;\ \omega_n, \omega_m) E_j(\omega_n) E_k(\omega_m) e^{-i[(\omega_n + \omega_m)t - (\varphi_n + \varphi_m)]}, \tag{3.6}$$

where it is easy to see that the resulting components of the second order polarization oscillate at different frequencies $\omega_n + \omega_m$ with respect to the oscillation frequencies of the field components. The sum over n and m produces different components: second harmonic generation (SHG) at $2\omega_1$ and $2\omega_2$, difference frequency generation (DFG) at $\omega_1 - \omega_2$, sum frequency generation (SFG) at $\omega_1 + \omega_2$, and optical rectification (OR) that is a non-oscillating term [47].

We can now focus on the SFG component, with $\omega_3 = \omega_1 + \omega_2$, that becomes:

$$P_i^{SFG}(\boldsymbol{r},t) = \varepsilon_0 \sum_{jk} [\chi_{ijk}^{(2)}(\omega_3;\ \omega_1,\omega_2)E_j(\omega_1)E_k(\omega_2) + \chi_{ijk}^{(2)}(\omega_3;\ \omega_2,\omega_1)E_j(\omega_2)E_k(\omega_1)]\, e^{-i(\omega_3 t-\varphi_3)} + c.c, \tag{3.7}$$

using the relation $\chi_{ijk}^{(2)}(-\omega_3;\ -\omega_1,-\omega_2) = \chi_{ijk}^{(2)}(\omega_3;\ \omega_1,\omega_2)^*$ [47].
Assuming that the nonlinear susceptibility has intrinsic permutation symmetry, $\chi_{ijk}^{(2)}(\omega_3;\ \omega_1,\omega_2) = \chi_{ikj}^{(2)}(\omega_3;\ \omega_1,\omega_2)$ indexes j and k can be interchanged, thus SFG polarization can be expressed by [47]:

$$\begin{aligned} P_i^{SFG}(\boldsymbol{r},t) &= 2\varepsilon_0 \sum_{jk} \chi_{ijk}^{(2)}(\omega_3;\ \omega_1,\omega_2)E_j(\omega_1)E_k(\omega_2)\, e^{-i(\omega_3 t-\varphi_3)} + c.c \\ &= \frac{1}{2}\varepsilon_0 \sum_{jk} \chi_{ijk}^{(2)}(\omega_3;\ \omega_1,\omega_2)E_{1,j}E_{2,k}\, e^{i(\boldsymbol{k}_3\cdot\boldsymbol{r}-\omega_3 t-\varphi_3)} + c.c, \end{aligned} \tag{3.8}$$

and neglecting the spatial and temporal dependence a more compact form is obtained:

$$P_i^{SFG} = \varepsilon_0 \sum_{jk} \chi_{ijk}^{(2)} E_{1,j}E_{2,k} \tag{3.9}$$

Equation 3.9 is useful to derive a fundamental property of the SFG signal that is the surface specificity, since $\chi^{(2)}$ vanishes for centrosymmetric materials.
When parity symmetry is applied to the polarization and electric field vectors, they change sign (because they are polar vectors), while $\chi_{ijk}^{(2)}$ does not change sign because a centrosymmetric material is identical under inversion, thus $\chi_{ijk}^{(2)} = \chi_{-i-j-k}^{(2)}$ [47].
It is then possible to write:

$$-P_i^{SFG} = \varepsilon_0 \sum_{jk} \chi_{ijk}^{(2)} E_{1,j}E_{2,k} = P_i^{SFG} \tag{3.10}$$

which only holds when $\chi_{ijk}^{(2)}$ is zero [47,48].
This property is largely exploited in SFG spectroscopy experiments: since gas phases and most bulk materials are centrosymmetric, they are not SFG active and they don't contribute to the SFG signal. Therefore, SFG spectroscopy is the perfect technique to obtain vibronic information about surfaces and interfaces that are intrinsically non-centrosymmetric media.

SFG in Reflection Geometry

In our case, the impinging electric fields consist of a visible beam and a tuneable infrared beam. The visible beam is green (532 *nm*) and couples with the HOMO-LUMO gap of molecules; this choice is functional because detection is more efficient in the visible range and at this frequency radiation is not ionizing, thus avoiding beam damage of organic materials [48].
In the description of reflection at a surface, it is useful to decompose an incident field $\boldsymbol{E}_I$ into components polarized parallel (*p*) and perpendicular (*s*) to the incidence plane as follows:

$$\begin{aligned} E_{I,x} &= -E_p \cos\theta \\ E_{I,y} &= E_s \\ E_{I,z} &= E_p \sin\theta, \end{aligned} \tag{3.11}$$

where θ and coordinate convention refers to Figure 3.2. The total electric field at the surface is given by the sum of the incident and reflected beams [48].

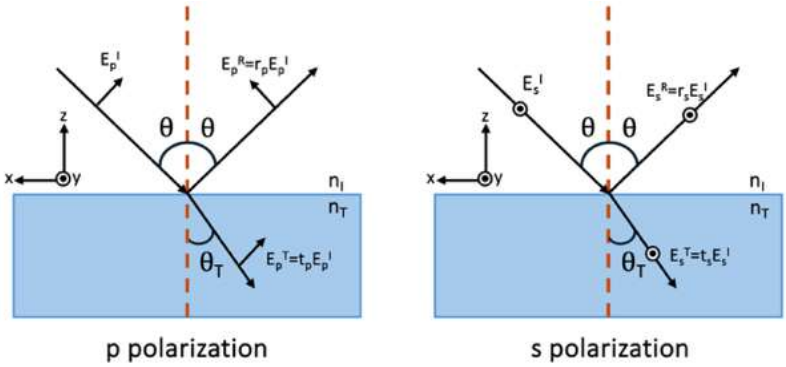

Figure 3.2: Reflection at an interface for p *and* s *polarized radiation. Image adapted from [48].*

If we define the Fresnel amplitude coefficients for reflection (r_p, r_s) as in [48], the components of the total electric field at the surface can be written as:

$$\begin{aligned} E_{I,x} &= -\big(1 - r_p\big)E_p \cos\theta \equiv K_x E_p \\ E_{I,y} &= (1 + r_s)\, E_s \equiv K_y E_s \\ E_{I,z} &= \big(1 + r_p\big)E_p \sin\theta \equiv K_z E_p \end{aligned} \tag{3.12}$$

The SFG-induced polarization in Equation 3.9 can now be expressed in terms of the amplitude of the incident fields $E_{I,1} = E_{IR}$ and $E_{I,2} = E_{VIS}$ exploiting Equation 3.12:

$$P_i^{SFG} = \varepsilon_0 \sum_{jk} \chi_{ijk}{}^{(2)} K_{IR,j} E_{IR} K_{VIS,k} E_{VIS} \tag{3.13}$$

The non-linear polarization generates a surface-bound SFG electric field. The emission angle of the SFG signal is determined by the phase-matching condition that expresses the momentum conservation parallel to the interface:

$$n_{SFG}\theta_{SFG} \sin\theta_{SFG} = n_{IR}\theta_{IR} \sin\theta_{IR} + n_{VIS}\theta_{VIS} \sin\theta_{VIS}\,, \tag{3.14}$$

where *n* is the refractive index of the propagation medium, *k* the wavevector and θ the angle between the beam and the normal to the surface [48], as depicted in Figure 3.3.

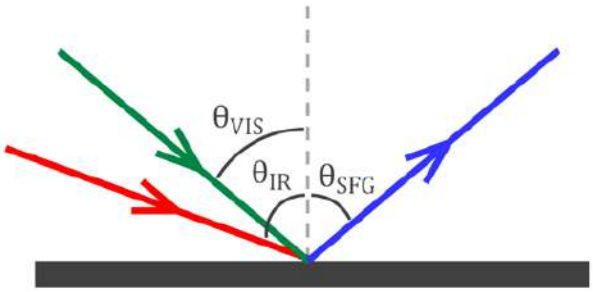

Figure 3.3: Generation of an SFG signal on a surface from IR and visible laser beams in reflection geometry Image taken from [23].

In our case, all beams propagate in the same medium, thus refractive indexes can be neglected. The generated SFG is related to the second order polarization by the non-linear SFG Fresnel factors L_i defined by Lambert *et al.* [48]:

$$E_{i,SFG} = L_i P_i^{(SFG)} \tag{3.15}$$

The intensity of the SFG signal is proportional to the square modulus of the electric field, therefore the following relations hold:

$$\begin{aligned} I_{SFG} &\propto \left| \sum_i E_{i,SFG} \right|^2 \\ &\propto \left| \sum_i L_i P_i^{(SFG)} \right|^2 \\ &\propto \left| \varepsilon_0 \sum_{jk} L_i \, \chi_{ijk}{}^{(2)} K_{IR,j} E_{IR} K_{VIS,k} E_{VIS} \right|^2 \end{aligned} \tag{3.16}$$

According to the axis convention of Figure 3.2 we note that *p* polarization can have x and z components, while *s* polarization only has y components.
The incident beam's polarizations determine the susceptibility tensor's components that can be probed; thus, it is important to have the control over polarizations in SFG experiments. The standard SFG notation for polarization uses three indexes i, j, k where each index can be *p* or *s* and they refer to each beam polarization in order of decreasing energy: i-SFG, j-Vis and k-IR [43,45,48].

Microscopic Approach

In the previous paragraph the relation between SFG intensity and $\chi^{(2)}$ was established, Equation 3.16, where among the various terms only the second order non-linear susceptibility changes significantly with infrared wavenumber. It is therefore solely responsible for the vibrational information obtained from a sum frequency spectrum [48].
In a microscopic approach, radiative electric field induces a dipole moment μ:

$$\mu = \mu_0 + \alpha \boldsymbol{E} + \beta \boldsymbol{E}^2 + \gamma \boldsymbol{E}^3 \tag{3.17}$$

where μ_0 is the static dipole of the material, α its polarizability and β, γ are the first and second order hyperpolarizabilities respectively, non-linear effects of the molecules adsorbed on the surface [49]. The tensor β is a third-rank tensor, the same dimension of $\chi^{(2)}$, describing the non-linear response of molecules on the surface to incident electric fields: different components refer to different vibrational modes. We can use a molecular bound coordinate system identified with indexes (a, b, c) instead of the surface one (i, j, k), an example is reported in Figure 3.4 where a molecule adsorbed on the surface is tilted of a θ angle. The molecular coordinate system is simply related to the surface one by three rotational matrixes $R(\psi)R(\theta)R(\varphi)$ that refer to the Euler angles (ψ, θ, φ).
The hyperpolarizability tensor becomes $R(\psi)R(\theta)R(\varphi)\beta$ and its macroscopic averaging can be written as:

$$\chi_{ijk}{}^{(2)} = \frac{N}{\varepsilon_0} \sum_{abc} \langle R(\psi)R(\theta)R(\varphi)\beta_{abc} \rangle \tag{3.18}$$

where N is density of adsorbed molecules and the matrix element represents an orientational averaging [48].

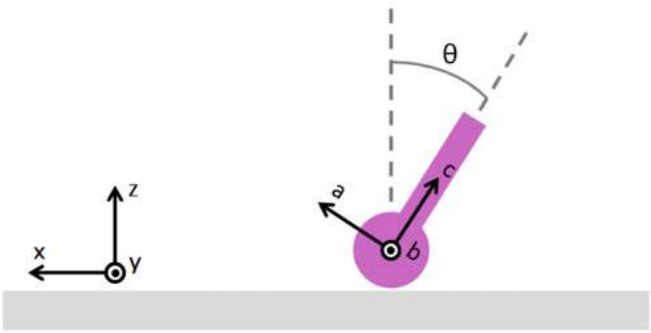

Figure 3.4: A molecule adsorbed on a surface, tilted at an angle θ. The two coordinate systems are related by a rotation matrix $R(\theta)$. Image taken from [48].

A quantum mechanical expression for β_{abc} can be derived using perturbation theory [50]. In the case of visible radiation ω_{VIS} far from electronic resonances and infrared radiation ω_{IR} close to a vibrational resonance ω_0, the following simplified version can be used:

$$\beta_{abc} = \frac{1}{2\hbar} \frac{M_{ab} T_c}{\omega_0 - \omega_{IR} - i\Gamma} \tag{3.19}$$

where Γ^{-1} is the relaxation time of the vibrational excited state, M_{ab} and T_c are the Raman and infrared transition moments respectively, as defined by Lambert *et al.* [49]. Equation 3.19 has the shape of a Lorentzian resonance and when inserted in Equation 3.18 it reveals the increase of the SFG signal intensity close to a vibrational resonance.
In addition to the requirement of non-centrosymmetry, another SFG selection rule can be derived from Equation 3.19: a resonance must be both Raman and Infrared active to be observed through an SFG transition [43]. The surface under investigation needs to have a net dipole (the component normal to the surface) in order to generate an SFG signal: an SFG-active medium should have a net dipole both locally and at a macroscopic level, at least in the range of a wavelength, and the external electric field should modify both the dipole and polarizability to satisfy the IR and Raman selection rules, respectively [48,51]. This requirement is not limiting, as the interaction with a surface usually results in a broken molecular symmetry, making even centrosymmetric molecules (that can't have both IR and Raman active modes according to the mutual exclusion rule) detectable with SFG [48,51].

3.1.2 Lineshape Modeling

The description that led us to Equation 3.19 is based on a simplified representation of real systems: a generic system composed of molecules adsorbed on a surface produces an SFG signal that is the combination of both the molecular and substrate contributions. The molecular contribution to the susceptibility tensor $\chi_{RES}^{(2)}$ varies significantly as the infrared radiation is tuned through the vibrational resonances. The substrate contribution doesn't change, in a first approximation, with the infrared tuning and, together with the constant part of the molecular susceptibility, it contributes to the non-resonant $\chi_{NR}^{(2)}$ susceptibility, usually approximated with a constant value. The total susceptibility can be therefore modelled with two separated contributions accounting for the molecular and bulk susceptibilities [43]:

$$\chi^{(2)} = \chi_{NR}^{(2)} + \chi_{RES}^{(2)} \tag{3.20}$$

When the substrate is metallic $\chi_{NR}^{(2)}$ can contribute significantly (as in the case of gold), due to a strong electronic response in the visible range, that can be mainly caused by surface plasmon resonances [48] and interband or intraband transitions [45,52].

The creation of excitons in semiconductor materials can also give rise to an intense non-resonant signal [52]. To a practical extent, it is common to replace the susceptibility tensor introducing an effective scalar susceptibility in the form [46]:

$$\chi^{(2)}(\omega_{IR}) = A_{NR}e^{i\varphi_{NR}} + \sum_n \frac{A_n e^{i\varphi_n}}{\omega_{IR} - \omega_n + i\Gamma_n} = e^{i\varphi_{NR}}\left[A_{NR} + \sum_n \frac{A_n e^{i\Delta\varphi_n}}{\omega_{IR} - \omega_n + i\Gamma_n}\right] \tag{3.21}$$

where the sum runs over the various resonances of the system. The parameters are real-valued amplitudes A_n, phases φ_n, resonance frequencies ω_n and resonance broadenings Γ_n related to the respective decoherence times. The non-resonant phase has been factorized introducing the phase differences $\Delta\varphi_n$, that represent the relative phase-shift of the nth resonance to the non-resonant background [46].
This interference term whether constructive, destructive, or intermediate can significantly affect the SFG peaks, as explained in [43]. The amplitude terms A_n are proportional to the density of molecules N and to the Raman and IR transition moments, respectively M_n and T_n:

$$A_n \propto NM_nT_n\delta\varrho_n\,, \tag{3.22}$$

and to the population difference between the ground and excited state $\delta\varrho_n$ [53].
Finally, combining Equation 3.21 and 3.16, it is possible to obtain the following expression:

$$I_{SFG}(\omega_{IR}) \propto \left|A_{NR} + \sum_n \frac{A_n e^{i\Delta\varphi_n}}{\omega_{IR} - \omega_n + i\Gamma_n}\right|^2 I_{VIS}I_{IR}(\omega_{IR}), \tag{3.23}$$

where the SFG intensities is proportional to the incoming infrared and visible beam intensities and depends on the infrared frequency ω_{IR}.
The frequency dependence of $I_{IR}(\omega_{IR})$ has been explicated to emphasize that, while visible radiation intensity is constant (except for laser instabilities), the infrared beam intensity strongly depends on the generated IR frequency due to the generation process itself and the increased absorption at specific frequencies. As a final remark, which will be useful in this work, we recall that in the case of surfaces or 2D materials in general the SFG signal is proportional to the square of the surface coverage/density.

3.1.3 Experimental Setup and Data Analysis

To obtain a reliable surface characterization, it is important to prepare the samples in a controlled environment to prevent contamination both during growth and the measurements. For this reason, the SFG setup is coupled to a UHV chamber (the preparation chamber) where samples are loaded and prepared. The presence of a low energy electron diffraction (LEED) setup is helpful to obtain information about the surface structure and crystallinity of the sample, while Auger electron spectroscopy (AES) provides chemical information about the surface composition.
The experimental chamber consists of a cylindrical diamagnetic stainless steel UHV vessel with 30 *cm* diameter, a pumping section and a high-pressure cell (HP cell) designed for the SFG experiments. The three sections are made independent through gate valves. The pumping section is located below the preparation chamber and hosts a cryogenic pump coupled with a titanium sublimation pump (TSP) and an ion pump. The preparation chamber is also pumped by a turbo molecular pump. When the gate valve between the preparation chamber and the pumping section is opened, a background pressure of 7×10^{-11} *mbar* can be achieved.

The presence of a fast entry lock loading system allows the sample loading into the UHV system without breaking the vacuum. It is independently pumped by a turbomolecular pump coupled with a backing pump for the pre-pumping, which grants a background pressure lower than 10^{-8} *mbar*.
A magnetic transfer arm is employed to load (or unload) the sample-holder from the fast entry lock to the two manipulators, one located in the preparation chamber and the one present in the HP cell. The sample-holder allows resistive sample heating up to 1300 *K* in UHV and 700 *K* at 1 *bar*. The sample is supported by a twisted tantalum wire cage (0.2 *mm* diameter) fitting in a groove on the sample's side. Such configuration minimizes the mechanical stress due to the wire thermal expansion and contraction, thus reducing sample misalignment and mechanical stress during heating and cooling.
The sample's temperature is measured via a K-type chromel-alumel thermocouple spot-welded at the back of the sample. The HP cell is located behind the preparation chamber and coupled with the SFG box. It consists of a steel cylinder (6 *cm* diameter) and two barium fluoride (BaF_2) windows that allow the transmission of the visible, IR and SFG radiation with nearly 100% efficiency. They can sustain a negative pressure difference up to 1 *bar*. IR and visible beams do not impinge at normal incidence with respect to the window surfaces, to avoid back reflection into the SFG setup (that may damage the optics). The cell is equipped with its own manipulator that provides (x,y,z) translations, polar rotation and the possibility to tilt the sample. Pressure is measured through a full range gauge (FRG) working in the 5×10^{-9}-10^{3} *mbar* range, that is made of a combination of a cold cathode gauge and a Pirani gauges. A gas line, which can handle up to three different gases, is present. The SFG cell can be independently pumped by a scroll pump and by a turbo pumping station.
As said before, the preparation chamber is dedicated to the preparation and characterization of samples. It is equipped with a LEED setup and an AES setup. A mass spectrometer, an ion gun (used to sputter the sample) and a gas line are also present. The pressure is measured using an ion gauge working in the range 7×10^{-11}-10^{-3} *mbar*. A sublimation evaporator is mounted on the chamber: the molecules are contained in a quartz crucible heated by a surrounding tungsten filament. For metals evaporation (in our case Co) a pure metal filament is mounted on the same evaporator and metal atoms are evaporated by resistive heating of the filament itself. The deposition rate can be monitored using a retractable quartz balance. The manipulator provides four degrees of freedom: the three translations (x,y,z) and the polar rotation.
SFG measurements were performed at the Visible and Infrared Spectroscopy Laboratory (VISpLab, University of Trieste) exploiting a customised setup purchased from the Lithuanian laser manufacturing company EKSPLA. All the components are controlled via LabVIEW software. Samples are prepared in a UHV chamber and SFG spectra are acquired in an HP cell that can be isolated from the preparation chamber by a gate valve.
SFG measurements are performed using pulsed laser radiation, specifically a green beam at 532 *nm* and infrared radiation in the range 2300 - 10000 *nm*, both generated starting from the 1064 *nm* fundamental of the laser. The two beams overlap at the sample to generate SFG output radiation.
The SFG signal intensity is measured as a function of the scanned IR wavenumber. The SFG optical setup can be divided in four principal stages as shown in Figure 3.5: fundamental IR laser radiation generation and amplification, second harmonic generation, tunable IR generation and finally SFG generation and detection [54].
The principal components and characteristics of each section are described in the following:

- a class IV PL2230 Series Laser, generating the fundamental infrared pulsed radiation at 1064 *nm*. The pulses are 30 *ps* long with a repetition rate of 50 Hz and maximum pulse energy of 25 *mJ.* The peak power of the fundamental radiation, defined as $P = E/\Delta t$ (*E* being the maximum pulse energy and Δt the pulse duration) is 1 *GW*, that gives 1.25 *W* mean power. The beam diameter is 6 *mm* [55].
- The green second harmonic radiation at 532 *nm* is generated in a H500 Harmonic Unit. Three outputs are produced at this stage: a beam at the fundamental wavelength with maximum pulse energy of 15 *mJ* and two visible beams. One of the visible beams, with 1 *mJ* maximum energy per pulse, is directly used to produce SFG radiation at the sample while the other, with 10 *mJ*

maximum energy per pulse, is exploited to generate the tunable IR radiation. In this unit the temporal overlap of IR and visible pulses can be modified by means of a delay line [54].

- An Optical Parametric Generator PG501/DFG1P exploits the fundamental radiation and one of the visible beams to generate 2300 - 10000 *nm* tunable mid-IR radiation with measured pulse average energy of 200 *mJ* [54].
- In the SFG box the polarizations of the tunable mid-IR and visible beams are selected, and the beams are spatially overlapped on the sample generating a SFG signal. The SFG passes through a monochromator to remove external contributions and is detected by a photomultiplier tube.

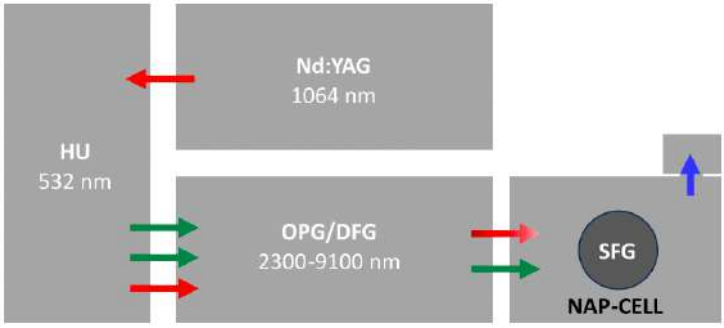

Figure 3.5: Scheme of the experimental setup (top view). The fundamental 1064 nm IR beam is generated in the laser unit, then enters Harmonic Unit (HU) to generate the second harmonics. Tunable IR radiation is provided by the OPG/DFG unit and the final IR and VIS beams are conveyed to the sample in the SFG box. The SFG radiation thus generated reaches the monochromator before being detected [54].

It is important to keep in mind that, while visible beam has constant energy and can only be affected by laser power instabilities with time, part of the generated mid-IR photons have high probability to be absorbed by air as their frequencies match the roto-vibrational spectrum of gas phase H_2O and CO_2 [56]. To minimize the presence of water vapour and other gas phase absorber molecules, the optical setup up to the end of the OPG/DFG box in Figure 3.5 is fluxed with N_2. However, the last part of the IR optical path (about 50 *cm*) is in air, resulting in the formation of fine absorption features in the IR radiation profile measured before its arrival at the sample: when analysing SFG spectra it is thus important to consider this effect to properly normalize the data.
Therefore, it may be necessary to normalize the data with a reference spectrum from a surface yielding no resonant contribution (like e.g. a GaAs single crystal surface or an Au(111) termination). Similarly, as done in this work, it can be sufficient to normalize the SFG spectra by the measured visible and IR impinging beam intensities to obtain a reasonable normalization. Therefore, starting from Equation 3.23, the normalized SFG intensities used is:

$$I_{norm}(\omega_{IR}) = \frac{I_{SFG}(\omega_{IR})}{I_{VIS}I_{IR}(\omega_{IR})} \propto \left| A_{NR} + \sum_n \frac{A_n e^{i\Delta\varphi_n}}{\omega_{IR} - \omega_n + i\Gamma_n} \right|^2 \tag{3.24}$$

The normalized SFG spectra were then analyzed by least-squares fitting to the widely adopted parametric, effective expression of the nonlinear second-order susceptibility described in the previous section [44,57]. In the graphs presented in this thesis, we plot the normalized IR–Vis SFG signal intensity (line dots), together with the best fit (lines) and the deconvolution of each n^{th} resonance with its interference with the non-resonant background (color-filled profiles). The latter are calculated with the parameters obtained from the fitting procedure keeping in mind that multiplet solutions are possible due to the non-unicity of the parameter sets [46].

Moreover, when necessary to account for sample inhomogeneity, the lineshape was convoluted with a Gaussian envelope. The latter is typically set and kept to zero when inhomogeneous broadening is negligible compared to the homogeneous contribution [58].

3.2 X-Ray Photoelectron Spectroscopy

XPS is a photon-in/electron-out technique which is largely employed to investigate 2D materials and surfaces thanks to its chemical and surface sensitivity.
To visualize the photoemission process the so-called three-step model is often employed. It is an approximation developed by Berglund and Spicer [59] where the photoemission event is illustrated as follows:

1. The electron absorbs a photon and is excited to an energy level above the vacuum level.
2. The excited electron travels inside the material and reaches the surface.
3. The electron crosses the surface as a plane wave and is released into vacuum, where it can be finally detected.

The kinetic energy E_k of the ejected electron is given by:

$$E_k = h\nu - E_B - \phi_s, \tag{3.25}$$

where E_B is the binding energy and ϕ_s the work function of the sample. The schematic representation of the photoemission process in Figure 3.6 shows some sharp core level peaks and a broad valence band feature, with E_F the Fermi level and E_{VAC} the vacuum level. The transition probability between an initial ground state ψ_i and a final state ψ_f is approximated by Fermi's golden rule:

$$\omega_{fi} \propto \frac{2\pi}{\hbar}\left|\langle\psi_f|H_I|\psi_i\rangle\right|^2 \delta\left(E_f - E_i - h\nu\right) \tag{3.26}$$

where $H_I = \frac{-e}{mc}\boldsymbol{A}\cdot\boldsymbol{p}$, $\boldsymbol{A}$ is the electromagnetic vector potential and $\boldsymbol{p}$ the electronic momentum operator. The relevant information about the direct photon-induced transition is contained within the transition matrix element $M_{fi} = \langle\psi_f|H_I|\psi_i\rangle$.

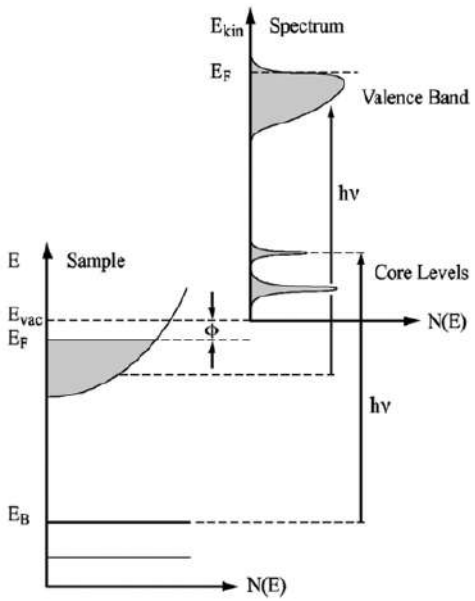

Figure 3.6 Schematic representation of the photoemission process. On the left the density of states of the sample, on the right the corresponding spectrum with both core levels and valence band features. Image from [60].

If the wavelength of the incoming radiation is large compared to atomic dimensions, the reduced transition matrix element can be expressed, within the electric dipole approximation, as:

$$M_{fi} \propto \langle \psi_f | \boldsymbol{d} | \psi_i \rangle = -e \langle \psi_f | \boldsymbol{r} \cdot \hat{\boldsymbol{e}} | \psi_i \rangle, \tag{3.27}$$

where $\boldsymbol{d}$ is the electric dipole operator, $\boldsymbol{r}$ the position operator and $\hat{\boldsymbol{e}}$ the polarization unit vector. The initial and final state wave functions are generally not known, but within the *one-electron view approximation*, they can be expressed as a product of the single-electron wave function and the $(N-1)$ electron wave function of the remaining system [61].
Therefore, the final state wave function is expressed as a product of a plane wave, ϕ^{f,E_k}, and the sum of the possible final states of the $N-1$ system, $\sum_s \psi_{f,s}\,(N-1)$, with energy $E(N-1)$. The initial state wave function is expressed as a product of the orbital from which the electron originated, $\phi^{i,k}$, and the wave function describing the remaining electrons, $\psi_i(N-1)$ with energy $E(N)$ [61]:

$$\langle \psi_f | \boldsymbol{r} | \psi_i \rangle = \langle \phi^{f,E_k} | \boldsymbol{r} | \phi^{i,k} \rangle \sum_s \langle\, \psi_{f,s}\,(N-1) | \psi_i(N-1) \rangle\,, \tag{3.28}$$

where the index *k* indicates that the electron with quantum number *k* has been photoemitted. The last term in Equation 3.28 represents the overlap between the total wave function of the $N-1$ electrons in the final and in the initial state. If one considers that the orbitals are locked in place and in energy before and after the excitation, $\psi_{f,s*}\,(N-1) = \psi_i(N-1)$, where s* is the only state in the sum that gives a non-zero term, one obtains the so-called *frozen orbital approximation*. This approximation allows to measure the negative Hartree-Fock energy, also called Koopmans' energy [62], which represents the energy of a system where the electron-electron interaction is neglected [61]. In other words, it corresponds to the negative of the orbital energy of the photoemitted electron (before emission). In Figure 3.7, an XPS spectrum with and without e-e interaction is shown.

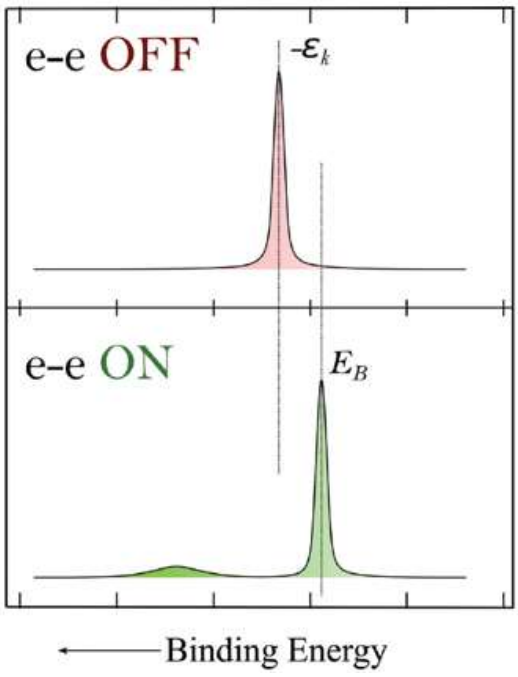

Figure 3.7 Schematic diagram of a photoemission spectrum with electron-electron interaction off (top) and with electron-electron interaction on (below). The e-e interaction leads to a line accompanied by so-called satellites, which reflect internal excitations of the system from which photoionization has taken place. Image from [63].

Although this approximation provides some insight into the XPS process, a more advanced treatment is needed to fully capture the photon-electron interaction and the effects of core-hole creation. If more than one coefficient in the sum over s in Equation 3.28 contributes significantly, this will be reflected by satellite lines in the spectra, as shown in the bottom panel of Figure 3.7.
The two main satellite features are divided into shake-up and shake-off contributions. Both are excited final states with the distinction that shake-off satellites are doubly ionized. For molecular samples, these appear in X-ray Photoelectron (XP) spectra as discrete peaks, as illustrated in Figure 3.8 b), while it is slightly different for metals. The most common excited final state in metals involves the creation of electron-hole pairs: an electron is promoted from just below the Fermi level into the conduction band. Due to the continuous nature of the electronic band structure in metals, a nearly infinite number of final states are available. This leads to a characteristic asymmetry of the main photoemission line towards higher binding energies, as illustrated in Figure 3.8 a).

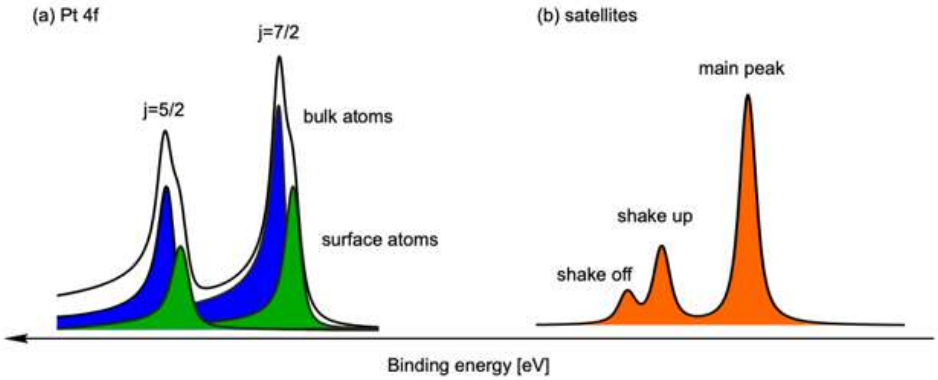

Figure 3.8 An illustration of a measured XP spectra. a) shows a Pt 4f XP spectrum, which exhibit spin-orbit splitting and chemical shifts. b) shows an example spectrum with shake-up and shake-off satellite peaks. Image from [64].

Since the final state includes the ion from which the photoelectron was emitted, the presence of an unpaired electron must be taken into account. In XPS, the total spin of the final state is $^1/_2$, as the emission of a photoelectron creates a single core hole, corresponding to one unpaired electron. If the orbital angular momentum of the electron is greater than zero, all but *s* electrons, the energy level splits into two distinct components due to spin-orbit coupling. This results in two peaks in the XP spectrum, a phenomenon known as spin-orbit splitting. As an example, consider photoemission from the Pt 4*f* core level. Electrons in a *f* orbital have an angular orbital momentum $l = 3$, leading to the total angular momenta $J = {}^5/_2$ and $^7/_2$ due to the LS coupling, as shown in Figure 3.8 (a).
In special cases, a splitting can also be observed for *s* orbitals. This happens when the system under study has an unfilled valence shell configuration [61]. After photoemission, this valence electron spin interacts with the angular momentum of the core hole, causing a splitting of the energy level. This results in two distinct peaks appearing in the XP spectrum. Such splitting, arising from the interaction with the open valence shell, is known as *core polarization.*

3.2.1 Practical Approach

When recording XP spectra, it is essential to consider the various factors that influence the intensity of a core-level signal. Without delving into the detailed mechanisms, the intensity of a core-level peak can be formally expressed as [63]:

$$I = N \cdot I_0 \cdot C \cdot T \cdot C_g \cdot F \tag{3.29}$$

Here, N is the number of photoemitting species in the volume probed by the X-ray beam. I_0 is the energy-resolved photocurrent corrected for the photoionization cross section of the specific core level, measured within the solid angle of the electron energy analyzer. C is a factor accounting for the attenuation of the photoelectrons in the solid. T represents the kinetic energy dependence of the electron energy analyzer's transmission function, including the effects of the analyzer slit and pass energy. C_g accounts for the attenuation of photoelectrons due to gas-phase scattering, which is relevant only in experiments conducted at elevated pressures. Finally, F is the photon flux at a specific energy. C strongly depends on the electron's inelastic mean free path (IMFP) and can be expressed as an exponential function like exp(-d/ λ), where d is the depth in the solid from where a photoelectron can escape, and λ is the IMFP. The value of λ depends on several factors, including the material's density, the distance the photoelectrons must travel, the number of valence electrons, and, most importantly, the kinetic energy of the photoelectrons. Although λ may appear to be a material-specific parameter, it generally follows the so-called *universal curve* observed in surface science.
While the IMFP is determined solely by the properties of the electrons and the material, the photoionization cross section reflects the probability that a photon will induce a specific electronic transition. As a result, different core levels of the same element can exhibit different excitation probabilities. Cross sections can also vary significantly between elements in a sample as shown in Figure 3.9, so it is important to verify that the value is sufficiently high for detection.

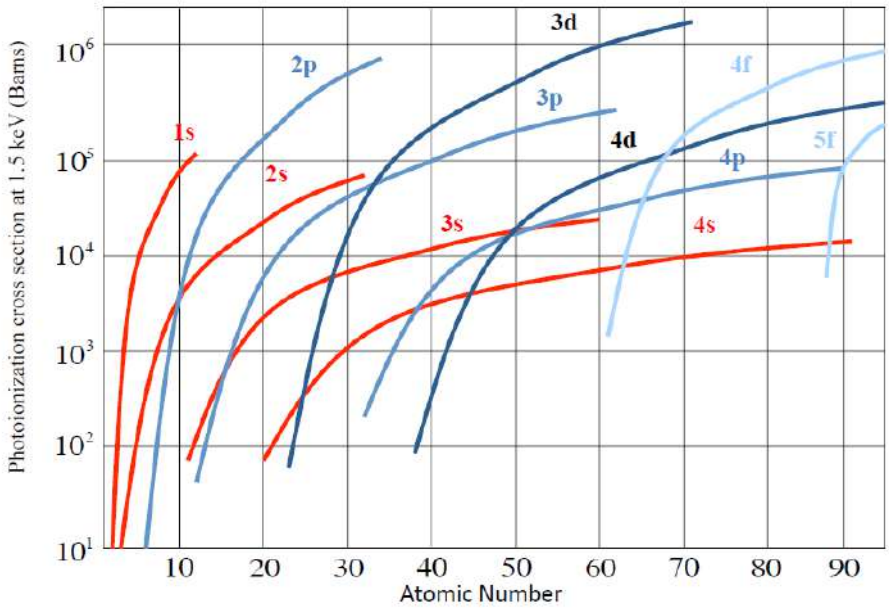

Figure 3.9 Photoionization cross-sections at 1.5 keV as a function of atomic number. Image from [61].

3.2.2 Lineshape and Data Analysis

The basic lineshape of the photoemission process can be described by a Lorentzian function:

$$I_{LOR}(E_{kin}) = I_0 \frac{\Gamma/2\pi}{(E_{kin} - E_0)^2 + \Gamma^2/4} \tag{3.30}$$

where E_0 is the position of the absolute maximum of the curve, and Γ is the FWHM. The lifetime of the core-hole state created by photoemission determines the natural linewidth, which can be estimated using Heisenberg's uncertainty principle:

$$\Gamma = \frac{h}{\tau} \tag{3.31}$$

This Lorentzian lineshape is typically broadened by a Gaussian contribution, arising from atomic vibrations (phonons) and the finite resolution of the analyser. An XP spectrum can thus be well described using a convolution of a Lorentzian lineshape with Gaussian broadening [65]. It is important to note that the XPS lineshape in conductors is usually asymmetric, exhibiting a tail at high binding energies caused by many-body interactions between photoelectrons and free electrons at the Fermi edge, which reduces the photoelectrons' kinetic energy. In 1969, Sebastian Doniach and Marijan Šunjić were able to describe this asymmetry with the following lineshape:

$$I_{DS}(E_{kin}) = I_0 \frac{\Gamma_E(1-\alpha)}{\left((E_{kin}-E_0)^2 + {\Gamma^2}/{4}\right)^{{(1-\alpha)}/{2}}} \xi(E_{kin}), \tag{3.32}$$

where Γ_E is the Euler's gamma function, α is the asymmetry factor ($0 \leq \alpha \leq 0.5$) and $\xi(E_{kin})$ is equal to:

$$\xi(E_{kin}) = \cos\left\{\frac{\pi\alpha}{2} + (1-\alpha)\tan^{-1}\left(\frac{E_{kin}-E_0}{{\Gamma}/{2}}\right)\right\} \tag{3.33}$$

Summarising, the XPS peaks FWHM is a convolution of both physical and experimental broadening, which add up in the following way:

$$\Delta E = \sqrt{{\Delta E_0}^2 + {\Delta E_{sc}}^2 + {\Delta E_p}^2 + {\Delta E_{ar}}^2}, \tag{3.34}$$

where ΔE_0 is the natural core level linewidth, ΔE_{sc} considers screening effects, ΔE_p is given by the linewidth of the photon source and ΔE_{ar} is the analyser resolution.
The fitting procedure is based on χ^2 minimization. In our case, the spectral components were fitted with Voigt profiles, which represent the convolution of a Lorentzian and a Gaussian lineshape; this symmetric profile is typical for insulators and molecules. Each peak is thus defined by five parameters that best fit the experimental data: Lorentzian width (Γ), asymmetry (α, in this case set to zero), gaussian (G), intensity (I_0) and binding energy.

$$f(E) = A + \frac{B}{1 + e^{\frac{(E-E_F)}{k_B T}}} \tag{3.35}$$

Before starting the fitting procedure, all spectra were aligned to the corresponding Fermi level.
Indeed, each Fermi level has been fitted with a Fermi-Dirac distribution, Equation 3.35, to be shifted until $E_F = 0\ eV$, thus becoming the zero-energy reference. After Fermi level alignment, it is necessary to proceed with spectra normalization and background subtraction.
In our case, the background subtraction is not straightforward, since each core level possesses a different background which needs an ad-hoc fitting procedure. For each experiment, the background spectrum has been collected before the evaporation of the element of interest. Specifically, for the C 1*s*, N 1*s*, O 1*s*, and Fe $2p_{3/2}$ levels, the background was measured after graphene preparation and before molecular evaporation, whereas for Co $2p_{3/2}$, it was acquired after the molecular layer had been deposited. For C 1*s* and N 1*s* core level, a linear background was subtracted by applying a mask. The mask assigns a value of 0 to spectral regions that must be excluded and a value of 1 to regions used for background evaluation. When the mask is applied, excluded features are removed (multiplied by 0), while the background portion of the spectrum remains unchanged (multiplied by 1). For the O 1*s*, Fe $2p_{3/2}$, and Co $2p_{3/2}$ core levels, the corresponding background spectrum was interpolated using the IgorPro analysis toolkit and subsequently subtracted from the spectrum of interest. When this method

didn't achieve optimal spectral alignment, a linear background subtraction was additionally applied using the same masking procedure described for C 1*s* and N 1*s*.

3.2.3 Near Ambient Pressure XPS

Photoemission spectroscopies generally require UHV conditions to minimize surface contamination and prevent collisions between photoemitted electrons and gas molecules. However, many surface phenomena of practical relevance, such as those involved in heterogeneous catalysis, corrosion, and materials degradation, occur under conditions far from UHV, often in the presence of reactive gases at elevated pressures. In such environments, gas-surface interactions more accurately reflect real operational environments, enabling observation of dynamic changes in surface composition, oxidation states, and reaction intermediates that are inaccessible under vacuum conditions.
Consequently, experimental techniques capable of probing surfaces at higher pressures are essential to bridging the so-called "pressure gap" in surface science and gaining mechanistic insights into materials and reactions under real operating conditions. Nevertheless, collecting unscattered electrons under AP conditions remains challenging, as the electron inelastic mean free path in the gas phase decreases inversely with pressure. Indeed, the photoemission intensity is attenuated by the gas phase according to Beer's law:

$$I(E_k, P) = I_0 e^{-z\sigma(E_k)P/k_B T} \tag{3.36}$$

where z is the path length of the electron through the gas phase, E_k is the kinetic energy of the photoelectron, P the gas pressure, k_B Boltzmann's constant and σ the energy-dependent inelastic cross section. The electronic mean free path can thus be quantified from Equation 3.36 [66]:

$$\lambda_e(E_k, P) = \frac{k_B T}{\sigma(E_k)P} \tag{3.37}$$

For example, for electrons with a kinetic energy equal to 400 *eV*, the inelastic mean free path at 1 *mbar* is of the order of *mm*. Its value decreases with increasing pressure: in fact at about 100 *mbar*, the mean free path is equal to 30 μm [67]. Consequently, specific strategies are required to reduce gas phase attenuation of photoelectrons, such as minimizing the electron travel distance z by positioning the sample closer to the analyzer entrance aperture, a critical consideration in NAP-XPS measurements. An example of a typical NAP-XPS analyzer structure is shown in Figure 3.10.

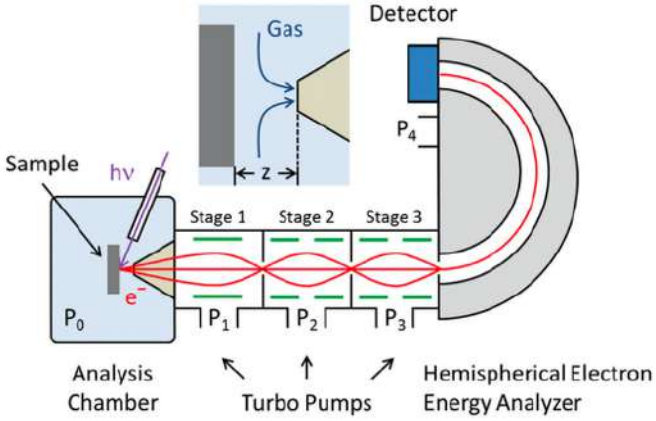

Figure 3.10 Schematic of an NAP-XPS setup. The sample is located in an ambient-pressure cell, and experiments are typically performed at normal emission. The analyzer nozzle is positioned very close to the sample, and the hemisphere is isolated from the near-ambient pressure environment by several differential pumping stages [66].

Since electron analyzers must operate under UHV conditions, they are designed to withstand a pressure difference of approximately 9-10 orders of magnitude between the measurement chamber and the analyzer hemisphere. This is achieved through multiple differential pumping stages, coupled with electrostatic lenses that focus the photoelectrons and by reducing the entrance aperture diameter *d*, thereby increasing collection efficiency. To maintain good signal intensities during NAP measurements, the first differential pumping stage must provide a substantial pressure reduction, typically several orders of magnitude. This means that the gas between the sample and the aperture is constantly pumped through the aperture by the first differential pumping stage, potentially affecting the sample environment due to their short separation [66]. The best compromise between a short distance z and a narrow aperture diameter d is typically reached when $\mathbf{z} \approx \mathbf{d}$ [68]. Typical apertures are order of a few hundreds of micron, which necessitates a tightly focused X-ray beam and, therefore, the use of high-performance synchrotron facilities such as MAX IV Laboratory, where all the X-ray spectroscopies measurements in this work were conducted.
Gas-phase core-level features are often observed under NAP conditions, and their ionization energies are referenced to the vacuum level. Typically, the sample and analyzer have different work function values, as shown in Figure 3.11.

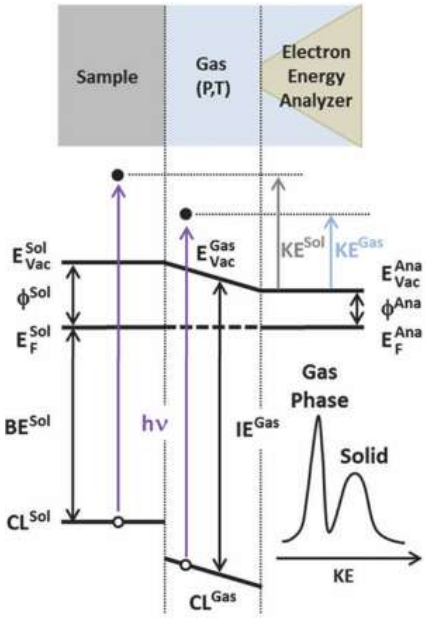

Figure 3.11 Energy level scheme in the presence of gas. The sample and the analyzer have different work functions, causing the vacuum level to vary linearly between them. Alignment of the Fermi levels ensures that the binding energy of photoelectrons emitted from the surface remains unaffected. In contrast, the gas-phase signal is sensitive to changes in the work function, as it is referenced to the vacuum level [66].

As a result, the vacuum level changes linearly between the sample and the analyzer depending on their separation. Consequently, changes in the sample's work function (ϕ_{sol}) induce a binding energy shift in the gas-phase signal, whereas surface features remain unaffected [69].

3.3 Near-Edge Absorption Fine Structure

NEXAFS is a specific type of x-ray absorption spectroscopy (XAS), focusing on the near-edge region of the absorption spectrum. It requires a synchrotron source capable of tuning the photon energy and is one of the most effective methods for obtaining reliable information about the geometric and electronic structure at surfaces. There are several ways to observe X-ray absorption. The most direct approach is to measure the X-ray intensity before and after passing through the object of interest. When an electron absorbs a photon, it can either be photoemitted or excited to an unoccupied state depending on the

amount of acquired energy. In both cases, a hole is created in an inner shell, with a finite lifetime. There are two primary mechanisms by which this hole can be filled: X-ray fluorescence and Auger electron emission, see Figure 3.12.

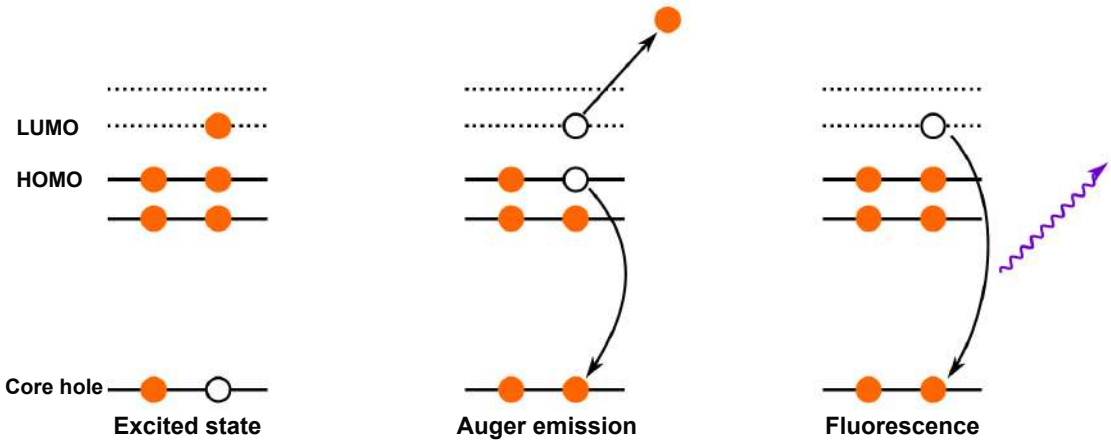

Figure 3.12 A schematic drawing of the excited state decay with a core hole present. The core hole is filled either by Auger decay after emission of an Auger electron or fluorescence decay which results in the emission of a photon. Image from [64].

In the first case, recombination produces a photon with energy corresponding to the electron transition, while in the second case, the excess energy is transferred to another electron, which is emitted from the atom. This electron is called an Auger electron.
These two recombination pathways allow investigation of X-ray absorption by detecting either photons or electrons. Detection of Auger electrons is usually preferred because Auger emission is more probable than fluorescence in low-Z elements, which are mainly present in biological molecules. Moreover, Auger signal detection offers a better surface sensitivity because electrons have a much shorter inelastic mean free path in solids with respect to fluorescence photons.
The NEXAFS experiments discussed in this work were performed in partial electron yield (PEY) mode, consisting in suppressing lower kinetic energy electrons emerging from the sample, by applying a retarding voltage. This mode is frequently used for studying adsorbates on surfaces because it significantly enhances surface sensitivity, allowing only electrons emitted from the outermost surface region to be detected. Further available options are the total electron yield (TEY) mode, where all electrons that emerge from the surface are detected and the Auger electron yield (AEY) mode, where electrons are energy-selected to detect only Auger electrons.

Dichroism

NEXAFS enables the extraction of valuable information about the geometric structure of molecules adsorbed on a surface. In particular, the investigation of transitions to molecular orbitals (MOs) is especially revealing. A key feature of molecular orbitals is their strong directional character, which leads to a one-to-one correlation between the spatial orientation of the orbitals and the molecular geometry. As a result, for oriented molecules and linearly polarized X-rays, the intensities of resonances associated with, for example, σ* and π* final states exhibit distinct and pronounced angular dependence. This angular dependence arises from the dipole matrix element, which, for linearly polarized X-rays with polarization vector $\boldsymbol{e}$, takes on a simplified form:

$$\langle \psi_f | \boldsymbol{e} \cdot \boldsymbol{p} | \psi_i \rangle = \boldsymbol{e} \langle \psi_f | \boldsymbol{p} | \psi_i \rangle = \boldsymbol{e} \cdot \mathbf{O} \tag{3.38}$$

where $\langle \psi_f | \boldsymbol{p} | \psi_i \rangle$ is the Transition Dipole Moment (TDM) and for a 1*s* initial state points in the direction of the final state orbital $\mathbf{O}$.
The cross section and therefore also the transition intensity become:

$$I_{fi} \propto \left|\langle \psi_f | \boldsymbol{e} \cdot \boldsymbol{p} | \psi_i \rangle\right|^2 = |\boldsymbol{e} \cdot \mathbf{O}|^2 \propto \cos^2 \delta \tag{3.39}$$

where δ is the angle between the vector field $\boldsymbol{E}$ and final state TDM $\mathbf{O}$.

Data Analysis

NEXAFS spectra were collected in Partial Electron Yield (PEY) mode at three incidence angles by rotating the samples relative to the beam axis. Measurements were performed at normal incidence (0°) and grazing incidence (70°) to extract geometric information about the system. Additional measurements were performed at (42°) an intermediate angle between normal and grazing incidence, to clearly follow the angular dependence.
Data processing was carried out using *XAS Plotter*, a program specifically developed by the FlexPES team at MAX IV in Lund for NEXAFS data analysis. All raw data were normalized to the incident photon flux using the drain current I_0 and background subtraction was performed using a polynomial fitting function.

3.4 Beamlines at MAX IV Laboratory

All NEXAFS measurements presented in this thesis were carried out at the FlexPES (Flexible PhotoElectron Spectroscopy) beamline, located at the 1.5 GeV ring of the MAX IV Laboratory in Lund, Sweden. The NAP-XPS and XPS measurements were conducted at the HIPPIE beamline, situated at the 3 GeV ring of the same synchrotron facility.
The FlexPES beamline offers the capability to perform a wide range of photoemission and soft X-ray absorption experiments within a photon energy range of 40 - 1500 *eV*. The photon source is a linearly polarizing undulator comprising 48 full periods and delivering a maximum effective magnetic field of 0.8 *T*. The optical layout is based on a collimated plane-grating monochromator (cPGM) design, featuring an astigmatic intermediate focus and switchable refocusing mirrors. The maximum beamline acceptance is 0.62 *mrad* × 1.36 *mrad* (horizontal × vertical), corresponding to full illumination of the first mirror (M1). Beam acceptance can be reduced using movable masks in the front end and/or baffles positioned before the monochromator. FlexPES comprises two experimental branches: the Surface & Material Science (SMS) and the Low Density Matter (LDM) branches.
All measurements reported in this thesis were carried out on the SMS branch. This branch includes two focal points: the first is located within a permanent UHV end station (EA01), dedicated to surface science studies, while the second is situated 2.5 *m* downstream on an open port (EA02), intended for user-provided end stations. The permanent EA01 end station is optimized for photoelectron and X-ray absorption spectroscopy investigations of surfaces and thin films. It consists of four chambers: an analysis chamber equipped with detectors, two preparation chambers with sample treatment and transfer capabilities, and a fast-entry load-lock chamber with a sample storage system (sample garage).
The HIPPIE beamline is a soft x-ray beamline equipped with a novel near-ambient pressure x-ray photoemission spectroscopy instrument, designed to perform *in-situ* and *operando* XPS experiments in gas pressure up to 30 *mbar*. A unique feature of the HIPPIE beamline is the capability to perform simultaneous NAP-XPS and PM-IRRAS measurements, combining electronic and vibrational spectroscopy in a complementary approach [70].
The beamline source is an APPLE-II-type elliptically polarizing undulator with full polarization control. The photon energy can be tuned in the range 250 - 2200 *eV* with photon fluxes > 10^{12}photons/s, and a beam size of about 60 *μm* x 25 *μm* (horizontal, vertical), which becomes about 100 *μm* x 25 *μm* due to a grazing incident angle on the sample. The ScientaOmicron HiPP-3 electron energy analyser has a differential pumping stage and electrostatic lens system that allows for AP operation at up to 30 *mbar* at 0.3 *mm* nozzle diameter. The gas inlet system consists of eight independent gas lines, each equipped with its own mass flow controller. Gas mixtures can be introduced either directly or via an adjustable

leak valve, while the outlet is also regulated by a valve, allowing fine control over both pressure and gas flow. This setup enables regulation of the gas pressure in the range of 10^{-8} to 30 *mbar*. The gas composition can be monitored using a quadrupole mass spectrometer connected to the first pumping stage of the analyzer. Further technical details about the setup are provided in reference [70].

3.5 Scanning Tunneling Microscopy and Spectroscopy

While XPS and XAS are excellent techniques for studying surface chemistry, they are less straightforward in the case of the determination of the local geometric structure. STM marked a significant advancement in surface science by enabling atomic-scale imaging of surfaces. Invented in 1983 by Gerd Binnig and Heinrich Rohrer, STM quickly became a standard technique in the field [71]. In STM measurements, a sharp metallic tip is positioned within a fraction of a nanometer from a conductive surface. The tip and the sample generally possess different work functions and Fermi levels. When both are grounded, their Fermi levels align, and no electrons can flow across the vacuum barrier, Figure 3.13 a).

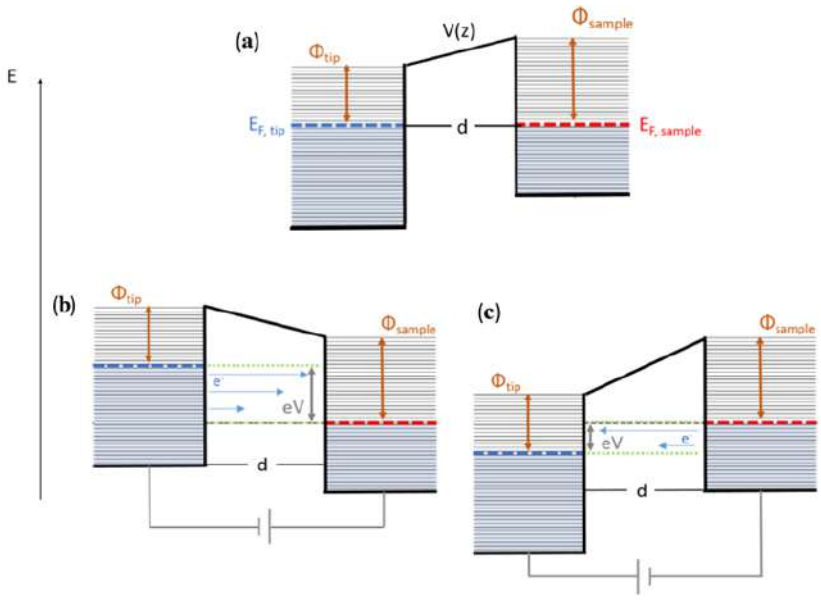

Figure 3.13 1D potential barrier model, defined by the work function. a) When the sample and the tip are in electrical contact, their Fermi levels align. b) If a positive potential is applied to the sample with respect to the tip, electrons can tunnel from the occupied states of the tip to the unoccupied states of the sample (blue arrows). c) When a negative potential is applied, the opposite occurs, with electrons tunneling from the sample to the tip.

Upon application of a bias voltage V, the Fermi levels shift relative to one another by an energy eV, enabling quantum tunneling of electrons. Depending on the polarity of the applied bias, electrons can tunnel either from occupied states of the tip into unoccupied states of the sample, or from occupied states of the sample into unoccupied states of the tip, Figure 3.13 b) and c). A tunneling current I can be measured and it depends on the thickness of the barrier d as:

$$I \propto e^{-2kd}, \tag{3.40}$$

where $k = \sqrt{\frac{2m\phi}{\hbar}}$ and ϕ is the average work function of both electrodes [72].

However, the tunneling probability depends on the density of states (DOS) of both the tip and the sample within the energy range defined by the applied bias voltage V and the Fermi level E_F. Consequently, STM images reflect a convolution of the DOS of the tip and the sample.
Surface topography is acquired by raster-scanning the tip over the sample surface while monitoring either (i) the tunneling current (constant-height mode) or (ii) the vertical position of the tip, adjusted by a feedback loop to maintain a constant tunneling current (constant-current mode).
In addition to topography, STM can also probe the electronic structure through scanning tunnelling spectroscopy (STS). Since the tunneling current is proportional to the integral of the sample DOS from Fermi level to *eV*, its derivative provides access to the local DOS at energy *eV*:

$$\frac{dI}{dV} \propto \rho_s(eV) \tag{3.41}$$

Direct numerical differentiation of the I-V curve is typically too noisy; therefore, a lock-in amplifier is employed. During the acquisition of a dI/dV spectrum, the feedback loop (which controls the tip-sample distance) is disabled, the voltage is swept and the lock-in signal is recorded.
If the dI/dV signal is recorded at a fixed bias while scanning the surface at a constant height, the spatial distribution of the density of states can be obtained (dI/dV maps).

STM Laboratory at MAX IV and Graz University

The STM images of the mono- and bi-metallic system based on FeTPyP and FeTPyP-Co presented in this work were acquired at the STM laboratory of the MAX IV Synchrotron (Lund, Sweden), in collaboration with Dr. Nikolay Vinogradov and Dr. Eleanor Frampton.
The experimental setup consists of a preparation chamber coupled to a VT UHV XA STM system from ScientaOmicron, allowing measurements to be performed at either room or liquid nitrogen (LN_2) temperature [73]. Adsorbates such as porphyrins are often highly mobile at room temperature on weakly interacting substrates like graphene. To suppress thermal diffusion and achieve more stable imaging conditions, low-temperature measurements are typically necessary. Furthermore, the tip itself becomes more stable at lower temperatures, with a reduced dynamic evolution of its atomic configuration.
The STM images and STS spectra of the hemin system, before and after Co deposition, were acquired at the STM laboratory at the University of Graz (Graz, Austria), in collaboration with Dr. Maximilian Laßhofer, Prof. Martin Sterrer and Prof. Giovanni Zamborlini. The experimental setup consists of a preparation chamber coupled with a Low-Temperature STM (LT-STM) setup, allowing measurements to be performed at liquid-nitrogen or liquid-helium temperatures, depending on the required stability and resolution.

3.6 Sample Preparation

Two substrates were used in this thesis: Au(111) and graphene grown on Ir(111). All experimental chambers employed in this work were equipped to carry out the same cleaning procedures. Au(111) sample was cleaned by cycles of Ar^+ sputtering at 1.5 *keV* and annealing at 775 *K*. Its surface quality was checked by LEED, confirming the well-defined Au(111) surface reconstruction. Ir(111) surface was cleaned by repeated cycles of Ar^+ sputtering at 2 *keV* and annealing at 1275 *K*, alternated with treatments in oxygen background (2×10^{-7} *mbar*) in the 500-1175 *K* temperature range to remove residual carbon contaminants. Graphene growth was achieved via chemical vapor deposition (CVD) of ethylene: the clean Ir(111) substrate was held at 1275 *K* and exposed to 5×10^{-8} *mbar* of C_2H_4 for 2 minutes, followed by an increase in pressure to 3×10^{-7} *mbar* for additional 2 minutes. Finally, temperature was gradually reduced while restoring UHV conditions. The resulting graphene layer was

monitored using LEED and, where possible, XPS or SFG. The observed diffraction pattern indicated the formation of a high-quality graphene layer, closely resembling the one reported by Pletikosić *et al.* [74]. After graphene formation, Fe(III) Meso-Tetra (4-Pyridyl) Porphine Chloride molecules (FeTPyPCl, purchased from Frontier Scientific), were deposited via thermal sublimation using a heated boron nitride crucible.

Before deposition, molecules were extensively outgassed at 470-525 *K* to remove contaminants and organic residuals. Sublimation was performed in the 635-685 *K* range, depending on the specific setup and the crucible-sample distance, achieving a deposition rate of approximately 0.04 *ML/min*. One monolayer (*ML*) is defined here as the amount of molecule required to form a uniform single layer covering the graphene substrate. Under these conditions, submonolayer coverages ($\leq$ 1 *ML*) can be achieved in about 15-20 minutes.

During deposition, the sample was maintained at 473 *K* to promote lateral diffusion and self-assembly of the molecules into ordered domains. The coverage was kept below 1 *ML* to enhance the formation of extended molecular islands. When available, a quartz crystal microbalance (QCM) was used for deposition rate calibration; otherwise, depending on the setup, coverage was estimated using AES or XPS. The Fe(III) center in the pristine FeTPyPCl molecules is stabilized by an axial chloride ligand, which is thermally detached from the porphyrins upon degassing before the deposition [75], as confirmed by the presence of HCl in the chamber observed with a quadrupole mass spectrometer (QMS), resulting in a reduction of the metal center to Fe(II).

The bimetallic heterostructure was created by evaporation of atomic Co by resistively heating a Co filament of 0.250 *mm* diameter at the SFG Laboratory and HIPPIE beamline. Co coverage will be expressed referring to a porphyrin monolayer so that 1 *ML* Co corresponds to the presence of 1 Co atom for each molecule in 1 *ML* FeTPyP. In general, Co will be dosed to achieve a FeTPyP : Co ratio slightly higher than unity, to avoid the creation of Co clusters on graphene due to excess Co [76]. The evaporation rate was calibrated by AES or XPS, depending on the available spectroscopy method. During deposition, the sample was kept at 423 *K*, a temperature high enough to promote molecular ordering and low enough to prevent Co intercalation beneath the graphene layer [77].

Hemin, also known as Ferriprotoporphyrin IX chloride, purchased from Frontier Scientific, was deposited via thermal evaporation from a boron nitride crucible following extensive outgassing at 470-525 *K*. Due to the relatively low purity of the starting material, since hemin is synthesized from bovine or porcine blood, the deposition process exhibited the following behavior: initially, only metal-free porphyrins and contaminants were evaporated, followed by a mixture of metalated and metal-free species, and eventually predominantly iron-containing molecules. This behavior is consistent with previous STM studies of heme, where isolated Ferriprotoporphyrins IX were imaged and their electronic structure characterized [78]. In that study, the authors also demonstrated that the axial chloride ligand thermally detaches from the molecule upon sublimation.

To maintain a stable deposition rate, the crucible temperature had to be gradually increased over time. A final temperature threshold was eventually reached beyond which no further evaporation occurred, likely due to polymerization of the molecules inside the crucible. For this work, sublimation was typically carried out in the 615-640 *K* range, depending on the specific experimental configuration and crucible-sample distance, with the substrate kept at room temperature. Under these conditions, a deposition rate of approximately 0.04 *ML/min* was achieved, allowing a sizeable submonolayer coverage ($\leq$ 1 *ML*) in about 15-20 minutes. The rate was calibrated by QCM when available; otherwise, XPS was used to estimate molecular coverage. Co deposition on Au(111) followed the same procedure described above adopted for the graphene system. The deposition rate was calibrated by XPS, and the substrate was kept at room temperature during the process.

4 | Co-Induced Structural Electronic and Vibronic modifications in a Self-Assembled FeTPyP Monolayer on Graphene

This chapter provides a detailed investigation of the structural, electronic and vibronic modifications induced in a monolayer of FeTPyP grown on Gr/Ir(111) following Co deposition, in UHV conditions. The experimental characterization was carried out using STM, XPS and IR-Vis SFG spectroscopy, supported by *ab initio* DFT simulations performed by Dr. Basant Roondhe (Prof. Paolo Giovannozzi's group, University of Udine).

4.1 Structural Properties

The STM measurements were carried out at the STM Laboratory of the MAX IV Laboratory (Lund, Sweden), in collaboration with Dr. Nikolay Vinogradov and Dr. Eleanor Frampton. All STM-derived quantitative evaluations correspond to averages of unit cell parameters measured across multiple high-resolution images. The uncertainty associated with each value is reported as three times the standard deviation of the mean ($3\sigma_m$), providing a conservative estimate that accounts for both statistical variability and instrumental noise. All STM measurements presented in this work were performed at liquid nitrogen (LN_2) temperature.

Upon deposition onto monolayer Gr/Ir(111), FeTPyP molecules self-assemble into long-range ordered islands, driven by lateral intermolecular interactions that prevail over the weak molecule-substrate interaction. Graphene on Ir(111) is known to form a quasi-free-standing layer, effectively decoupling the molecular layer from the underlying metal substrate [79]. Additionally, the surface trans-effect is negligible: the π-mediated weak interaction between graphene and molecules prevents formation of a direct bond between the substrate and the metal centers [35,36]. Moreover, graphene is chemically inert, making it an ideal support for AP investigations [80].

FeTPyP molecules organize into a close-packed arrangement, described by an oblique unit cell containing two non-equivalent FeTPyP molecules, rotated relative to each other, as shown in Figure 4.1 a). The unit cell parameters are a = 3.24 ± 0.06 *nm*, b = 1.50 ± 0.09 *nm* (outlined in blue in panel a) and θ = 129° ± 2°. The structure is characterized by alternating rows, more clearly visible in the zoomed-in view in Figure 4.1 b), with superimposed H shapes that highlight the different molecular orientations. Additionally, the absence of features at the center of the molecules at 1.8 *V* confirms the loss of chlorine atoms during degassing of the molecular powder before evaporation [78]. Figure 4.1 c) shows the DFT-simulated STM image visualized using a Python-based script to process charge density data obtained from DFT calculations. The simulation accurately reproduces the experimental results, capturing the molecular arrangement driven by optimized interactions between the electronegative N atoms of the pyridyl end groups and the peripheral H atoms from the neighboring pyrrole moieties [35,81]. To better visualize the simulated charge redistribution within the unit cell, which contains two inequivalent FeTPyP molecules interacting with the graphene substrate (depicted in brown and black, respectively), a (2×2) oblique supercell was simulated, with both top and side views shown in panel d) of Figure 4.1.

The visualization was performed using VESTA, where regions of electron accumulation are shown in yellow and regions of electron depletion in cyan, using an isovalue of ± 0.044 $e^-/Å^3$, respectively. Blue areas correspond to artifacts arising from the finite size and periodic boundary conditions of the simulation cell. The charge redistribution was calculated as the difference between the total charge density of the combined system (FeTPyP/Gr) and the sum of the charge densities of the isolated components in the positions assumed in the total system:

$$\Delta\varrho = \varrho_{FeTPyP/Gr} - \varrho_{Gr} - \varrho_{FeTPyP} \tag{4.1}$$

integrating over the in-plane coordinates of the unit cell for each z component in order to get $\Delta\varrho(z)$ profile, shown in panel d) of Figure 4.1. The charge transfer calculated between graphene and the molecular layer is almost zero, as previously demonstrated in similar systems based on CoTPyP and MnTPyP on Gr/Ir(111) [36,37], with 0.042e^- per unit cell transferred from graphene to the molecular plane.

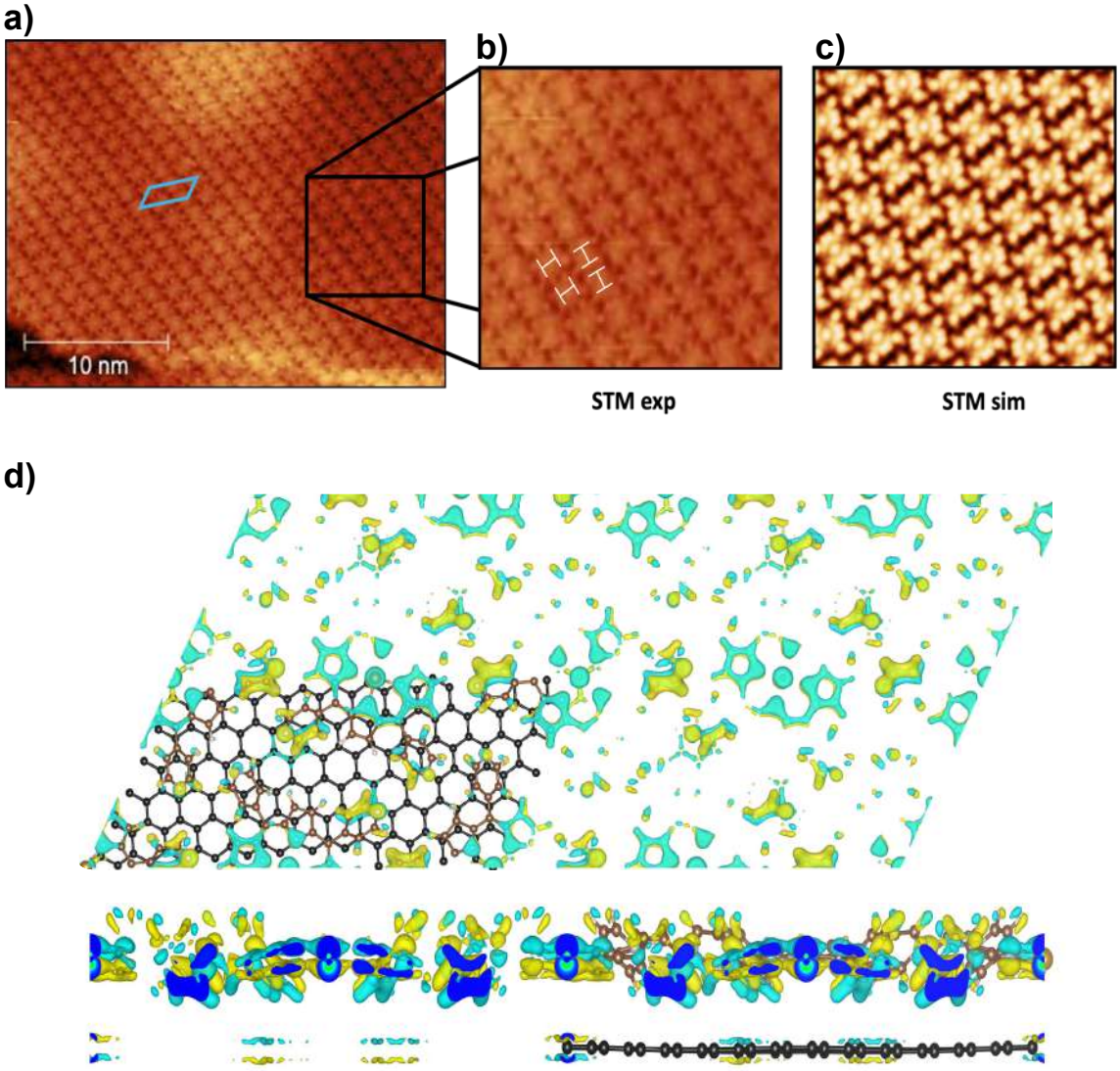

Figure 4.1 a) STM image of a FeTPyP island showing a close-packed structure with alternating rows, forming an oblique unit cell (outlined in blue). Applied bias and tunneling current: V= 1.8 V, I= 100 pA. b) A zoomed-in experimental image of a), where the alternating rows are more clearly visible. For clarity, a superimposed "H" highlights the different molecular orientations. c) DFT-simulated STM image of the same structure at constant height, visualized using a Python-based script. d) Top and side views of the simulated charge redistribution within the unit cell containing two inequivalent FeTPyP molecules, visualized using VESTA. For clarity, a (2×2) oblique supercell enhances the visualization of the charge distribution patterns. The redistribution arises from the interaction between the FeTPyP molecules (brown) and the graphene substrate (black). Regions of electron accumulation and depletion are depicted in yellow and cyan, using an isovalue of ± 0.044 $e^-/Å^3$, respectively, highlighting the direction of charge transfer. Blue areas represent artifacts resulting from the end of the periodicity in the simulation cell.

Following the characterization of the monometallic system, cobalt was evaporated on the sample kept at room temperature, inducing a complete molecular rearrangement, as shown in Figure 4.2 a). Two distinct regimes are observed: at intermediate Co coverage (FeTPyP : Co = 2 : 1) Figure 4.2 b), and at saturation coverage (FeTPyP : Co = 1 : 1) Figure 4.2 c), in which each molecule coordinates with four Co atoms, and each Co atom is shared among four molecules.

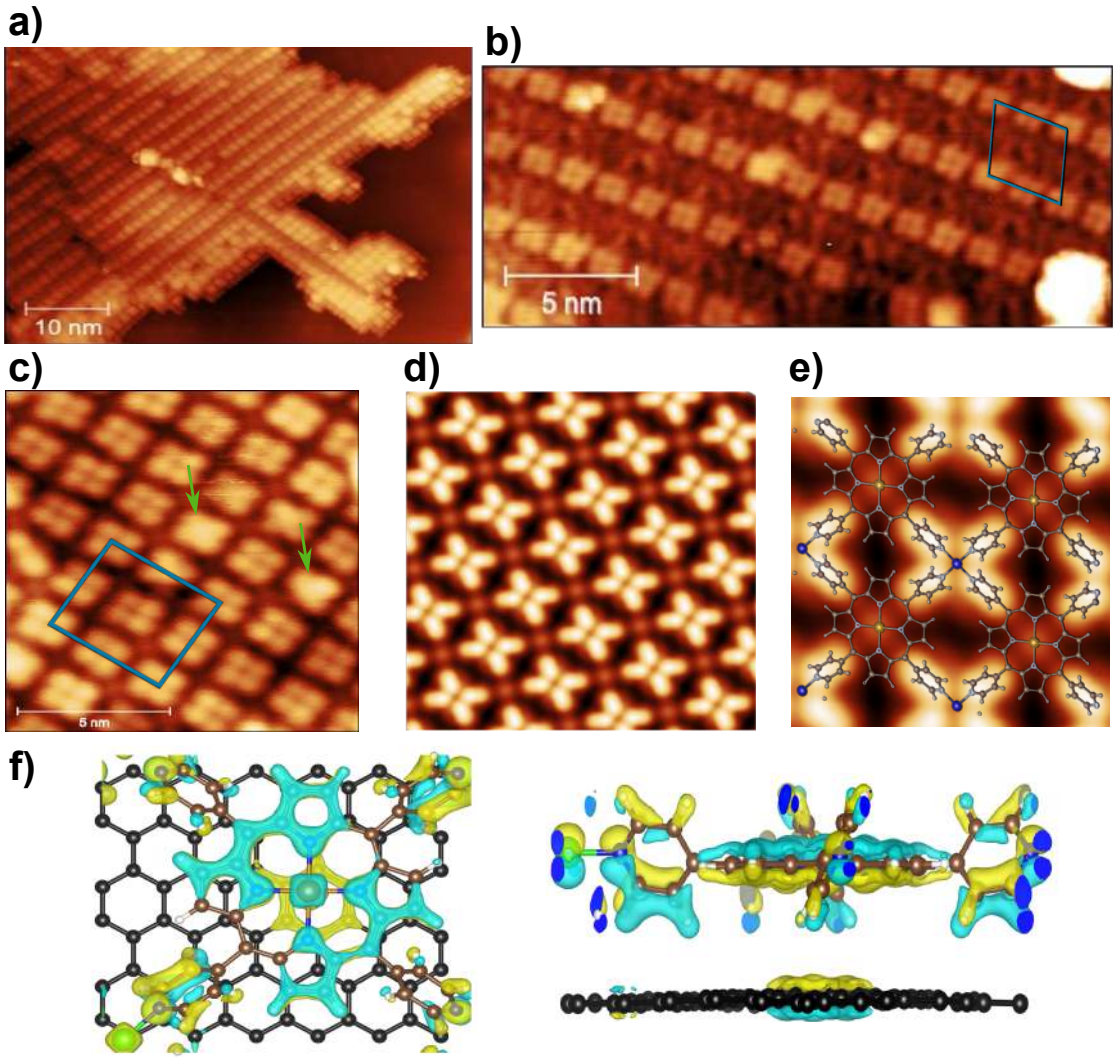

Figure 4.2 a) STM image of FeTPyP layer after Co deposition: two regimes are observed for the intermediate and saturation Co coverage. Applied bias and tunneling current: V= 1.85 V, I= 60 pA. b) STM image of the FeTPyP-Co structure at intermediate Co coverage. The (2×2) oblique unit cell, arising from the tilt of the pyridinic groups, is highlighted in blue. Applied bias and tunneling current: V= 2 V, I= 250 pA. c) STM image of the FeTPyP-Co structure at Co saturation coverage. The (2×2) square unit cell is highlighted in blue, while the green arrows indicate brighter squares corresponding to the presence of Co clusters. Applied bias and tunneling current: V= 2 V, I= 280 pA. d) DFT-simulated STM image of the same structure at constant height, visualized using a Python-based script. Fe atoms are located between the squares, while Co atoms are inside them. e) DFT-simulated STM image zoom, together with a bimetallic molecular sketch highlighting the presence of Co atoms (blue) at the centers of the squares and Fe atoms (yellow) between them. f) Simulated top and side views of the charge redistribution within the unit cell, visualized using VESTA, which contains one FeTPyP molecule and a Co atom. The charge redistribution arises from the interaction between the FeTPyP-Co molecule (brown) and graphene (black). Regions of electron accumulation and depletion are depicted in yellow and cyan, using an isovalue of ± 0.034 $e^{-}/Å^{3}$ respectevely, highlighting the direction of charge transfer. Blue areas represent artifacts due to the end of the periodicity in the simulation cell.

Saturation is first achieved at the edges of the FeTPyP islands, due to the kinetic hindrance emerging from both Co diffusion into the FeTPyP islands and from the induced geometric rearrangement of the molecular layer. The initially close-to hexagonal arrangement shown in Figure 4.1 a) evolves towards a (2x2) oblique unit cell in the intermediate coverage regime, highlighted with blue lines in Figure 4.2 b), with unit cell parameters a = 2.86 ± 0.06 *nm*, b = 2.55 ± 0.03 *nm* and θ = 101.0° ± 3.6°.
The saturation structure is represented by a (2x2) square unit cell with a=b= 3.9 ± 0.1 *nm* and θ = 91.0° ± 1.9°, where, based on similar systems, Co atoms are located in the middle of each square while Fe atoms are between them [35–37], as confirmed by the DFT simulation in Figure 4.2 d). For better clarity, Figure 4.2 e) shows a rotated, zoomed view of the same simulation, overlaid with a bimetallic molecular sketch highlighting the presence of Co atoms (blue) at the center of the squares and Fe atoms (yellow) between them. At first glance, the structure at intermediate Co coverage (panel b) of Figure 4.2) appears to form a (2×1) oblique unit cell, whereas at saturation (panel c) of Figure 4.2) a (1×1) square unit cell is evident. However, the pyridinic moieties are tilted alternately clockwise and anticlockwise, enlarging the effective periodicity of the structure unit cell. This arrangement is not captured in the DFT-simulated STM image shown in panel d) of Figure 4.2, since the simulation includes only one molecule per unit cell. Consequently, while the main geometry of the layer is replicated, the tilt of the pyridinic moieties is absent. It is also worth noting that the periodicity observed at intermediate coverage differs from that reported in recent works on similar systems, namely CoTPyP- and MnTPyP-Co/Gr/Ir(111) [35,36,37]. This discrepancy suggests that the identity of the central metal atom plays a key role in determining the overall molecular assembly, a phenomenon likely governed by subtle electronic effects and geometrical distortions that influence the coordination environment, surface interaction and intermolecular packing. Such sensitivity to molecular composition highlights the potential of tailored ligands and metal centers in steering the formation of designed nanoscale structures at surfaces.

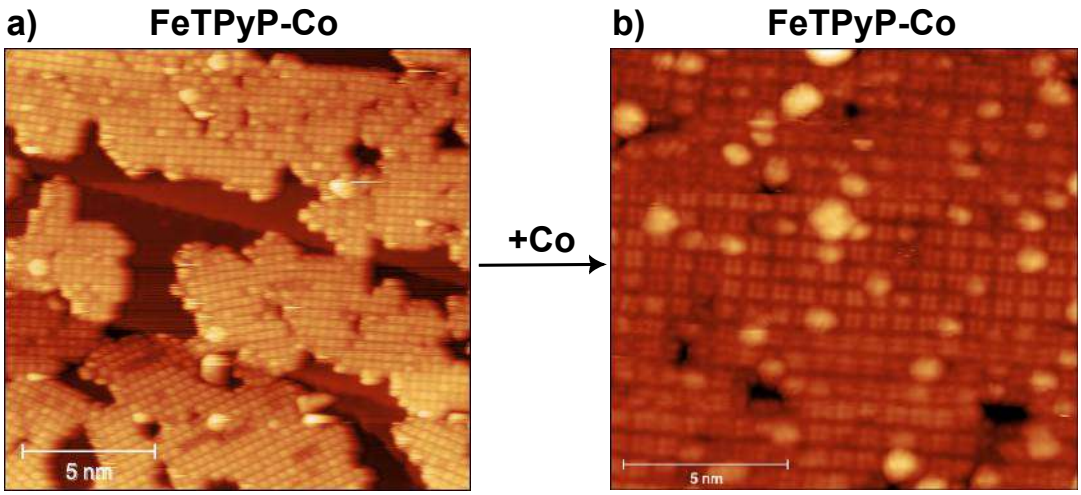

Figure 4.3 In a) FeTPyP-Co system at Co coverage slightly above the stoichiometric 1:1 (FeTPyP:Co) ratio, with bright spots observed in the square of the chessboard. b) Same system with increased Co loading, revealing larger bright features that confirm the formation of a Co cluster. Applied bias and tunneling current in a): V= -1.80 V, I= 200 pA and in b): V= 2 V I= 280 pA.

Figure 4.2 f) shows the top and side views of the simulated charge redistribution following Co deposition, calculated and visualized using the same procedure as for the monometallic system. In contrast to the monometallic FeTPyP case, the presence of Co in the bimetallic configuration induces significant charge redistribution, resulting in a net transfer of 0.328e^- per unit cell from the molecular layer to graphene. It is worth noting that, in the top-view image, the charge redistribution between the macrocycle and the pyridinic rings exhibits 2-fold rather than 4-fold symmetry, again due to the single molecule included in the unit cell's simulation. Moreover, in Figure 4.2 c), brighter squares, indicated by green arrows, are observable in comparison to others, suggesting the possibility of stabilizing Co clusters

at the pyridinic moieties in presence of excess local Co coverage. To further investigate this behavior, the amount of deposited Co atoms was further increased well beyond the stoichiometric 1:1 coverage. Figure 4.3 shows two STM images of FeTPyP-Co layers with different Co loadings. In panel a) of Figure 4.3, the Co coverage exceeds the stoichiometric 1:1 FeTPyP:Co ratio. At this stage, all FeTPyP-Co islands adopt a square unit cell, with bright protrusions appearing on some squares of the chessboard. Upon further increasing the Co concentration, as shown in panel b) of Figure 4.3, both the number and size of these bright features increase, indicating the formation of Co clusters stabilized at room temperature between the organic backbone. This was not observed previously for the similar CoTPyP-Co and MnTPyP-Co cases.

However, it is not possible to create a homogenous system with only Co clusters at the pyridinic sites. Initially, Co atoms preferentially coordinate with other Co atoms stabilized between the organic backbones. Beyond a certain coverage threshold, however, Co atoms begin to nucleate on the graphene substrate. Moreover, the thermal stability of these clusters has not been investigated in this work, and, unless otherwise specified, Co concentrations will remain below the cluster formation yield.

An additional important observation arises upon closer comparison between panels c) and d) of Figure 4.2, which are now, for clarity, shown as panels a) and b) of Figure 4.4. In panel b) of Figure 4.4, Fe atoms are clearly visible between the bright squares (highlighted by a green circle). These features are also visible in the experimental STM image shown in panel a) of Figure 4.4. However, upon closer inspection, certain regions between the squares (circled in blue) appear darker in the experimental image and are not reproduced by the simulation. This contrast difference is attributed to O adsorption at Fe sites.

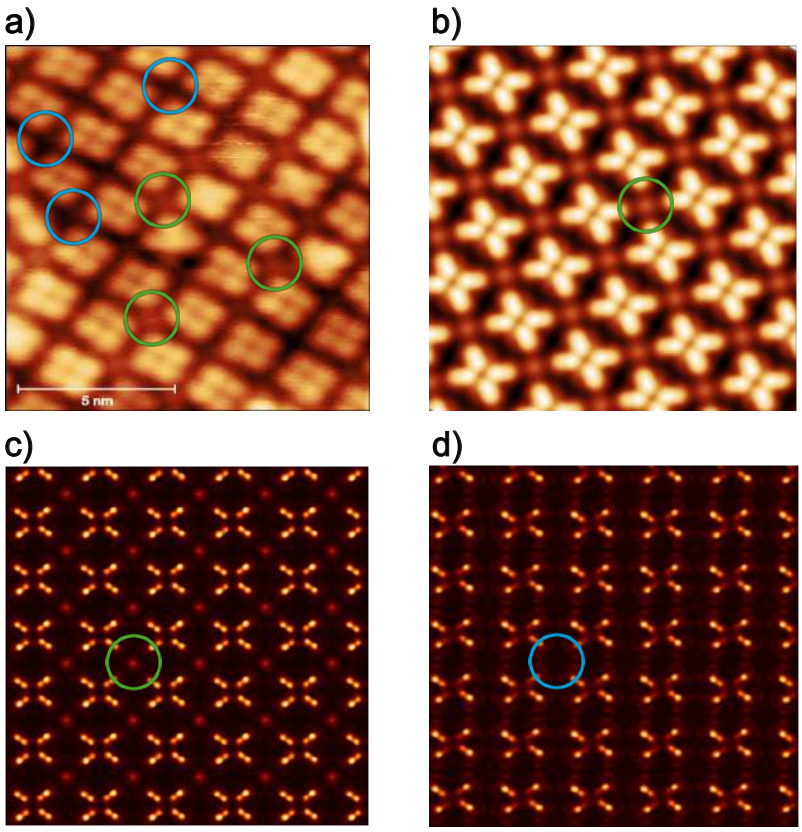

Figure 4.4 Panel a) and b) show a comparison between the STM image and DFT simulated STM image of FeTPyP-Co at Co saturation, performed using a Python-based script. Fe atoms are highlighted with green circles, while sites where Fe appears "absent" due to oxygen adsorption are circled in blue. Panels c) and d) present DFT STM simulations visualized using Critic2, illustrating the system before and after the addition of an O atom above the Fe center. Following oxygen adsorption, the Fe atom (green circle in panel c)) is no longer visible (blue circle in panel d)), confirming the high reactivity of the layer toward O_2 after Co deposition.

As shown by DFT charge transfer calculations and supported by the XPS data discussed in the following section, Co deposition induces an electronic change in the layer, modifying the Fe oxidation state, making it highly reactive toward O_2 or H_2O dissociation at room temperature, already from the residual background. In STM studies, oxygen adatoms often appear as dark spots at certain biases due to their low local density of states at the Fermi level [82]. To validate this interpretation, constant-height STM simulations were visualized using Critic2 for the bimetallic system both before and after introducing an O atom atop the Fe center. Panels c) and d) of Figure 4.4 illustrate this: initially, Fe atoms are visible (an example outlined in green); after oxygen coordination, these features vanish (an example circled in blue), confirming that the dark regions in experimental STM images are ascribable to axial Fe-O coordination.
Before proceeding with the electronic characterization, it is worth noting that different approaches were employed to simulate STM images depending on the investigated system. For the UHV pristine configurations, a Python-based script was used to directly process the charge density data obtained from the DFT calculations. This method was suitable for clean systems with relatively simple topographies. However, for the O/FeTPyP-Co system, Critic2 was used instead. This tool provides enhanced capabilities for post-processing charge densities and offers more accurate rendering of the local electronic structure, especially in systems involving adsorbates or charge redistribution over complex molecular frameworks. Critic2 allows finer control over isosurface levels and visual integration planes, which is essential for interpreting charge localization and tunneling pathways in the presence of O. The visual and quantitative differences between the STM images from both tools arise primarily from these methodological distinctions especially in how charge density is interpolated and rendered. Despite these differences, both approaches are consistent with the qualitative trends observed in the system and are chosen based on suitability for each specific case.

4.2 Electronic Properties

The experimental characterization of the electronic structure of the FeTPyP-Co layer is particularly challenging even under UHV conditions, especially for the Fe and Co core levels, due to the very low absolute surface concentration of Fe and Co species, of the order of 1% of a monolayer relative to graphene. Nevertheless, the combination of high-brightness synchrotron radiation and a highly efficient electron energy analyzer enables the reliable detection of such species, allowing for meaningful spectral analysis and peak fitting. To optimize elemental sensitivity, while minimizing radiation-induced damage, tunable synchrotron radiation was used to maximize the photoemission cross section of each core level, requiring a compromise between experimental resolution constrained by the analyzer pass energy, slit aperture and the risk of beam-induced degradation. To further mitigate molecular damage during measurements, a slow raster scan of the sample (0.5 $\mu m/s$) was implemented to limit prolonged local exposure to the intense X-ray beam. This was possible thanks to the homogenous sample growth, as confirmed by STM. Core-level spectra were acquired using photon energies tailored to each element, to maintain consistent surface sensitivity: Fe and Co $2p_{3/2}$ at 1000 *eV*, O 1*s* at 750 *eV*, N 1*s* at 514 *eV*, C 1*s* and Ir $4f_{7/2}$ with 400 *eV* photons. All fit parameters are summarized in Appendix A.1.
A complete set of Fe $2p_{3/2}$, Co $2p_{3/2}$, O and N 1*s* core-level spectra for the as-prepared mono- and bi-metallic monolayers in UHV is presented in Figure 4.5 (bottom and top panels, respectively), along with their corresponding best-fit curves and spectral components. The complex multi-peak structure observed in the Fe and Co $2p_{3/2}$ core level spectra in Figure 4.5 arises from multiplet splitting (MS) [83,84], a phenomenon caused by the interaction between the core hole created during photoemission and unpaired electrons in the valence band [83]. This effect is particularly pronounced for high-spin electronic configurations of Fe(II), Fe(III), Co(II), Co(III) ions, giving rise to complex spectra with many overlapping components that are typically extremely challenging, if not impossible, to fully resolve experimentally. For the monometallic system, the best fit for Fe $2p_{3/2}$, Figure 4.5 a) (bottom) was obtained using three Voigt envelopes centred at 707.6 (green), 708.9 and 711.6 eV.

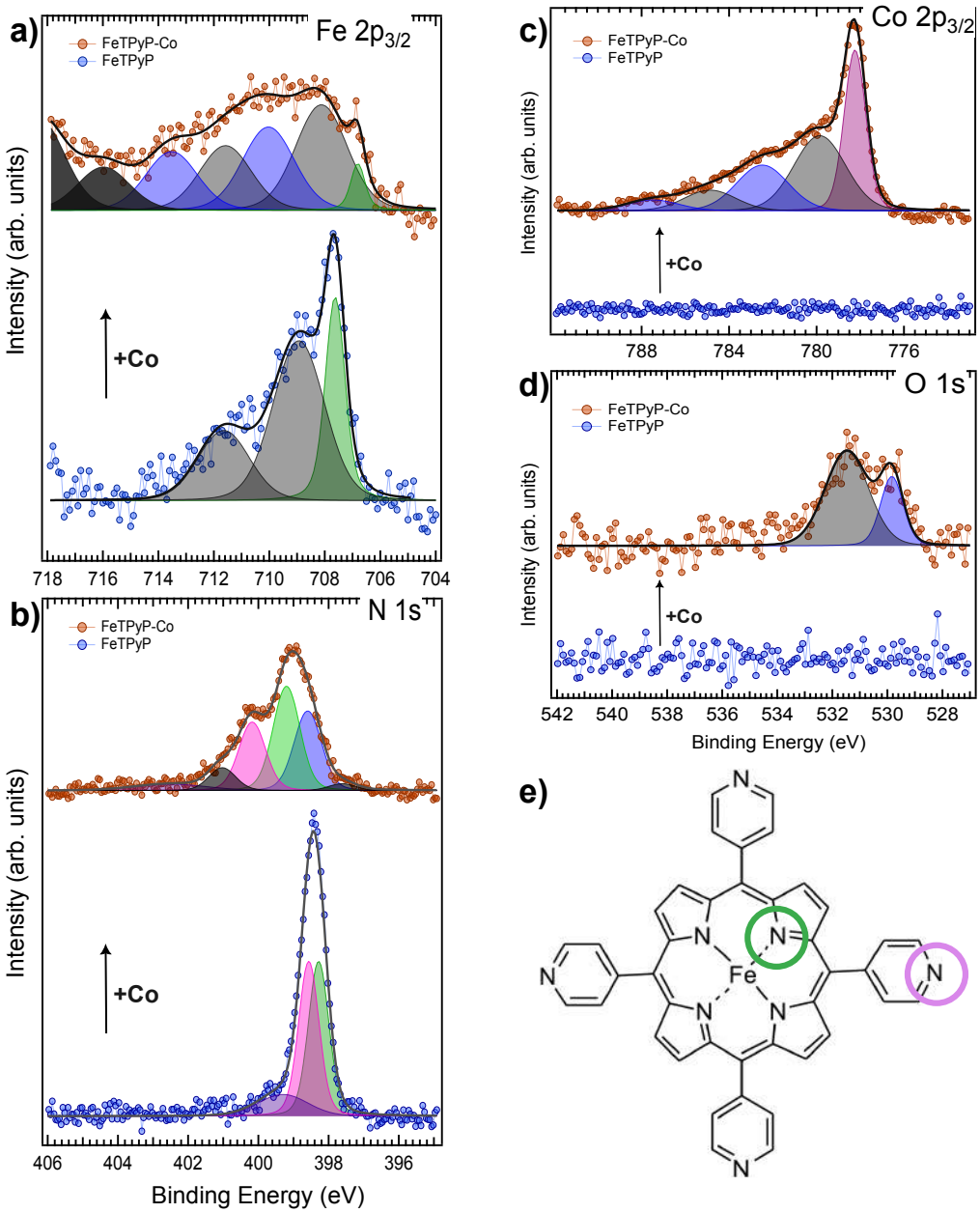

Figure 4.5 Synchrotron radiation XPS spectra together with best fit and resolved components of 1ML of FeTPyP on Gr/Ir(111) before (blue) and after (orange) Co deposition slightly above the stoichiometric 1:1 (FeTPyP:Co) ratio, acquired under UHV conditions at room temperature. a), b), c) and d) show cobalt influence on Fe $2p_{3/2}$, N 1s, Co $2p_{3/2}$ and O 1s core levels, respectively (see text for details). e) Schematic of FeTPyP with color-coded nonequivalent N species matching the resolved components in b). Photon energies: a,c) 1000 eV, b) 514 eV and d) 750 eV.

The latter two peaks are attributed to MS components of Fe(II), whereas the lowest binding energy peak is assigned to a well-screened final state of Fe(II), in agreement with the Gunnarsson-Schönhammer (GS) model and considering that Fe(0) is expected at 706.6 eV.
GS contribution arises from the transfer of a screening charge from valence states of the substrate to an unoccupied molecular orbital that is pulled below the Fermi level by the core hole [85–87] and it has been already identified in cobalt-based systems such as CoTPyP/Gr/Ir(111) [88] and CoTPyP–Co/Gr/Ir(111) [35] CoTPP/ and CoTTBPP/Ag(111) [87].
These assignments are supported by the systematic analysis conducted by Biesinger *et al.* [84], who investigated the multiplet splitting structure of first-row transition metals in various oxidation states. In

their study, FeO served as a reference for Fe(II), while the multiplet structure of Fe(III) was determined from an average of four crystalline phases: α- and γ- Fe_2O_3 together with α- and γ-FeOOH. Based on these considerations, we conclude that the central Fe atom in the monometallic system is in the +2 oxidation state. A summary of the peak assignments is presented in Table 4.1. To maintain physical consistency and avoid overfitting, all peaks were constrained to share a common optimized Lorentzian width Γ = 0.31 *eV*. The Gaussian width was allowed to vary between GS and MS components but kept fixed among the MS peaks, yielding G = 0.67 and 2.03 *eV* for GS and MS features, respectively.

Fe $2p_{3/2}$	Reference [84]		
FeTPyP (this work)	Fe(0)	Fe(II) (FeO)	
707.6	706.6	708.4	
708.9		709.7	
711.6		710.9	
FeTPyP-Co (this work)	Fe(0)	Fe(II) (FeO)	Fe(III)
706.8	706.6	708.4	710.0
708.1		709.7	711.0
710.0		710.9	711.9
711.6			713.0
713.5			714.1
716.0			719.5
718.3			

Table 4.1 The experimental Fe $2p_{3/2}$ binding energies (in eV) for the mono- and bi-metallic systems (panel a) of Figure 4.5) are reported in the first column, along with reference values for Fe(0) and Fe(II) and Fe(III) compounds. In particular, the binding energy for Fe(III) is given as the average of four different crystalline phases, as reported in [84]. For each system, the most intense peak is highlighted in bold, identifying Fe(II) as the predominant oxidation state in both cases.

A single FeTPyP molecule contains eight nitrogen atoms, grouped into two chemically inequivalent species: four iminic nitrogen atoms coordinated to the central Fe (green), and four peripheral pyridinic nitrogen atoms (pink), as in the molecular scheme in Figure 4.5 e). The N 1s spectrum from FeTPyP/Gr/Ir(111), (Figure 4.5 b), bottom panel) was best reproduced using two main unresolved Voigt components, with binding energies at 398.3, 398.6 *eV*, together with a third feature at 399.3 *eV* assigned to a shake-up satellite. The two main components are assigned to iminic and pyridinic nitrogen atoms, respectively. According to the literature, the binding energy (BE) of the iminic nitrogen in tetrapyrrolic macrocycles can vary by up to 2 *eV*, depending on the metal center and the supporting substrate, but typically lies within the 397-399 *eV* range [37,88–90].
Pyridinic nitrogen in M-TPyP (where M denotes a metalated porphyrin) and in 2HTPyP usually appears at a binding energy that is 0.3-1.0 *eV* higher than that one of the iminic component [29,37,88], in agreement with our observations. Moreover, based on the molecular stoichiometry, the iminic and pyridinic contributions were constrained to share the same intensity. A common lineshape was imposed for the elastic features, using an optimized Lorentzian width of Γ = 0.14 *eV* and Gaussian broadening of 0.61 *eV*. The shake-up feature was fitted using the same Lorentzian width, while the Gaussian width was allowed to vary independently and is significantly broader. The lower panels of Figure 4.5 c) and d) confirm the absence of oxygen and cobalt, further supporting the high purity of the pristine FeTPyP monolayer.
Upon Co deposition, STM reveals significant geometric modifications, with Co atoms tetra-coordinated to the pyridinic nitrogen atoms between adjacent molecules. Despite the low concentration (~1% of a

monolayer), the presence of Co is clearly detectable in the XPS spectrum (Figure 4.5 d), top panel), where the Co $2p_{3/2}$ core level is best fitted using five Voigt components at 778.3, 779.9, 782.5, 784.9 and 787.5 *eV*. All peaks share a common optimized Lorentzian width of 0.2 *eV*. The lowest binding energy feature exhibits a Gaussian width of 1.1 *eV*, while the remaining components share a broader Gaussian width of 2.67 *eV* to avoid overfitting. Experimentally, the correct attribution of an oxidation state from the XPS data is not trivial, as it is influenced by charge transfer effects that may virtually reduce the metal center, as well as by final-state phenomena such as multiplet splitting and the possible presence of a GS screened component, as previously observed for the Fe $2p_{3/2}$ core level. Furthermore, the high reactivity of the system toward molecular oxygen makes the determination of the metal oxidation state more complex, yielding a mixture of non-equivalent Fe and Co species already under UHV and the best possible preparation conditions.
However, the interaction of Co single adatoms with the pyridyl moieties results in a change of the oxidation state of cobalt (see Table 4.2), which neither remains in the elemental Co(0) nor in the Co(II) state typical of metalated porphyrin centers, despite the similar tetra-coordinated environment [35,37,88]. This interpretation is supported by the presence of a low-binding-energy component at 778.3 *eV* (pink) in the Co $2p_{3/2}$ spectrum, which we assign to Co(I), consistent with the GS screening model, as already observed for the Fe $2p_{3/2}$ level. Comparable assignments have been made in previous studies on monolayers of MTPyP-Co on Gr/Ir(111) with M=Co/Mn [35,37] and CoTPP/Ag(111) [87] where the main Co(I) features were found at 778.6, 778.5 and 778.2 *eV*, respectively. Subsequently, the presence of oxygen bound to Co atoms, along with its spectral evolution under CO and O_2 pressures (discussed in the following chapter) and the influence of oxidized iron in the macrocycle, as already confirmed by STM, supports the identification of two discrete families of spectral components. These features, observed at 779.9/784.9 *eV* (grey) and 782.5/787.5 *eV* (blue), are ascribed, respectively, to lower and higher oxidized Co species.

Co $2p_{3/2}$				
FeTPyP-Co (this work)	Co(0)[84]	CoTPyP-Co(I)[88]	MnTPyP-Co(I)[37]	Co(II) (CoO)[84]
778.3	778.1	778.6	778.5	780.0
779.9			780.0	782.1
782.5			781.6	785.5
784.9			784.7	786.5
787.5				

Table 4.2 The experimental Co $2p_{3/2}$ binding energies (in eV) for the mono- and bi-metallic systems are reported in the first column, along with reference values for Co(0), Co(I) and Co(II). The main peak is highlighted in bold, identifying Co(I) as the predominant oxidation state.

The presence of oxygen under UHV conditions is also confirmed by O 1*s* core level, where two distinct features emerge at 529.8 and 531.5 *eV*, panel c) of Figure 4.5. The lower binding energy component (529.8 *eV*) is attributed to oxygen bound to metal centers, specifically Fe and Co, consistent with literature assignments for metal-oxygen species [91–93] and will be further discussed in subsequent chapters. The higher binding energy component at 531.5 *eV* is assigned to oxygen bound to Gr. This assignment is supported by previous studies by Vinogradov *et al.* [94] and Kyrkjebø *et al.* [95], who observed multiple O 1*s* peaks in oxidized graphene systems, including those corresponding to enolate and epoxy species, i.e., atomic oxygen bonded to graphene via single or double bonds, at binding energies consistent with our observed component. These findings confirm that Co atoms incorporation in the monometallic system makes it extremely reactive towards O_2 activation, even under UHV conditions (10^{-9} *mbar*), as already observed in STM images.

The pyridinic nitrogen peak in the N 1*s* spectrum is expected to shift upon coordination with cobalt. Interestingly, the spectrum shown in panel b) of Figure 4.5 reveals the presence of three distinct molecular families following Co deposition, which we tentatively assign as follows. The first, characterized by iminic (green) and pyridinic (pink) nitrogen components from molecules coordinated to single Co atoms at the pyridinic sites. These components are shifted by 0.9 *eV* toward higher binding energies compared to the pristine layer, now appearing at 399.2 *eV* and 400.2 *eV*, respectively. This shift indicates that the electronic configuration of the macrocycle is significantly altered upon network formation [37,88]. The second molecular family is represented by the dark components at 397.6 *eV* (iminic) and 401.0 *eV* (pyridinic), corresponding to molecules in which Co clusters are coordinated at the pyridinic sites. The low binding energy feature at 397.6 *eV* suggests strong electronic interaction between nitrogen and the Fe metal center. This observation is consistent with the findings of Scardamaglia *et al.* [96], who reported a N 1*s* feature at 397.4 *eV* in nitrogen-doped graphene on Ir(111), attributed to nitrogen atoms closer to the metallic substrate. By analogy, we assign the 397.6 *eV* component to iminic nitrogen located closer to Fe atoms, likely promoted by structural and electronic reorganization of the macrocycle induced by the presence of Co clusters at the pyridinic terminations, assigned to the feature at 401.0 *eV*.

Finally, the component at 398.6 *eV* (blue one) is attributed to nitrogen atoms involved in O-M-N (oxygen-metal-nitrogen) coordination, where the nitrogen atoms (iminic/pyridinic) are bound to a metal center (Fe/Co) that simultaneously interacts with the O axial ligand. This assignment is consistent with studies showing that nitrogen atoms in complex coordination environments, such as O-M-N linkages, can exhibit modified N 1*s* binding energies compared to standard M-N bonding.

While electron-withdrawing groups like oxygen typically increase the binding energy when directly attached to nitrogen [97], selected geometries and electronic configurations, such as those in oxynitride systems, can lead to a lowering of the binding energies, as demonstrated by Bittencourt *et al.* [98] for O-Ti-N coordination. Finally, the shake-up satellite is now centered at 402.5 *eV*.

Further evidence of the electronic reorganization is given by the influence of Co coordination on the Fe $2p_{3/2}$ core level (top panel of Figure 4.5 a)), reflecting the cooperativity between the metal centers mediated by the organic backbone. Notably, unlike in MnTPyP-Co and CoTPyP-Co systems, where the central metal adopts a +3 oxidation state upon Co deposition [35,37], iron does not oxidize to Fe(III). The best fit is obtained with seven Voigt components at 706.8, 708.1, 710.0, 711.6, 713.5 *eV* and for higher oxidized states at 716.0 and 718.3 *eV* (dark ones). For all components, the lineshape was chosen to be the same as for the monometallic case (Γ = 0.31 *eV*, G = 2.03 *eV*) except for the first peak, where G width narrows to 0.43 *eV*. The first two components (706.8 and 708.1 *eV*) display a rigid shift of approximately 0.8 *eV* toward lower binding energy with respect to the pristine system. Based on GS screening, together with the presence of elemental iron Fe(0) at 706.6 *eV*, we attribute the feature at 706.8 *eV* (green) to the formation of Fe(I) species, in analogy with what is observed in Co spectra. Moreover, due to the presence of oxygen, two new components arise at 710 and 713.5 *eV* (blue), consistent with Fe(III) species as reported by Biesinger *et al.* [84]. Nevertheless, the dominant component at 708.1 *eV* remains characteristic of Fe(II), allowing us to conclude that, after Co deposition, iron is initially in a +1 oxidation state and, due to its high reactivity, gradually evolves to +2 due to the exposure to the system background gas pressure. This Fe(I) state is likely transient, being this species very reactive, and thus highly sensitive to environmental conditions. Indeed, the intensity of the Fe(I) component varies between measurements, depending on the background pressure and the total acquisition time, which makes it difficult to precisely quantify the relative amounts of oxidized Fe and Co species. However, by combining STM data with the Fe, Co $2p_{3/2}$ and O 1*s* core-level spectra, we infer that the O-metal signal in the O 1*s* spectra originates predominantly from iron oxidation, with approximately 70% of the oxygen atoms bound to Fe and the remaining 30% to Co.

The observed oxidation states are also supported by spin-polarized DFT calculations using the PBE exchange-correlation functional, with Bader charge analysis used to quantify the electronic population at each metal center. For FeTPyP/Gr, the Bader charge of Fe is ≈ 3.98e^-, close to that expected for Fe(II).

In the bimetallic FeTPyP-Co/graphene system, the Bader charges are Fe ≈ 4.52e^- and Co ≈ 4.58e^-. These values are significantly higher (electron gain) relative to the monometallic case, indicating a reduction toward the +1 oxidation state for both Fe and Co. The charge redistribution is mediated by Fe-Co coupling through the porphyrin macrocycles and facilitated by the graphene substrate, which acts as a charge reservoir.

Finally, the C 1*s* and Ir 4$f_{7/2}$, core-level spectra were measured on bare graphene (Gr), after the growth of the FeTPyP monolayer, and following peripheral Co coordination, as shown in panels a) and b) of Figure 4.6. The binding energy and shape of the Gr-related C 1*s* peak are minimally affected by the adsorption of the weakly interacting molecular layer. However, a decrease in peak intensity is observed, attributable to attenuation caused by the molecular adlayer. New C 1*s* components associated with the porphyrin macrocycle and its peripheral substituents emerge at higher binding energies, extending up to approximately 285.6 *eV*, along with a shoulder at ~283.6 *eV*, similar to the case of CoTPyP and MnTPyP on Gr/Ir(111) [37,99]. Upon Co coordination, the shoulder assigned to the porphyrin core exhibits a chemical shift of approximately +330 *meV*, accompanied by spectral broadening, providing additional evidence of the significant electronic influence of Co on the organic backbone, consistent with DFT calculations. In contrast, while the C 1*s* spectrum shows clear modifications, the Ir 4$f_{7/2}$ core-level spectrum (right panel, Figure 4.6) remains unchanged, indicating that the underlying metal substrate is not perturbed by the molecular assembly.

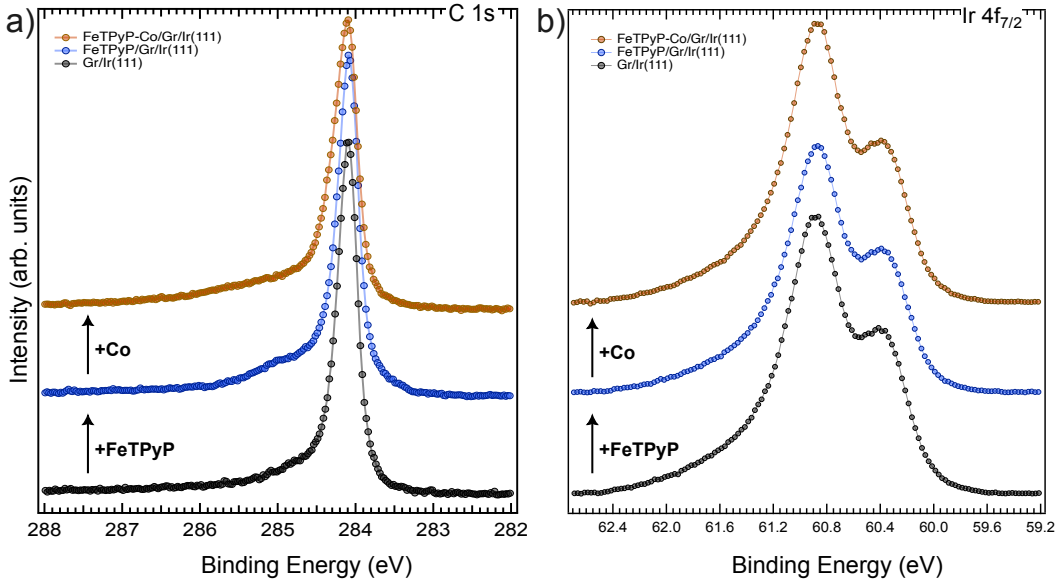

Figure 4.6 C 1s and Ir 4$f_{7/2}$ core level of bare graphene, 1 ML of FeTPyP, and 1 ML of FeTPyP-Co are shown in panels a) and b), respectively. a) The monolayer spectrum displays a decreased intensity of the main peak and the appearance of a shoulder at higher binding energies associated with the pophyrins. Co deposition induces a shift of +330 meV of the molecular carbon shoulder. b) Ir 4$f_{7/2}$ data are shown, revealing the absence of chemical shift of the surface component, indicating that the metal substrate remains unperturbed by the molecular assembly.

4.3 Vibrational Properties

The vibrational fingerprints of the FeTPyP and FeTPyP-Co layers were investigated using IR–Vis SFG spectroscopy. All fit parameters are summarized in Appendix A.1. Figure 4.7 shows the vibrational profiles of the as-prepared mono- and bi-metallic organic frameworks in the 1200-1400 and 1500-1650 cm^{-1} regions, acquired using *ppp* polarization in UHV conditions, along with the best-fit curves and vibrational resolved components corresponding to each vibrational resonance.

These results demonstrate that the significant structural and electronic modifications induced by peripheral cobalt coordination, discussed in previous sections, also impact the vibronic resonances of the molecular layer. In this study, the molecular coverage was approximately 0.7 *ML*, below full monolayer saturation. According to previous experiments, this submonolayer regime promotes long-range molecular ordering by minimizing steric hindrance contributions associated with the molecular realignment. In contrast, cobalt was deposited slightly exceeding the stoichiometric 1:1 FeTPyP:Co ratio and at the same time below the level that induces cluster formation on the graphene substrate. For the pristine FeTPyP layer, three main vibrational resonances are observed in both the low- and mid-wavenumber regions. Based on their spectral positions and intensities, the modes are assigned as follows: at 1217 and 1594 cm^{-1} pyridinic ring bending modes (blue) [26,100,101] at 1239 cm^{-1} combined macrocycle and peripheral ring bending/stretching modes (pink) [26,100] and at 1359, 1531 and 1579 cm^{-1} predominant macrocycle deformations (cyan, red, and yellow) [26,37,100,101].

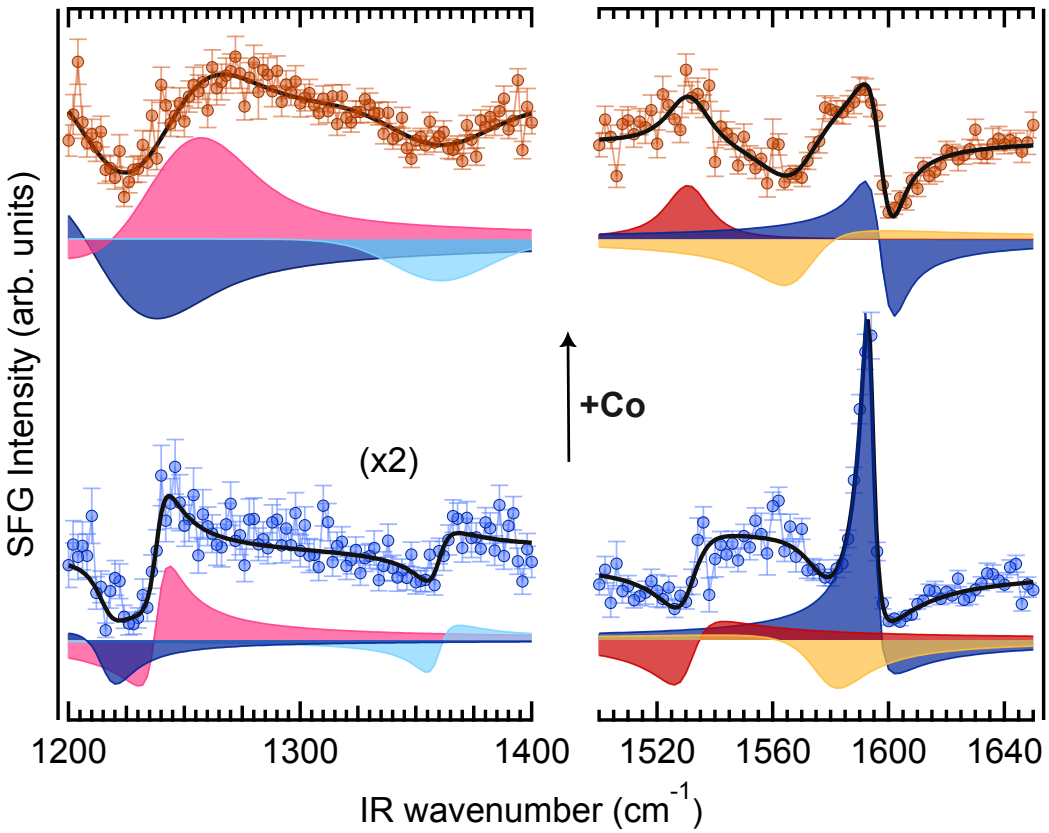

Figure 4.7 SFG spectra, best fit and components of 0.7 ML of FeTPyP (bottom) and FeTPyP-Co/Gr/Ir(111) (top) with Co deposition slightly exceeding the stoichiometric 1:1 FeTPyP:Co ratio while preventing cluster formation on graphene. Pyridinic modes are highlighted in blue, mixed pyridinic-macrocycle modes in pink, and macrocycle modes in cyan, red and yellow. The addition of peripheral Co atoms introduces spectral inhomogeneity, particularly evident in the low-wavenumber region with a Gaussian contribution equal to 18 cm^{-1}, along with an increase in the non-resonant background and phase shifts in selected modes, indicating a change in the electronic structure of the system.

For the pristine system, the Gaussian broadening was below the experimental uncertainty and thus kept to zero, reflecting the high molecular order demonstrated by the STM images. Upon Co deposition, several modifications arise. First, an increase in the non-resonant background amplitude and a phase shift affecting selected vibrational features are observed, both indicative of changes in the electronic structure, consistent with the XPS data. Similar effects have been reported for MnTPyP-Co [37] and CoTPyP-Co networks [35]. In the latter case, STS and DFT calculations attributed the enhanced non-

resonant background to a reduction in the HOMO-LUMO gap following Co coordination. This reduction introduces new electronic excitation channels, thereby enhancing the SFG signal. Moreover, the addition of Co introduces inhomogeneity into the system, due to the coexistence of Co clusters and single-atom Co and Fe centers exhibiting different oxidation states arising from their distinct configurations at the pyridinic and iminic sites, respectively, as revealed by STM and XPS measurements. This structural and chemical disorder is reflected in the SFG spectra by means of an induced and sizeable Gaussian broadening of the resonances, which is otherwise typically negligible compared to the Lorentzian (homogeneous) contribution. However, this broadening becomes more pronounced in the 1200-1400 cm^{-1} region (optimized G = 18 cm^{-1} while Γ_{blue} = 9, Γ_{pink} = 6 and Γ_{cyan} = 6 cm^{-1}) compared to the 1500-1650 cm^{-1} range (optimized G = 3 cm^{-1} while Γ_{red} = 8, Γ_{yellow} = 12 and Γ_{blue} = 3 cm^{-1}) likely because vibrational modes at higher wavenumbers correspond to more localized and energetically rigid molecular vibrations, which are less susceptible to environmental disorder. This Gaussian broadening is accompanied by a shift of the components originally at 1239 and 1579 cm^{-1}, now at 1246 and 1560 cm^{-1}. Notably, the component associated with the pyridinic group is blue-shifted to 1598 cm^{-1}, and can potentially serve as an indirect spectroscopic fingerprint of Co coordination and ligation at this site, particularly in chemical reactivity experiments. Table 4.3 shows the energies of the fitted resonances

FeTPyP (this work)	FeTPyP-Co (this work)	Mode
1217	1217	$\delta(\mathrm{py})$
1239	1246	$\upsilon(\mathrm{C_\alpha - N}) + \delta(\mathrm{C_\beta - H})$, $\upsilon(\mathrm{C_m - pyr}) + \delta(\mathrm{C-H})_{pyr}$
1359	1359	$\upsilon(\mathrm{C_\alpha - N})$
1531	1531	$\upsilon(\mathrm{C_\beta - C_\beta}) + \delta(\mathrm{C_\beta - H})$, $\upsilon(\mathrm{C_\beta - C_\beta})$, $\upsilon(\mathrm{C_\alpha - C_m})$
1579	1560	
1594	1598	$\delta(\mathrm{py})$

Table 4.3 SFG vibrational resonances energy (in cm^{-1}) of FeTPyP and FeTPyP-Co monolayers on Gr/Ir(111). Tentative mode attribution by comparison with experimental values for FeTPyP [100,101] MnTPyP [37], and CoTPyP [26,35]. The carbon labels refer to Figure 2.2.

4.4 Conclusion

In summary, the deposition of FeTPyP on graphene under UHV conditions leads to the formation of a self-assembled, ordered monolayer that is electronically decoupled from the underlying metal substrate. This layer is capable of hosting Co atoms, which coordinate between the peripheral nitrogen atoms of adjacent porphyrins, inducing a significant geometric and electronic rearrangement of the network.

STM measurements reveal that the initial close-packed structure of FeTPyP reorganizes into a (2×2) oblique lattice in Co intermediate coverage, and into a square lattice upon saturation. Through this process, non-equivalent metal centers are stabilized within the organic framework, yielding a bimetallic network with emergent properties. Notably, increasing Co loading within a certain threshold, Co atoms preferentially bind to each other, forming small clusters that remain stabilized at room temperature between the organic backbone.

Detailed electronic and vibrational characterization of FeTPyP and FeTPyP-Co monolayers was performed using synchrotron-based XPS and tabletop laser IR–Vis SFG. Coordination of the second metal atom influences the oxidation states of both metal centers. Co is not present as metallic Co(0) but instead exhibits a +1 oxidation state, thereby confirming coordination at the pyridinic terminations. Simultaneously, Fe is likely reduced to a +1 state, as supported by spin-polarized DFT calculations with

Bader charge analysis; however, the high reactivity of this oxidation state hinders its stabilization. Indeed, STM and DFT reveal oxygen bound to Fe atoms, a finding further confirmed by XPS through the detection of oxidized components in both the Fe and Co $2p_{3/2}$ core-level spectra. This necessary preliminary characterization of the MON opens now the way towards the investigation of the reactivity of the layers beyond UHV conditions.

5 | Co Influence on Layer Reactivity: FeTPyP vs FeTPyP-Co toward O_2 and CO

This chapter provides a detailed investigation of the reactivity of FeTPyP and FeTPyP-Co monolayers toward O_2 and CO, explored up to near-ambient pressure conditions. For FeTPyP, reactivity was probed exclusively by IR-Vis SFG spectroscopy, whereas for FeTPyP-Co, a combination of NAP-XPS and IR-Vis SFG was employed. The experimental findings are further supported by dedicated *ab initio* DFT simulations. All fit parameters are summarized in Appendix A.2.

5.1 Molecular Oxygen Ligation at Single Metal Atom Sites

Oxygen-oxygen bond formation and cleavage are fundamental steps in the oxygen evolution reaction (OER) and the oxygen reduction reaction (ORR), respectively. Both processes are of great technological importance in renewable energy applications, particularly in metal-air batteries, which are emerging as promising alternatives to Li-based systems [8].
A key challenge in developing stable and efficient bifunctional catalysts is defined by the theoretical prediction that the best materials for OER and ORR cannot coincide [8]. A solution can be given exploiting heterometallic reactive centers embedded in 2D organic crystalline networks grown on functional templates. Based on these considerations, we investigated the chemical reactivity of FeTPyP and FeTPyP-Co layers supported on Gr/Ir(111) under O_2 pressure by means of SFG and NAP-XPS. The experimental findings are validated by density functional theory calculations, including Bader charges and charge density difference analysis. Notably, even under UHV conditions, the bimetallic layer displays pronounced reactivity toward O_2, making it a promising candidate for further investigation at higher O_2 pressures.

5.1.1 Vibrational Properties

To confirm the inert character of FeTPyP toward molecular oxygen, the monometallic layer was examined by SFG. In Figure 5.1 a), only normalized spectra are reported. A comparison between the SFG spectra under UHV (cyan) and in 0.06 *mbar* O_2 (red) reveals only a weak signal intensity variation in the 1500-1650 cm^{-1} region. This variation is more plausibly attributed to a reorganization of the FeTPyP layer in the presence of O_2 rather than to a direct Fe-O_2 interaction.
Considering the minimal spectral changes upon O_2 exposure, we conclude that the FeTPyP layer remains inert toward molecular oxygen. This result is consistent with recent studies on MnTPyP and MnTPyP-Co/Gr/Ir(111) systems, where O_2 exposure likewise did not lead to a direct Mn-O_2 interaction in the monometallic case, in contrast to the reactivity observed for the bimetallic system [23]. In the latter case, distinct pressure-dependent regimes were identified: below 10^{-6} *mbar*, only O_2 ligation occurs, whereas above this threshold, O_2 activation takes place, yielding dissociation. In the present work, we find that O_2 activation occurs already under UHV conditions if Mn is repleaced by Fe. We therefore focus directly on higher pressures, specifically 0.01 *mbar*, as shown in Figure 5.1 b).
The spectrum related to the bimetallic system exhibits substantial changes upon O_2 exposure, as shown in Figure 5.1 b). Notably, the presence of O_2 increases layer homogeneity compared to the UHV case. While all vibrational components maintain the same Lorentzian (homogeneous) contribution described in the UHV section, the Gaussian broadening, which reflects system inhomogeneity, decreases significantly: from G = 18 cm^{-1} and G= 3 cm^{-1}, in the 1200-1400 and 1500-1650 cm^{-1} regions under UHV conditions (orange spectrum), to G = 6 cm^{-1} and G = 2 cm^{-1} during O_2 exposure (red spectrum), and G = 5 cm^{-1} and G = 2 cm^{-1} after gas removal (green spectrum).

This reduction reflects the strong reactivity of the layer toward O_2. Before exposure, different coordination environments at iminic and pyridinic moieties contributed to inhomogeneity. During and after O_2 exposure, however, the high reactivity of the layer toward molecular oxygen yields a larger fraction of Fe and Co atoms bound to oxygen, as also confirmed by NAP-XPS measurements shown in the next section, thereby reducing the overall inhomogeneity.

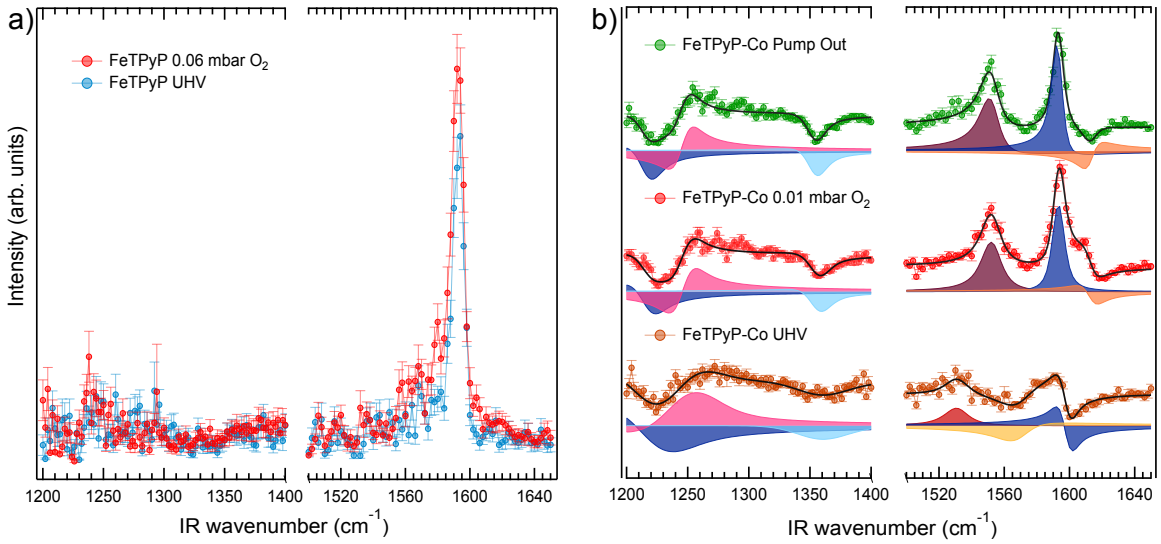

Figure 5.1 a) SFG normalized spectra of pristine FeTPyP layer (0.7 ML) in UHV (cyan) and under 0.06 mbar O_2 (red). b) SFG spectra, best fit and vibrational components of the pristine FeTPyP-Co layer (0.7 ML with Co deposition slightly exceeding the stoichiometric 1:1 FeTPyP:Co ratio avoiding cluster formation on graphene) in UHV (orange), under 0.01 mbar O_2 (red) and after recovering UHV conditions (green).

In addition, several spectral modifications are observed in O_2 background. For the macrocycle modes, the component outline in cyan increases in intensity and redshifts from 1359 to 1356 cm^{-1}, while only a single component at 1552 cm^{-1} (dark purple) is observed in the 1520-1580 cm^{-1} region. Both changes persist after gas removal, indicating a non-reversible process that can be attributed to macrocycle deformations induced by O atoms bound to Fe sites. Moreover, after recovering UHV conditions, the 1356 cm^{-1} component further redshifts at 1354 cm^{-1}, which could be attributed to the absence of O_2 ligation at Fe sites. In the pyridinic region, increased ordering is also evident: in the higher wavenumber range, the dominant contribution (blue) redshifts from 1598 to 1593 cm^{-1}, with an associated increase in intensity, consistent with oxygen binding to Co sites. Notably, a new component (orange) appears at 1613 cm^{-1}, which changes phase after gas removal, providing clear and indirect evidence of O_2 ligation at the Co sites.
Oxygen ligation and activation are further confirmed by DFT calculations, shown in Figure 5.2. The charge redistribution was calculated as the difference between the total charge density of the combined system (M/Gr + O_2, with M=FeTPyP-Co) and the sum of the charge densities of the isolated components in the positions assumed in the total system:

$$\Delta\varrho = \varrho_{M/Gr+O_2} - \varrho_{O_2} - \varrho_{M/Gr} \tag{4.2}$$

integrating over the in-plane coordinates of the unit cell for each z component in order to get $\Delta\varrho(z)$ profile. Its visualization was performed using VESTA, where regions of electron accumulation are shown in yellow and regions of electron depletion in cyan, using an isovalue of ± 0.055 $e^-/Å^3$ respectively. The blue areas correspond to artifacts arising from the finite size and periodic boundary conditions of the simulation cell. At both Co and Fe sites, O_2 adsorbs in the form of superoxide species, with the calculated charge transfer amounting to 0.529e^- from Co to O_2 and 0.485e^- from Fe to O_2. The O-O bond lengths

are estimated as 1.30 Å on Co and 1.28 Å on Fe, compared to a gas-phase value of 1.21 Å, indicating bond elongation and therefore possible activation upon O_2 adsorption, in agreement with SFG data.

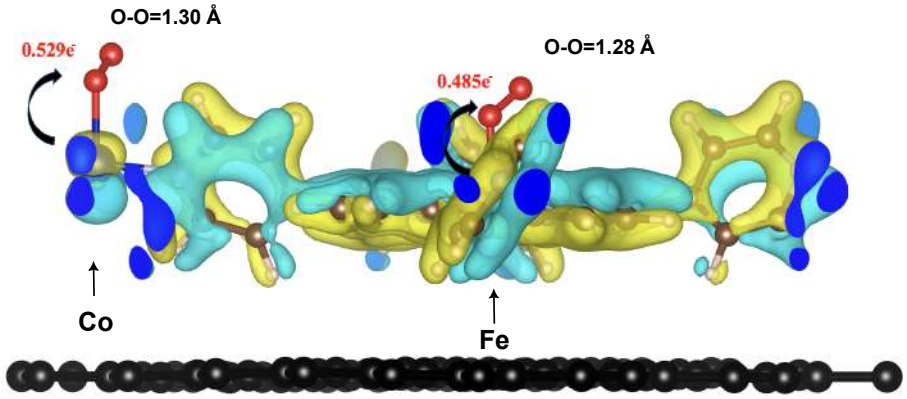

Figure 5.2 Simulated side view of charge redistribution within the unit cell, visualized using VESTA. The system contains one FeTPyP molecule and one Co atom, with O_2 molecule adsorbed on each metal site. Charge redistribution arises from the interaction between the adsorbed O_2 molecules and FeTPyP-Co (brown) on Gr (black). Regions of electron accumulation and depletion are depicted in yellow and cyan, using an isovalue of ± 0.055 $e^-/Å^3$ respectively, highlighting the direction of charge transfer. Blue areas represent artifacts due to the end of the periodicity in the simulation cell.

5.1.2 Electronic Characterization

O_2 ligation and activation are confirmed by NAP-XPS spectra shown in Figure 5.3. Before discussing the spectra in O_2 background, it is important to note that the UHV reference spectra (bottom row of each panel) differ from those previously presented in the UHV characterization section (Figure 4.5). This discrepancy is likely due to different sample preparation conditions, in particular, a longer exposure to the residual UHV background pressure. As a result, the total area of the oxygen components (bottom row of panel d) is approximately twice the corresponding features' area shown in Figure 4.5.
This difference is also reflected in the UHV spectra of Fe and Co $2p_{3/2}$ core levels. For Fe, the area of the GS components, attributed to Fe(I), decreases by ~30%, while the overall areas of Fe(II) (grey, main peak at 708.1 *eV*) and Fe(III) (blue, main peak at 710 *eV*) both increase by ~10%, if compared to Figure 4.5. Together, Fe(II) and Fe(III) become the predominant species in the system. For Co, the spectrum exhibits a pronounced minimum between the GS component (pink), assigned to Co(I), which remains nearly unchanged, whereas the contributions from less (grey) and more oxidized (blue) Co species increase by ~50%.
Upon exposure to O_2, the presence of gas-phase molecular oxygen is evident from two peaks at 538.7 and 539.8 *eV*. These features arise from the characteristic multiplet splitting of the O 1*s* core hole final states of O_2, a well-established fingerprint of gas-phase molecular oxygen in XPS [102].
The previously identified contributions at 529.9 and 531.5 *eV* (O-metal and O-graphene, respectively) exhibit a rigid shift of 0.4 *eV* toward lower binding energies, now located at 529.4 and 531.1 *eV*. Their areas increase to nearly three times the initial values. In addition, a distinct component emerges at 533.7 *eV,* lying between values typically associated with molecular oxygen physisorbed and chemisorbed on metals. More specifically, O_2 on metals is typically observed at binding energies approximately ~2 *eV* higher than in our case [103]. Strongly chemisoberd superoxo (O_2^-) species have been reported at 529.6-530.5 *eV* on Pt [103] and at 532.1 *eV* as active O_2^- on Co [91], whereas weakly chemisoberd dioxygen on Co appears at 532.9 *eV* [23]. Therefore, the feature observed here is ascribed to weakly chemisorbed dioxygen at metal sites, with the 0.6 *eV* shift in binding energy rationalized by O_2 ligation occurring at Fe centers as well as at Co centers. DFT calculations are consistent with this

interpretation, identifying the species as superoxo (O_2^-) bound end-on at both Fe and Co sites, as shown in Figure 5.2. Specifically, charge transfer from Fe (~0.485e^-) is slightly smaller than from Co (~0.529e^-) toward adsorbed O_2 molecule, leading to O 1*s* contributions at slightly higher and lower binding energies, respectively [104]. Considering that these two contributions are close in energy, they cannot be resolved experimentally and instead give origin to a broadened component centered at 533.7 *eV*. Upon restoring UHV conditions, this feature disappears completely, in agreement with SFG measurements.

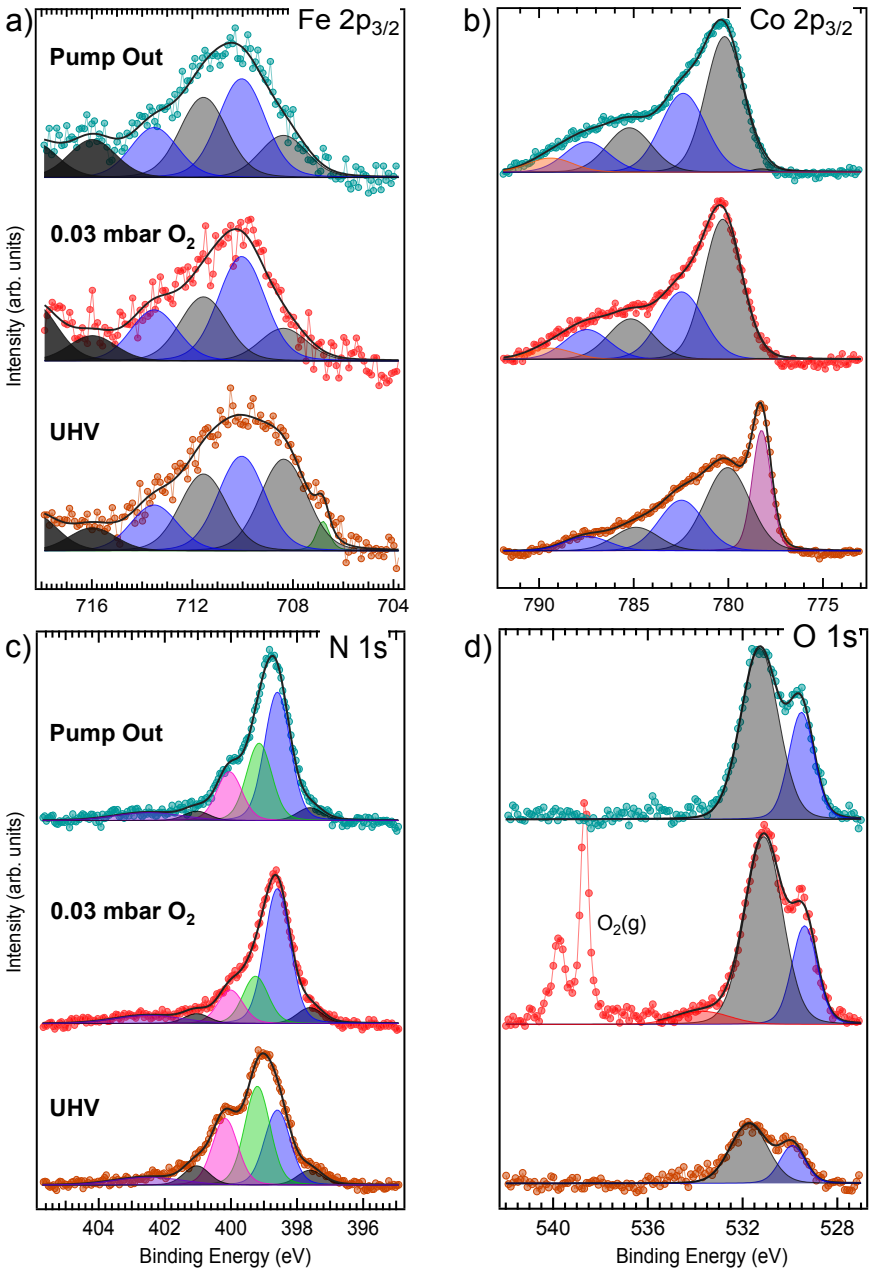

Figure 5.3 Synchrotron radiation XPS spectra of the a) Fe $2p_{3/2}$, b) Co $2p_{3/2}$, c) N 1s and d) O 1s core levels of 1ML of FeTPyP on Gr/Ir(111) with Co deposition slightly above the stoichiometric 1:1 (FeTPyP:Co) ratio, collected at room temperature in UHV (bottom row, orange), at equilibrium in 0.03 mbar O_2 (central row, red), and after recovering UHV conditions (top row, cyan). Photon energies: a,b) 1000 eV, c) 514 eV and d) 750 eV.

A pronounced modification is also observed in the N 1*s* spectra following the introduction of the O_2. Under O_2 pressure, the area of the O-M-N (blue) component nearly doubles compared to the UHV case,

whereas the iminic and pydinic contributions decrease by the same amount. The almost unchanged relative ratios of the spectral components after restoring UHV conditions indicate that, following O_2 exposure, the predominant molecular species correspond to those with oxidized Fe and Co sites. This confirms the irreversibility of the process, in agreement with SFG results.
In the Fe $2p_{3/2}$ spectra, O_2 exposure leads to complete quenching of the GS component, accompanied by a ∼40% decrease in total Fe(II) contributions (grey) and a ∼10% increase in total Fe(III) components (blue), with the main peak at 710 *eV*, which becomes the dominant Fe species. This distribution persists even after UHV recovery, providing clear evidence of the system's irreversibility. Similarly, in the Co $2p_{3/2}$ spectra, the GS component disappears completely under 0.03 *mbar* O_2. The less oxidized Co contributions shift rigidly by ∼0.3 *eV* toward higher binding energies, now at 780.3/785.2 *eV* (grey), and their contribution increased by ∼50%. A comparable increase ∼50% is also observed for the more oxidized Co species contributions at 782.5/787.5 *eV* (blue). The predominant Co species is in the +2 oxidation state, represented by the dominant component at 780.3 *eV*, while a new feature emerges at 789.4 *eV* (orange) which could be ascribed to a MS component of Co(III) [84].
Upon pumping out the gas, the Co spectrum remains essentially unchanged, again confirming the irreversible nature of the process. As in the UHV case, the oxidation states were compared with spin-polarized DFT calculations using the PBE exchange-correlation functional, with Bader charge analysis used to quantify the electronic population at each metal center. The simulated results are fully consistent with the experiment: during O_2 adsorption, the calculated Bader charge for Co is $\approx 8.0e^-$, consistent with Co(II), while for Fe it is $\approx 6.3e^-$, consistent with oxidation toward Fe(III).

5.2 Carbon Monoxide Ligation at Single Metal Atom Sites

Carbon monoxide adsorption has been extensively investigated in surface science since the earliest UHV studies [105], with the aim of providing fundamental insight into adsorption and bond formation processes and, ultimately, of developing more efficient catalysts for CO-involving reactions. Its chemical simplicity, combined with its most stable configuration, typically the *on-top* (terminal) geometry, where the carbon atom binds directly to the metal surface, makes CO an optimal molecular probe for studying the adsorption (surface science) and ligation (biochemistry) sites' properties. In addition, its strong dipole moment makes it easily detectable by means of dipole-sensitive techniques like SFG, where it usually generates an intense signal [35,106–108].
On this basis, the reactive sites of FeTPyP and FeTPyP-Co monolayers were investigated by exposing the system to a CO background at room temperature by means of IR-Vis SFG and NAP-XPS. The experimental observations are validated using density functional theory calculations, including Bader charges and charge density difference analysis. All fit parameters are summarized in Appendix A.3.

5.2.1 Vibrational Properties

The C-O stretching band of CO adsorbed *on-top* is generally observed from 1800 cm^{-1} up to 2120 cm^{-1} on metal surfaces, clusters, single metal atoms and metal-organic molecules [35,76,106,109,110] with the gas-phase value at 2143 cm^{-1} [111].
In the present work, the SFG spectra of both mono- and bi-metallic layers, acquired in the 1850-2050 cm^{-1} CO stretching region under UHV and CO pressure conditions, are shown in panels a) and b) of Figure 5.4. As already described in the UHV characterization, notable structural and electronic changes occurs upon Co coordination, which are further confirmed by CO adsorption. Indeed, in the monometallic system, the SFG spectrum remains flat even upon exposure to CO pressures up to 0.01 *mbar*, indicating that Fe sites, in the +2 oxidation state as discussed in the UHV characterization (Section 4.2), are inert toward CO ligation. On the other hand, the bimetallic system (1:0.4, FeTPyP:Co ratio) exhibits pronounced modifications in the SFG spectrum. Three intense resonances are observed at 1909, 1946 and 1969 cm^{-1}, associated with adsorbed CO under equilibrium conditions with its gas phase, and they reversibly disappear when UHV conditions are restored. This behavior reflects a

dynamic equilibrium between CO adsorption and desorption rates, dictated by both temperature and the CO background pressure.

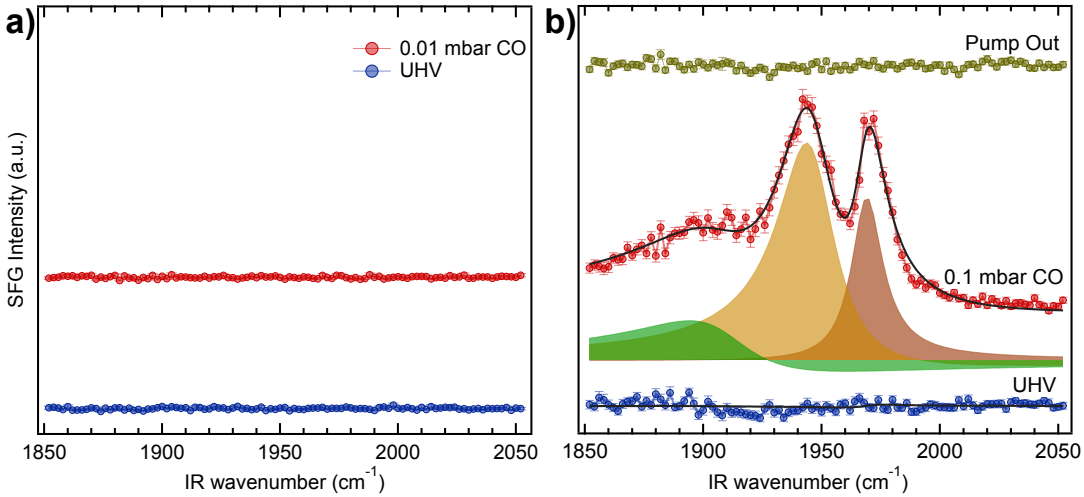

Figure 5.4 a) SFG spectra of FeTPyP/Gr/Ir(111) in UHV and 0.01 mbar of CO. No significant changes are observed for the monometallic system, indicating Fe(II) is inert toward CO adsorption. b) SFG spectra, best fit and resolved vibrational components of FeTPyP-Co/Gr/Ir(111), showing three vibrational features under 0.1 mbar of CO: the fundamental and hot-band transitions of CO on Co atoms (red and yellow), and the fundamental transition of CO on Fe atoms (green), which becomes active toward CO. The pump out spectrum (yellow) demonstrates the reversibility of the process.

The features at 1969 and at 1946 cm^{-1}, previously observed in CoTPyP and MnTPyP-Co monolayers grown on Gr/Ir(111) [23,35], are assigned to the 0→1 fundamental and 1→2 hot-band vibrational transitions of CO adsorbed at the Co sites. Indeed, multiple resonances associated with the same vibronic mode could, in principle, arise from non-equivalent adsorption sites or geometries [112,113] but this usually induces larger chemical shifts. CO adsorption at Co clusters would instead generate bands above 2000 cm^{-1} [76,114], which are absent here. Vibronic splitting due to excitonic coupling could also be considered, but it generally results in much smaller energy separations [106].
Finally, vibrational anharmonicity provides a natural explanation: adsorbed CO can be regarded as a localized oscillator with an anharmonic interatomic potential. As a result, a resonance originating from the $\nu \rightarrow \nu + 1$ transition occurs at progressively lower energy as ν increases [35,76,115]. Based on these considerations, the component at 1946 cm^{-1} is consistent with the hot-band transitions, separated from the fundamental transition by 23 cm^{-1} (≈2.9 meV). Concerning the amplitude ratio between the fundamental and hot-band resonances, we find that it depends on the intensity of the incident IR beam. In SFG, the resonant amplitude scales with the population difference between the initial and final vibrational states; this population difference is affected by the IR excitation intensity, accounting for the observed behavior and further supporting our assignment. In addition, the $\nu = 1 \rightarrow 2$ transition has a higher dynamic dipole moment, leading to a more intense resonant signal [116]. Interestingly, a third component, unobserved in our previous works on CoTPyP- and MnTPyP-Co/Gr/Ir(111) [23,35] appears at a lower wavenumber (at 1909 cm^{-1}, indicated in green in panel b) of Figure 5.4). At first glance, it could be interpreted as the $\nu = 2 \rightarrow 3$ transition. However, this assignment is excluded by anharmonicity considerations: the spacing between this third feature (green) and the hot-band (yellow), 37 cm^{-1}, is larger than the spacing between the hot-band (yellow) and the fundamental (red), 23 cm^{-1}, which is inconsistent with the expected anharmonic potential behavior. A more plausible explanation is that, in the presence of Co, as independently confirmed by XPS, electronic reorganization occurs, making Fe atoms active toward CO adsorption. This hypothesis is further supported by DFT simulations, which confirm CO adsorption at both Fe and Co centers, as shown in Figure 5.5.

The charge redistribution was calculated as the difference between the total charge density of the combined system (M/Gr + CO, with M=FeTPyP-Co) and the sum of the charge densities of the isolated components in the positions assumed in the total system:

$$\Delta\varrho = \varrho_{M/Gr+Co} - \varrho_{CO} - \varrho_{M/Gr} \tag{4.2}$$

integrating over the in-plane coordinates of the unit cell for each z components in order to get the $\Delta\varrho(z)$ profile. Its visualization was performed using VESTA, where regions of electron accumulation are shown in yellow and regions of electron depletion in cyan, using an isovalue of ± 0.076 $e^-/Å^3$, respectively. The blue areas correspond to artifacts arising from the finite size and periodic boundary conditions of the simulation cell.
At Co sites, the CO ligand adopts an upright orientation, whereas at Fe sites it is slightly tilted. The calculated charge transfer amounts to 0.288e^- from Co to CO and 0.049e^- from Fe to CO per unit cell. The C-O bond lengths are estimated as 1.15 Å on Co and 1.14 Å on Fe, compared to a gas-phase value of 1.13 Å, indicating that the CO molecule remains intact and does not dissociate upon adsorption.

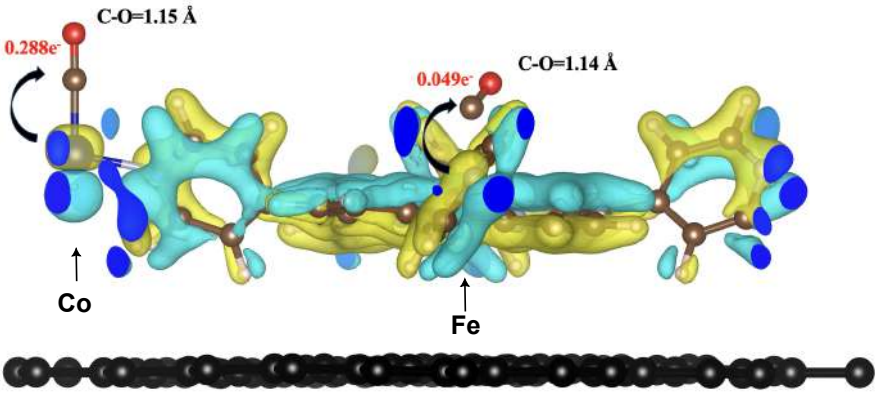

Figure 5.5 Simulated side view of charge redistribution within the unit cell, visualized using VESTA. The system contains one FeTPyP molecule and one Co atom, with CO molecule adsorbed on each metal site. Charge redistribution arises from the interaction between the adsorbed CO molecules and FeTPyP-Co (brown) on Gr(black). Regions of electron accumulation and depletion are depicted in yellow and cyan, using an isovalue of ± 0.076 $e^-/Å^3$ respectively, highlighting the direction of charge transfer. Blue areas represent artifacts due to the end of the periodicity in the simulation cell.

These results suggest that at saturation CO adsorption is stronger at Co than at Fe sites. At first glance, a discrepancy appears when compared with the experimental SFG spectra in Figure 5.4, where the CO adsorbed on Fe (green component) appears at lower wavenumbers, indicating a stronger adsorption relative to Co. This apparent inconsistency arises from the fact that the DFT simulations were performed assuming a 1:1 FeTPyP:Co ratio, which differs from the experimental conditions. Indeed, as the Co loading increases toward the 1:1 ratio, agreement between simulation and experiment is achieved, as will be shown in Figure 5.8 c).
The extreme surface sensitivity of IR-Vis SFG enables a detailed *in situ* investigation of the adsorption process as a function of progressively increasing pressure, from UHV to saturation (mind that saturation is approximately ≤ 1 % *ML*, i.e., the absolute coverage of the single available Co sites). This allows both a quantitative investigation of the kinetics (cooperativity effects), and the determination of the CO adsorption energies on Fe and Co. To probe how cooperativity varies between Co and Fe sites as a function of Co concentration, three different systems were prepared with different Co relative loadings: a) 4%, b) 40% and c) 70% with respect to the FeTPyP coverage. In all cases, Co was kept below the limit 1:1 ratio to minimize anti-cooperative effects arising from direct lateral interactions and exclude contributions from contaminant Co clusters located either between pyridinic sites or on the graphene

surface. Trivially, the amount of adsorbed CO on a monolayer FeTPyP-Co/Gr/Ir(111) increases with CO pressure, as it is determined by the stationary equilibrium between adsorption and desorption. The CO stretching region in the 1850-2050 cm^{-1} range was monitored *in situ* at room temperature as a function of the increasing CO pressure, from UHV to 0.1 *mbar.* The uptake data are plotted in Figure 5.6, where the measured SFG intensity (colour scale) is displayed as a function of both IR wavenumber and CO background pressure.

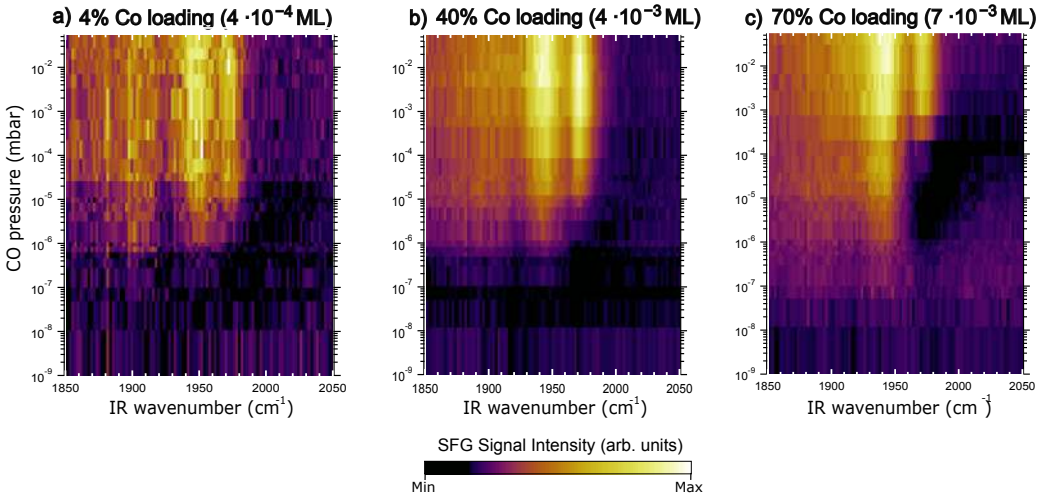

Figure 5.6 a), b) and c) are IR-Vis SFG intensity maps (colour scale), with different Co loadings, as a function of the IR wavenumber and of the background CO pressure spanning over 8 orders of magnitude, measured at equilibrium and at room temperature.

In each of the three preparation of the bimetallic system, the SFG spectrum under UHV conditions is completely flat, but already around 5 × 10^{-9} *mbar*, a weak signal starts to be detectable at 1909 and 1942 cm^{-1}, progressively increasing with pressure and associated with CO adsorbed on Fe and the CO hot-band contribution on Co atoms, respectively. A second resonance starts growing at 1968 cm^{-1} at 10^{-6} *mbar*, corresponding to the fundamental transition of CO on Co, initially with a different phase. In the lower Co concentration case, a), a clear minimum is observed approximately at 1920 cm^{-1} between the 1909 and 1942 cm^{-1} components, which gradually disappears as the Co concentration increases.
It is worth noting that even at the higher Co loading (panel c) of Figure 5.6), the CO adsorbed on Fe, as previously confirmed by DFT simulations in Figure 5.5, appears at lower wavenumbers indicating stronger adsorption compared to Co. The wavenumber position can be rationalized by the same DFT simulations, which show that the CO molecule adopts a tilted configuration on Fe site. This geometry changes its dipole coupling with the molecular layer, shifting its vibrational contribution toward the lower-wavenumber region.
Regarding the resonant amplitudes, it is worth recalling that the hot-band of CO on Ru(0001) and Ir(111) was previously observed by means of broadband SFG [115,116], unlike in our case. In that configuration, the impinging IR beam has a bandwidth of several 100 cm^{-1}, enabling hot-band excitation through absorption of two photons with different energies, resonant with both 0→1 and 1→2 transitions, respectively. SFG spectra obtained under such conditions provide a more accurate representation of the population ratio between the ground and first excited vibrational levels. By contrast, in a scanning-IR SFG configuration the excitation is provided by a narrow IR pulse (of the order of 1 cm^{-1} width). Ideally, to study the hot-band in a scanning configuration, the fundamental transition should be excited resonantly with a dedicated fixed-wavelength IR pulse, while performing the SFG measurement using a second IR beam. In our case, however, at each point of the spectrum the system is both pumped and probed by the same scanning wavelength IR pulse, and the 0→1 and 1→2 transitions are excited by IR photons with the same energy. The hot-band is populated and detectable only because of the intrinsic broad linewidth of the partially overlapping resonances. Consequently, an independent quantitative

analysis of the single hot and fundamental resonances would not be physically meaningful, as their contributions cannot be disentangled.
For this reason, in the case of CO ligation at Co sites, we tracked the evolution of the sum of the resonant signals, keeping in mind that the signal amplitude is proportional to the state population (coverage). To simplify the model and obtain physical insight, the spectra imaged in Figure 5.6 were fitted with globally optimized widths and phases. For the fundamental resonance of CO on Co, we obtain $\Gamma_{CO,0\to1}$ = 8.0 ± 0.2 cm^{-1} and $\omega_{CO,0\to1}$ = 1968.0 ± 0.2 cm^{-1}, while for its hot-band we get $\Gamma_{1\to2}$ = 14.8 ± 0.3 cm^{-1} and $\omega_{1\to2}$ = 1942.0 ± 0.3 cm^{-1}. For the fundamental resonance of CO on Fe, we find $\Gamma_{CO,0\to1}$ = 27.6 ± 0.6 cm^{-1} and $\omega_{CO,0\to1}$ = 1909.0 ± 0.7 cm^{-1}. Since the peak positions remain constant during uptake, both the wavenumber and the Lorentzian linewidth were kept fixed for all spectra. The phases of the hot-band and Fe-related resonances also remained unchanged and were, therefore, linked throughout the uptake, whereas the phase of the CO fundamental transition on Co was allowed to vary, reflecting its pressure-dependent evolution. The uptake profile obtained from the best fit of the data plotted in Figure 5.6 is reported in Figure 5.7. These profiles were derived by plotting the resonance amplitudes as a function of the CO background pressure.

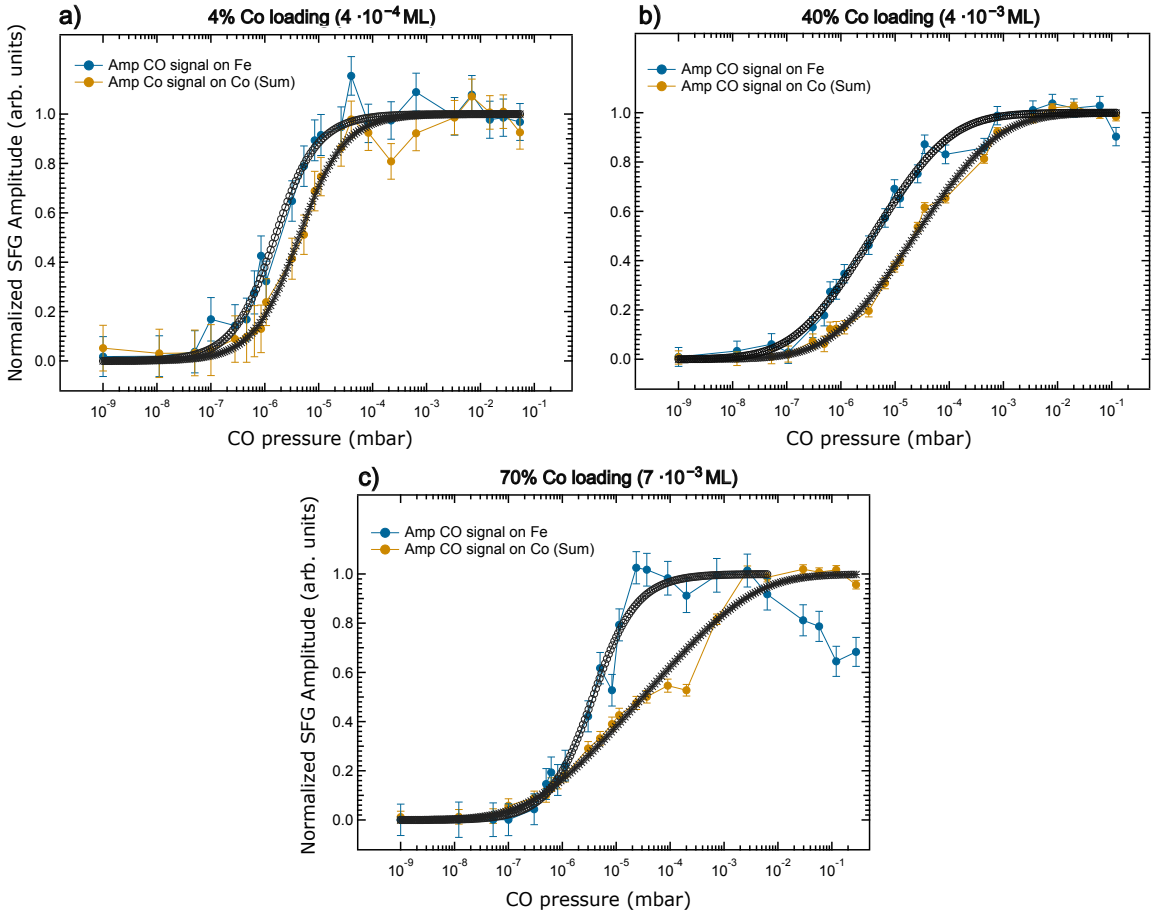

Figure 5.7 a), b) and c) show CO saturation curves at different Co loadings, obtained from the evolution of the IR-Vis SFG amplitude of the C-O internal stretch resonances (markers) extracted from the best fit of the data reported in Figure 5.6, with the associated 1σ confidence interval. For clarity, in black only the best fit of the saturation curve according to the Temkin model (black) is reported.

The evolution of the resonance amplitude associated with CO adsorption at the Fe sites is shown in blue, while the sum of the amplitudes of the fundamental and hot-band resonances of CO adsorbed on Co sites is plotted in yellow. It can be readily observed that, independently of the Co loadings, Fe atoms get saturated by CO earlier than Co atoms. The saturation pressures, however, vary with Co

concentration: for the lowest Co loading (panel a) of Figure 5.7), Fe sites saturate around 10^{-4} *mbar*, while Co sites saturate between 10^{-4}–10^{-3} *mbar*; for intermediate loading (panel b) of Figure 5.7), Fe saturates slightly above 10^{-3} *mbar* and Co around 10^{-2} *mbar*; and for the highest loading (panel c) of Figure 5.7), Fe saturates around 10^{-4} *mbar*, whereas Co requires 10^{-2}–10^{-1} *mbar*. Interestingly, at the highest Co coverage (Figure 5.7 c)), an anomalous trend is observed for Fe sites: after reaching saturation, their signal decreases as Co sites approach saturation. This behavior may originate from a change in the electronic configuration of the layer, caused by CO saturation at Co sites, such that adsorption on Fe sites become less favored. The uptake profiles are best fitted with two different models: the Temkin isotherm and the Hill equation. For clarity, only the Temkin fit is displayed in the graphs (black lines), although both Temkin and Hill fits were applied to the data, as the curves look very similar and would substantially overlap in the plots. These models are widely used in catalysis, biochemistry, and pharmacology. The Temkin isotherm accounts for coverage-dependent adsorption energies, while the Hill equation provides insight into the degree of cooperativity between adjacent adsorption sites. Specifically, we can evaluate the adsorption energy of CO on FeTPyP-Co using the Temkin isotherm, an extended version of the Langmuir isotherm. The model has been largely misused and cited in its dimensionally inconsistent form in the literature. Recently, significant effort has been made to clarify this issue and recover its correct form and approximations [117]. Here, we adopt the following expression, already applied to describe adsorption on metal porphyrins [118]:

$$E_{ads}(\theta) = E_{ads}^{0}\left(1 + \alpha_T \frac{\theta}{\theta_{sat}}\right), \tag{5.1}$$

where E_{ads} is the coverage-dependent adsorption heat, E_{ads}^{0} is the initial adsorption heat (formally the non-cooperative limit, which corresponds to the zero-coverage limit), α_T is the Temkin parameter, θ and θ_{sat} are the coverage and saturation coverage, respectively. The approximation of a linear adsorption heat dependence on θ reflects the degree of (anti)-cooperativity of the process, with α_T assuming values < 0 (anti-cooperativity), $= 0$ (no cooperativity), or > 0 (cooperativity). From the SFG data, we extract the evolution of the normalized coverage term θ/θ_{sat}, obtained from the normalization of the resonant amplitude of the C-O stretching mode to its saturation value. In parallel, the Hill equation provides complementary insight into the degree of cooperativity between adsorption sites [119]. Originally introduced by Hill more than a century ago to describe the cooperative binding of oxygen to hemoglobin [120], the model relates the fraction of occupied receptors to the ligand concentration as:

$$\frac{\theta}{\theta_{sat}} = \frac{p^n}{p_{0.5}^n + p^n}, \tag{5.2}$$

where θ/θ_{sat} represents the ratio between occupied and total available binding sites, p is the gas pressure, $p_{0.5}$ is the pressure at which half of the receptors are occupied, and n is the Hill coefficient [119]. The latter can assume only positive values, larger or smaller than 1, corresponding to cooperative and anti-cooperative binding, respectively. The n = 1 case indicates a non-cooperative response, in which adsorption at one site is not influenced by the occupation of the neighboring sites. It is worth recalling that both the Temkin and Hill models reproduce the non-cooperative Langmuir isotherm, for α_T = 0 and n = 1, respectively. For the different Co loadings, the following best-fit values were obtained and visualized in Figure 5.8 (panels a) and b)). In each panel, the Temkin coefficient (α_T, left axis) and the Hill coefficient (n, right axis) are plotted as a function of Co loading and the parameters summarized for clarity in Table 5.2.1.

At low Co concentration, both Fe and Co sites are consistent with a non-cooperative CO adsorption mechanism ($\alpha_T \approx 0$, $n \approx 1$). With increasing Co loading, a shift towards anti-cooperative behavior is observed on both sites, obtaining α_T = -0.09 and n = 0.64 for Fe and α_T = -0.11 and n = 0.63 for Co. At

the highest Co loading, Fe sites revert to a non-cooperativity response, whereas Co sites exhibit stronger anti-cooperativity.

	α_T	n	$p_{0.5}(mbar)$	E^0_{ads}(eV)
4% Co loading	0.01 ± 0.02	0.99 ± 0.14	(4.24 ± 0.65) × 10^{-6}	0.75 ± 0.01
Fe	0.004 ± 0.024	1.10 ± 0.15	(1.53 ± 0.20) × 10^{-6}	0.77 ± 0.01
40% Co loading	-0.11 ± 0.01	0.63 ± 0.02	(2.25 ± 0.11) × 10^{-5}	0.744 ± 0.003
Fe	-0.09 ± 0.01	0.64 ± 0.04	(3.80 ± 0.33) × 10^{-6}	0.78 ± 0.01
70% Co loading	-0.18 ± 0.01	0.49 ± 0.02	(3.12 ± 0.24) × 10^{-5}	0.766 ± 0.004
Fe	0.01 ± 0.02	1.10 ± 0.11	(3.67 ± 0.41) × 10^{-6}	0.75 ± 0.01

Table 5.2.1 Temkin and Hill coefficient (α_T, n), half-saturation pressure ($p_{0.5}$) and adsorption energy at zero coverage (E^0_{ads}) with associated 1σ confidence interval, obtained by fitting the uptake curves in Figure 5.7.

The half-saturation pressures ($p_{0.5}$) extracted from the uptake profiles further support this trend. Independent of the Co loading, Fe sites always reach half-coverage at lower pressures than Co sites. The adsorption energies at zero CO coverage (E^0_{ads}), shown in panel c of Figure 5.8, reveal a clear site preference in the early stages of the uptake: CO binds preferentially to Fe atoms at low Co concentrations. However, as the Co loading approaches the FeTPyP:Co = 1:1 ratio, a crossover occurs, with stronger CO adsorption observed on Co relative to Fe. This trend is fully consistent with the DFT calculations shown in Figure 5.5.

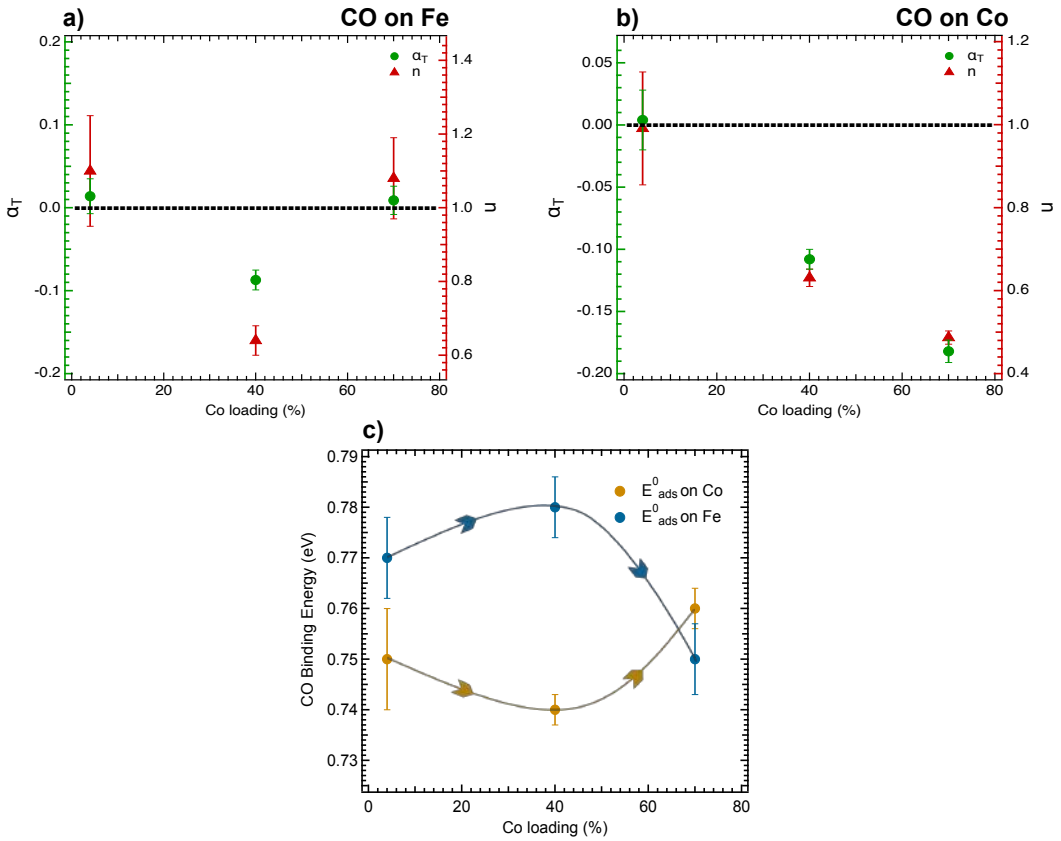

Figure 5.8 a) and b) reported Temkin (left axis) and Hill (right) coefficients as a function of Co loading. The dashed line indicates the non-cooperative regime, separating cooperative (above) from anti-cooperative (below) behavior. While Fe displays a minimum, Co sites exhibit a linearly increasing anti-coopertivity. c) The initial adsorption heat E^0_{ads} for Fe (blue) and Co (yellow) is shown as a function of Co loading, indicating that CO initially prefers to bind to Fe sites and gradually shifts to Co sites as Co approaches saturation.

The value obtained for E_{ads}^{0} indicates weak binding (for comparison, the adsorption energy of CO/Ir(111) is 1.4–1.9 eV) [121], accounting for the observed reversibility of ligation at room temperature. In the FeTPyP-Co system, we find clear evidence of anti-cooperativity ($n < 1;\ \alpha_T < 0$) despite the large intermolecular distance (of the order of a few *nm*) between the most adjacent Co and Fe sites within the network, which rules out the presence of lateral interaction. Indeed, for CO adsorption on bare metal surfaces, such as Ir(111) [116], Pt(111) [122] and Ru(0001) [115,123], blueshifts of 30-80 cm^{-1} of the fundamental CO resonance are observed during the uptakes at RT. These shifts are well explained by strong CO dipole-dipole coupling between adjacent molecules, separated by only a few Å. By contrast, in the FeTPyP-Co system, STM images show that the shortest distance between two adjacent adsorbed CO molecules on the metal sites is significantly larger: ~1.9 *nm* between Fe-Fe and Co-Co sites and ~1.4 *nm* between Fe-Co sites. At such distances, direct lateral interactions between ligands can be considered negligible, in line with previous observations for CO/FePc [106], CO/CoTPyP-Co [76] and CO/MnTPyP-Co [23]. Indeed, the direct dipole-dipole interaction potential energy can be written in the form:

$$U(r) = \frac{d^2}{4\pi\varepsilon_0 r^3} \tag{4.4}$$

where r is the intermolecular distance, d the dipole moment, and ε_0 the vacuum permittivity. Using $d=d_{CO}$ = 0.112 *D* [76,106] and r = 1.8 *nm* for Fe-Fe and Co-Co sites and r = 1.4 *nm* for Fe-Co sites, the resulting interaction energies are U = 1.43 × 10^{-6} *eV* and U=2.85 × 10^{-6} *eV*, respectively. These correspond to a wavenumber blue-shift of the order of 0.01 cm^{-1} and 0.02 cm^{-1}.
Thus, direct dipole-dipole coupling can be safely excluded as a candidate for the observed anti-cooperativity. Likewise, we can rule out the possibility of Förster transfer of excitations [115,116]. According to Förster's model, an excited oscillator can exchange vibrational energy with an unexcited one by means of dipole-dipole coupling. The local-oscillator behavior of CO on Ru(001) has a breakdown at around 0.33 *ML*, due to the strong dipole-dipole coupling among adsorbates and the resulting vibrational energy delocalization [115], similarly to the case of CO/Ir(111) [116]. As a consequence, the hot-band is quenched while the fundamental resonance broadens with increasing CO coverage, which is not compatible with our data. Furthermore, we already demonstrated above that in our case the dipole-dipole interactions are negligible, ruling out this mechanism as well.
Therefore, the observed anti-cooperativity is most plausibly attributed to structural and electronic effects of the heterostructure itself, such as charge transfer and distortion of the organic backbone induced by carbonylation, in close analogy to what has been demonstrated for related systems CoTPyP-Co/ and MnTPyP-Co/Gr/Ir(111) [23,76].

5.2.2 Electronic Properties

CO ligation on the bimetallic system (Co slightly above the stoichiometric FeTPyP:Co ratio 1:1, avoiding at the same time Co clusters on graphene) is further confirmed by NAP-XPS investigation. Core level spectra of Fe and Co $2p_{3/2}$ along with O and N 1*s* were collected at room temperature before, during and after CO exposure, as shown in Figure 5.9. The maximum CO pressure used was 0.03 *mbar,* chosen as a compromise: sufficiently high to ensure saturation of Fe and Co sites, as observed in the SFG measurements, while remaining as low as possible to minimize the contribution of residual O_2, which is the common contaminant in the CO high-pressure bottle (99.97% purity). In the bottom row of each panel in Figure 5.9, the core level spectra of the as-prepared FeTPyP-Co layer are shown, previously described in the UHV characterization (Section 4.2). Upon CO exposure at room temperature, a stationary adsorption-desorption equilibrium is established.
Modifications in the O 1*s* spectrum (panel d) of Figure 5.9, red) are observed, with the CO gas phase appearing at 538.1 *eV* [124]. In addition, between the gas phase contribution and the O species bound to graphene (grey, 531.5 *eV*) and to metal sites, shifted 0.1 *eV* toward lower binding energies (blue,

529.7 *eV*), a new component arises at 533.9 *eV* (red). This feature is attributed to CO adsorbed at metal sites, with values up to 534.1 *eV* also reported for weakly bound terminal species [125]
The presence of CO ligation is further supported by DFT calculations, as shown in Figure 5.5, while the disappearance of this component upon pumping out the gas is fully consistent with SFG observation. These binding energies are in line with previous NAP-XPS studies of CO adsorption on MnTPyP-Co/Gr layer [23], with the key distinction in the markedly higher reactivity of the FeTPyP-Co system toward O_2 activation, as already demonstrated in the UHV characterization. Notably, the relative contributions between the O-graphene (grey) and O-metal (blue) deviate from the trend observed under UHV and O_2 conditions. Specifically, under CO exposure, the O-graphene component increases to nearly three times its initial value, whereas the O-metal contribution grows by only ~20%.

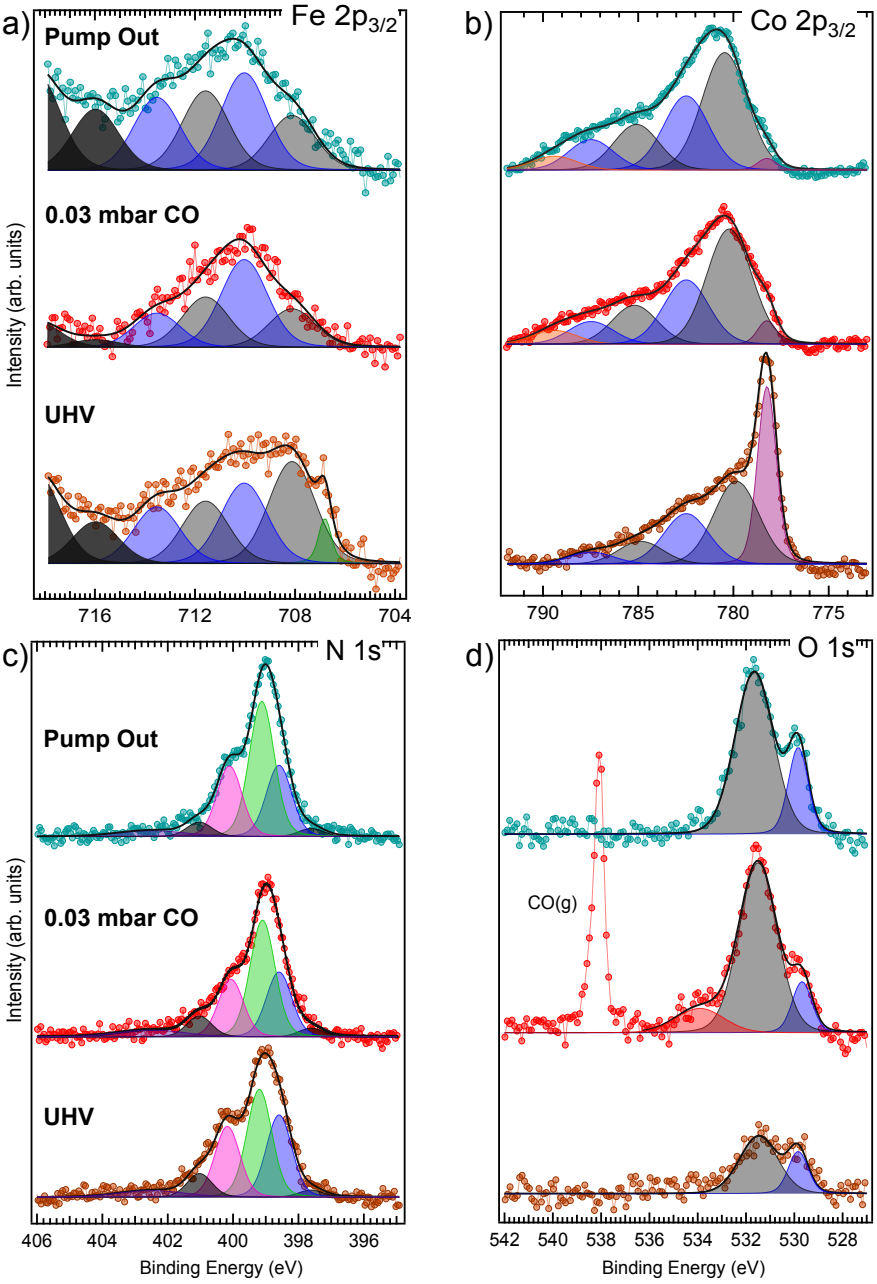

Figure 5.9 Synchrotron radiation XPS spectra of the a) Fe $2p_{3/2}$, b) Co $2p_{3/2}$, c) N 1s and d) O 1s core levels of the FeTPyP-Co/Gr layer collected at room temperature in UHV (bottom row, orange), at equilibrium in 0.03 mbar CO (central row, red), and after recovering UHV conditions (top row, cyan). Photon energies: a,b) 1000 eV, c) 514 eV and d) 750 eV.

Upon pump out, the O-graphene signal remains nearly unchanged, while the O-metal contribution further increases by ∼70%. Taken together with the disappearance of the CO-related feature, these results indicate that, under CO pressure, a dynamic equilibrium is established between CO adsorption, O_2 ligation/activation, and CO recombination. A plausible scenario is that CO molecules either adsorb on metal sites or recombine with the O atom bound to these sites, thereby regenerating the metal for further interactions. Concurrently, the residual presence of O_2 during CO exposure promotes its ligation and activation at the metal sites. Following activation, some O atoms spillover onto the graphene support, while those remaining at the metal sites may undergo further recombination with CO.
A similar trend is observed in the N 1*s* spectra (panel c) of Figure 5.9). The O-M-N component (blue), already identified in the UHV characterization, decreases by ∼20% during CO exposure and partially recovers (+10%) after pump out. In parallel, the iminic and pyridinic contributions (green and pink) evolve differently: the iminic component increases by ∼8% under CO pressure and by ∼16% after pump out, whereas the pyridinic component decreases by ∼20% during CO exposure but fully recovers after gas removal. Despite the growth of the of O-metal species after pump out, the N 1*s* spectrum does not fully revert to its UHV spectral distribution, particularly for the iminic and O-M-N components. This indicates that CO adsorption not only modifies the local coordination but also induces structural distortions of the organic macrocycle and the pyridinic terminations. As previously discussed in the vibrational characterization, and consistent with observations on MnTPyP-Co/ and CoTPyP-Co/Gr/Ir(111) networks [23,76], such distortions alter the electronic environment of the coordinating nitrogen atoms, accounting for the observed spectral evolution.
Both metal species are strongly affected by CO exposure. In the Fe $2p_{3/2}$ spectra, the most evident effect is the quenching of the Gunnarsson-Schönhammer component (green), reflecting suppression of the charge transfer mechanism responsible for this feature under UHV conditions. At the same time, the intensity of the higher oxidation contributions (dark) is modulated, while the predominant feature shifts to 710 *eV*, consistent with Fe in the +3 oxidation state. Notably, while the carbonylation process is reversible, consistent with SFG observations, the residual contamination is not; as a result, the GS feature does not recover, whereas the contributions associated with higher oxidation states regain intensity. This behavior is consistent with the strong reactivity of the system toward O_2, already evidenced under UHV conditions.
A similar, though not identical, response is observed for Co. Upon CO adsorption, the GS component (pink, ascribed to Co(I)) is reduced by ∼85%, in contrast to Fe core level, in which the complete quenching of the GS component is observed. This difference may be explained by the extreme reactivity of Fe(I) towards O_2; therefore, after CO recombination at metal sites, Fe centers are instantaneously reoxidized, whereas Co atoms reoxidize more slowly. After pump out, the GS component does not regenerate and it decreases further by ∼50%, consistent with the gradual oxidation of Co sites. During and after CO exposure the dominant feature is located at 780.2 *eV*, the same position found after O_2 exposure, characteristic of Co(II), while a new component emerges at 789.4 *eV* (orange) which, as observed in the Section 5.1.2, could be due to MS component of Co(III) [84].
As in the UHV and O_2 cases, the observed oxidation states were compared with spin-polarized DFT calculations using the PBE exchange-correlation functional, with Bader charge analysis used to quantify the electronic population at each metal center. The simulated results are only partially consistent with the experiment: during CO adsorption, the calculated Bader charge for Co is ≈ 8.1e^-,consistent with Co(II), while for Fe it is ≈ 6.8e^-, indicative of high-spin Fe(II). Ideally, without concurrent O_2 exposure, both Fe and Co would therefore be expected to stabilize predominantly in the +2 oxidation state. Moreover, based on the SFG measurements and by analogy with the MnTPyP-Co/Gr/Ir(111) network [23], where the GS component of Co was restored after pump out, one would expect both metals to return to the +1 oxidation state upon gas removal. However, these expectations are experimentally hindered by the pronounced reactivity of the layer toward O_2, whose presence cannot be fully removed under the present experimental conditions.

5.3 Conclusion

In summary, the FeTPyP layer is inert toward both CO and O_2, whereas distinct properties emerge in the bimetallic system. As demonstrated in the UHV studies, the incorporation of Co into the monometallic FeTPyP layer forms a FeTPyP-Co network, in which Fe(I) exhibits pronounced reactivity toward both O_2 and CO ligation, highlighting the markedly different electronic properties of the bimetallic system.
Leveraging the extreme surface sensitivity of IR-Vis SFG, the evolution of the vibration components was tracked as a function of CO pressure over eight orders of magnitude up to close-to-ambient conditions. By varying the Co loading, the evolution of cooperative mechanism beyond the nanometer range was investigated, including the determination of relative adsorption energies at zero CO coverage, where the initial preference for CO binding on Fe sites shifts to Co above a specific Co loading threshold. The unavoidable presence of O_2 in the background pressure limits XPS analysis under CO exposure. Nevertheless, combined with DFT calculations, the oxidation states of Fe and Co could be determined. In an idealized case, starting from +1 oxidation states, both metals would be expected to switch to +2 under CO pressure and revert to +1 after restoring UHV conditions. However, the oxidation states are experimentally found to be +2 for Co and +3 for Fe, and the system displays a non-reversible behavior. This discrepancy arises from the high reactivity of the network toward O_2, where its activation is observed already under UHV conditions. XPS, IR-Vis SFG measurements and DFT calculations confirm the O_2 ligation (forming weakly chemisorbed superoxo O_2^- species) and activation at both metal sites, with the Co and Fe oxidation states (+2 and +3, respectively) in perfect agreement with the theoretical calculations.

6 | Structural and Electronic Characterization of a Heme Monolayer on Au(111) under UHV conditions

This chapter provides a detailed investigation of the geometric and electronic structures of a heme (Ferriprotoporphyrin IX) monolayer grown on Au(111). The characterization of the layer was carried out by means of microscopy (STM) and spectroscopy techniques (XPS and NEXAFS) under UHV conditions.

6.1 Structural Properties

The STM measurements were carried out at the STM Laboratory of the Graz University (Austria) in collaboration with Dr. Maximilian Laßhofer, Prof. Martin Sterrer and Prof. Giovanni Zamborlini. All STM-derived quantitative evaluations correspond to averages of unit cell parameters measured across multiple high-resolution images. The uncertainty associated with each value is reported as three times the standard deviation of the mean ($3\sigma_m$), providing a conservative estimate that accounts for both statistical variability and instrumental noise. All STM measurements presented in this work were performed at liquid nitrogen (LN_2) temperature.
Upon deposition at RT onto Au(111), heme molecules organize into long-range ordered islands. The order is driven by lateral intermolecular interactions, which prevail over the weak molecule-substrate coupling. A close-up view is shown in Figure 6.1 a).

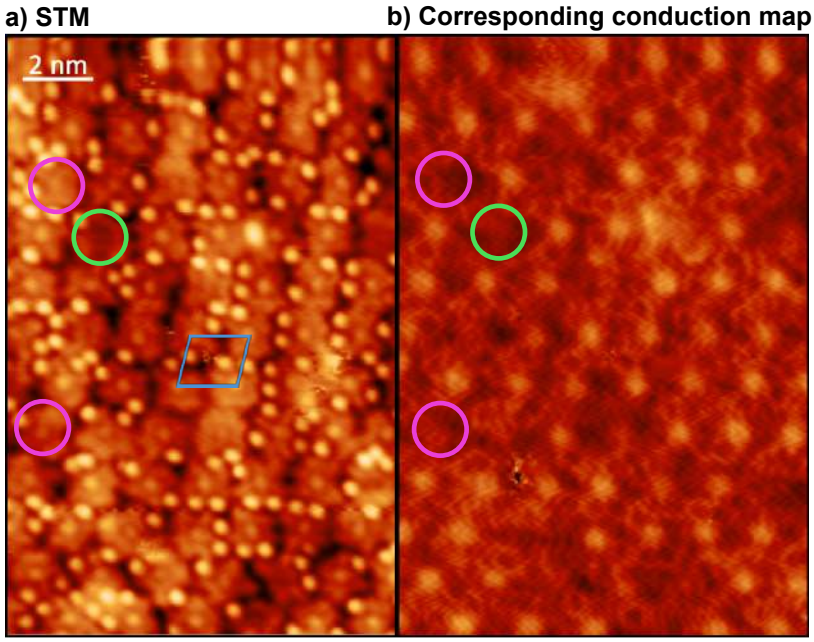

Figure 6.1 a) STM image of a heme monolayer on Au(111) with the oblique unit cell outlined in blue. b) Corresponding conduction map, which enables clear identification of Fe-free molecules (circled in green and pink), which appear as depressions, and Fe-filled molecules, which appear as bright protusions. Applied bias: V = -0.45 V.

The molecules form a close-packed arrangement well described by an oblique unit cell, with lattice parameters a = 1.57 ± 0.03 *nm*, b = 1.46 ± 0.02 *nm* and θ = 105° ± 2°, outlined in light blue in Figure 6.1 a). This arrangement is consistent with the findings of Tao *et al.* [126], who reported that Fe-protoporphyrin IX adsorbed on graphite also forms a hexagonal lattice describable by an oblique unit cell. The absence of features at the molecular center at −0.45 *V* bias voltage further confirms the loss

of chlorine atoms during the degassing step prior to evaporation [78]. The corresponding conduction map in Figure 6.1 b) reveals the mixed composition of the deposited layer. As will be discussed in the next section, exclusive deposition of Fe-filled molecules (heme) is not achievable. Instead, both Fe-filled and Fe-free (protoporphyrin IX) molecules are co-deposited in a variable ratio, depending on the outgassing and evaporation history of the crucible, as will be explained in Section 6.2. In the corresponding conduction map, bright protrusions correspond to Fe-filled molecules, whereas depressions (circled in green and pink) correspond to Fe-free species.
It should be noted, however, that the identification of empty sites in STM images is not always straightforward. Indeed, at certain bias voltages, Fe-free molecules may also appear with a central bright protusion in the STM images (two examples are circled in pink in panel a) of Figure 6.1), which could be misassigned as Fe-filled molecules. Therefore, the conduction maps are essential, as the absence of the central feature (circled in pink) provides an unambiguous signature of Fe-free molecules.
In addition to the molecular centers visible in the STM image, bright protrusions are observed at the molecular periphery, without a clear periodic arrangement. For better visualization, a close-up of Figure 6.1 a) is reported in Figure 6.2 a).

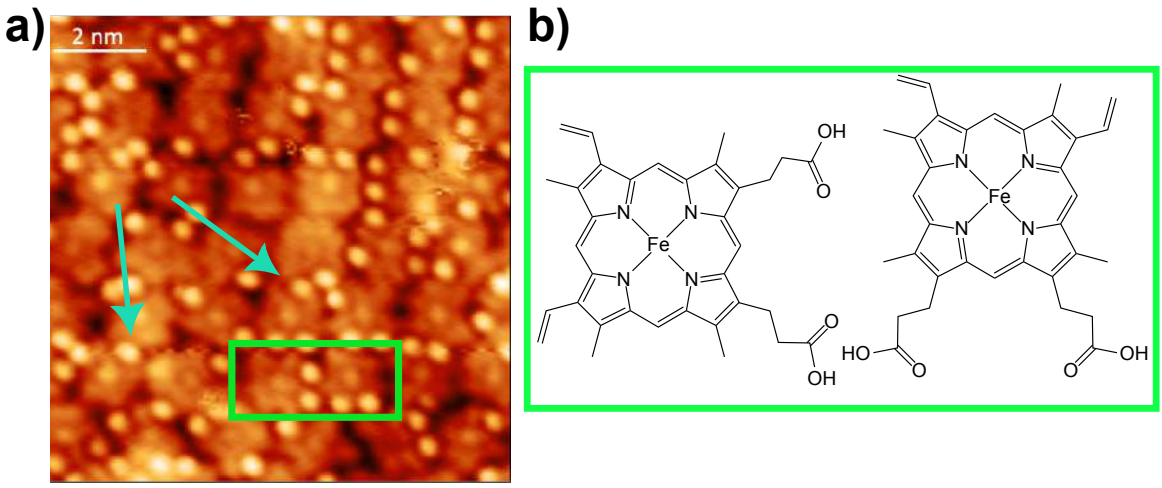

Figure 6.2 a) Zoom-in of Figure 6.1 a). The rectangle highlighted in green indicates two hemin molecules rotated by 90°, with the corresponding schematic shown in b). Cyan arrows mark carboxylic groups that overlap with neighboring molecules.

Among these bright protrusions, a particular orientation is highlighted by the green rectangle in Figure 6.2 a), corresponding to two heme molecules rotated azimuthally by 90° relative to each other, as illustrated in panel b) of Figure 6.2. The bright protrusions are therefore attributed to the carboxylic acid (-COOH) groups of the molecule. However, as shown in panel a) of Figure 6.1, not all molecules display exactly two bright protrusions, as would be expected from the number of carboxylic groups present in each molecule. A plausible explanation is that these features are only visible when the carboxylic groups are tilted out of the molecular plane. When they lie coplanar with the macrocycle, they do not appear bright and thus seem absent in the STM images.
Moreover, depending on the configurations, some carboxylic terminations may overlap a neighboring macrocycle, with their protrusions extending toward the molecular center, as indicated by the cyan arrows in Figure 6.2 a). This interpretation is inspired by the work of Garcia-Lekue *et al.* [127], who, investigating protoporphyrin IX on Cu substrates, observed hydrogen bonding between the carboxylic groups and the iminic nitrogen atoms of adjacent molecules. Their NEXAFS measurements revealed that the carboxylic groups are not coplanar with the tetrapyrrole ring, which led them to propose a schematic illustration for high (> 1 *ML*) and low (< 1 *ML*, comparable to our case) molecular coverages, as reported in Figure 6.3. The adsorption model, proposed in their work for the low coverage regime,

does not directly apply here, since Fe-free molecular centers exhibit the same flat adsorption configuration of the Fe-filled ones, as shown in the STM image reported in Figure 6.1.

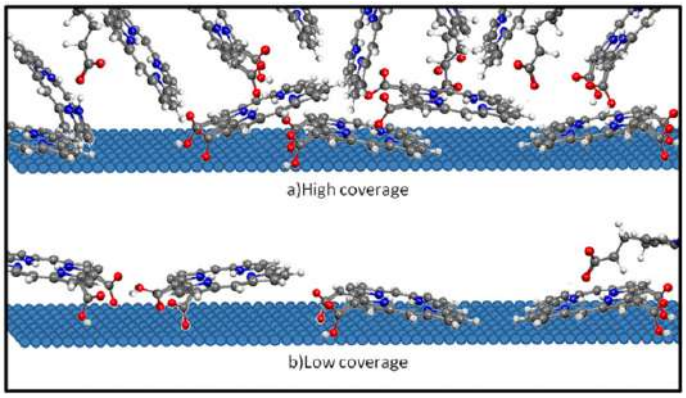

Figure 6.3 Schematic illustration of the adsorption geometry of protoporphyrin IX on Cu(110) at low temperatures, extracted from the NEXAFS data, for high a) and sub-monolayer b) coverage. Image taken from [127].

Conversely, the configuration with tilted carboxylic groups pointing toward the centers of neighboring macrocycles (right case in the low coverage regime) is consistent with our observations (cyan arrows in panel a) of Figure 6.2). To further support this interpretation, complementary techniques (XPS and NEXAFS) are presented in the next section, to highlight this intriguing molecular arrangement.

6.2 Electronic Properties

As demonstrated by the structural characterization of Heme/Au(111), the layer consists of a mixture of Fe-filled and Fe-free molecules, reflecting the composition of the starting biological material, since hemin is typically derived from porcine or bovine blood. This mixed composition is further confirmed by XPS, as revealed through the evolution of N 1*s* core level by comparing evaporations at progressively higher crucible temperatures (Figure 6.4). Each evaporation was performed for the same duration, yielding approximately 1 *ML* in 25 minutes, and was carried out on a freshly cleaned Au(111) sample. Two main components are identified: one at approximately 398 *eV* and the other around 400 *eV*, which are respectively attributed to Fe-filled and Fe-free molecular contributions, for the following reasons. At lower evaporation temperatures (598 *K*, blue spectrum), the ~400 *eV* feature dominates, with only a minor contribution from the ~398 *eV* component. As the evaporation temperature increases to 618 *K* (pink spectrum), the contributions from the two components become comparable. At 628 *K* (orange spectrum), the ~ 398 *eV* component becomes predominant, and its intensity further increases at 638 *K* (green spectrum), accompanied by a corresponding decrease of the ~400 *eV* feature. This evolution demonstrates that the ~400 *eV* features originates from Fe-free molecules, whereas the ~398 *eV* component is associated with Fe-filled species, consistent with STM observations. Thus, increasing the evaporation temperature leads to an increased amount of Fe-filled molecules deposited on the substrate.
However, obtaining a layer composed exclusively of Fe-filled molecules is impossible. Indeed, beyond 628 *K*, maintaining a stable evaporation rate requires increasing the temperature by approximately 5 *K* for each subsequent deposition step. This inevitably leads to a point at which no further molecules are evaporated, likely due to molecular polymerization. A detailed analysis of the Fe $2p_{3/2}$, N, O and C 1*s* core levels of a hemin monolayer grown on Au(111) under UHV conditions is presented in Figure 6.5. All fit parameters are reported in Appendix A.4.
The Fe $2p_{3/2}$ core level, panel a) of Figure 6.5, is best fitted with four Voigt components located at 707.5 *eV* (green), 708.8, 710.3 and 712.0 *eV* (grey). The first component, as previously observed for the

FeTPyP/Gr/Ir(111) system in Section 4.2, corresponds to a well-screened final state of Fe(II), consistent with the Gunnarsson-Schönhammer model. Higher binding energy components are attributed to MS features of Fe(II), in agreement with the systematic study of the multiplet splitting structure of first-row transition metals in various oxidation states, conducted by Biesinger *et al.* [84].

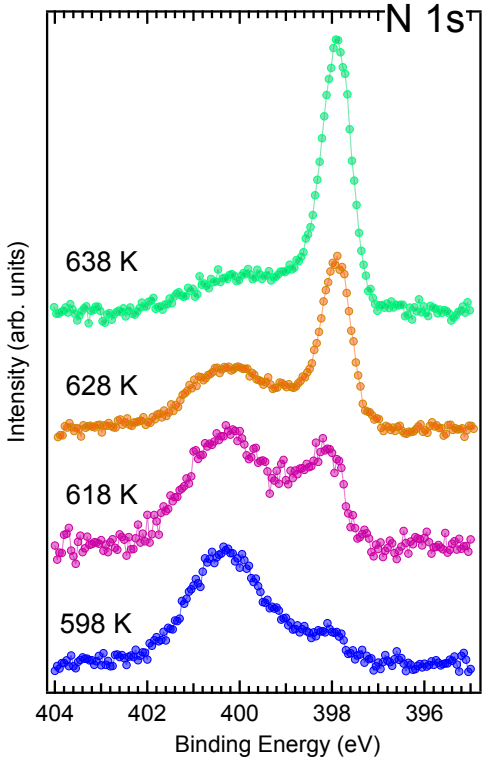

Figure 6.4 Evolution of the N 1s core level after successive evaporations of hemin on Au(111). The number on the left side of each curve denotes the temperature to which the crucible was heated. Before each deposition the substrate was cleaned.

On this basis, and considering the main component located at 708.8 *eV*, we conclude that the central Fe atom is in the +2 oxidation state. To ensure physical consistency and avoid overfitting, all peaks were constrained to share a common optimized Lorentzian width Γ = 0.31 *eV*. The Gaussian width was allowed to vary between GS and MS components, yielding G = 0.83 and 1.79 *eV* for the GS and MS features, respectively. Figure 6.5 b) shows the O 1*s* core level spectrum, which is best modelled by two Voigt envelopes at 531.6 and 533.6 *eV* (orange and dark grey, respectively). These correspond to the chemically distinct oxygen atoms of the carboxylic acid groups, assigned to C=**O** and C–**O**H, respectively. No evidence of deprotonation is observed, as this would appear as an additional CO**O**$^{-}$ component at 530.9 *eV* [128]. Each heme molecule contains two carboxyl groups (-COOH), so a 1:1 stoichiometric ratio between the C=O and C–OH contributions would be expected. However, the experimental spectra show an approximate area ratio of 2:1. We attribute this deviation to the formation of intermolecular hydrogen bonds between neighboring carboxylic groups of adjacent molecules, consistent with the different configurations observed in the STM images. In such configurations, the hydroxyl hydrogen of one carboxylic group interacts with the carbonyl oxygen of a neighboring molecule, partially redistributing the electron density within the C-OH bond and thereby shifting its binding energy to lower values.

Further evidence of hydrogen-bond formation emerges from the N 1*s* spectrum shown in Figure 6.5 c), which is best fitted with three Voigt components at 397.9, 399.1, and 400.5 *eV* (red, cyan, and dark grey, respectively). The feature at 397.9 *eV* is assigned to nitrogen atoms coordinated to Fe in the metalated molecules, while the components at 399.1 and 400.5 *eV* arise from the contribution of Fe-free

molecules, consistent with the N 1*s* evolution reported in Figure 6.4. However, the assignment of these latter higher binding energy components is not straightforward.
In porphyrin-based systems, it is well-established that the N 1*s* signal of nitrogen atoms coordinated to the metal center lies between those of iminic (=N-, typically 397/398 *eV*) and pyrrolic (-NH-, typically 399/401 *eV*) nitrogen [89,129,130]. This trend does not appear to apply here, as evidenced by the N 1*s* evolution in Figure 6.4. A possible explanation can be drawn from the study of 2HTPP metalation on Au(111), in which two N 1*s* components at approximately 399 and 400 *eV* were observed and both attributed to pyrrolic nitrogen atoms, with the higher binding energy feature arising from their interaction with the Au substrate [131].

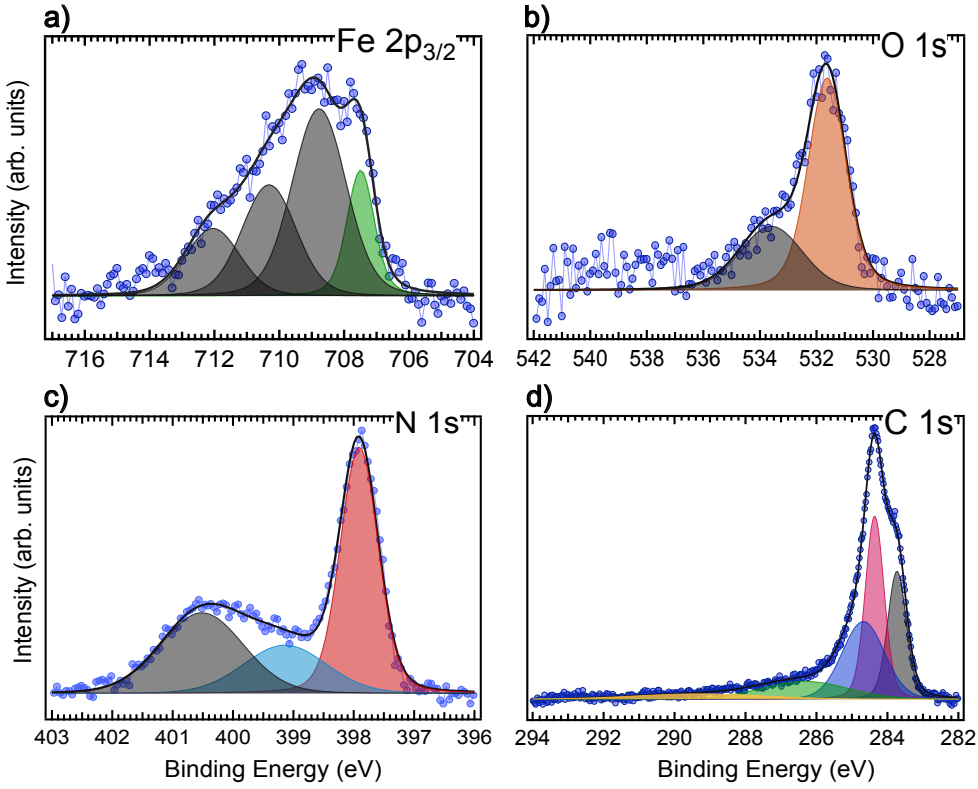

Figure 6.5 Synchrotron radiation XPS spectra of the a) Fe 2p$_{3/2}$, b) O 1s, c) N 1s and d) C 1s core levels of hemin (1 ML) deposited on Au(111) collected at room temperature in UHV. Photon energies: a) 1000 eV, b) 660 eV, c) 514 eV and d) 400 eV.

In contrast, during self-metalation of phthalocyanines on Ag(100), the N component coordinated to the metal center appeared to have a lower binding energy than both the iminic and pyrrolic contributions, which is consistent with our observations [132].
Interestingly, investigations of protoporphyrin IX (H2PPIX) metalation on Cu(100) and Cu(110) found no evidence of an iminic contribution at room temperature; only nitrogen atoms coordinated to the metal center and pyrrolic components were detected. This behavior was attributed to hydrogen bonding formation between H atoms of one molecule and the iminic N sites in the macrocycle of another, effectively converting iminic nitrogen into an (-NH-)-like environment and eliminating the corresponding low BE iminic signal [128]. An example of this configuration is shown on the right side in Figure 6.3 b).
Considering these findings and the N 1*s* evolution observed here, where the area ratio of the 399.1 and 400.5 *eV* components approaches unity as the Fe-free contribution decreases, as will be discussed in Figure 7.2, we assign the 399.1 *eV* component to iminic (=N-) nitrogen and the 400.5 *eV* component to pyrrolic (-NH-) nitrogen. The fact that, in Figure 6.5 c), the contribution of the pyrrolic component is nearly twice the iminic one can be rationalized by STM data: the images reveal configurations where carboxylic groups from one molecule overlap a neighboring macrocycle (highlighted by cyan arrows

shown in Figure 6.2). When the neighboring molecule is Fe-free, hydrogen bonding may form between a -OH group and an iminic nitrogen site, reducing the population of iminic N while increasing that of pyrrolic-like (-NH-) nitrogen atoms, thereby enhancing the higher BE component contribution.
Finally, the C 1*s* core level spectrum (panel d) of Figure 6.5), is best fitted with five Voigt components at 283.7, 284.4, 284.7, 286.3 and 289.3 *eV*. These features can be tentatively assigned as follows: the peak at 283.7 *eV* is attributed to methyl groups (grey) [133], the 284.4 *eV* component corresponds to C-C/C-H bonds (pink) [134], the 284.7 *eV* feature arises from C-N contribution (blue) [134], the 286.3 *eV* component is assigned to carbon atoms in carboxylic groups (-COOH, green) [134] and the feature at 289.3 *eV* is attributed to a shake-up (yellow).
To elucidate the geometric arrangement of molecular moieties at the interface, partial-yield NEXAFS spectra of the N and C K-edges, as well as of the Fe L-edge, were acquired (Figure 6.6) at incidence angles $\theta = 0°$ (normal to sample surface) and $\theta = 70°$ (grazing) to extract information about the molecular orientation. Additional measurements were performed at $\theta = 42°$, an intermediate angle between normal and grazing incidence, to clearly follow the angular dependence. In flat-lying porphyrin systems, σ* resonances dominate at normal incidence, where the electric field vector lies in the surface plane, while π* resonances are enhanced at grazing incidence, where the electric field vector lies close to the surface normal in the scattering plane.

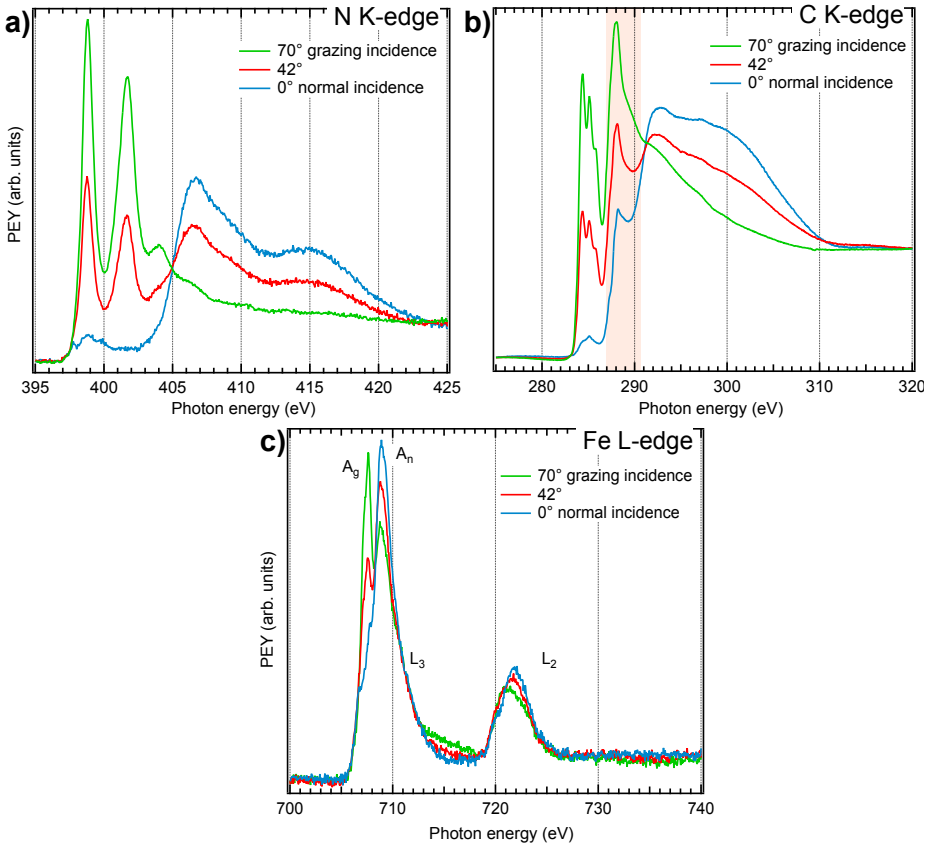

Figure 6.6 Synchrotron radiation NEXAFS spectra of N, C K–edges and Fe $L_{3,2}$–edge of hemin (1 ML) deposited on Au(111) collected at room temperature under UHV conditions. Each panel shows spectra acquired at grazing incidence (green), normal incidence (blue) and an intermediate angle (red).

The N K-edge spectra shown in panel a of Figure 6.6, exhibit three distinct π* features observed at 398.8, 401.7 and 404.0 *eV*, assigned to π*(e_g), π*(b_{2u}, e_g), and π*(a_{2u}) transitions of nitrogen atoms coordinated to Fe center [135,136], along with two σ* resonances at 406.7 and 416.0 *eV*. The strong dichroism observed between grazing and normal incidence indicates predominantly flat adsorption of the macrocycle, in agreement with the STM images. However, the residual intensity of the 398.8 *eV* feature at normal incidence suggests a saddle-shaped configuration of the macrocycle. The C K-edge

spectra, presented in panel b) of Figure 6.6, show transitions at 284.4, 285.1 and 288.0 *eV*. The first two peaks correspond to π* transitions associated with the macrocycle (C-C and C-N contributions) [137–139]. Their residual intensity at normal incidence further supports a saddle-shaped distortion of the macrocycle, as also indicated by the N K-edge spectra. The higher-energy resonance at 288.0 *eV*, highlighted by the light orange rectangle, is assigned to π* transitions associated with the carboxylic groups [127]. Moreover, this feature exhibits residual intensity at normal incidence, indicating that the carboxylic groups are not fully coplanar with the macrocycle and may adopt a tilted orientation relative to the surface, in agreement with the STM observations and supporting our interpretation. These findings provide evidence for the three-dimensional configuration of the peripheral residues, which may influence the chemical reactivity of the layer. Finally, the Fe L-edge spectra are shown in panel c of Figure 6.6. Two main resonances are observed in the L_3 region, with a similar trend reflected in the L_2 region. The first feature, at 707.6 *eV* (A_g), exhibits maximum intensity at grazing incidence, whereas the second, at 708.9 *eV* (A_n), dominates at normal incidence. This angular dichroism indicates different spatial orientations of the final states involved in the transitions. The A_g component is assigned to transitions into out-of-plane 3*d* orbitals, namely d_{z^2}(a_{1g}) and d_{xz}/d_{yz}(e_g). Conversely, the A_n resonance is attributed to transitions into in-plane 3*d* orbitals, specifically $d_{x^2-y^2}$(b_{1g}), d_{xy}(b_{2g}), which lie predominantly in the plane of the molecule and thus parallel to the substrate [140,141].

6.3 Conclusion

In summary, STM and NEXAFS measurements indicate that the deposition of hemin on Au(111) under UHV conditions leads to the formation of an ordered layer, with the macrocycle lying flat in a saddle-shaped configuration. STM images show bright spots for each molecule, attributed to the carboxylic terminations. However, the number of these features does not match the stoichiometric number of carboxylic groups expected per molecule. This suggests that the bright spots are only observed when the carboxylic groups are not flat-lying and overlapping with adjacent neighbors, as supported by NEXAFS results. XPS data further indicate that, depending on the molecular arrangement, hydrogen bonds can form either between carboxylic groups of adjacent molecules or between a carboxylic group and the iminic nitrogen atoms of a neighboring molecule, when the termination is oriented toward the center of an Fe-free species.
This preliminary characterization of the heme layer provides the starting point for exploring its reactivity under near-ambient pressure conditions, particularly to examine whether the carboxylic groups tilted out of the molecular plane can influence the layer's reactivity when located near the center of an Fe-filled molecule.

7 | Heme Reactivity toward CO and O_2: Role of Carboxylic Groups in O_2 Ligation

Following the UHV characterization, the reactivity of a heme monolayer on Au(111) toward CO and O_2 was investigated under near-ambient pressure conditions by means of NAP-XPS. The study was carried out analogously to the FeTPyP and FeTPyP-Co systems, with the aim of evaluating whether the presence of carboxylic groups in hemin influences its reactivity.

7.1 Reactivity toward Carbon Monoxide

The behavior of a hemin monolayer on Au(111) under 0.3 *mbar* of CO was monitored through its Fe $2p_{3/2}$, O, N and C 1*s* core level spectra, as shown in Figure 7.1. The spectra represent the layer in three states: as-prepared in UHV (blue), under CO pressure (red) and after pumping out the gas (cyan). All fitting parameters are reported in Appendix A.5.

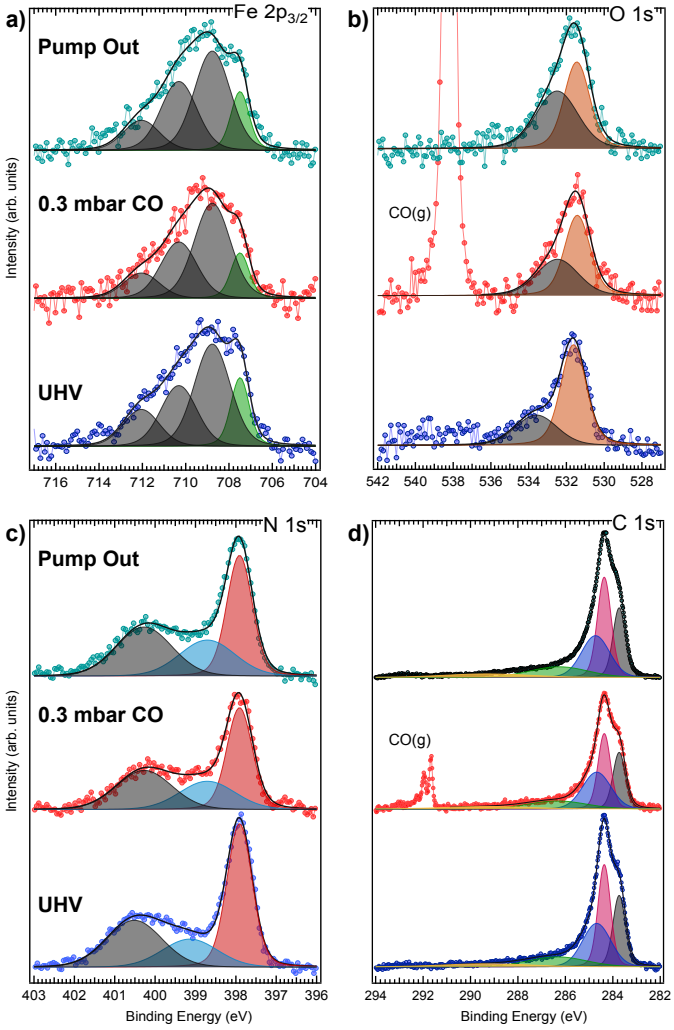

Figure 7.1 Synchrotron radiation XPS spectra at the a) Fe $2p_{3/2}$, b) O 1s, c) N 1s and d) C 1s core levels of the heme layer collected at room temperature in UHV (bottom row, blue), at equilibrium in 0.3 mbar CO (central row, red), and after recovering UHV conditions (top row, cyan). Photon energies: a) 1000 eV, b) 660 eV, c) 514 eV and d) 400 eV.

For each core level, the bottom panel displays the UHV heme spectrum previously discussed in Section 6.2. In summary, the deposited layer consists of a mixture of Fe-free and Fe-filled molecules, as revealed by the N 1*s* spectrum. Evidence of hydrogen-bond formation is indirectly reflected in both the O and N 1*s* core levels. Depending on the molecular configurations, hydrogen bonding can occur between two different carboxylic groups of adjacent molecules, or between a carboxylic group and the iminic nitrogen (-N=) atoms when Fe is not present in the macrocycle. The latter effect arises from the non-coplanarity of the carboxylic groups, as supported by both STM and NEXAFS measurements presented in Chapter 6. Upon exposure to 0.3 *mbar* of CO, the presence of gas-phase carbon monoxide is evident from the higher binding energy components in both C and O 1*s* core level, corresponding to the gas-phase signal [124,142]. No other significant changes are observed in C 1*s* and Fe $2p_{3/2}$ spectra, which remain consistent with Fe in the +2 oxidation state throughout the process and display spectral profiles, after pumping out the gas, identical to those in UHV.
This indicates that CO does not interact with the Fe center. In contrast, the O 1*s* spectrum (red) shows that the grey dark component at 533.6 *eV*, assigned to C-OH in the UHV characterization, undergoes an irreversible shift of 1.1 *eV* toward lower binding energies. Concurrently, the iminic and pyrrolic nitrogen components of the Fe-free molecules in the N 1*s* spectrum (cyan and grey dark components) shift by 0.4 and 0.2 *eV*, respectively, toward lower binding energy. These findings suggest that CO may interact with the -OH groups of the carboxylic acid terminations. Such interaction perturbs the hydrogen-bonding interaction with the iminic nitrogen atoms of Fe-free macrocycles, leading to an electronic rearrangement and the observed irreversible binding energy shifts. However, conclusive evidence for CO interaction with-OH groups is lacking, as the changes observed in the O and N 1*s* spectra may also arise from residual contaminants present in the CO high-pressure bottle (99.97% purity). Therefore, we conclude that Heme/Au(111) system is inert toward CO and proceed to investigate its reactivity towards O_2.

7.2 O_2 Reactivity and Role of Carboxylic Terminations

The interaction of O_2 with a heme monolayer was investigated by monitoring the evolution of the Fe $2p_{3/2}$, O, N and C 1*s* core level spectra acquired in UHV (blue), under 0.1 *mbar* of O_2 (red) and after pumping out the gas (cyan), as shown in Figure 7.2. All fit parameters are reported in Appendix A.6.
It is important to note that the UHV spectra presented here differ from those discussed in the previous section (and during the UHV characterization in Chapter 6). As discussed in Section 6.2, maintaining a constant evaporation rate required increasing the deposition temperature by 5 *K* for each successive deposition step, until no further evaporation was possible, likely due to molecular polymerization. In the present case, the evaporation temperature was 628 *K*, corresponding to the last N 1*s* spectrum shown in Figure 6.4.
At this temperature, a larger fraction of Fe-filled (heme) molecules was evaporated compared to the Fe-free (protoporphyrin IX) species, accounting for the observed differences across all core-level spectra. In particular, the N 1*s* spectrum (blue) in panel c) of Figure 7.2 shows that the red component at 397.9 *eV*, attributed to N atoms coordinated to Fe, nearly doubles compared to the UHV spectrum in Figure 6.6, while the contributions from Fe-free molecules decrease by approximately 30%. Consistently, the Fe $2p_{3/2}$ spectrum exhibits an overall increase in all spectral components, along with the appearance of a new feature at 713.9 *eV*, possibly corresponding to a MS component of Fe(II) [84] which was not detected in the previous sample preparation due to the lower amount of Fe. In the C 1*s* core level, panel d) of Figure 7.2, a reduction of the Gaussian width by 0.1 *eV* is observed for the C-C/C-H component (pink) and 0.4 *eV* for the C-N component (blue). The observed narrowing suggests an increase in the structural homogeneity, consistent with a higher fraction of Fe-filled molecules in the layer. In the O 1*s* region, Figure 7.2 b), two components are identified corresponding to C=O and C-OH contributions of the carboxylic groups, consistent with the observations in Section 6.2. Exposure of the system to 0.1 *mbar* of O_2 (middle row of each panel, red spectrum) leads to pronounced changes in the O 1*s* spectrum. In addition to the O_2 gas phase components at higher binding energies [102], two new

features emerge at 530.6 *eV* (blue) and 532.5 *eV* (pink). These components evolve concurrently; they grow simultaneously in O_2 atmosphere and decrease together after pumping out the gas, with a residual contribution indicating partial irreversibility of the process at RT.
Concurrently, changes are observed in the Fe $2p_{3/2}$ spectrum: the most intense component shifts by +0.2 *eV*, while no further shifts in binding energies are detected, suggesting the absence of a significant change in the Fe oxidation state. The overall spectral intensities decrease under O_2 exposure, likely due to the attenuation from gas-phase scattering, as also observed in the CO case discussed previously. In contrast to CO, however, the intensities do not fully recover after pumping out the gas, consistent with the persistence of the additional O 1*s* components.
This behavior indicates that an irreversible modification of the system has occurred, although its interpretation remains nontrivial given the unchanged Fe oxidation state.

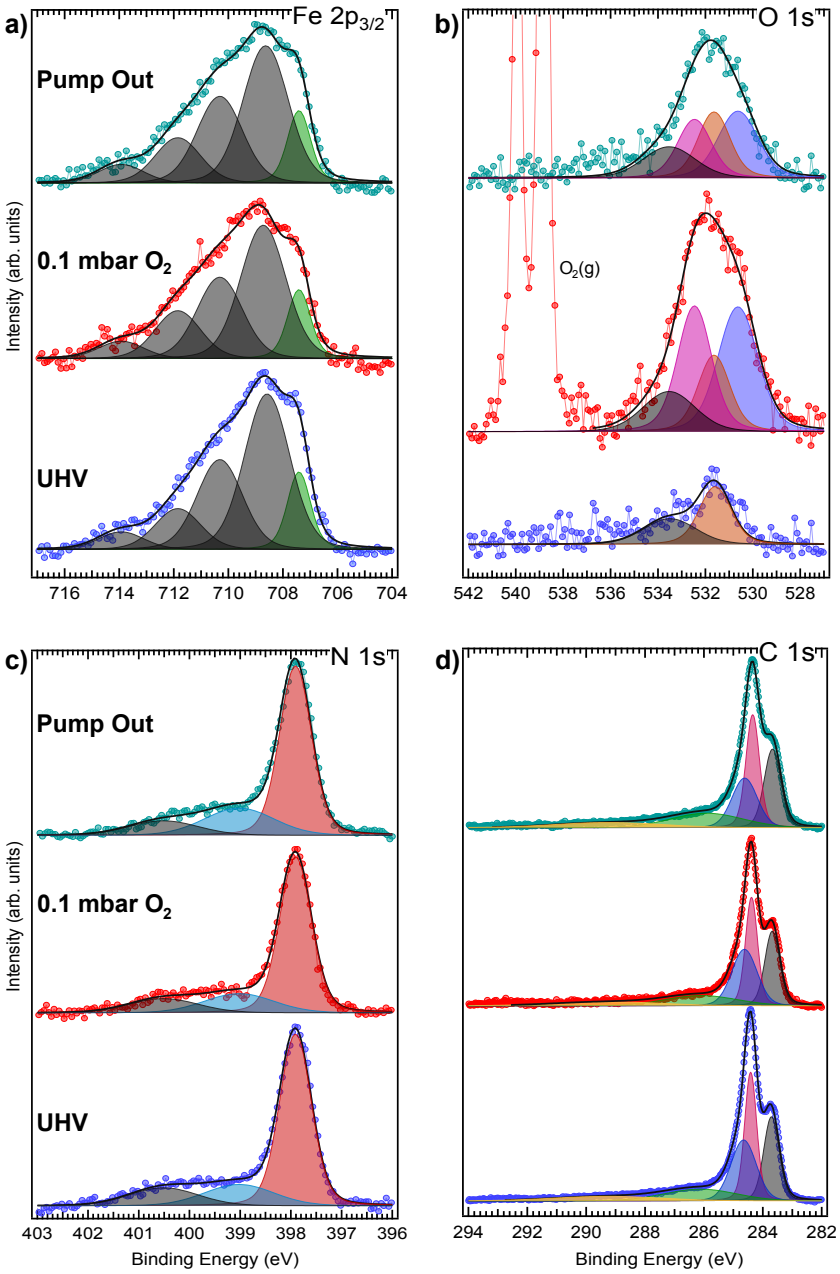

Figure 7.2 Synchrotron radiation XPS spectra of the a) Fe $2p_{3/2}$, b) O 1s, c) N 1s and d) C 1s core levels of the heme layer collected at room temperature under UHV conditions (bottom row, blue), at equilibrium in 0.1 mbar O_2 (central row, red), and after recovering UHV conditions (top row, cyan). Photon energies: a) 1000 eV, b) 660 eV, c) 514 eV and d) 400 eV.

In biological systems, it is well established that the first step in O_2 activation by heme proteins involves the coordination of molecular oxygen to the metal center. Despite decades of investigation, the precise electronic structure of the Fe-O_2 species in heme complexes remains a subject of debate. Historically, the discussion has converged on three principal models: Pauling, Weiss and McClure-Goddard descriptions [143]. In the Pauling model, the Fe-O_2 species is described as a low-spin Fe(II) bound to neutral O_2, with both dioxygen and ferrous center in the singlet (S=0) state. The Weiss model, instead, proposes a ferric-superoxide complex, Fe(III)-O_2^-. The McClure-Goddard model represents a hybrid between Fe(II)-O_2 and Fe(III)-O_2^- configurations, involving partial electron transfer and spin coupling, leading to a mixed (S=1) system [143,144]. However, none of these models fully accounts for the present observations.
Here, Fe is clearly found in the +2 oxidation state. According to the Pauling or McClure-Goddard descriptions, one would expect the formation of neutral or only weakly bound dioxygen to the metal center. However, such species would not remain stable after pumping out the gas. A more stable adduct would require O_2 to bind in a peroxo or superoxo species, but the Weiss model would imply Fe(III), which is not observed in our spectra.
In the case of oxyhemoglobin and oxymyoglobin, an alternative explanation that merges aspects of the Pauling and Weiss models has been proposed [145]. Upon O_2 coordination to the ferrous center, a Fe(III)-O_2^- species initially forms. The negative charge on the superoxo ligand is then stabilized through hydrogen bonding with the distal histidine in the heme pocket, effectively restoring the Fe oxidation state to +2, in agreement with the Pauling description. In our system, the role of the distal histidine could be mimicked by the tilted carboxlic groups, which in certain configurations are non-coplanar with the macrocycle and positioned near a neighboring molecular center (cyan arrows in the STM image, Figure 6.2). This arrangement could enable hydrogen bonding between the Fe-bound O_2 and the carboxylic groups, effectively recreating the second coordination sphere and stabilizing the Fe-O_2 species. This interpretation also explains the appearance of the new components in the O 1*s* spectra. In the FeOOH species, the two oxygen atoms are chemically distinct: the oxygen atom proximal to the hydrogen of the carboxylic groups, FeO***O***H, gives rise to the 532.5 *eV* component while the oxygen atom directly bound to Fe, Fe***O***OH, corresponds to the component at 530.6 eV. A similar behavior has been reported in the CoTPyP/Gr system, where stabilization of a hydroperoxyl-water (OOH-H_2O) cluster was observed at the Co single-metal atom catalytic site at room temperature in O_2+H_2O water atmosphere [99] In that case, two additional components appeared in the O 1*s* core level spectrum at 533.4 and 531.8 *eV* assigned to O***O***H and ***O***OH species, with an energy separation of 1.6 *eV*, close to the 1.9 *eV* separation observed in the present case. Our interpretation is further supported by the C 1*s* core level, panel d) of Figure 7.2, where the -COOH contributions (green component) shift by approximately 0.2 *eV* toward lower binding energies after pumping out the gas, compared to the UHV spectrum. Concurrently, changes are also observed in the N 1*s* core level, cyan spectrum in Figure 7.2 c), with a different area ratio of the iminic and pyrrolic components (cyan and dark grey) in the Fe-free molecules contribution. These changes could result from O_2 interaction with the -OH terminations, in a similar way to the previously discussed CO case

7.3 Conclusion

In summary, the heme layer is almost inert toward CO, with no interaction detected with the metal centers according to NAP-XPS data. Possible interactions with the -OH groups of the carboxylic terminations cannot be ruled out. However, there is insufficient evidence to attribute these changes specifically to CO rather than the residual contaminants present in the CO high-pressure bottle. In contrast, exposure to 0.1 *mbar* of O_2 induces pronounced changes in the O 1*s* hemin core level, with two additional components evolving concurrently and persisting after pumping out the gas, indicating an irreversible process. Consistent with the O 1*s* observations, modifications are also detected in the Fe $2p_{3/2}$ spectrum, where the spectral components do not fully recover to those of the as-prepared layer after pumping out the gas, while Fe centers preserve the +2 oxidation state.

Considering the several models in the literature describing the electronic contribution of Fe-O_2 species in heme complexes, our experimental results are best interpreted by analogy with the role of a second coordination sphere offered by the distal histidine in oxyhemoglobin and oxymyoglobin. In our surface scenario, the tilted carboxylic groups mimic the distal histidine, forming hydrogen bonds with O_2 molecules and possibly stabilizing the interaction between the Fe center and the O_2 molecule.
Therefore, depending on the molecular configuration, a carboxylic group that overlaps an Fe-filled molecule and terminates near its center can stabilize O_2, effectively mimicking the second coordination sphere observed in biological systems.

8 | Heme Trans-metalation process: *In Situ* Synthesis of Co-Protoporphyrin IX

In the previous chapters, the properties of a heme monolayer grown on Au(111) were investigated. Chapter 6 addressed its structural and electronic properties under UHV conditions, while Chapter 7 examined its reactivity toward CO and O_2 at near-ambient pressure. A key outcome of these studies was the identification of a mixed layer composed of both Fe-filled and Fe-free molecules. Based on these considerations, Co atoms were deposited after the layer formation with the aim of occupying the empty metal sites and thereby creating a bimetallic structure. The resulting Co-modified layer (heme+Co) was subsequently exposed to 0.1 mbar of O_2 to explore its potential for catalytic processes and energy-storage applications. Its structural characterization was carried out by STM, while the electronic properties were probed by XPS across a pressure range from UHV to near-ambient pressures of molecular oxygen.

8.1 Structural Properties

Following the preparation of a heme monolayer on Au(111), as reported in Figure 6.1, Co atoms were deposited, with a total coverage below 1% of a *ML*, with the aim of occupying the Fe-free sites. The corresponding STM image of this sample is shown in Figure 8.1, where three distinct molecular species can be identified, higlighted in green, pink and cyan.

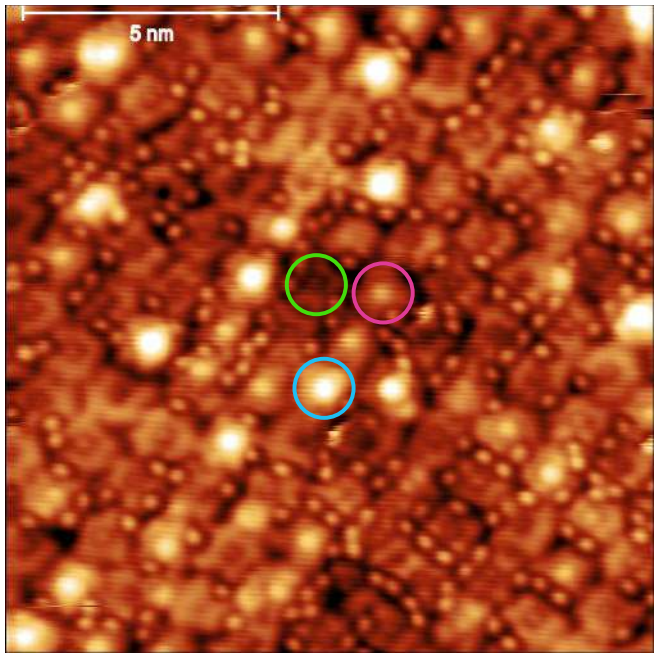

Figure 8.1 STM image of a heme monolayer on Au(111) after deposition of Co atoms (Co coverage <1% of a ML). Three different molecular species are revealed, circled in green, white and cyan. Applied bias: V = -0.1 V.

At this bias voltage, these three molecular species exhibit distinct macrocyclic contrasts: a dark feature (outlined in green), a bright protrusion (circled in pink), and a larger protrusion (outlined in cyan). These variations arise upon Co deposition and likely correspond to different stages of the second metal incorporation. To further investigate this behavior, a close-up STM image was acquired at two different bias voltages (left panels of Figure 8.2), together with its corresponding conduction maps (right panels

of Figure 8.2). Despite the limited resolution, the three molecular species remain clearly distinguishable in both STM images, following the same color scheme as in Figure 8.1.

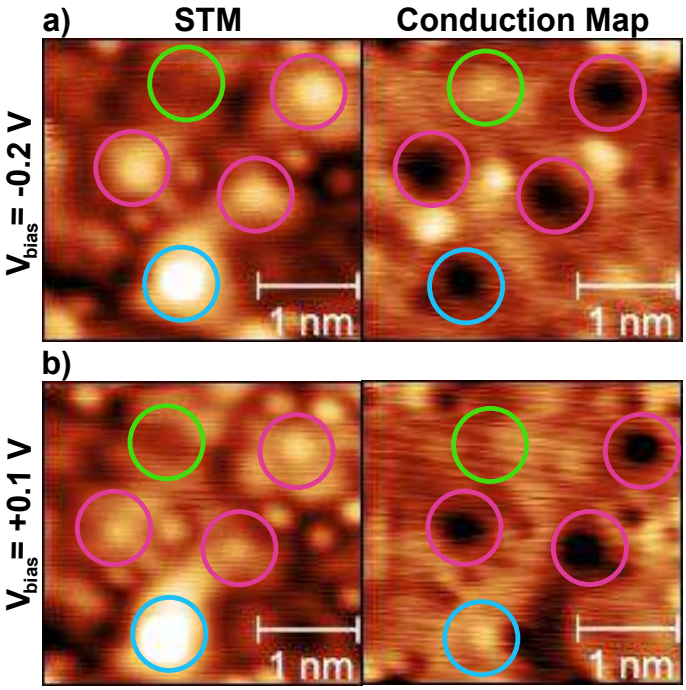

Figure 8.2 STM topographies and corresponding conduction maps of a close-up region acquired at two different bias voltages: a) V = -0.2 V and b) V= +0.1 V. The same color scheme as in Figure 8.1 is used: green for macrocycles with dark contrast, white for macrocycles with a bright protusion and cyan for macrocycles with a larger protusion.

In the conduction map acquired at V = -0.2 *V*, Figure 8.2 a), the molecule outlined in green appears as a bright protusion, whereas the species circled in pink and cyan both display dark depressions, with no distinction between the latter two at this bias. However, upon changing the bias voltage to V= +0.1 *V* (Figure 8.2 b)) a clear difference emerges: the molecule outlined in cyan now exhibits a bright protusion, while the one circled in white remains dark. For the green-circled molecule, although the resolution is limited, no dark depression is observed at either bias voltage. These observations indicate that the three molecular species correspond to distinct configurations resulting from Co incorporation. However, given the known coexistence of Fe-free molecules within the layer, a definitive assignment cannot be made based solely on the conduction maps.

To gain chemical insight, STS measurements were performed. The resulting spectra, acquired by positioning the tip over each of the three molecular species (green, pink and cyan), and recording the dI/dV as a function of the applied bias voltage, are presented in Figure 8.3. The STS spectra provide deeper insight into the structural modification induced by Co deposition. Focusing on the molecular species outlined in green, the corresponding spectrum exhibits a shoulder around -0.2 *V*, a dip at the Fermi level and a feature around +2 *V*. This behavior is consistent with that observed for FeTPP molecules adsorbed on Au(111), with the tip positioned above the Fe center [146]. Consequently, we assign the molecular species with a dark macrocycle appearance to Fe-filled molecules. For the species outlined in pink, the corresponding spectrum displays a pronounced maximum near the Fermi level. Similar features have been observed in STS studies of $CoTPPBr_2I_2$ and CoTPP respectively adsorbed on Au(111), where positioning the tip above the Co center produces a sharp resonance near the Fermi level, attributed to the Kondo effect [147,148]. Based on CoTPP/Au(111), this effect arises due to exchange interaction of spin between out-of-plane Co orbitals and the conduction electrons of Au [149]. Therefore we ascribe the pink circled molecules, which display a bright protusion at the macrocycle, to Co-filled molecules (Co-protoporphyrin IX).

The third molecular species, highlighted in cyan, differs markedly from both Fe- and Co-filled configurations in both STM and STS measurements.
According to the literature, at certain bias voltages, the large bright protusion observed in the STM images may be associated with a metal center displaced out of the macrocycle plane [150].
This suggests that this species corresponds to an intermediate state, which could arise either from (i) a Co atom on top of an empty macrocycle or (ii) a Co atom located above an Fe-filled molecule. To gain a deeper understanding of the processes occurring upon Co deposition, complementary electronic characterization is required and will be presented in the next section.

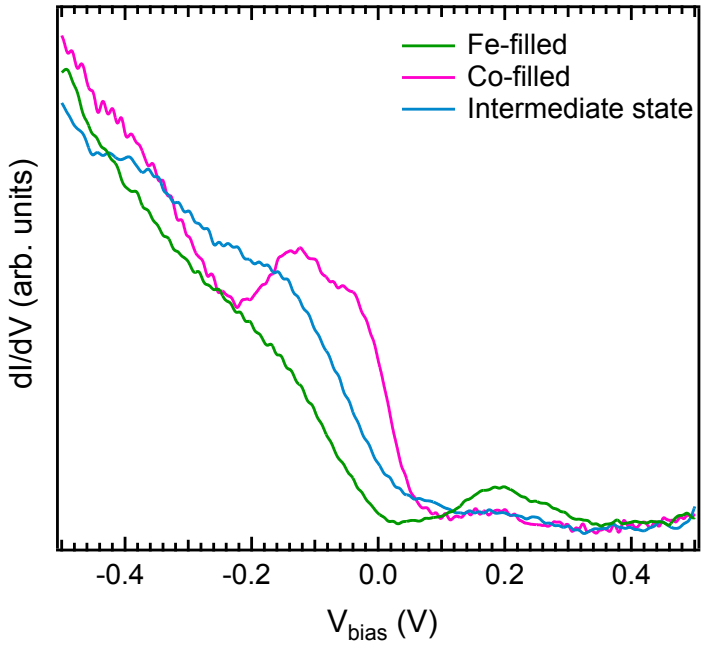

Figure 8.3 Raw STS spectra acquired with the tip positioned above each of the three molecular species, following the same color scheme used in Figures 8.1 and 8.2. The green circled molecule is identified as Fe-filled (green spectrum), the pink-circled one as Co-filled (pink spectrum) and the cyan-circled molecule as an intermediate state (cyan spectrum).

8.2 Electronic Properties

From the structural characterization, three distinct molecular species were identified upon Co deposition. By combining STM, conduction maps and STS, we established that the layer contains Fe-filled molecules, Co-filled molecules and a third intermediate species. The nature of this intermediate state is not straightforward. It may originate either from Co atoms on top of an empty macrocycle or from Co in an out-of-plane configuration on a Fe-filled molecule, thus capturing partial metalation or trans-metalation, respectively. To clarify this point, the electronic properties of the modified layer were further investigated by XPS. All fit parameters are reported in Appendix A.7.
Figure 8.4 shows the N 1*s* core level spectra of the as-prepared layer (blue) and those of the same sample after stepwise Co deposition. The spectrum obtained after the first 10-minute Co deposition is shown in brown, while an additional 5 minutes of Co exposure yields the orange spectrum. After the full 15 minutes of Co deposition (orange spectrum), the total Co coverage corresponds to approximately 1% of a *ML*, which corresponds roughly to the amount of Fe centers in a heme monolayer.
Upon Co addition, the contribution previously assigned to N atoms coordinated to Fe (397.9 *eV*, red) decreases by approximately 40%, while a new component appears at 398.6 *eV* (purple). This new feature can initially be attributed to N atoms coordinating to Co, consistent with the structural evidence of Co incorporation. However, upon further analysis, this assignment is not fully supported. As the Co loading increases (half the deposition time of the previous step, orange spectrum), the purple

component increases by only ~20%, whereas the spectral weight associated with Fe-free molecules (cyan and dark grey components) remains essentially unchanged throughout the different Co depositions. These observations indicate that the new feature cannot originate from Co coordination to empty molecules, but instead involves Fe-filled molecules undergoing a trans-metalation process.
Combining these results with the structural evidence discussed in the previous section, upon Co deposition, the 397.9 *eV* feature reflects N atoms coordinate to a metal center (either Fe or Co), whereas the new component at 398.6 *eV* is attributed to an intermediate trans-metalation state within Fe-filled molecules, in which Co and Fe likely adopt an out-of-plane configuration relative to the macrocycle plane, located above and below it, respectively.

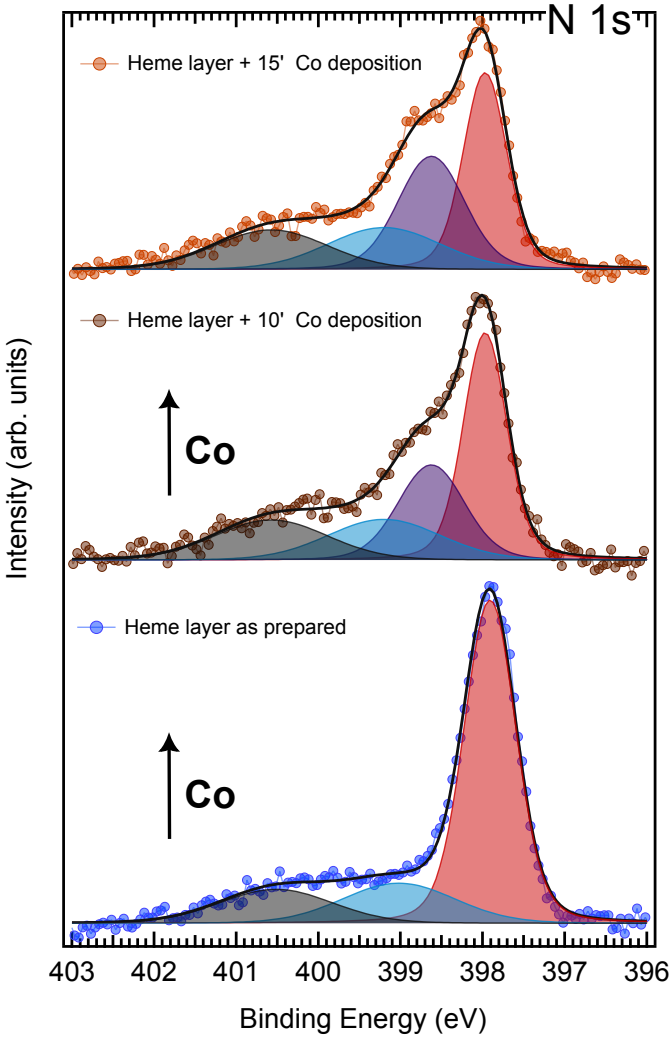

Figure 8.4 Evolution of the N 1s core level upon Co deposition under UHV conditions. The spectrum of the as-prepared layer is shown in blue, the modified spectrum after the first 10 minutes of Co deposition in brown, and the same spectrum following an additional 5 minutes of Co deposition in orange. The total Co coverage is approximately 1% of a ML.

For the remaining core-level spectra, the Heme/Au(111) sample was prepared under conditions similar to those used to obtain the core levels shown in Figure 7.2. The resulting N 1*s* spectrum in UHV (blue, Figure 8.4) matches the corresponding N 1*s* reference (blue, Figure 7.2), leading us to conclude that an equivalent layer was reproduced. Accordingly, only the N 1*s* evolution was monitored during Co addition, while the other core levels were acquired after the final Co deposition. Therefore, the remaining core-level spectra of the modified layer after the full 15-minute Co deposition are directly

compared with the corresponding reference of the pristine layer (blue spectra) from Figure 7.2, which are reproduced in the bottom panels of Figure 8.5.
Starting with the Fe $2p_{3/2}$ core level, Figure 8.5 a), several modifications are observed upon Co deposition. A new component appears at 706.5 *eV* (purple), while the higher binding energy feature previously observed at 713.9 *eV* and assigned to the MS component of Fe(II), disappears. This evolution likely reflects the ~40% overall decrease in the Fe $2p_{3/2}$ spectral area. Based on the observations, these spectral changes can be rationalized as follows. Upon Co addition, two parallel processes occur: for a significant fraction of the molecules, a complete trans-metalation takes place, with Co atoms occupying the macrocycle center and Fe atoms being released onto the Au substrate. For the remaining molecules, an intermediate configuration occurs in which both Co and Fe remain coordinated to the same macrocycle in an axial geometry.

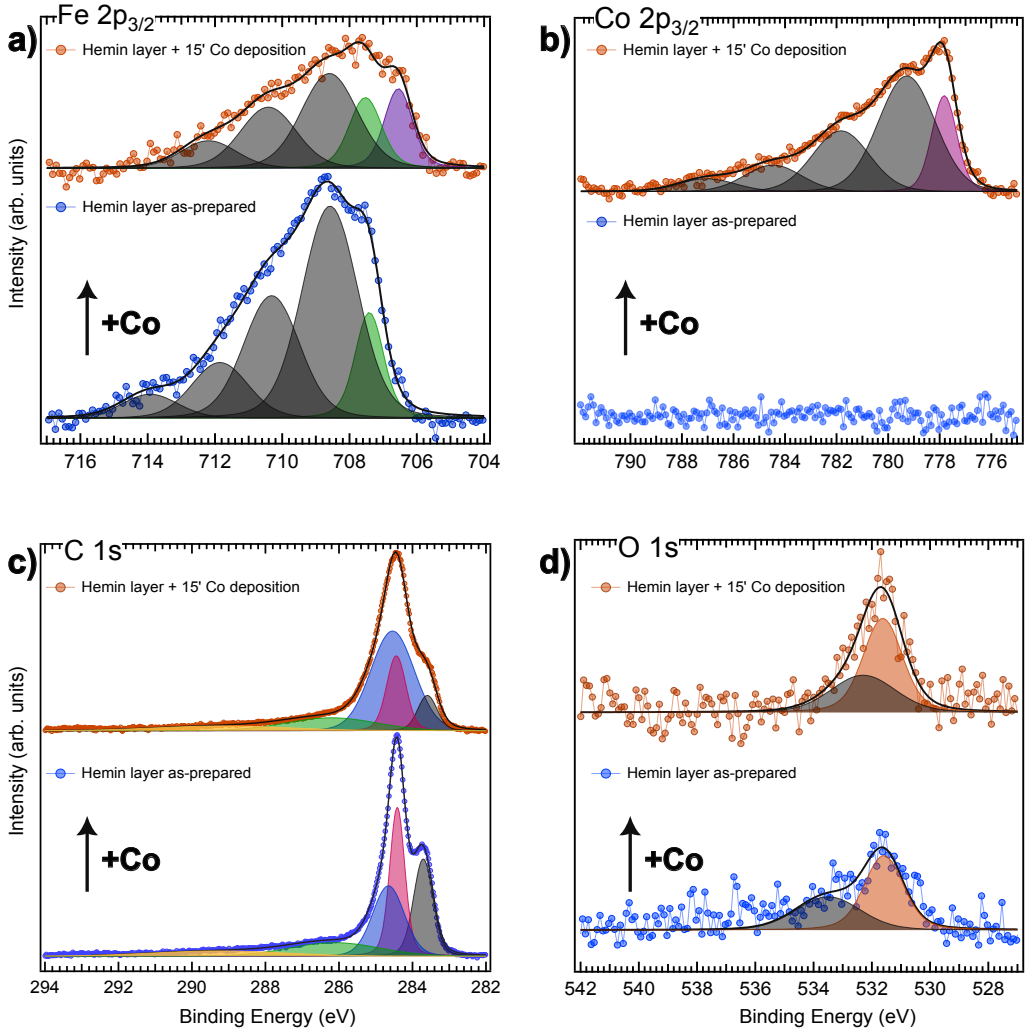

Figure 8.5 Synchrotron radiation XPS spectra of the a) Fe $2p_{3/2}$, b) Co $2p_{3/2}$, c) C 1s and d) O 1s core levels of the heme layer collected at room temperature under UHV conditions (bottom row, blue) and after 15 minutes of Co deposition (top row, orange), the total Co coverage is approximately 1% of a ML. Photon energies: a),b) 1000 eV, c) 400 eV and d) 660 eV.

The reduced Fe signal is therefore attributed to (i) isolated Fe atoms that may segregate into the Au(111) bulk, and (ii) Fe atoms in the intermediate state, which are partially screened due to their possible displacement below the macrocycle plane associated with the formation of a metallic dimer with Co.
On this basis, the new feature at 706.5 *eV*, consistent with Fe(0) [84], is also assigned to Fe atoms displaced beneath the macrocycle and in contact with the Au surface. To avoid overfitting and ensure

physical consistency, this Fe component was constrained to share the same optimized Lorentzian width (Γ = 0.31 *eV*) and Gaussian width (G = 0.81 *eV*). Upon Co addition, the grey components, previously attributed in Chapter 6 to MS features of Fe(II), retain their original lineshape, whereas the Gaussian width of the formerly assigned to a well-screened final state of Fe(II) (green), increases by 0.1 *eV*.
Figure 8.5 b) shows the evolution of the Co $2p_{3/2}$ spectra upon Co deposition. Analogous to the interpretation of the Fe $2p_{3/2}$ spectrum, the Co spectral components are rationalized by considering three distinct Co environments. Upon deposition, a fraction of Co atoms replaces Fe within the macrocycle, while another fraction adopts an intermediate configuration, likely positioned above the macrocycle plane without fully completing the trans-metalation process. Finally, a fraction of Co atoms remains uncoordinated on the Au(111) surface, where they either aggregate into small clusters or bind to surface defect sites, such as step edges. On this basis, the final spectrum was best fitted using five Voigt envelopes at 777.8, 779.3, 781.8, 784.5 and 787.0 eV. The 777.8 *eV* component (pink) is attributed to Co atoms adsorbed on the substrate, Co(0) [84], and those in the intermediate state, while the higher binding energy features correspond to MS features of Co(II) (grey), arising from Co atoms caged in the macrocycle center [84]. To prevent overfitting, all the components were constrained to a common optimized Lorentzian width (Γ = 0.20 *eV*), while the Gaussian contribution is 1.0 *eV* for the lowest binding energy component (pink) and 2.49 *eV* for the remaining MS features (grey components).
Evidence of the intermediate Co-Fe state is further supported by the C 1*s* core level reported in Figure 8.5 c). Compared to the as-prepared layer, the main change occurs in the component assigned to C-N contributions (blue), which shifts by 0.2 *eV* toward lower binding energy and becomes the dominant spectral feature. This behaviour is consistent with our previous observations about the intermediate state, which induces modifications in the macrocycle and consequently in C-N bonds.
The Gaussian width of this component also evolves, increasing from approximately 0.9 *eV* to 1.3 *eV*, reflecting the presence of different species at the molecular centers: Fe-filled, Co-filled and (Co-Fe)-filled intermediate state.
Further changes are also observed in the O 1*s* core level, top panel of Figure 8.5 d), where the C-OH components shift by 1.2 *eV* toward lower binding energy with respect to the case without Co. This shift indicates a modified interaction between the hydroxyl groups in the carboxylic terminations and the new species formed upon Co deposition, a further, indirect proof of a direct interaction between these latter moieties and the center of the macrocycle, suggesting molecular overlapping.

8.3 Effect of Dioxygen Exposure on Trans-metalation

After establishing the structural and electronic properties of the modified layer in UHV, attention was turned to its behavior under near-ambient pressure conditions, with a particular focus on its interaction and reactivity toward O_2. To this end, the evolution of the Fe $2p_{3/2}$, Co $2p_{3/2}$ O, C and N 1*s* core levels was monitored, comparing the as-prepared layer (orange, previously discussed in Section 8.2) with the spectra acquired under 0.1 *mbar* of O_2 (red) and after subsequent gas removal (cyan), Figure 8.6. All fit parameters are reported in Appendix A.8.
Starting with the Fe $2p_{3/2}$ core level (panel a) of Figure 8.6), substantial changes are observed upon O_2 exposure. The component at 706.5 *eV*, attributed to Fe(0) species on the Au substrate and to Fe in the intermediate state located below the macrocycle plane, is suppressed. This is accompanied by an approximately 80% decrease in the green component (the well-screened Fe(II) state) and the evolution of the most intense feature, which is now located at 710.5 *eV*, consistent with Fe in a +3 oxidation state [84]. Moreover, a new component arises at 714.6 *eV*, assignable to a MS feature associated with Fe(III) [84]. After gas removal, the spectrum does not recover its original UHV profile, indicating that an irreversible oxidation process has occurred.
Panel b) of Figure 8.6 shows the evolution of the Co $2p_{3/2}$ core level, where significant changes are also evident upon O_2 exposure, similar to those observed for Fe. The component assigned to Co(0) and to Co in the intermediate state decreases by approximately 80%, while the most intense feature shifts by 0.4 *eV* to higher binding energy, now centered at 779.6 *eV*, consistent with Co in the +2 oxidation state

[84]. Additionally, a new component appears at 789.2 *eV*, which could be attributed to the MS feature associated with Co(III) [84]. Similar to Fe, the Co $2p_{3/2}$ spectrum after gas removal does not recover its initial profile, confirming the occurrence of an irreversible process.
For both Fe and Co, the lowest binding energy components (purple and pink, respectively) decrease upon O_2 exposure. Specifically, in the Fe case, this component is totally suppressed, whereas for Co it is only partially reduced.
As will be further discussed in this section, based on the analysis of the other core levels, this behavior likely arises from two concurrent effects: (i) the trans-metalation process further promoted and facilitated by the O_2 exposure, and (ii) the screening induced by atomic oxygen adsorbed at the macrocycle center. The combination of the latter with the distinct geometrical position of Fe and Co (located below and above the molecular plane, respectively) can rationalize why the Fe contribution is fully suppressed, while the corresponding Co component remains detectable.

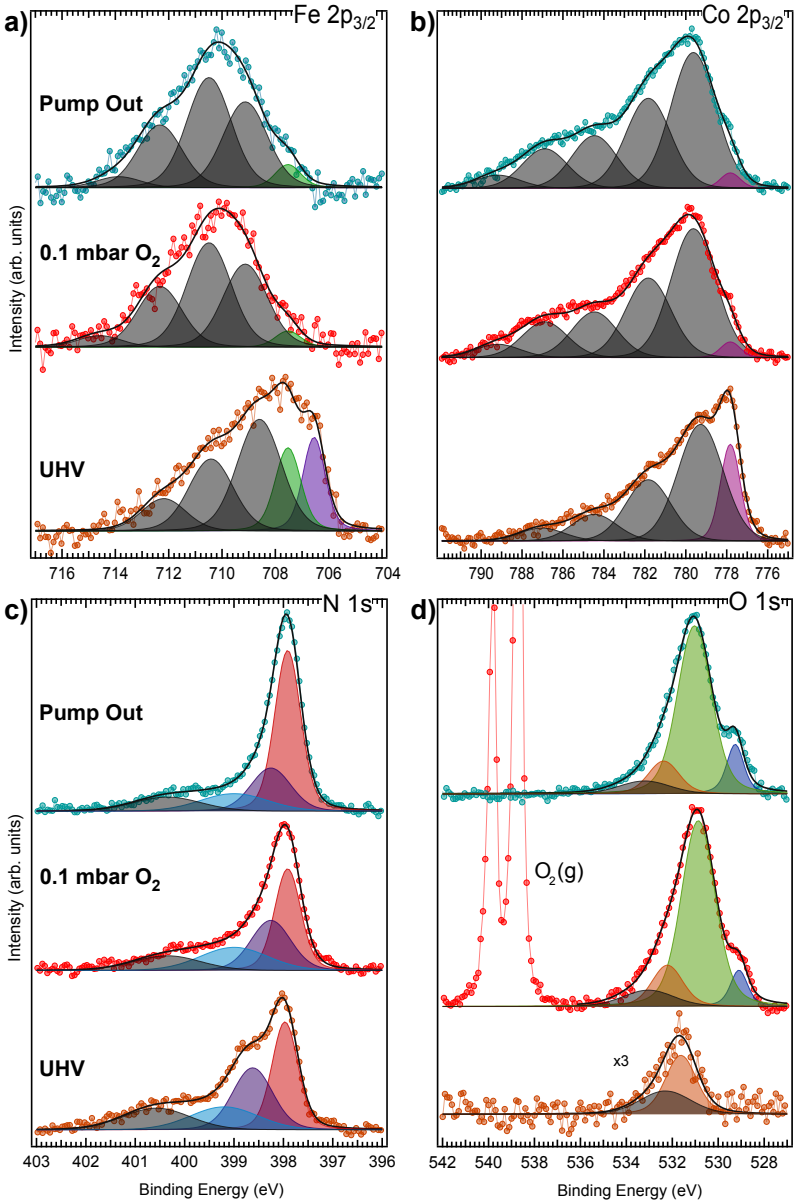

Figure 8.6 Synchrotron radiation XPS spectra of the a) Fe $2p_{3/2}$, b) Co $2p_{3/2}$, c) N 1s and d) O 1s core levels of the heme layer collected at room temperature under UHV conditions (bottom row, blue), at equilibrium in 0.1 mbar O_2 (central row, red), and after recovering UHV conditions (top row, cyan). Photon energies: a),b) 1000 eV, c) 514 eV and d) 660 eV

Further insight into the processes occurring during O_2 exposure is provided by N 1*s* core level, panel c) of Figure 8.6. Upon O_2 exposure (red spectrum), the component, previously attributed to the intermediate trans-metalation state (purple), shifts by 0.3 *eV* toward lower binding energy and decreases by ~20%, with an additional ~15% decrease after pumping out the gas (cyan spectrum). Concurrently, the feature associated with N atoms coordinated to metal centers (Fe or Co) increases by 50% compared to the UHV signal. This trend indicates that trans-metalation is promoted when exposing the system to high pressures of molecular oxygen. Furthermore, the shift of the purple component toward lower binding energy suggests partial oxidation of the mixed Co-Fe state within the macrocycle, suggesting O_2 decomposition at the metal centers. From the combined analysis of the Fe, Co and N core levels, the following processes are proposed to occur during O_2 exposure. With the presence of Fe and Co atoms on the Au substrate, interaction with O_2 leads to molecular activation: one O atom remains coordinated to the metal atom, while the other diffuses across the surface. These oxygen atoms may: (i) bind to Fe or Co atoms caged in the macrocycle, (ii) interact with Fe atoms in the intermediate states, pulling them out from the macrocycle and facilitating Co incorporation into the molecular center, (iii) in cases where Fe atoms are not completely displaced, the metal dimers remain bound to the macrocycle, possibly forming Co-Fe-O or Co-O-Fe bridge-like configurations, or (iv) bind to Co atoms in the intermediate state leading to the formation of O-Co-Fe complexes. The presence of atomic oxygen coordinated to metal atoms is further confirmed by O 1*s* core level spectra shown in Figure 8.6 d). Exposure of the system to 0.1 *mbar* of O_2 results in an irreversible spectral evolution, characterized by the appearance of two new components at 529.1 and 530.8 *eV* (blue and green, respectively) and a shift of +0.6 and +0.7 *eV* in the carboxylic contributions (orange and black, respectively).

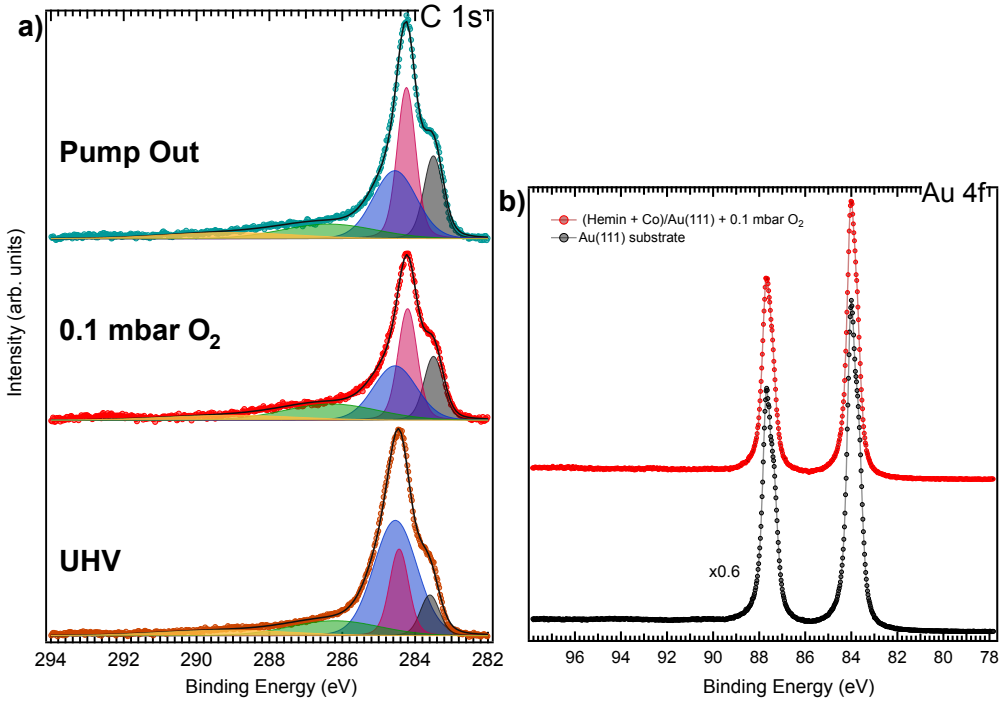

Figure 8.7 Synchrotron radiation XPS spectra of the a) C 1s $2p_{3/2}$ of the heme layer collected at room temperature under UHV conditions (bottom row, blue), at equilibrium in 0.1 mbar O_2 (central row, red), and after recovering UHV conditions (top row, cyan). b) Au 4f core level recorded for a clean substrate (black, UHV) and during exposure of the (heme+Co)/Au(111) system to 0.1 mbar O_2. Photon energies: a),b) 400 eV.

The first component is well established and can be attributed to atomic oxygen bound to metal species [91–93]. The assignment of the second component, however, is not straightforward.

Literature suggests that a peak at around 530.8 *eV* could arise from oxygen adsorbed at the Au surface or subsurface sites [151], but this interpretation is inconsistent with our observation. Indeed, the Au $4f_{7/2}$ core level spectra (panel b) of Figure 8.7) show no additional components when comparing the clean Au substrate (black spectrum) with the (heme+Co)/Au(111) system under O_2 pressure. The absence of new features rules out the possible Au-oxide formation, which is typically accompanied by surface restructuring [152]. Instead, only an overall attenuation in intensity is observed, suggesting that oxygen atoms just further screen the substrate signal.
Another possible explanation could involve distinguishing the contributions of oxygen atoms bound to Fe and Co sites on the Au substrate (component at 529.1 *eV*) from those coordinated within the macrocycle (component at 530.8 *eV*). However, this interpretation is not plausible, since the area of the latter feature should be comparable to the contributions of the oxygen species already present in the molecule (carboxylic terminations, orange and black components) on a stoichiometric basis. Similarly, atomic oxygen interacting with peripheral CH_X (-CH_2-, -CH_3) groups, potentially leading to partial oxidative degradation of these species, is ruled out by C 1*s* core level spectra (panel a) of Figure 8.7). During O_2 exposure, the previously described interaction of atomic oxygen with metal centers occurs, leading to a carbon spectrum (cyan) in which the components closely resemble those in Figure 7.2 (cyan spectrum), where only Fe-free and Fe-filled molecules are present. Minor changes in Gaussian widths and component positions are observed, consistent with the presence of different environments at the molecular centers. Nevertheless, the overall similarity of the spectral features indicates increased system homogeneity compared with the as-prepared layer (orange spectrum), i.e., a higher fraction of molecules containing a single central atom, further confirming that the trans-metalation process is promoted by O_2 exposure.
Based on these considerations, the O 1*s* spectrum can be framed within the context of final-state screening effects, analogous to observations reported for CO adsorption on several metal substrates [153,154]. Depending on the strength of the coupling between the adsorbate and the surface, multiple features can appear in the O 1*s* core level, reflecting different degrees of charge-transfer screening. In systems with strong coupling, the lower binding energy component corresponds to a well-screened final state, referred to as the *adiabatic* feature and is typically the most intense peak, whereas the higher binding energy components represent satellite features. Conversely, in weakly interacting systems, such as CO adsorbed on Ag(110), inefficient screening gives rise to intense giant satellites, and the resulting XPS final states no longer accurately represent the ground-state configuration due to the limited coupling and ultrafast timescale of the photoionization process.
By analogy, the two components observed in the present system under O_2 exposure may originate from the same chemical species: an oxygen atom bound to the metal center. The feature at 529.1 *eV* may be associated with the *adiabatic* component, well-screened state, while that at 530.8 *eV* likely corresponds to a satellite feature. Given the strong coupling between atomic oxygen and the metal centers, the overall spectral shape would be expected to resemble the O 1*s* spectra for CO strongly adsorbed on metal surfaces, like in the Ni(100) case. Instead, the shape observed here, characterized by the presence of a giant satellite, more closely resembles that of weakly bound CO adsorption. This apparent inconsistency may arise from the fundamentally different nature of the systems involved, namely, an individual oxygen atom bound to a metal center embedded within an organic matrix weakly coupled to the Au substrate, versus a molecular adsorbate directly interacting with a metallic surface. Furthermore, in a related yet unpublished study on FeTCNB monolayer grown on Au(111), exposure to O_2 resulted in dioxygen activation at the Fe centers, yielding an O 1*s* core-level components identical to that observed in our case, thereby supporting our hypothesis.
Although this interpretation provides a consistent framework for understanding the O 1*s* spectral features, no similar observations are reported in the literature to our knowledge and therefore it remains tentative. Further theoretical calculations will be required to validate this model and to quantitatively assess the role of final-state screening in the observed spectra.

8.4 Conclusion

From the previous Chapters, it is known that, starting from a heme monolayer grown on Au(111), both Fe-free and Fe-filled molecules are present within the layer. To create a bimetallic structure, Co atoms were subsequently deposited with the initial purpose of filling the macrocycles of the empty molecules. However, microscopy and spectroscopy measurements reveal that, after deposition, the Fe-free molecules do not interact with Co atoms, in contrast to the Fe-filled species. Indeed, a trans-metalation process occurs, leading to a final system comprising Fe-free, Fe-filled and Co-filled porphyrins, along with an intermediate configuration in which both Co and Fe are embedded within the macrocycle. After the characterization of the layer, the system was exposed to 0.1 *mbar* of O_2, where, interestingly, the trans-metalation process is promoted. The coexistence on the substrate of both Fe released during transmetalation and Co atoms that did not interact with Fe-filled molecules provides active sites that facilitate O_2 activation. Consequently, atomic oxygen can diffuse across the surface and interact with the molecular metal centers. Several processes can then occur: oxygen atoms may bind to Fe- or Co-filled molecules, or interact with the intermediate states. In the latter case, if Fe atoms are located beneath the macrocycle, oxygen can pull them completely out, facilitating Co incorporation and thus promoting trans-metalation. Alternatively, as evidenced by the N 1*s* core level spectra, O remains bound to the intermediate states. Together with these findings, an interpretative picture for the O 1*s* core level spectra has been proposed in the context of final-state screening effects. This interpretation may pave the way for a revised understanding of O 1*s* spectra when atomic oxygen species are bound to single metal sites embedded within metallorganic layers.

9 | Conclusions and Future Perspectives

The aim of this work was to investigate novel 2D materials based on metalorganic architectures, inspired by strategies already adopted by nature for processes such as light harvesting, chemical conversion and synthesis. These systems provide a versatile platform for stabilizing single metal atoms on surfaces, with properties that can be tuned through the surface trans-effect, interactions with axial ligands, lateral coordination and the chemical nature of peripheral residues. Specifically, we focused on iron-centered 2D materials, namely FeTPyP and hemin, deposited on weakly interacting substrates such as Gr/Ir(111) and Au(111), respectively. The structural and electronic properties of these layers were characterized under UHV and near-ambient pressure conditions. Subsequently, Co atoms were deposited in both systems to probe their structural and electronic response and to explore their behavior under reactive conditions.

Starting from the FeTPyP system, the molecules self-assemble on the Gr/Ir(111) system into a close-packed structure, driven by intermolecular interactions between the electronegative N atoms of the pyridyl end groups and the peripheral H atoms from the neighbouring pyrrole moieties, with Fe centers in the +2 oxidation state. Upon Co deposition, the second metal coordinates at the pyridinic terminations altering the lateral coupling and producing a network with distinct geometrical and electronic properties. Whereas in analogous systems Co at the pyridinic sites is typically found in the +1 oxidation state [35,37], this is the first instance in which the metal embedded in the macrocycle is reduced upon Co coordination, forming Fe(I), a species highly reactive towards O_2.

Under near-ambient pressure, the monometallic layer remains inert toward O_2 and CO, whereas the bimetallic network exhibits distinct reactivity, with both metal sites participating in the reactions. In the case of O_2 exposure, IR-Vis SFG and NAP-XPS measurements reveal clear evidence of O_2 ligation and activation, confirming the reactivity previously observed under UHV conditions and highlighting potential applicative approaches. For CO exposure, IR-Vis SFG spectroscopy was employed to investigate the cooperativity and the adsorption energy, at the nanometer scale, for both Co- and Fe-centered sites as a function of Co loading. Interestingly, increasing Co loading leads to a stronger anti-cooperative trend among Co sites, whereas Fe sites exhibit a non-cooperative behavior for the low and high Co loadings, and an anti-cooperative trend at the intermediate coverage. Regarding the adsorption energy, CO preferentially binds to Fe sites up to a Co loading threshold, beyond which this tendency reverses.

NAP-XPS measurements combined with DFT calculations enabled the determination of the oxidation states of both metal centers. Upon Co deposition, both Fe and Co are found to be theoretically compatible with a +1 oxidation state. However, due to the high reactivity of Fe(I) toward O_2, Fe is predominantly observed experimentally in the +2 oxidation state. Exposure to O_2 further oxidizes Co to +2 and Fe to +3 oxidation states, in excellent agreement with theoretical predictions. In contrast, under CO exposure, experiment results diverge from theory. Co and Fe oxidation states are expected to change to +2 under CO pressure, returning to +1 after gas removal. Experimentally, however, the residual oxygen presence during CO exposure stabilizes Co and Fe in the +2 and +3 oxidation states, respectively.

To further explore the influence of molecular environment and peripheral groups on metal reactivity, hemin, the core component of hemoglobin, was deposited on Au(111). The resulting layer consists of a mixture of Fe-free and Fe-filled molecules due to the limited purity of the biological precursor. STM measurements, supported by NEXAFS analysis, reveal the presence of intact molecules on the surface, with the carboxylic terminations, visible in the STM images only when they are not coplanar with the molecular plane. Different molecular configurations are observed, with some carboxylic groups located close to the macrocycle of an adjacent molecule. Depending on the molecular arrangement, hydrogen-bond interactions can form either between the carboxylic groups of neighboring molecules or between a carboxylic termination and the imininc nitrogen atom, when the Fe center is absent in the macrocycle. XPS analysis shows that the Fe centers are predominantly in the +2 oxidation state.

The reactivity of the layer was then tested toward CO and O_2 exposure, revealing distinct behavior. In the case of CO, there is insufficient evidence for a direct interaction with the heme layer, indicating that the system is inert toward this gas. In contrast, O_2 stabilization occurs at Fe sites when carboxylic terminations are positioned close to neighboring molecules. Here, carboxylic groups mimic the distal histidine in oxyhemoglobin and oxymyoglobin, forming hydrogen bonds with O_2 and stabilizing the Fe-O_2 interaction, effectively reproducing the second coordination sphere seen in biological systems.
To create a bimetallic structure, Co atoms were deposited after the formation of the heme layer in an attempt to occupy the vacant metal centers. However, Co preferentially interacts with the heme molecules, resulting in a system composed of Fe-free, Fe-filled and Co-filled species, along with an intermediate configuration in which both Co and Fe are simultaneously present within the molecular macrocycle. Upon O_2 exposure, the trans-metalation process is promoted due to the coexistence of Fe and Co atoms on the substrate.
In this scenario, oxygen activation occurs, leading to the formation of atomic oxygen species that diffuse across the surface, where several processes, including trans-metalation, take place.
These results open a promising perspective for future experiments. The identification of Fe(I) species is particularly significant, as this oxidation state is proposed to play a key role in nitrogenase enzymes during N_2 ligation and activation [155–158]. In biological systems, the formation of Fe(I) centers within the FeMo-cofactor is thought to weaken and cleave the N≡N bond, initiating the reduction process that ultimately leads to NH_3 formation. Future efforts will focus on strategies to efficiently stabilize Fe(I) species in metalorganic networks, providing a possible pathway toward the artificial emulation of nitrogenase activity.
The observed trans-metalation process provides a strategy to engineer active sites at the atomic level, while the O_2 stabilization represents a first successful mimic of the second coordination sphere, which is still unexplored in the surface science scenario and cannot be disregarded to achieve an effective biomimetic approach. In the near future, a further step toward understanding the role of the third dimension will be addressed by employing an electrospray source, a novel evaporation technique that enables the deposition of larger molecules, thereby providing a pathway to replicate the second coordination environment of natural enzymes.

APPENDIX – Fit Parameters

This section presents the fitting parameters associated with the XPS and SFG spectra discussed in the results chapter. The XPS data were modeled using Doniach-Šunjić line shapes with the asymmetry parameter fixed at $\alpha = 0$, resulting in Voigt profiles. As α remains zeero for all fits, it is not included in the the parameter tables. The fitting parameters reported for the XPS spectra below include the Lorentzian width (Γ), Gaussian width (G), amplitude (A), and binding energy (BE), or the binding energy shift (ΔBE) relative to the first peak. All energies and widths are given in electronvolts (eV).
The SFG spectra were fitted using Equation 3.23, with parameters defined accordingly, and convoluted with a Gaussian profile when necessary to account for sample inhomogeneity.
Each vibrational resonance is characterized by its amplitude (A), relative phase ($\Delta\varphi$), frequency (ω), and Lorentzian width (Γ), together with the non-resonant background amplitude A_{nr} and Gaussian width (G), where applicable. All the spectra were acquired using *ppp* polarization.

A.1 FeTPyP and FeTPyP-Co on Gr/Ir(111)

UHV	FeTPyP		FeTPyP-Co		FeTPyP-Co	
	N 1s		N 1s		O 1s	
	Value	σ	Value	σ	Value	σ
Γ_1	0.14		0.14		0.18	
G_1	0.61		0.83		0.87	
A_1	0.37	0.01	0.020	0.003	0.050	0.003
BE_1	398.29	0.01	397.61	0.10	529.84	0.04
Γ_2	0.14		0.14		0.18	
G_2	0.61		0.84		1.77	
A_2	0.37	0.01	0.250	0.004	0.100	0.004
ΔBE_2	0.28	0.01	0.99	0.09	1.63	0.05
Γ_3	0.14		0.14			
G_3	1.60		0.83			
A_3	0.13	0.01	0.300	0.004		
ΔBE_3	1.02	0.05	1.59	0.09		
Γ_4			0.14			
G_4			0.83			
A_4			0.200	0.003		
ΔBE_4			2.57	0.09		
Γ_5			0.14			
G_5			0.83			
A_5			0.070	0.004		
ΔBE_5			3.42	0.10		
Γ_6			0.14			
G_6			2.37			
A_6			0.050	0.005		
ΔBE_6			4.88	0.20		

Table A.1 Fit parameters of N and O 1s core levels in the FeTPyP and FeTPyP-Co spectra presented in Section 4.2, collected in UHV.

UHV	FeTPyP		FeTPyP-Co		FeTPyP-Co	
	Fe $2p_{3/2}$		Fe $2p_{3/2}$		Co $2p_{3/2}$	
	Value	σ	Value	σ	Value	σ
Γ_1	0.31		0.31		0.20	
G_1	0.67		0.43		1.06	
A_1	0.030	0.001	0.005	0.001	0.350	0.003
BE_1	707.63	0.01	706.81	0.03	778.25	0.01
Γ_2	0.31		0.31		0.20	
G_2	2.03		2.03		2.67	
A_2	0.060	0.001	0.040	0.001	0.370	0.005
ΔBE_2	1.31	0.03	1.31	0.04	1.61	0.02
Γ_3	0.31		0.31		0.20	
G_3	2.03		2.03		2.67	
A_3	0.030	0.001	0.030	0.001	0.230	0.005
ΔBE_3	4.02	0.06	3.22	0.05	4.23	0.04
Γ_4			0.31		0.20	
G_4			2.03		2.67	
A_4			0.020	0.001	0.100	0.005
ΔBE_4			4.77	0.07	6.63	0.08
Γ_5			0.31		0.20	
G_5			2.03		2.67	
A_5			0.020	0.001	0.050	0.004
ΔBE_5			6.72	0.08	9.23	0.14
Γ_6			0.31			
G_6			2.03			
A_6			0.020	0.001		
ΔBE_6			9.17	0.12		
Γ_7			0.31			
G_7			2.03			
A_7			0.030	0.002		
ΔBE_7			11.5	0.07		

Table A.1.1 Fit parameters of Fe and Co $2p_{3/2}$ core levels in the FeTPyP and FeTPyP-Co spectra presented in Section 4.2, collected in UHV.

UHV	FeTPyP		FeTPyP-Co		FeTPyP		FeTPyP-Co	
	1200 −1400 cm^{-1}		1200 −1400 cm^{-1}		1500 −1650 cm^{-1}		1500 − 1650 cm^{-1}	
	Value	σ	Value	σ	Value	σ	Value	σ
A_{nr}	4.7	0.1	8.3	0.1	5.9	0.1	7.0	0.1
G	0		18	3	0		2.6	0.4
A_1	14	4	75	4	24	2	15	2
$\Delta\varphi_1$	52	10	31	3	142	5	275	8
ω_1	1217	4	1217	4	1531	2	1531	2
Γ_1	9	2	9	2	8	3	8	3
A_2	20	2	55	3	34	3	27	3
$\Delta\varphi_2$	174	7	223	5	63	4	129	14
ω_2	1239	1	1246	3	1579	2	1570	3
Γ_2	6	1	6	1	12	2	12	2
A_3	9	1	25	6	28	1	21	1
$\Delta\varphi_3$	150	8	85	8	334	2	33	5
ω_3	1359	2	1359	2	1593.6	0.2	1597.8	0.5
Γ_3	6	2	6	2	2.8	0.2	2.8	0.2

Table A.1.2 Fit parameters of the FeTPyP and FeTPyP-Co IR-Vis SFG spectra presented in Section 4.3, collected in the 1200-1400 and 1500-1650 cm^{-1} ranges under UHV conditions

A.2 FeTPyP-Co on Gr/Ir(111): Reactivity toward O_2

	UHV		0.01 mbar O_2		Pump Out	
FeTPyP-Co	1200 −1400 cm^{-1}		1200 −1400 cm^{-1}		1200 −1400 cm^{-1}	
	Value	σ	Value	Value	Value	σ
A_{nr}	8.3	0.1	6.3	0.1	6.6	0.1
G	18	3	5.7	0.5	4.7	0.5
A_1	75	4	52	17	82	4
$\Delta\varphi_1$	31	3	53	14	73	3
ω_1	1217	4	1217	4	1217	4
Γ_1	9	2	9	2	9	2
A_2	55	3	50	10	38	3
$\Delta\varphi_2$	223	5	153	17	167	6
ω_2	1246	3	1246	3	1246	3
Γ_2	6	1	6	1	6	1
A_3	25	6	32	2	37	2
$\Delta\varphi_3$	85	8	67	5	71	3
ω_3	1359	2	1356	1	1353.8	0.7
Γ_3	6	2	6	2	6	2

Table A.2 Fit parameters of the FeTPyP-Co IR-Vis SFG spectra presented in Section 5.1.1, collected in UHV, at 0.03 mbar O_2 and after restoring the UHV conditions, in the 1200-1400 cm^{-1} range.

	UHV		0.01 mbar O_2		Pump Out	
FeTPyP-Co	1500 −1650 cm^{-1}		1500−1650 cm^{-1}		1500 −1650 cm^{-1}	
	Value	Value	Value	Value	Value	σ
A_{nr}	7.0	0.1	4.8	0.1	5.3	0.1
G	2.6	0.4	2.1	0.2	1.7	0.2
A_1	15	2	37	3	39	2
$\Delta\varphi_1$	275	8	279	4	306	3
ω_1	1531	2	1552.4	0.6	1552.4	0.6
Γ_1	8	3	6.6	0.6	6.6	0.6
A_2	27	3	30	2	32	1
$\Delta\varphi_2$	129	14	267	4	306	3
ω_2	1570	3	1593.1	0.3	1593.1	0.3
Γ_2	12	2	2.8	0.5	2.8	0.5
A_3	21	1	20	2	38	1
$\Delta\varphi_3$	33	5	43	6	119	2
ω_3	1597.8	0.5	1613	1	1613.0	1
Γ_3	2.81	0.2	5	1	5	1

Table A.2.1 Fit parameters of the FeTPyP-Co IR-Vis SFG spectra presented in Section 5.1.1, collected in UHV, at 0.03 mbar O_2 and after restoring the UHV conditions, in the 1500-1650 cm^{-1} range.

	UHV		0.03 mbar O_2		Pump Out	
	O 1s		O 1s		O 1s	
	Value	σ	Value	σ	Value	σ
Γ_1	0.18		0.184		0.184	
G_1	1.16		1.164		1.164	
A_1	0.100	0.003	0.250	0.004	0.280	0.004
BE_1	529.89	0.03	529.39	0.01	529.52	0.01
Γ_2	0.184		0.184		0.184	
G_2	1.77		1.77		1.77	
A_2	0.220	0.004	0.710	0.004	0.640	0.004
ΔBE_2	1.84	0.03	1.728	0.01	1.77	0.01
Γ_3			0.184			
G_3			2.55			
A_3			0.07	0.01		
ΔBE_3			4.29	0.13		

Table A.2.2 Fit parameters of O 1s core level in the FeTPyP-Co spectra presented in Section 5.1.2, collected in UHV at 0.03 mbar O_2 and after restoring UHV conditions.

	UHV		0.03 mbar O_2		Pump Out	
	N 1s		N 1s		N 1s	
	Value	σ	Value	σ	Value	σ
Γ_1	0.14		0.14		0.14	
G_1	0.83		0.83		0.83	
A_1	0.070	0.003	0.070	0.003	0.060	0.004
BE_1	397.61	0.03	397.61	0.03	397.61	0.04
Γ_2	0.14		0.14		0.14	
G_2	0.84		0.84		0.84	
A_2	0.340	0.004	0.610	0.004	0.580	0.005
ΔBE_2	0.99	0.03	0.99	0.03	0.99	0.04
Γ_3	0.14		0.14		0.14	
G_3	0.83		0.83		0.83	
A_3	0.440	0.004	0.210	0.004	0.350	0.005
ΔBE_3	1.59	0.03	1.65	0.03	1.54	0.04
Γ_4	0.14		0.14		0.14	
G_4	0.83		0.83		0.83	
A_4	0.300	0.003	0.150	0.003	0.220	0.004
ΔBE_4	2.57	0.03	2.41	0.03	2.44	0.04
Γ_5	0.14		0.14		0.14	
G_5	0.83		0.83		0.83	
A_5	0.040	0.003	0.040	0.003	0.040	0.004
ΔBE_5	3.43	0.03	3.43	0.05	3.43	0.06
Γ_6	0.14		0.14		0.14	
G_6	2.37		2.37		2.37	
A_6	0.090	0.005	0.100	0.005	0.090	0.006
ΔBE_6	4.88	0.08	4.88	0.08	4.88	0.11

Table A.2.3 Fit parameters of N 1s core level in the FeTPyP-Co spectra presented in Section 5.1.2, collected in UHV at 0.03 mbar O_2 and after restoring UHV conditions.

	UHV		0.03 mbar O_2		Pump Out	
	Fe $2p_{3/2}$		Fe $2p_{3/2}$		Fe $2p_{3/2}$	
	Value	σ	Value	σ	Value	σ
Γ_1	0.31		0.31		0.31	
G_1	0.43		0.43		0.43	
A_1	0.004	0.001	0		0	
BE_1	706.81	0.05	706.81		706.81	
Γ_2	0.31		0.31		0.31	
G_2	2.03		2.03		2.03	
A_2	0.040	0.001	0.010	0.001	0.020	0.001
ΔBE_2	1.56	0.05	1.57	0.13	1.57	0.08
Γ_3	0.31		0.31		0.31	
G_3	2.03		2.03		2.03	
A_3	0.040	0.001	0.040	0.002	0.040	0.001
ΔBE_3	3.23	0.05	3.23	0.04	3.23	0.04
Γ_4	0.31		0.31		0.31	
G_4	2.03		2.03		2.03	
A_4	0.030	0.001	0.030	0.002	0.030	0.001
ΔBE_4	4.75	0.06	4.75	0.08	4.75	0.05
Γ_5	0.31		0.31		0.31	
G_5	2.03		2.03		2.03	
A_5	0.020	0.001	0.020	0.001	0.020	0.001
ΔBE_5	6.71	0.09	6.71	0.11	6.71	0.09
Γ_6	0.31		0.31		0.31	
G_6	2.03		2.03		2.03	
A_6	0.009	0.001	0.009	0.001	0.015	0.001
ΔBE_6	9.17	0.20	9.17	0.30	9.17	0.14
Γ_7	0.31		0.31		0.31	
G_7	2.03		2.03		2.03	
A_7	0.010	0.002	0.020	0.002	0.010	0.002
ΔBE_7	11.50	0.15	11.50	0.14	11.50	0.20

Table A.2.4 Fit parameters of Fe $2p_{3/2}$ core level in the FeTPyP-Co spectra presented in Section 5.1.2 , collected in UHV at 0.03 mbar O_2 and after restoring UHV conditions.

	UHV		0.03 mbar O_2		Pump Out	
	Co $2p_{3/2}$		Co $2p_{3/2}$		Co $2p_{3/2}$	
	Value	σ	Value	σ	Value	σ
Γ_1	0.20		0.20		0.20	
G_1	1.06		1.06		1.06	
A_1	0.360	0.002	0		0	
BE_1	778.25	0.04	778.25		706.25	
Γ_2	0.20		0.20		0.20	
G_2	2.67		2.24		2.24	
A_2	0.570	0.004	0.81	0.01	0.780	0.004
ΔBE_2	1.80	0.01	2.05	0.01	1.95	0.01
Γ_3	0.20		0.20		0.20	
G_3	2.67		2.67		2.67	
A_3	0.340	0.004	0.46	0.01	0.50	0.01
ΔBE_3	4.23	0.02	4.23	0.03	4.15	0.02
Γ_4	0.20		0.20		0.20	
G_4	2.67		2.67		2.67	
A_4	0.160	0.004	0.27	0.01	0.30	0.01
ΔBE_4	6.63	0.04	6.91	0.04	6.99	0.01
Γ_5	0.20		0.20		0.20	
G_5	2.67		2.67		2.67	
A_5	0.100	0.003	0.20	0.01	0.20	0.01
ΔBE_5	9.23	0.06	9.23	0.05	9.23	0.04
Γ_6			0.20		0.20	
G_6			2.67		2.67	
A_6			0.080	0.01	0.09	0.01
ΔBE_6			11.15	0.12	11.15	0.08

Table A.2.5 Fit parameters of Co $2p_{3/2}$ core level in the FeTPyP-Co spectra presented in Section 5.1.2, collected in UHV at 0.03 mbar O_2 and after restoring UHV conditions.

A.3 FeTPyP-Co on Gr/Ir(111): Reactivity toward CO

CO on Fe					
4% Co loading		40% Co loading		70% Co loading	
A_r	σ	A_r	σ	A_r	σ
0.02	0.08	0.01	0.04	0.001	0.064
0.02	0.08	0.03	0.04	0.001	0.072
0.04	0.09	0.06	0.04	0.001	0.068
0.17	0.09	0.03	0.05	0.001	0.065
0.14	0.09	0.13	0.04	0.04	0.06
0.17	0.09	0.19	0.04	0.15	0.06
0.28	0.09	0.27	0.04	0.19	0.06
0.43	0.08	0.28	0.04	0.16	0.06
0.32	0.08	0.35	0.04	0.22	0.06
0.65	0.08	0.46	0.04	0.42	0.06
0.79	0.08	0.57	0.03	0.62	0.06
0.90	0.08	0.69	0.04	0.53	0.06
0.92	0.08	0.65	0.03	0.79	0.07
0.95	0.08	0.75	0.03	1.03	0.07
1.16	0.08	0.87	0.04	1.02	0.07
0.96	0.08	0.83	0.04	0.98	0.07
0.97	0.08	0.86	0.04	0.91	0.07
1.09	0.07	0.99	0.03	0.99	0.07
0.99	0.07	1.01	0.03	1.01	0.06
1.08	0.08	1.04	0.04	0.92	0.06
0.98	0.07	1.02	0.04	0.81	0.06

Table A.3 Evolution of the IR-Vis SFG amplitude of the C-O internal stretch resonances on Fe atoms at different Co loadings, presented in Figure 5.7, from UHV up to 10^{-2} CO mbar.

CO on Co					
4% Co loading		40% Co loading		70% Co loading	
A_r	σ	A_r	σ	A_r	σ
0.05	0.09	0.01	0.03	0.01	0.02
0.03	0.10	0.002	0.030	0.01	0.03
0.03	0.09	0.009	0.030	0.02	0.03
0.04	0.10	0.02	0.03	0.06	0.03
0.09	0.09	0.07	0.03	0.09	0.02
0.10	0.10	0.06	0.03	0.10	0.03
0.12	0.10	0.12	0.03	0.14	0.03
0.13	0.09	0.13	0.03	0.15	0.03
0.24	0.09	0.13	0.03	0.18	0.03
0.41	0.08	0.20	0.03	0.29	0.03
0.51	0.08	0.31	0.02	0.33	0.03
0.69	0.08	0.38	0.02	0.39	0.03
0.75	0.08	0.40	0.02	0.43	0.03
0.86	0.08	0.54	0.02	0.48	0.03
0.98	0.07	0.62	0.02	0.50	0.03
0.93	0.07	0.65	0.02	0.55	0.03
0.81	0.07	0.81	0.02	0.53	0.02
0.92	0.07	0.92	0.02	0.82	0.02
0.99	0.07	0.97	0.02	1.01	0.02
1.07	0.07	1.02	0.02	0.99	0.02
1.07	0.07	1.02	0.02	1.02	0.02

Table A.3.1 Evolution of the IR-Vis SFG amplitude of the C-O internal stretch resonances on Fe atoms at different Co loadings, presented in Figure 5.7, from UHV up to 10^{-2} CO mbar.

	UHV		0.03 mbar CO		Pump Out	
	N 1s		N 1s		N 1s	
	Value	σ	Value	σ	Value	σ
Γ_1	0.14		0.14		0.14	
G_1	0.83		0.83		0.83	
A_1	0.020	0.003	0.030	0.003	0.020	0.003
BE_1	397.61	0.10	397.61	0.08	397.61	0.08
Γ_2	0.14		0.14		0.14	
G_2	0.84		0.84		0.84	
A_2	0.250	0.004	0.20	0.01	0.220	0.004
ΔBE_2	0.99	0.09	0.99	0.07	0.99	0.08
Γ_3	0.14		0.14		0.14	
G_3	0.83		0.83		0.83	
A_3	0.320	0.004	0.30	0.01	0.400	0.004
ΔBE_3	1.59	0.09	1.49	0.08	1.51	0.08
Γ_4	0.14		0.14		0.14	
G_4	0.83		0.83		0.83	
A_4	0.210	0.003	0.170	0.003	0.210	0.003
ΔBE_4	2.57	0.09	2.46	0.08	2.50	0.08
Γ_5	0.14		0.14		0.14	
G_5	0.83		0.83		0.83	
A_5	0.070	0.004	0.060	0.004	0.040	0.003
ΔBE_5	3.42	0.10	3.43	0.08	3.43	0.09
Γ_6	0.14		0.14		0.14	
G_6	2.37		2.37		2.37	
A_6	0.050	0.005	0.05	0.01	0.050	0.005
ΔBE_6	4.88	0.18	4.88	0.20	4.88	0.20

Table A.3.2 Fit parameters of N 1s core level in the FeTPyP-Co spectra presented in Section 5.2.2 , collected in UHV at 0.03 mbar CO and after restoring UHV conditions.

	UHV		0.03 mbar CO		Pump Out	
	O 1s		O 1s		O 1s	
	Value	σ	Value	σ	Value	σ
Γ_1	0.18		0.18		0.18	
G_1	0.87		0.87		1.16	
A_1	0.050	0.003	0.060	0.004	0.100	0.004
BE_1	529.84	0.04	529.68	0.01	529.84	0.01
Γ_2	0.18		0.18		0.18	
G_2	1.77		1.77		1.77	
A_2	0.120	0.004	0.360	0.004	0.340	0.004
ΔBE_2	1.63	0.05	1.82	0.01	1.82	0.01
Γ_3			0.18			
G_3			2.23			
A_3			0.060	0.005		
ΔBE_3			4.23	0.13		

Table A.3.3 Fit parameters of O 1s core level in the FeTPyP-Co spectra presented in Section 5.2.2, collected in UHV at 0.03 mbar CO and after restoring UHV conditions.

	UHV		0.03 mbar CO		Pump Out	
	Fe $2p_{3/2}$		Fe $2p_{3/2}$		Fe $2p_{3/2}$	
	Value	σ	Value	σ	Value	σ
Γ_1	0.31		0.31		0.31	
G_1	0.43		0.43		0.43	
A_1	0.005	0.001	0		0	
BE_1	706.81	0.03	706.81		706.81	
Γ_2	0.31		0.31		0.31	
G_2	2.03		2.03		2.03	
A_2	0.040	0.001	0.010	0.001	0.020	0.001
ΔBE_2	1.31	0.04	1.31	0.08	1.31	0.07
Γ_3	0.31		0.31		0.31	
G_3	2.03		2.03		2.03	
A_3	0.030	0.001	0.030	0.001	0.040	0.001
ΔBE_3	3.22	0.05	3.23	0.04	3.22	0.04
Γ_4	0.31		0.31		0.31	
G_4	2.03		2.03		2.03	
A_4	0.020	0.001	0.020	0.001	0.030	0.001
ΔBE_4	4.77	0.07	4.77	0.07	4.77	0.05
Γ_5	0.31		0.31		0.31	
G_5	2.03		2.03		2.03	
A_5	0.020	0.001	0.010	0.001	0.030	0.001
ΔBE_5	6.72	0.08	6.72	0.11	6.72	0.07
Γ_6	0.31		0.31		0.31	
G_6	2.03		2.03		2.03	
A_6	0.020	0.001	0.003	0.001	0.020	0.001
ΔBE_6	9.17	0.12	9.17	0.12	9.17	0.09
Γ_7	0.31		0.31		0.31	
G_7	2.03		2.03		2.03	
A_7	0.030	0.002	0.009	0.002	0.040	0.002
ΔBE_7	11.50	0.07	11.50	0.08	11.50	0.07

Table A.3.4 Fit parameters of Fe $2p_{3/2}$ core levels relative to the FeTPyP-Co spectra presented in Section , collected in UHV, 0.03 mbar CO and Pump Out.

	UHV		0.03 mbar CO		Pump Out	
	Co $2p_{3/2}$		Co $2p_{3/2}$		Co $2p_{3/2}$	
	Value	σ	Value	σ	Value	σ
Γ_1	0.20		0.20		0.20	
G_1	1.06		1.06		1.06	
A_1	0.350	0.003	0.050	0.002	0.020	0.002
BE_1	778.25	0.01	778.25	0.04	706.25	0.07
Γ_2	0.20		0.20		0.20	
G_2	2.67		2.67		2.67	
A_2	0.370	0.005	0.520	0.004	0.50	0.004
ΔBE_2	1.61	0.02	1.99	0.04	1.99	0.07
Γ_3	0.20		0.20		0.20	
G_3	2.67		2.67		2.67	
A_3	0.230	0.005	0.290	0.004	0.30	0.004
ΔBE_3	4.23	0.04	4.23	0.04	4.23	0.07
Γ_4	0.20		0.20		0.20	
G_4	2.67		2.67		2.67	
A_4	0.100	0.005	0.180	0.004	0.20	0.04
ΔBE_4	6.63	0.08	6.95	0.05	6.85	0.080
Γ_5	0.20		0.20		0.20	
G_5	2.67		2.67		2.67	
A_5	0.050	0.004	0.100	0.004	0.10	0.004
ΔBE_5	9.23	0.14	9.23	0.07	9.23	0.080
Γ_6			0.20		0.20	
G_6			2.67		2.67	
A_6			0.060	0.004	0.060	0.004
ΔBE_6			11.15	0.11	11.15	0.12

Table A.3.5 Fit parameters of Co $2p_{3/2}$ core level in the FeTPyP-Co spectra presented in Section 5.2.2, collected in UHV at 0.03 mbar CO and after restoring UHV conditions

A.4 Heme on Au(111)

UHV	Hemin							
	N 1s		O 1s		C 1s		Fe $2p_{3/2}$	
	Value	σ	Value	σ	Value	σ	Value	σ
Γ_1	0.15		0.47		0.13		0.31	
G_1	0.66		1.33		0.55		0.83	
A_1	0.440	0.004	0.060	0.002	3.00	0.04	0.020	0.001
BE_1	397.91	0.01	531.63	0.03	283.73	0.01	707.50	0.02
Γ_2	0.15		0.47		0.13		0.31	
G_2	1.55		2.35		0.55		1.79	
A_2	0.20	0.01	0.030	0.002	4.30	0.06	0.050	0.002
ΔBE_2	1.23	0.05	1.97	0.12	0.63	0.01	1.28	0.05
Γ_3	0.15				0.13		0.31	
G_3	1.54				1.33		1.79	
A_3	0.30	0.01			3.90	0.08	0.030	0.002
ΔBE_3	2.61	0.02			0.95	0.02	2.82	0.12
Γ_4					0.13		0.31	
G_4					2.82		1.79	
A_4					1.80	0.01	0.020	0.002
ΔBE_4					2.61	0.08	4.55	0.10
Γ_5					0.13			
G_5					4.20			
A_5					0.80	0.06		
ΔBE_5					5.56	0.20		

Table A.4 Fit parameters of N, O 1s and Fe $2p_{3/2}$ core levels in the heme spectra presented in Section 6.2, collected in UHV.

5. Heme on Au(111): Reactivity toward CO

	UHV		0.3 mbar CO		Pump Out	
	N 1s		N 1s		N 1s	
	Value	σ	Value	σ	Value	σ
Γ_1	0.15		0.15		0.15	
G_1	0.66		0.66		0.66	
A_1	0.440	0.004	0.30	0.01	0.40	0.01
BE_1	397.91	0.01	397.91	0.01	397.91	0.01
Γ_2	0.15		0.15		0.15	
G_2	1.55		1.54		1.54	
A_2	0.20	0.01	0.180	0.008	0.230	0.007
ΔBE_2	1.23	0.05	0.80	0.07	0.80	0.05
Γ_3	0.15		0.15		0.15	
G_3	1.54		1.54		1.54	
A_3	0.30	0.01	0.250	0.007	0.320	0.006
ΔBE_3	2.61	0.02	2.36	0.03	2.36	0.02

Table A.5 Fit parameters of N 1s core level in the heme spectra presented in Section 7.1, collected in UHV.

	UHV		0.3 mbar CO		Pump Out	
	O 1s		O 1s		O 1s	
	Value	σ	Value	σ	Value	σ
Γ_1	0.47		0.47		0.47	
G_1	1.33		1.33		1.33	
A_1	0.060	0.002	0.050	0.005	0.050	0.004
BE_1	531.63	0.03	531.43	0.04	531.45	0.03
Γ_2	0.47		0.47		0.47	
G_2	2.35		2.35		2.35	
A_2	0.030	0.002	0.320	0.005	0.050	0.005
ΔBE_2	1.97	0.12	1.05	0.20	1.05	0.11

Table A.5.1 Fit parameters of O 1s core level in the heme spectra presented in Section 7.1, collected in UHV at 0.3 mbar CO and after restoring UHV conditions.

	UHV		0.3 mbar CO		Pump Out	
	C 1*s*		C 1*s*		C 1*s*	
	Value	σ	Value	σ	Value	σ
Γ_1	0.13		0.13		0.13	
G_1	0.55		0.55		0.55	
A_1	3.00	0.04	2.40	0.04	2.90	0.04
BE_1	283.73	0.01	283.73	0.01	283.73	0.01
Γ_2	0.13		0.13		0.13	
G_2	0.55		0.55		0.61	
A_2	4.30	0.06	3.20	0.06	4.50	0.07
ΔBE_2	0.63	0.01	0.63	0.01	0.63	0.01
Γ_3	0.13		0.13		0.13	
G_3	1.33		1.33		1.33	
A_3	3.90	0.08	3.30	0.09	3.70	0.09
ΔBE_3	0.95	0.02	0.95	0.02	1.00	0.02
Γ_4	0.13		0.13		0.13	
G_4	2.82		2.82		2.82	
A_4	1.80	0.01	1.40	0.08	1.90	0.06
ΔBE_4	2.61	0.08	2.61	0.12	2.55	0.09
Γ_5	0.13		0.13		0.13	
G_5	4.20		4.20		4.20	
A_5	0.80	0.06	0.60	0.09	0.90	0.07
ΔBE_5	5.56	0.20	5.56	0.40	5.56	0.20

Table A.5.2 Fit parameters of C 1s core level in the heme spectra presented in Section 7.1, collected in UHV at 0.3 mbar CO and after restoring UHV conditions.

	UHV		0.3 mbar CO		Pump Out	
	Fe $2p_{3/2}$		Fe $2p_{3/2}$		Fe $2p_{3/2}$	
	Value	σ	Value	σ	Value	σ
Γ_1	0.31		0.31		0.31	
G_1	0.83		0.83		0.83	
A_1	0.020	0.001	0.010	0.003	0.020	0.001
BE_1	707.50	0.02	707.50	0.06	707.50	0.03
Γ_2	0.31		0.31		0.31	
G_2	1.79		1.79		1.79	
A_2	0.050	0.002	0.040	0.004	0.050	0.002
ΔBE_2	1.28	0.05	1.28	0.20	1.28	0.05
Γ_3	0.31		0.31		0.31	
G_3	1.79		1.79		1.79	
A_3	0.030	0.002	0.030	0.0044	0.030	0.002
ΔBE_3	2.82	0.12	2.82	0.15	2.82	0.09
Γ_4	0.31		0.31		0.31	
G_4	1.79		1.79		1.79	
A_4	0.020	0.002	0.010	0.001	0.010	0.001
ΔBE_4	4.55	0.10	4.55	0.13	4.55	0.12

Table A.5.3 Fit parameters of Fe $2p_{3/2}$ core level in the heme spectra presented in Section 7.1, collected in UHV at 0.3 mbar CO and after restoring UHV conditions.

A.6 Heme on Au(111): Reactivity toward O_2

	UHV		0.1 mbar O_2		Pump Out	
	N 1s		N 1s		N 1s	
	Value	σ	Value	σ	Value	σ
Γ_1	0.15		0.15		0.15	
G_1	0.66		0.66		0.66	
A_1	0.80	0.01	0.760	0.001	0.82	0.01
BE_1	397.91	0.01	397.91	0.01	397.91	0.01
Γ_2	0.15		0.15		0.15	
G_2	1.54		1.54		1.54	
A_2	0.20	0.01	0.170	0.002	0.27	0.01
ΔBE_2	1.11	0.06	1.11	0.02	1.11	0.09
Γ_3	0.15		0.15		0.15	
G_3	1.54		1.54		1.54	
A_3	0.20	0.01	0.140	0.002	0.20	0.01
ΔBE_3	2.61	0.04	2.61	0.01	2.61	0.07

Table A.6 Fit parameters of N 1s core level in the heme spectra presented in Section 7.2, collected in UHV at 0.1 mbar O_2 and after restoring UHV conditions.

	UHV		0.1 mbar O_2		Pump Out	
	O 1s		O 1s		O 1s	
	Value	σ	Value	σ	Value	σ
Γ_1	0.47		0.47		0.47	
G_1	1.33		1.72		1.72	
A_1	0.030	0.002	0.070	0.002	0.040	0.002
BE_1	531.59	0.05	530.63	0.03	530.63	0.05
Γ_2	0.47		0.47		0.47	
G_2	2.35		1.33		1.33	
A_2	0.020	0.002	0.040	0.003	0.030	0.002
ΔBE_2	1.91	0.14	1.01	0.06	1.01	0.07
Γ_3			0.47		0.47	
G_3			1.43		1.43	
A_3			0.060	0.003	0.030	0.003
ΔBE_3			1.83	0.03	1.83	0.05
Γ_4			0.47		0.47	
G_4			2.35		2.35	
A_4			0.030	0.003	0.020	0.003
ΔBE_4			2.90	0.11	2.90	0.05

Table A.6.1 Fit parameters of O 1s core level in the heme spectra presented in Section 7.2, collected in UHV at 0.1 mbar O_2 and after restoring UHV conditions.

	UHV		0.1 mbar O_2		Pump Out	
	C 1*s*		C 1*s*		C 1*s*	
	Value	σ	Value	σ	Value	σ
Γ_1	0.13		0.13		0.13	
G_1	0.55		0.53		0.61	
A_1	3.60	0.02	3.10	0.03	3.60	0.03
BE_1	283.71	0.01	283.68	0.01	283.67	0.01
Γ_2	0.13		0.13		0.13	
G_2	0.42		0.42		0.48	
A_2	4.40	0.04	3.70	0.06	4.30	0.06
ΔBE_2	0.71	0.01	0.71	0.01	0.67	0.01
Γ_3	0.13		0.13		0.13	
G_3	0.95		0.95		0.95	
A_3	4.10	0.05	3.80	0.08	3.40	0.07
ΔBE_3	0.95	0.01	0.95	0.01	0.95	0.01
Γ_4	0.13		0.13		0.13	
G_4	2.82		2.82		2.82	
A_4	2.20	0.03	1.90	0.05	2.70	0.04
ΔBE_4	2.42	0.04	2.42	0.06	2.24	0.04
Γ_5	0.13		0.13		0.13	
G_5	4.20		4.20		4.20	
A_5	1.20	0.04	1.10	0.05	1.40	0.04
ΔBE_5	5.56	0.08	5.56	0.15	5.56	0.08

Table A.6.2 Fit parameters of C 1s core level in the heme spectra presented in Section 7.2, collected in UHV at 0.1 mbar O_2 and after restoring UHV conditions.

	UHV		0.1 mbar O_2		Pump Out	
	Fe $2p_{3/2}$		Fe $2p_{3/2}$		Fe $2p_{3/2}$	
	Value	σ	Value	σ	Value	σ
Γ_1	0.31		0.31		0.31	
G_1	0.83		0.83		0.83	
A_1	0.030	0.001	0.020	0.002	0.020	0.001
BE_1	707.41	0.02	707.41	0.03	707.41	0.02
Γ_2	0.31		0.31		0.31	
G_2	1.79		1.79		1.79	
A_2	0.090	0.001	0.080	0.005	0.080	0.001
ΔBE_2	1.17	0.02	1.31	0.02	1.22	0.02
Γ_3	0.31		0.31		0.31	
G_3	1.79		1.79		1.79	
A_3	0.060	0.001	0.050	0.004	0.050	0.001
ΔBE_3	2.90	0.03	2.90	0.03	2.90	0.03
Γ_4	0.31		0.31		0.31	
G_4	1.79		1.79		1.79	
A_4	0.020	0.001	0.030	0.003	0.030	0.001
ΔBE_4	4.44	0.05	4.44	0.05	4.44	0.05
Γ_5	0.31		0.31		0.31	
G_5	1.79		1.79		1.79	
A_5	0.010	0.001	0.010	0.001	0.010	0.001
ΔBE_5	6.52	0.11	6.52	0.11	6.52	0.10

Table A.6.3 Fit parameters of Fe $2p_{3/2}$ core level in the heme spectra presented in Section 7.2, collected in UHV at 0.1 mbar O_2 and after restoring UHV conditions.

A.7. Heme+Co on Au(111)

UHV	Heme		Heme + 10' Co		Heme + 5' Co	
	N 1s		N 1s		N 1s	
	Value	σ	Value	σ	Value	σ
Γ_1	0.15		0.15		0.15	
G_1	0.66		0.54		0.54	
A_1	0.80	0.01	0.500	0.004	0.430	0.004
BE_1	397.91	0.01	397.97	0.01	397.97	0.01
Γ_2	0.15		0.15		0.15	
G_2	1.54		0.87		0.87	
A_2	0.20	0.01	0.30	0.01	0.40	0.01
ΔBE_2	1.11	0.06	0.65	0.01	0.65	0.01
Γ_3	0.15		0.15		0.15	
G_3	1.54		1.54		1.54	
A_3	0.20	0.01	0.20	0.01	0.20	0.01
ΔBE_3	2.61	0.04	1.23	0.03	1.23	0.03
Γ_4			0.15		0.15	
G_4			1.54		1.54	
A_4			0.20	0.01	0.20	0.01
ΔBE_4			2.61	0.03	2.61	0.03

Table A.7 Fit parameters of N 1s core level in the spectra presented in Figure 8.4, collected after successive Co deposition steps under UHV conditions.

A.8 Heme+Co on Au(111): Reactivity toward O_2

Heme + 15' Co	UHV		0.1 mbar O_2		Pump Out	
	N 1s		N 1s		N 1s	
	Value	σ	Value	σ	Value	σ
Γ_1	0.15		0.15		0.15	
G_1	0.54		0.54		0.54	
A_1	0.430	0.004	0.40	0.01	0.640	0.004
BE_1	397.97	0.01	397.92	0.01	397.92	0.01
Γ_2	0.15		0.15		0.15	
G_2	0.87		0.87		0.87	
A_2	0.37	0.01	0.30	0.01	0.30	0.01
ΔBE_2	0.65	0.01	0.34	0.01	0.34	0.01
Γ_3	0.15		0.15		0.15	
G_3	1.54		1.54		1.54	
A_3	0.20	0.01	0.20	0.01	0.20	0.01
ΔBE_3	1.23	0.03	1.09	0.02	1.09	0.02
Γ_4	0.15		0.15		0.15	
G_4	1.54		1.54		1.54	
A_4	0.20	0.01	0.10	0.01	0.10	0.01
ΔBE_4	2.60	0.03	2.44	0.03	2.44	0.03

Table A.7.1 Fit parameters of N 1s core level in the heme+Co spectra presented in Section 8.3, collected in UHV at 0.1 mbar O_2 and after restoring UHV conditions.

Heme + 15' Co	UHV		0.1 mbar O_2		Pump Out	
	O 1s		O 1s		O 1s	
	Value	σ	Value	σ	Value	σ
Γ_1	0.47		0.47		0.47	
G_1	1.33		0.60		0.60	
A_1	0.030	0.003	0.04	0.02	0.050	0.001
BE_1	531.63	0.05	529.10	0.03	397.26	0.01
Γ_2	0.47		0.47		0.47	
G_2	2.35		1.48		1.48	
A_2	0.020	0.003	0.400	0.002	0.310	0.002
ΔBE_2	0.67	0.20	1.77	0.03	1.77	0.01
Γ_3			0.47		0.47	
G_3			1.33		1.33	
A_3			0.070	0.004	0.060	0.003
ΔBE_3			3.12	0.04	3.12	0.03
Γ_4			0.47		0.47	
G_4			2.35		2.35	
A_4			0.040	0.004	0.040	0.003
ΔBE_4			3.94	0.10	3.94	0.09

Table A.7.2 Fit parameters of O 1s core level in the heme+Co spectra presented in Section 8.3, collected in UHV at 0.1 mbar O_2 and after restoring UHV conditions.

Heme + 15' Co	UHV		0.1 mbar O_2		Pump Out	
	C 1s		C 1s		C 1s	
	Value	σ	Value	σ	Value	σ
Γ_1	0.13		0.13		0.13	
G_1	0.55		0.55		0.55	
A_1	1.30	0.01	2.10	0.01	2.62	0.01
BE_1	283.60	0.01	2883.50	0.01	283.50	0.01
Γ_2	0.13		0.13		0.13	
G_2	0.55		0.55		0.53	
A_2	2.80	0.02	3.60	0.02	4.62	0.02
ΔBE_2	0.85	0.01	0.71	0.01	0.74	0.01
Γ_3	0.13		0.13		0.13	
G_3	1.33		1.33		1.33	
A_3	8.00	0.04	3.80	0.03	4.80	0.03
ΔBE_3	0.95	0.01	1.06	0.01	1.03	0.01
Γ_4	0.13		0.13		0.13	
G_4	2.82		2.96		2.96	
A_4	2.10	0.03	2.40	0.03	2.20	0.03
ΔBE_4	2.61	0.19	2.81	0.02	2.83	0.02
Γ_5	0.13		0.13		0.13	
G_5	4.20		4.20		4.20	
A_5	1.10	0.03	1.00	0.05	1.30	0.03
ΔBE_5	5.56	0.06	5.56	0.08	5.56	0.06

Table A.7.3 Fit parameters of C 1s core level in the heme+Co spectra presented in Section 8.3, collected in UHV at 0.1 mbar O_2 and after restoring UHV conditions.

Hemin + 15' Co	UHV		0.1 mbar O_2		Pump Out	
	Co $2p_{3/2}$		Co $2p_{3/2}$		Co $2p_{3/2}$	
	Value	σ	Value	σ	Value	σ
Γ_1	0.20		0.20		0.20	
G_1	1.03		1.03		1.03	
A_1	0.140	0.001	0.020	0.002	0.020	0.002
BE_1	777.83	0.01	777.83		777.83	
Γ_2	0.20		0.20		0.20	
G_2	2.49		2.49		2.49	
A_2	0.380	0.003	0.410	0.003	0.440	0.003
ΔBE_2	1.45	0.01	1.80	0.05	1.80	0.05
Γ_3	0.20		0.20		0.20	
G_3	2.48		2.48		2.48	
A_3	0.200	0.003	0.30	0.03	0.290	0.002
ΔBE_3	4.01	0.03	4.01	0.06	4.01	0.05
Γ_4	0.20		0.20		0.20	
G_4	2.49		2.49		2.49	
A_4	0.090	0.003	0.150	0.003	0.170	0.002
ΔBE_4	6.65	0.06	6.64	0.06	6.64	0.05
Γ_5	0.20		0.20		0.20	
G_5	2.49		2.49		2.49	
A_5	0.042	0.002	0.120	0.003	0.130	0.002
ΔBE_5	9.21	0.11	9.06	0.07	9.07	0.06
Γ_6			0.20		0.20	
G_6			2.49		2.49	
A_6			0.040	0.003	0.040	0.002
ΔBE_6			11.36	0.12	11.36	0.10

Table A.7.4 Fit parameters of Co $2p_{3/2}$ core level in the heme+Co spectra presented in Section 8.3, collected in UHV at 0.1 mbar O_2 and after restoring UHV conditions.

Hemin + 15' Co	UHV		0.1 mbar O_2		Pump Out	
	Fe $2p_{3/2}$		Fe $2p_{3/2}$		Fe $2p_{3/2}$	
	Value	σ	Value	σ	Value	σ
Γ_1	0.31		0.31		0.31	
G_1	0.81		0.81		0.81	
A_1	0.020	0.001	0		0	
BE_1	776.55	0.02	776.55		776.55	
Γ_2	0.31		0.31		0.31	
G_2	0.97		0.97		0.97	
A_2	0.020	0.001	0.004	0.001	0.005	0.001
ΔBE_2	0.98	0.02	0.98	0.14	0.98	0.10
Γ_3	0.31		0.31		0.31	
G_3	1.79		1.79		1.79	
A_3	0.040	0.001	0.030	0.001	0.030	0.001
ΔBE_3	2.05	0.03	2.58	0.04	2.57	0.04
Γ_4	0.31		0.31		0.31	
G_4	1.79		1.79		1.79	
A_4	0.030	0.001	0.040	0.001	0.040	0.001
ΔBE_4	3.86	0.04	3.94	0.03	3.94	0.03
Γ_5	0.31		0.31		0.31	
G_5	1.79		1.79		1.79	
A_5	0.010	0.001	0.020	0.001	0.020	0.001
ΔBE_5	5.64	0.08	5.79	0.06	5.79	0.06
Γ_6			0.31		0.31	
G_6			1.79		1.79	
A_6			0.004	0.001	0.004	0.002
ΔBE_6			8.04	0.03	7.32	0.29

Table A.7.5 Fit parameters of Fe $2p_{3/2}$ core level in the heme+Co spectra presented in Section 8.3, collected in UHV at 0.1 mbar O_2 and after restoring UHV conditions.

Bibliography

(1) Heveling, J. Heterogeneous Catalytic Chemistry by Example of Industrial Applications. *J. Chem. Educ.* **2012**, *89* (12), 1530–1536. https://doi.org/10.1021/ed200816g.
(2) Chorkendorff, I.; Niemantsverdriet, J. W. Concepts of Modern Catalysis and Kinetics.
(3) Ertl, G. REACTIONS AT SURFACES: FROM ATOMS TO COMPLEXITY.
(4) Ateka, A.; Rodriguez-Vega, P.; Ereña, J.; Aguayo, A. T.; Bilbao, J. A Review on the Valorization of CO2. Focusing on the Thermodynamics and Catalyst Design Studies of the Direct Synthesis of Dimethyl Ether. *Fuel Process. Technol.* **2022**, *233*, 107310. https://doi.org/10.1016/j.fuproc.2022.107310.
(5) Rossetti, I.; Tripodi, A. Catalytic Production of Renewable Hydrogen for Use in Fuel Cells: A Review Study. *Top. Catal.* **2024**, *67* (19–20), 1286–1305. https://doi.org/10.1007/s11244-022-01563-z.
(6) Nocito, F.; Daraselia, D.; Dibenedetto, A. Catalytic Biomass Conversion into Fuels and Materials: Sustainable Technologies and Applications. *Catalysts* **2025**, *15* (10), 948. https://doi.org/10.3390/catal15100948.
(7) Ojelade, O. A.; Zaman, S. F.; Ni, B.-J. Green Ammonia Production Technologies: A Review of Practical Progress. *J. Environ. Manage.* **2023**, *342*, 118348. https://doi.org/10.1016/j.jenvman.2023.118348.
(8) Fu, J.; Cano, Z. P.; Park, M. G.; Yu, A.; Fowler, M.; Chen, Z. Electrically Rechargeable Zinc–Air Batteries: Progress, Challenges, and Perspectives. *Adv. Mater.* **2017**, *29* (7), 1604685. https://doi.org/10.1002/adma.201604685.
(9) Yang, X.-F.; Wang, A.; Qiao, B.; Li, J.; Liu, J.; Zhang, T. Single-Atom Catalysts: A New Frontier in Heterogeneous Catalysis. *Acc. Chem. Res.* **2013**, *46* (8), 1740–1748. https://doi.org/10.1021/ar300361m.
(10) Lopez, N. On the Origin of the Catalytic Activity of Gold Nanoparticles for Low-Temperature CO Oxidation. *J. Catal.* **2004**, *223* (1), 232–235. https://doi.org/10.1016/j.jcat.2004.01.001.
(11) Crespo-Quesada, M.; Yarulin, A.; Jin, M.; Xia, Y.; Kiwi-Minsker, L. Structure Sensitivity of Alkynol Hydrogenation on Shape- and Size-Controlled Palladium Nanocrystals: Which Sites Are Most Active and Selective? *J. Am. Chem. Soc.* **2011**, *133* (32), 12787–12794. https://doi.org/10.1021/ja204557m.
(12) Valden, M.; Lai, X.; Goodman, D. W. Onset of Catalytic Activity of Gold Clusters on Titania with the Appearance of Nonmetallic Properties. *Science* **1998**, *281* (5383), 1647–1650. https://doi.org/10.1126/science.281.5383.1647.
(13) Campbell, C. T. Electronic Perturbations. *Nat. Chem.* **2012**, *4* (8), 597–598. https://doi.org/10.1038/nchem.1412.
(14) Furukawa, H.; Cordova, K. E.; O'Keeffe, M.; Yaghi, O. M. The Chemistry and Applications of Metal-Organic Frameworks. *Science* **2013**, *341* (6149), 1230444. https://doi.org/10.1126/science.1230444.
(15) Gottfried, J. M. Surface Chemistry of Porphyrins and Phthalocyanines. *Surf. Sci. Rep.* **2015**, *70* (3), 259–379. https://doi.org/10.1016/j.surfrep.2015.04.001.
(16) Vesselli, E. Tetrapyrroles at Near-Ambient Pressure: Porphyrins and Phthalocyanines beyond the Pressure Gap. *J. Phys. Mater.* **2020**, *3* (2), 022002. https://doi.org/10.1088/2515-7639/ab7ab2.
(17) Lu, Y.; Yeung, N.; Sieracki, N.; Marshall, N. M. Design of Functional Metalloproteins. *Nature* **2009**, *460* (7257), 855–862. https://doi.org/10.1038/nature08304.
(18) Senge, M.; Ryan, A.; Letchford, K.; MacGowan, S.; Mielke, T. Chlorophylls, Symmetry, Chirality, and Photosynthesis. *Symmetry* **2014**, *6* (3), 781–843. https://doi.org/10.3390/sym6030781.
(19) Zhao, M.; Wang, H.-B.; Ji, L.-N.; Mao, Z.-W. Insights into Metalloenzyme Microenvironments: Biomimetic Metal Complexes with a Functional Second Coordination Sphere. *Chem. Soc. Rev.* **2013**, *42* (21), 8360. https://doi.org/10.1039/c3cs60162e.

(20) Ragsdale, S. W. Metals and Their Scaffolds To Promote Difficult Enzymatic Reactions. *Chem. Rev.* **2006**, *106* (8), 3317–3337. https://doi.org/10.1021/cr0503153.
(21) Dydio, P.; Key, H. M.; Nazarenko, A.; Rha, J. Y.-E.; Seyedkazemi, V.; Clark, D. S.; Hartwig, J. F. An Artificial Metalloenzyme with the Kinetics of Native Enzymes. *Science* **2016**, *354* (6308), 102–106. https://doi.org/10.1126/science.aah4427.
(22) Auwärter, W.; Écija, D.; Klappenberger, F.; Barth, J. V. Porphyrins at Interfaces. *Nat. Chem.* **2015**, *7* (2), 105–120. https://doi.org/10.1038/nchem.2159.
(23) Baronio, S. Reactivity of Porphyrin- and Phthalocyanine-Based Assemblies at Surfaces from UHV to near-Ambient Pressure. PhD Thesis.
(24) Sturmeit, H. M.; Cojocariu, I.; Windischbacher, A.; Puschnig, P.; Piamonteze, C.; Jugovac, M.; Sala, A.; Africh, C.; Comelli, G.; Cossaro, A.; Verdini, A.; Floreano, L.; Stredansky, M.; Vesselli, E.; Hohner, C.; Kettner, M.; Libuda, J.; Schneider, C. M.; Zamborlini, G.; Cinchetti, M.; Feyer, V. Room-Temperature On-Spin-Switching and Tuning in a Porphyrin-Based Multifunctional Interface. *Small* **2021**, *17* (50), 2104779. https://doi.org/10.1002/smll.202104779.
(25) Seufert, K.; Bocquet, M.-L.; Auwärter, W.; Weber-Bargioni, A.; Reichert, J.; Lorente, N.; Barth, J. V. Cis-Dicarbonyl Binding at Cobalt and Iron Porphyrins with Saddle-Shape Conformation. *Nat. Chem.* **2011**, *3* (2), 114–119. https://doi.org/10.1038/nchem.956.
(26) Armillotta, F. Dioxygen at Biomimetic Single Metal-Atom Sites: Stabilization or Activation? The Case of CoTPyP/Au(111).
(27) Hiroto, S.; Miyake, Y.; Shinokubo, H. Synthesis and Functionalization of Porphyrins through Organometallic Methodologies. *Chem. Rev.* **2017**, *117* (4), 2910–3043. https://doi.org/10.1021/acs.chemrev.6b00427.
(28) Shubina, T. E.; Marbach, H.; Flechtner, K.; Kretschmann, A.; Jux, N.; Buchner, F.; Steinrück, H.-P.; Clark, T.; Gottfried, J. M. Principle and Mechanism of Direct Porphyrin Metalation: Joint Experimental and Theoretical Investigation. *J. Am. Chem. Soc.* **2007**, *129* (30), 9476–9483. https://doi.org/10.1021/ja072360t.
(29) Li, Y.; Xiao, J.; Shubina, T. E.; Chen, M.; Shi, Z.; Schmid, M.; Steinrück, H.-P.; Gottfried, J. M.; Lin, N. Coordination and Metalation Bifunctionality of Cu with 5,10,15,20-Tetra(4-Pyridyl)Porphyrin: Toward a Mixed-Valence Two-Dimensional Coordination Network. *J. Am. Chem. Soc.* **2012**, *134* (14), 6401–6408. https://doi.org/10.1021/ja300593w.
(30) Armillotta, F.; D'Incecco, E.; Corva, M.; Stredansky, M.; Gallet, J.; Bournel, F.; Goldoni, A.; Morgante, A.; Vesselli, E.; Verdini, A. Self-Metalation of Porphyrins at the Solid–Gas Interface. *Angew. Chem. Int. Ed.* **2021**, *60* (49), 25988–25993. https://doi.org/10.1002/anie.202111932.
(31) Doyle, C. M.; Cunniffe, J. P.; Krasnikov, S. A.; Preobrajenski, A. B.; Li, Z.; Sergeeva, N. N.; Senge, M. O.; Cafolla, A. A. Ni–Cu Ion Exchange Observed for Ni(Ii)–Porphyrins on Cu(111). *Chem. Commun.* **2014**, *50* (26), 3447. https://doi.org/10.1039/c3cc48913b.
(32) Shen, K.; Narsu, B.; Ji, G.; Sun, H.; Hu, J.; Liang, Z.; Gao, X.; Li, H.; Li, Z.; Song, B.; Jiang, Z.; Huang, H.; Wells, J. W.; Song, F. On-Surface Manipulation of Atom Substitution between Cobalt Phthalocyanine and the Cu(111) Substrate. *RSC Adv.* **2017**, *7* (23), 13827–13835. https://doi.org/10.1039/C7RA00636E.
(33) Hötger, D.; Abufager, P.; Morchutt, C.; Alexa, P.; Grumelli, D.; Dreiser, J.; Stepanow, S.; Gambardella, P.; Busnengo, H. F.; Etzkorn, M.; Gutzler, R.; Kern, K. On-Surface Transmetalation of Metalloporphyrins. *Nanoscale* **2018**, *10* (45), 21116–21122. https://doi.org/10.1039/C8NR04786C.
(34) Auwärter, W.; Weber-Bargioni, A.; Riemann, A.; Schiffrin, A.; Gröning, O.; Fasel, R.; Barth, J. V. Self-Assembly and Conformation of Tetrapyridyl-Porphyrin Molecules on Ag(111). *J. Chem. Phys.* **2006**, *124* (19), 194708. https://doi.org/10.1063/1.2194541.
(35) Armillotta, F.; Bidoggia, D.; Baronio, S.; Sala, A.; Costantini, R.; dell'Angela, M.; Cojocariu, I.; Feyer, V.; Morgante, A.; Peressi, M.; Vesselli, E. Co(III), Co(II), Co(I): Tuning Single Cobalt Metal Atom Oxidation States in a 2D Coordination Network. *Adv. Funct. Mater.* **2024**, *34* (48). https://doi.org/10.1002/adfm.202408200.

(36) Bidoggia, D.; Armillotta, F.; Sala, A.; Vesselli, E.; Peressi, M. Site-Dependent Oxidation States of Single Cobalt Atoms in a Porphyrin-Based Monolayer on Graphene. *J. Phys. Chem. C* **2024**, *128* (4), 1737–1745. https://doi.org/10.1021/acs.jpcc.3c05562.
(37) Baronio, S.; De Col, M.; Yadav, A.; Roondhe, B.; Mischke, V.; Resel, O.; Bidoggia, D.; Alessandro Namar; Vinogradov, N.; Scardamaglia, M.; Valvidares, M.; Gargiani, P.; Cinchetti, M.; Zamborlini, G.; Giannozzi, P.; Vesselli, E. Single Atom Coordination in a Manganese-Cobalt Bi-Metallic Framework on Graphene: Geometric and Electronic Structures. *Nanoscale* **2025**. https://doi.org/10.1039/D5NR01383F.
(38) Wurster, B.; Grumelli, D.; Hötger, D.; Gutzler, R.; Kern, K. Driving the Oxygen Evolution Reaction by Nonlinear Cooperativity in Bimetallic Coordination Catalysts. *J. Am. Chem. Soc.* **2016**, *138* (11), 3623–3626. https://doi.org/10.1021/jacs.5b10484.
(39) Chen, X.; Zhou, Z.; Karahan, H. E.; Shao, Q.; Wei, L.; Chen, Y. Recent Advances in Materials and Design of Electrochemically Rechargeable Zinc–Air Batteries. *Small* **2018**, *14* (44), 1801929. https://doi.org/10.1002/smll.201801929.
(40) Sun, W.; Wang, F.; Zhang, B.; Zhang, M.; Küpers, V.; Ji, X.; Theile, C.; Bieker, P.; Xu, K.; Wang, C.; Winter, M. A Rechargeable Zinc-Air Battery Based on Zinc Peroxide Chemistry. *Science* **2021**, *371* (6524), 46–51. https://doi.org/10.1126/science.abb9554.
(41) Zhao, D.; Zhuang, Z.; Cao, X.; Zhang, C.; Peng, Q.; Chen, C.; Li, Y. Atomic Site Electrocatalysts for Water Splitting, Oxygen Reduction and Selective Oxidation. *Chem. Soc. Rev.* **2020**, *49* (7), 2215–2264. https://doi.org/10.1039/C9CS00869A.
(42) Huang, Z.; Wang, J.; Peng, Y.; Jung, C.; Fisher, A.; Wang, X. Design of Efficient Bifunctional Oxygen Reduction/Evolution Electrocatalyst: Recent Advances and Perspectives. *Adv. Energy Mater.* **2017**, *7* (23), 1700544. https://doi.org/10.1002/aenm.201700544.
(43) Humbert, C.; Noblet, T. A Unified Mathematical Formalism for First to Third Order Dielectric Response of Matter: Application to Surface-Specific Two-Colour Vibrational Optical Spectroscopy. *Symmetry* **2021**, *13* (1), 153. https://doi.org/10.3390/sym13010153.
(44) Tian, C. S.; Shen, Y. R. Recent Progress on Sum-Frequency Spectroscopy. *Surf. Sci. Rep.* **2014**, *69* (2–3), 105–131. https://doi.org/10.1016/j.surfrep.2014.05.001.
(45) Vidal, F.; Tadjeddine, A. Sum-Frequency Generation Spectroscopy of Interfaces. *Rep. Prog. Phys.* **2005**, *68* (5), 1095–1127. https://doi.org/10.1088/0034-4885/68/5/R03.
(46) Busson, B.; Tadjeddine, A. Non-Uniqueness of Parameters Extracted from Resonant Second-Order Nonlinear Optical Spectroscopies. *J. Phys. Chem. C* **2009**, *113* (52), 21895–21902. https://doi.org/10.1021/jp908240d.
(47) Boyd, R. W. *Nonlinear Optics*, Fourth edition.; Elsevier, AP Academic Press: London, 2020. https://doi.org/10.1016/C2015-0-05510-1.
(48) Lambert, A. G.; Davies, P. B.; Neivandt, D. J. Implementing the Theory of Sum Frequency Generation Vibrational Spectroscopy: A Tutorial Review. *Appl. Spectrosc. Rev.* **2005**, *40* (2), 103–145. https://doi.org/10.1081/ASR-200038326.
(49) Lambert, A. G. Resonantly Enhanced Sum Frequency Spectroscopy of Adsorption on Hydrophilic Mica Substrates. PhD Thesis, 2001. https://doi.org/10.17863/CAM. 16301.
(50) Hunt, J. H.; Guyot-Sionnest, P.; Shen, Y. R. Observation of C-H Stretch Vibrations of Monolayers of Molecules Optical Sum-Frequency Generation. *Chem. Phys. Lett.* **1987**, *133* (3), 189–192. https://doi.org/10.1016/0009-2614(87)87049-5.
(51) Wang, H.-F.; Velarde, L.; Gan, W.; Fu, L. Quantitative Sum-Frequency Generation Vibrational Spectroscopy of Molecular Surfaces and Interfaces: Lineshape, Polarization, and Orientation. *Annu. Rev. Phys. Chem.* **2015**, *66* (1), 189–216. https://doi.org/10.1146/annurev-physchem-040214-121322.
(52) Humbert, C.; Noblet, T.; Dalstein, L.; Busson, B.; Barbillon, G. Sum-Frequency Generation Spectroscopy of Plasmonic Nanomaterials: A Review. *Materials* **2019**, *12* (5), 836. https://doi.org/10.3390/ma12050836.

(53) Rupprechter, G. Sum Frequency Generation and Polarization–Modulation Infrared Reflection Absorption Spectroscopy of Functioning Model Catalysts from Ultrahigh Vacuum to Ambient Pressure. In *Advances in Catalysis*; Elsevier, 2007; Vol. 51, pp 133–263. https://doi.org/10.1016/S0360-0564(06)51004-1.
(54) EKSPLA. Scanning SFG Spectrometer, 2025. https://ekspla.com/product/sfgspectrometer/.
(55) EKSPLA. EKSPLA PL2230 Series, Diode Pumped High Energy Picosecond Nd:YAG Lasers., 2025. https://ekspla.com/products/diode-pumped-high-energy-picosecond-laser-pl2230/.
(56) Tucker, M. D.; Rowe, R. C.; Miseo, E. V.; Valentine, J. R. Air Quality Monitoring by Open Path Fourier Transform Infrared (FTIR) Spectrometry; 1997; p 972391. https://doi.org/10.4271/972391.
(57) Hayashi, M.; Lin, S. H.; Raschke, M. B.; Shen, Y. R. A Molecular Theory for Doubly Resonant IR−UV-Vis Sum-Frequency Generation. *J. Phys. Chem. A* **2002**, *106* (10), 2271–2282. https://doi.org/10.1021/jp012633l.
(58) Velarde, L.; Wang, H.-F. Unified Treatment and Measurement of the Spectral Resolution and Temporal Effects in Frequency-Resolved Sum-Frequency Generation Vibrational Spectroscopy (SFG-VS). *Phys. Chem. Chem. Phys.* **2013**, *15* (46), 19970. https://doi.org/10.1039/c3cp52577e.
(59) Berglund, C. N.; Spicer, W. E. Photoemission Studies of Copper and Silver: Theory. *Phys. Rev.* **1964**, *136* (4A), A1030–A1044. https://doi.org/10.1103/PhysRev.136.A1030.
(60) Damascelli, A.; Hussain, Z.; Shen, Z.-X. Angle-Resolved Photoemission Studies of the Cuprate Superconductors. *Rev. Mod. Phys.* **2003**, *75* (2), 473–541. https://doi.org/10.1103/RevModPhys.75.473.
(61) Hüfner, S. *Photoelectron Spectroscopy*; Advanced Texts in Physics; Springer Berlin Heidelberg: Berlin, Heidelberg, 2003. https://doi.org/10.1007/978-3-662-09280-4.
(62) Koopmans, T. Über die Zuordnung von Wellenfunktionen und Eigenwerten zu den Einzelnen Elektronen Eines Atoms. *Physica* **1934**, *1* (1–6), 104–113. https://doi.org/10.1016/S0031-8914(34)90011-2.
(63) D'Acunto, G. Reaction Mechanisms and Dynamics in the Early Stage of High-κ Oxide Atomic Layer Deposition. PhD Thesis, 2022.
(64) Johansson, N. Synchrotron-Based In Situ Electron Spectroscopy Applied to Oxide Formation and Catalysis. PhD Thesis, 2017.
(65) Hofmann, S. *Auger- and X-Ray Photoelectron Spectroscopy in Materials Science: A User-Oriented Guide*; Springer Series in Surface Sciences; Springer Berlin Heidelberg: Berlin, Heidelberg, 2013; Vol. 49. https://doi.org/10.1007/978-3-642-27381-0.
(66) Starr, D. E. A Brief Overview of the Principles of Ambient Pressure X-Ray Spectroscopies. In *ACS Symposium Series*; Head, A. R., Nemšák, S., Eren, B., Eds.; American Chemical Society: Washington, DC, 2021; Vol. 1396, pp 1–17. https://doi.org/10.1021/bk-2021-1396.ch001.
(67) Salmeron, M.; Schlogl, R. Ambient Pressure Photoelectron Spectroscopy: A New Tool for Surface Science and Nanotechnology. *Surf. Sci. Rep.* **2008**, *63* (4), 169–199. https://doi.org/10.1016/j.surfrep.2008.01.001.
(68) Amann, P.; Degerman, D.; Lee, M.-T.; Alexander, J. D.; Shipilin, M.; Wang, H.-Y.; Cavalca, F.; Weston, M.; Gladh, J.; Blom, M.; Björkhage, M.; Löfgren, P.; Schlueter, C.; Loemker, P.; Ederer, K.; Drube, W.; Noei, H.; Zehetner, J.; Wentzel, H.; Åhlund, J.; Nilsson, A. A High-Pressure x-Ray Photoelectron Spectroscopy Instrument for Studies of Industrially Relevant Catalytic Reactions at Pressures of Several Bars. *Rev. Sci. Instrum.* **2019**, *90* (10), 103102. https://doi.org/10.1063/1.5109321.
(69) Shavorskiy, A.; Bluhm, H. Ambient-Pressure X-Ray Photoelectron Spectroscopy. In *Heterogeneous Catalysts for Clean Technology*; Wilson, K., Lee, A. F., Eds.; Wiley, 2013; pp 437–468. https://doi.org/10.1002/9783527658985.ch14.
(70) Zhu, S.; Scardamaglia, M.; Kundsen, J.; Sankari, R.; Tarawneh, H.; Temperton, R.; Pickworth, L.; Cavalca, F.; Wang, C.; Tissot, H.; Weissenrieder, J.; Hagman, B.; Gustafson, J.; Kaya, S.; Lindgren, F.; Källquist, I.; Maibach, J.; Hahlin, M.; Boix, V.; Gallo, T.; Rehman, F.; D'Acunto, G.; Schnadt, J.;

Shavorskiy, A. HIPPIE: A New Platform for Ambient-Pressure X-Ray Photoelectron Spectroscopy at the MAX IV Laboratory. *J. Synchrotron Radiat.* **2021**, *28* (2), 624–636. https://doi.org/10.1107/S160057752100103X.
(71) Binnig, G.; Rohrer, H. SCANNING TUNNELING MICROSCOPY.
(72) Yin, Y. The Investigation of Scanning Tunneling Microscopy and Spectroscopy on High-Tc Superconductors: Cuprates and Pnictides.
(73) Vinogradov, N. Scanning Tunneling Microscope, 2022. https://www.maxiv.lu.se/beamlines-accelerators/support-labs/microscopy-labs/scanning-tunneling-microscope/.
(74) Pletikosić, I.; Kralj, M.; Pervan, P.; Brako, R.; Coraux, J.; N'Diaye, A. T.; Busse, C.; Michely, T. Dirac Cones and Minigaps for Graphene on Ir(111). *Phys. Rev. Lett.* **2009**, *102* (5), 056808. https://doi.org/10.1103/PhysRevLett.102.056808.
(75) Stein, A.; Rolf, D.; Lotze, C.; Czekelius, C.; Franke, K. J.; Tegeder, P. Electronic Structure of an Iron Porphyrin Derivative on Au(1 1 1). *J. Phys. Condens. Matter* **2019**, *31* (4), 044002. https://doi.org/10.1088/1361-648X/aaf296.
(76) Armillotta, F.; Sala, A.; Vesselli, E. Ligation of Carbon Monoxide at Cobalt Single-Metal-Atom Sites in a Surface-Confined Metal–Organic Network: Oxidation State, Anharmonicity, and Long-Range Lateral Interactions. *J. Phys. Chem. C* **2024**, *128* (37), 15613–15623. https://doi.org/10.1021/acs.jpcc.4c03692.
(77) Decker, R.; Brede, J.; Atodiresei, N.; Caciuc, V.; Blügel, S.; Wiesendanger, R. Atomic-Scale Magnetism of Cobalt-Intercalated Graphene. *Phys. Rev. B* **2013**, *87* (4), 041403. https://doi.org/10.1103/PhysRevB.87.041403.
(78) Yu, A.; Li, S.; Dhital, B.; Lu, H. P.; Ho, W. Tunneling Electron Induced Charging and Light Emission of Single Panhematin Molecules. *J. Phys. Chem. C* **2016**, *120* (37), 21099–21103. https://doi.org/10.1021/acs.jpcc.6b04087.
(79) Scardamaglia, M.; Lisi, S.; Lizzit, S.; Baraldi, A.; Larciprete, R.; Mariani, C.; Betti, M. G. Graphene-Induced Substrate Decoupling and Ideal Doping of a Self-Assembled Iron-Phthalocyanine Single Layer. *J. Phys. Chem. C* **2013**, *117* (6), 3019–3027. https://doi.org/10.1021/jp308861b.
(80) Liao, L.; Peng, H.; Liu, Z. Chemistry Makes Graphene beyond Graphene. *J. Am. Chem. Soc.* **2014**, *136* (35), 12194–12200. https://doi.org/10.1021/ja5048297.
(81) Baker Cortés, B. D.; Enache, M.; Küster, K.; Studener, F.; Lee, T.; Marets, N.; Bulach, V.; Hosseini, M. W.; Stöhr, M. Structural Transformation of Surface-Confined Porphyrin Networks by Addition of Co Atoms. *Chem. – Eur. J.* **2021**, *27* (48), 12430–12436. https://doi.org/10.1002/chem.202101217.
(82) Blanco, J. M.; González, C.; Jelínek, P.; Ortega, J.; Flores, F.; Pérez, R.; Rose, M.; Salmeron, M.; Méndez, J.; Wintterlin, J.; Ertl, G. Origin of Contrast in STM Images of Oxygen on Pd(111) and Its Dependence on Tip Structure and Tunneling Parameters. *Phys. Rev. B* **2005**, *71* (11). https://doi.org/10.1103/physrevb.71.113402.
(83) Fadley, C. S.; Shirley, D. A. Multiplet Splitting of Metal-Atom Electron Binding Energies. *Phys. Rev. A* **1970**, *2* (4), 1109–1120. https://doi.org/10.1103/physreva.2.1109.
(84) Biesinger, M. C.; Payne, B. P.; Grosvenor, A. P.; Lau, L. W. M.; Gerson, A. R.; Smart, R. St. C. Resolving Surface Chemical States in XPS Analysis of First Row Transition Metals, Oxides and Hydroxides: Cr, Mn, Fe, Co and Ni. *Appl. Surf. Sci.* **2011**, *257* (7), 2717–2730. https://doi.org/10.1016/j.apsusc.2010.10.051.
(85) Sch□nhammer, K.; Gunnarsson, O. Exactly Soluble Limits of a Model for Core Level Spectra of Adsorbates. *Z. F□r Phys. B Condens. Matter Quanta* **1978**, *30* (3), 297–303. https://doi.org/10.1007/bf01320035.
(86) Gunnarsson, O. CO on Cu(lOO) —Explanation of the Three-Peak Structure in the X-Ray-Photoemission-Spectroscopy Core Spectrum. *P H C R E V E W E T T E R S* **1978**, *41* (23).
(87) Lukasczyk, T.; Flechtner, K.; Merte, L. R.; Jux, N.; Maier, F.; Gottfried, J. M.; Steinrück, H.-P. Interaction of Cobalt(II) Tetraarylporphyrins with a Ag(111) Surface Studied with Photoelectron Spectroscopy. *J. Phys. Chem. C* **2007**, *111* (7), 3090–3098. https://doi.org/10.1021/jp0652345.

(88) Armillotta, F.; Bidoggia, D.; Biasin, P.; Annese, A.; Cossaro, A.; Verdini, A.; Floreano, L.; Peressi, M.; Vesselli, E. Spectroscopic Fingerprints of Iron-Coordinated Cobalt and Iron Porphyrin Layers on Graphene. *Cell Rep. Phys. Sci.* **2023**, *4* (5), 101378. https://doi.org/10.1016/j.xcrp.2023.101378.
(89) Bai, Y.; Buchner, F.; Wendahl, M. T.; Kellner, I.; Bayer, A.; Steinrück, H.-P.; Marbach, H.; Gottfried, J. M. Direct Metalation of a Phthalocyanine Monolayer on Ag(111) with Coadsorbed Iron Atoms. *J. Phys. Chem. C* **2008**, *112* (15), 6087–6092. https://doi.org/10.1021/jp711122w.
(90) Schio, L.; Bavdek, G.; Grazioli, C.; Obersnù, C.; Cossaro, A.; Goldoni, A.; Calloni, A.; Bossi, A.; Bussetti, G.; Orbelli Biroli, A.; Vittadini, A.; Floreano, L. Seeding the Vertical Growth of Laterally Coherent Coordination Polymers on the Rutile-TiO_2(110) Surface. *Nanoscale* **2024**, *16* (27), 13071–13078. https://doi.org/10.1039/d4nr01309c.
(91) Bozzini, B.; Previdi, A.; Amati, M.; Bevilacqua, M.; Cordaro, G.; Corva, M.; Donazzi, A.; Dotelli, G.; Gregoratti, L.; Pelosato, R.; Vorokhta, M.; Vesselli, E. In Situ Near-Ambient Pressure X-Ray Photoelectron Spectroscopy Discloses the Surface Composition of Operating NdBaCo2O5+δ Solid Oxide Fuel Cell Cathodes. *J. Power Sources* **2019**, *436*, 226815. https://doi.org/10.1016/j.jpowsour.2019.226815.
(92) Haber, J.; Stoch, J.; Ungier, L. X-Ray Photoelectron Spectra of Oxygen in Oxides of Co, Ni, Fe and Zn. *J. Electron Spectrosc. Relat. Phenom.* **1976**, *9* (5), 459–467. https://doi.org/10.1016/0368-2048(76)80064-3.
(93) Gao, X.; Yokota, N.; Oda, H.; Tanaka, S.; Hokamoto, K.; Chen, P. One Step Preparation of Fe–FeO–Graphene Nanocomposite through Pulsed Wire Discharge. *Crystals* **2018**, *8* (2), 104. https://doi.org/10.3390/cryst8020104.
(94) Vinogradov, N. A.; Schulte, K.; Ng, M. L.; Mikkelsen, A.; Lundgren, E.; Mårtensson, N.; Preobrajenski, A. B. Impact of Atomic Oxygen on the Structure of Graphene Formed on Ir(111) and Pt(111). *J. Phys. Chem. C* **2011**, *115* (19), 9568–9577. https://doi.org/10.1021/jp111962k.
(95) Kyrkjebø, S.; Cassidy, A.; Akhtar, N.; Balog, R.; Scheffler, M.; Hornekær, L.; Holst, B.; Flatabø, R. Graphene and Graphene Oxide on Ir(111) Are Transparent to Wetting but Not to Icing. *Carbon* **2021**, *174*, 396–403. https://doi.org/10.1016/j.carbon.2020.12.030.
(96) Scardamaglia, M.; Susi, T.; Struzzi, C.; Snyders, R.; Di Santo, G.; Petaccia, L.; Bittencourt, C. Spectroscopic Observation of Oxygen Dissociation on Nitrogen-Doped Graphene. *Sci. Rep.* **2017**, *7* (1). https://doi.org/10.1038/s41598-017-08651-1.
(97) Artyushkova, K. Misconceptions in Interpretation of Nitrogen Chemistry from X-Ray Photoelectron Spectra. *J. Vac. Sci. Technol. A* **2020**, *38* (3). https://doi.org/10.1116/1.5135923.
(98) Bittencourt, C.; Rutar, M.; Umek, P.; Mrzel, A.; Vozel, K.; Arčon, D.; Henzler, K.; Krüger, P.; Guttmann, P. Molecular Nitrogen in N-Doped TiO_2 Nanoribbons. *RSC Adv.* **2015**, *5* (30), 23350–23356. https://doi.org/10.1039/c4ra14410d.
(99) Armillotta, F.; Bidoggia, D.; Baronio, S.; Biasin, P.; Annese, A.; Scardamaglia, M.; Zhu, S.; Bozzini, B.; Modesti, S.; Peressi, M.; Vesselli, E. Single Metal Atom Catalysts and ORR: H-Bonding, Solvation, and the Elusive Hydroperoxyl Intermediate. *ACS Catal.* **2022**, *12* (13), 7950–7959. https://doi.org/10.1021/acscatal.2c02029.
(100) Popovici, S.; Leyffer, W.; Holze, R. The Mechanism of Dioxygen Reduction at Iron *Meso*-Tetrakis (Pyridyl) Porphyrin: A Spectroelectrochemical Study. *J. Porphyr. Phthalocyanines* **1998**, *02* (03), 249–260. https://doi.org/10.1002/(sici)1099-1409(199805/06)2:3%253C249::aid-jpp77%253E3.0.co;2-3.
(101) Blom, N.; Odo, J.; Nakamoto, K.; Strommen, D. P. Resonance Raman Studies of Metal Tetrakis(4-N-Methylpyridyl)Porphine: Band Assignments, Structure-Sensitive Bands, and Species Equilibria. *J. Phys. Chem.* **1986**, *90* (13), 2847–2852. https://doi.org/10.1021/j100404a015.
(102) Avval, T. G.; Chatterjee, S.; Hodges, G. T.; Bahr, S.; Dietrich, P.; Meyer, M.; Thißen, A.; Linford, M. R. Oxygen Gas, O2(g), by near-Ambient Pressure XPS. *Surf. Sci. Spectra* **2019**, *26* (1), 014021. https://doi.org/10.1116/1.5100962.

(103)Puglia, C.; Nilsson, A.; Hernnäs, B.; Karis, O.; Bennich, P.; Mårtensson, N. Physisorbed, Chemisorbed and Dissociated O2 on Pt(111) Studied by Different Core Level Spectroscopy Methods. *Surf. Sci.* **1995**, *342* (1–3), 119–133. https://doi.org/10.1016/0039-6028(95)00798-9.
(104)Dupin, J.-C.; Gonbeau, D.; Vinatier, P.; Levasseur, A. Systematic XPS Studies of Metal Oxides, Hydroxides and Peroxides. *Phys. Chem. Chem. Phys.* **2000**, *2* (6), 1319–1324. https://doi.org/10.1039/a908800h.
(105)Sung, S. S.; Hoffmann, R. How Carbon Monoxide Bonds to Metal Surfaces. *J. Am. Chem. Soc.* **1985**, *107* (3), 578–584. https://doi.org/10.1021/ja00289a009.
(106)Corva, M.; Ferrari, A.; Rinaldi, M.; Feng, Z.; Roiaz, M.; Rameshan, C.; Rupprechter, G.; Costantini, R.; Dell'Angela, M.; Pastore, G.; Comelli, G.; Seriani, N.; Vesselli, E. Vibrational Fingerprint of Localized Excitons in a Two-Dimensional Metal-Organic Crystal. *Nat. Commun.* **2018**, *9* (1), 4703. https://doi.org/10.1038/s41467-018-07190-1.
(107)Li, X.; Pramhaas, V.; Rameshan, C.; Blaha, P.; Rupprechter, G. Coverage-Induced Orientation Change: CO on Ir(111) Monitored by Polarization-Dependent Sum Frequency Generation Spectroscopy and Density Functional Theory. *J. Phys. Chem. C* **2020**, *124* (33), 18102–18111. https://doi.org/10.1021/acs.jpcc.0c04986.
(108)Li, X.; Haunold, T.; Werkovits, S.; Marks, L. D.; Blaha, P.; Rupprechter, G. CO Adsorption and Disproportionation on Smooth and Defect-Rich Ir(111). *J. Phys. Chem. C* **2022**, *126* (15), 6578–6589. https://doi.org/10.1021/acs.jpcc.2c01141.
(109)Lukashuk, L.; Yigit, N.; Rameshan, R.; Kolar, E.; Teschner, D.; Hävecker, M.; Knop-Gericke, A.; Schlögl, R.; Föttinger, K.; Rupprechter, G. Operando Insights into CO Oxidation on Cobalt Oxide Catalysts by NAP-XPS, FTIR, and XRD. *ACS Catal.* **2018**, *8* (9), 8630–8641. https://doi.org/10.1021/acscatal.8b01237.
(110)Khassin, A. A.; Yurieva, T. M.; Kaichev, V. V.; Bukhtiyarov, V. I.; Budneva, A. A.; Paukshtis, E. A.; Parmon, V. N. Metal–Support Interactions in Cobalt-Aluminum Co-Precipitated Catalysts: XPS and CO Adsorption Studies. *J. Mol. Catal. Chem.* **2001**, *175* (1–2), 189–204. https://doi.org/10.1016/S1381-1169(01)00216-3.
(111)Plyler, E. K.; Blaine, L. R.; Connor, W. S. Velocity of Light from the Molecular Constants of Carbon Monoxide. *J. Opt. Soc. Am.* **1955**, *45* (2), 102. https://doi.org/10.1364/JOSA.45.000102.
(112)Podda, N.; Corva, M.; Mohamed, F.; Feng, Z.; Dri, C.; Dvorák, F.; Matolin, V.; Comelli, G.; Peressi, M.; Vesselli, E. Experimental and Theoretical Investigation of the Restructuring Process Induced by CO at Near Ambient Pressure: Pt Nanoclusters on Graphene/Ir(111). *ACS Nano* **2017**, *11* (1), 1041–1053. https://doi.org/10.1021/acsnano.6b07876.
(113)Yao, Y.; Chen, L.; Mao, X.; Yang, Y.; Chen, J.; Zhou, L. In Situ PM-IRRAS Study of CO Adsorption on Au Surfaces: Solving the Puzzle. *J. Phys. Chem. C* **2021**, *125* (16), 8606–8619. https://doi.org/10.1021/acs.jpcc.1c01638.
(114)Swart, I.; Fielicke, A.; Rayner, D. M.; Meijer, G.; Weckhuysen, B. M.; de Groot, F. M. F. Controlling the Bonding of CO on Cobalt Clusters by Coadsorption of H_2. *Angew. Chem. Int. Ed.* **2007**, *46* (28), 5317–5320. https://doi.org/10.1002/anie.200605165.
(115)Hess, Ch.; Bonn, M.; Funk, S.; Wolf, M. Hot-Band Excitation of CO Chemisorbed on Ru(001) Studied with Broadband-IR Sum-Frequency Generation. *Chem. Phys. Lett.* **2000**, *325* (1–3), 139–145. https://doi.org/10.1016/S0009-2614(00)00627-8.
(116)Zhang, V. L.; Arnolds, H.; King, D. A. Hot Band Excitation of CO/Ir{111} Studied by Broadband Sum Frequency Generation. *Surf. Sci.* **2005**, *587* (1–2), 102–109. https://doi.org/10.1016/j.susc.2005.04.039.
(117)Chu, K. H. Revisiting the Temkin Isotherm: Dimensional Inconsistency and Approximate Forms. *Ind. Eng. Chem. Res.* **2021**, *60* (35), 13140–13147. https://doi.org/10.1021/acs.iecr.1c01788.
(118)Johnson, K. N.; Chilukuri, B.; Fisher, Z. E.; Hipps, K. W.; Mazur, U. Role of the Supporting Surface in the Thermodynamics and Cooperativity of AxialLigand Binding to Metalloporphyrins at Interfaces. *Curr. Org. Chem.* **2022**, *26* (6), 553–562. https://doi.org/10.2174/1385272826666220209122508.

(119)Weiss, J. N. The Hill Equation Revisited: Uses and Misuses. *FASEB J.* **1997**, *11* (11), 835–841. https://doi.org/10.1096/fasebj.11.11.9285481.
(120)Hill, A. V. XLVII. THE COMBINATIONS OF HAEMOGLOBIN WITH OXYGEN AND WITH CARBON MON- OXIDE. I.
(121)Abild-Pedersen, F.; Andersson, M. P. CO Adsorption Energies on Metals with Correction for High Coordination Adsorption Sites – A Density Functional Study. *Surf. Sci.* **2007**, *601* (7), 1747–1753. https://doi.org/10.1016/j.susc.2007.01.052.
(122)Crossley, A.; King, D. A. Infrared Spectra for Co Isotopes Chemisorbed on Pt "111": Evidence for Strong Absorbate Coupling Interactions. *Surf. Sci.* **1977**, *68*, 528–538. https://doi.org/10.1016/0039-6028(77)90245-X.
(123)Pfnür, H.; Menzel, D. HIGH RESOLUTION VIBRATIONAL SPECTROSCOPY OF CO ON Ru(OO1): THE IMPORTANCE OF LATERAL INTERACTIONS. https://doi.org/10.1016/0039-6028(80)90275-7.
(124)O'Connor, C. R.; Boscoboinik, J. A.; Karatok, M.; Van Spronsen, M. A. Carbon Monoxide, CO(g), by High-Resolution near-Ambient-Pressure x-Ray Photoelectron Spectroscopy. *Surf. Sci. Spectra* **2020**, *27* (1), 014002. https://doi.org/10.1116/1.5131166.
(125)Eren, B.; Heine, C.; Bluhm, H.; Somorjai, G. A.; Salmeron, M. Catalyst Chemical State during CO Oxidation Reaction on Cu(111) Studied with Ambient Pressure XPS and NEXAFS. *J. Am. Chem. Soc.*
(126)Tao, N. J.; Cardenas, G.; Cunha, F.; Shi, Z. In Situ STM and AFM Study of Protoporphyrin and Iron(III) and Zinc(II) Protoporphyrins Adsorbed on Graphite in Aqueous Solutions. *Langmuir* **1995**, *11* (11), 4445–4448. https://doi.org/10.1021/la00011a043.
(127)Garcia-Lekue, A.; González-Moreno, R.; Garcia-Gil, S.; Pickup, D. F.; Floreano, L.; Verdini, A.; Cossaro, A.; Martín-Gago, J. A.; Arnau, A.; Rogero, C. Coordinated H-Bonding between Porphyrins on Metal Surfaces. *J. Phys. Chem. C* **2012**, *116* (29), 15378–15384. https://doi.org/10.1021/jp302784r.
(128)González-Moreno, R.; Sánchez-Sánchez, C.; Trelka, M.; Otero, R.; Cossaro, A.; Verdini, A.; Floreano, L.; Ruiz-Bermejo, M.; García-Lekue, A.; Martín-Gago, J. Á.; Rogero, C. Following the Metalation Process of Protoporphyrin IX with Metal Substrate Atoms at Room Temperature. *J. Phys. Chem. C* **2011**, *115* (14), 6849–6854. https://doi.org/10.1021/jp200533a.
(129)Diller, K.; Papageorgiou, A. C.; Klappenberger, F.; Allegretti, F.; Barth, J. V.; Auwärter, W. In Vacuo Interfacial Tetrapyrrole Metallation. *Chem. Soc. Rev.* **2016**, *45* (6), 1629–1656. https://doi.org/10.1039/C5CS00207A.
(130)Marbach, H. Surface-Mediated *in Situ* Metalation of Porphyrins at the Solid–Vacuum Interface. *Acc. Chem. Res.* **2015**, *48* (9), 2649–2658. https://doi.org/10.1021/acs.accounts.5b00243.
(131)Edmondson, M.; Frampton, E. S.; Judd, C. J.; Champness, N. R.; Jones, R. G.; Saywell, A. Order, Disorder, and Metalation of Tetraphenylporphyrin (2 *H* -TPP) on Au(111). *Chem. Commun.* **2022**, *58* (42), 6247–6250. https://doi.org/10.1039/D2CC00820C.
(132)Smykalla, L.; Shukrynau, P.; Zahn, D. R. T.; Hietschold, M. Self-Metalation of Phthalocyanine Molecules with Silver Surface Atoms by Adsorption on Ag(110). *J. Phys. Chem. C* **2015**, *119* (30), 17228–17234. https://doi.org/10.1021/acs.jpcc.5b04977.
(133)Lee, A. F.; Gawthrope, D. E.; Hart, N. J.; Wilson, K. A Fast XPS Study of the Surface Chemistry of Ethanol over Pt{111}. *Surf. Sci.* **2004**, *548* (1–3), 200–208. https://doi.org/10.1016/j.susc.2003.11.004.
(134)Artemenko, A.; Shchukarev, A.; Štenclová, P.; Wågberg, T.; Segervald, J.; Jia, X.; Kromka, A. Reference XPS Spectra of Amino Acids. *IOP Conf. Ser. Mater. Sci. Eng.* **2021**, *1050* (1), 012001. https://doi.org/10.1088/1757-899X/1050/1/012001.
(135)Diller, K.; Klappenberger, F.; Marschall, M.; Hermann, K.; Nefedov, A.; Wöll, Ch.; Barth, J. V. Self-Metalation of 2H-Tetraphenylporphyrin on Cu(111): An x-Ray Spectroscopy Study. *J. Chem. Phys.* **2012**, *136* (1), 014705. https://doi.org/10.1063/1.3674165.

(136)Okajima, T.; Yamamoto, Y.; Ouchi, Y.; Seki, K. NEXAFS Spectra of Metallotetraphenylporphyrins with Adsorbed Nitrogen Monoxide. *J. Electron Spectrosc. Relat. Phenom.* **2001**, *114–116*, 849–854. https://doi.org/10.1016/S0368-2048(00)00268-1.
(137)Zamborlini, G.; Jugovac, M.; Cossaro, A.; Verdini, A.; Floreano, L.; Lüftner, D.; Puschnig, P.; Feyer, V.; Schneider, C. M. On-Surface Nickel Porphyrin Mimics the Reactive Center of an Enzyme Cofactor. *Chem. Commun.* **2018**, *54* (95), 13423–13426. https://doi.org/10.1039/C8CC06739B.
(138)Schmidt, N. A.; Fink, R.; Hieringer, W. Assignment of Near-Edge x-Ray Absorption Fine Structure Spectra of Metalloporphyrins by Means of Time-Dependent Density-Functional Calculations. *J. Chem. Phys.* **2010**, *133* (5), 054703. https://doi.org/10.1063/1.3435349.
(139)Willey, T. M.; Bagge-Hansen, M.; Lee, J. R. I.; Call, R.; Landt, L.; Van Buuren, T.; Colesniuc, C.; Monton, C.; Valmianski, I.; Schuller, I. K. Electronic Structure Differences between H2-, Fe-, Co-, and Cu-Phthalocyanine Highly Oriented Thin Films Observed Using NEXAFS Spectroscopy. *J. Chem. Phys.* **2013**, *139* (3), 034701. https://doi.org/10.1063/1.4811487.
(140)Carlotto, S.; Sambi, M.; Sedona, F.; Vittadini, A.; Bartolomé, J.; Bartolomé, F.; Casarin, M. $L_{2,3}$ -Edges Absorption Spectra of a 2D Complex System: A Theoretical Modelling. *Phys. Chem. Chem. Phys.* **2016**, *18* (40), 28110–28116. https://doi.org/10.1039/C6CP04787D.
(141)Cojocariu, I.; Carlotto, S.; Sturmeit, H. M.; Zamborlini, G.; Cinchetti, M.; Cossaro, A.; Verdini, A.; Floreano, L.; Jugovac, M.; Puschnig, P.; Piamonteze, C.; Casarin, M.; Feyer, V.; Schneider, C. M. Ferrous to Ferric Transition in Fe-Phthalocyanine Driven by NO_2 Exposure. *Chem. – Eur. J.* **2021**, *27* (10), 3526–3535. https://doi.org/10.1002/chem.202004932.
(142)Eren, B.; Head, A. R. Carbon Monoxide Adsorption on Manganese Oxide/Cobalt: An Ambient Pressure X-Ray Photoelectron Spectroscopy Study. *J. Phys. Chem. C* **2020**, *124* (6), 3557–3563. https://doi.org/10.1021/acs.jpcc.9b08942.
(143)Huang, X.; Groves, J. T. Oxygen Activation and Radical Transformations in Heme Proteins and Metalloporphyrins. *Chem. Rev.* **2018**, *118* (5), 2491–2553. https://doi.org/10.1021/acs.chemrev.7b00373.
(144)Wilson, S. A.; Green, E.; Mathews, I. I.; Benfatto, M.; Hodgson, K. O.; Hedman, B.; Sarangi, R. X-Ray Absorption Spectroscopic Investigation of the Electronic Structure Differences in Solution and Crystalline Oxyhemoglobin. *Proc. Natl. Acad. Sci.* **2013**, *110* (41), 16333–16338. https://doi.org/10.1073/pnas.1315734110.
(145)Chen, H.; Ikeda-Saito, M.; Shaik, S. Nature of the Fe−O_2 Bonding in Oxy-Myoglobin: Effect of the Protein. *J. Am. Chem. Soc.* **2008**, *130* (44), 14778–14790. https://doi.org/10.1021/ja805434m.
(146)Wang, W.; Pang, R.; Kuang, G.; Shi, X.; Shang, X.; Liu, P. N.; Lin, N. Intramolecularly Resolved Kondo Resonance of High-Spin Fe (II) -Porphyrin Adsorbed on Au (111). *Phys. Rev. B* **2015**, *91* (4), 045440. https://doi.org/10.1103/PhysRevB.91.045440.
(147)Meng, X.; Möller, J.; Menchón, R. E.; Weismann, A.; Sánchez-Portal, D.; Garcia-Lekue, A.; Herges, R.; Berndt, R. Kondo Effect of Co-Porphyrin: Remarkable Sensitivity to Adsorption Sites and Orientations. *Nano Lett.* **2024**, *24* (1), 180–186. https://doi.org/10.1021/acs.nanolett.3c03669.
(148)Zhao, A.; Hu, Z.; Wang, B.; Xiao, X.; Yang, J.; Hou, J. G. Kondo Effect in Single Cobalt Phthalocyanine Molecules Adsorbed on Au(111) Monoatomic Steps. *J. Chem. Phys.* **2008**, *128* (23), 234705. https://doi.org/10.1063/1.2940338.
(149)Hui Chang, M.; Jung, J.; Seo, J.; Jeong Kang, M.; Kim, Y.-H.; Kahng, S.-J. Molecule-Supported Magnetic-Atom Dimers on Au(111): Multiple Structures and Kondo Resonances. *Appl. Surf. Sci.* **2025**, *679*, 161168. https://doi.org/10.1016/j.apsusc.2024.161168.
(150)Herritsch, J.; Guo, C.; Heuplick, L. J.; Hutter, M.; Fan, Q.; Münster, F.; Kachel, S. R.; Zugermeier, M.; Gottfried, J. M. On-Surface Chemistry of Pb(II) Tetraphenylporphyrin on Au(111): Reversible Metalation, Thermal Degradation, and Formation of a Covalent Organic Framework. *Phys. Chem. Chem. Phys.* **2025**, *27* (20), 10875–10883. https://doi.org/10.1039/D5CP00422E.

(151)Günther, S.; Böcklein, S.; Wintterlin, J.; Niño, M. A.; Menteş, T. O.; Locatelli, A. Locating Catalytically Active Oxygen on Ag(1 1 1)—A Spectromicroscopy Study. *ChemCatChem* **2013**, *5* (11), 3342–3350. https://doi.org/10.1002/cctc.201300355.
(152)Klyushin, A. Yu.; Rocha, T. C. R.; Hävecker, M.; Knop-Gericke, A.; Schlögl, R. A near Ambient Pressure XPS Study of Au Oxidation. *Phys. Chem. Chem. Phys.* **2014**, *16* (17), 7881. https://doi.org/10.1039/c4cp00308j.
(153)Wurth, W.; Coulman, D.; Puschmann, A.; Menzel, D.; Umbach, E. Relation between X-Ray Photoemission Spectroscopy Binding Energies and Absorption Resonance Energies for CO Adsorbates. *Phys. Rev. B* **1990**, *41* (18), 12933–12936. https://doi.org/10.1103/PhysRevB.41.12933.
(154)Krause, S.; Mariani, C.; Prince, K. C.; Horn, K. SCREENING EFFECTS IN PHOTOEMISSION FROM WEAKLY BOUND.
(155)Doukeh, R.; Crăciun, D.; Lupan, A.; Brânzanic, A. M. V.; Silaghi-Dumitrescu, R. Effect of the Coordination Environment on the Ability of Iron to Bind/Activate N2: A Theoretical Study with Relevance to the Nitrogenase Mechanism. *Polyhedron* **2023**, *243*, 116571. https://doi.org/10.1016/j.poly.2023.116571.
(156)Rohde, M.; Sippel, D.; Trncik, C.; Andrade, S. L. A.; Einsle, O. The Critical E_4 State of Nitrogenase Catalysis. *Biochemistry* **2018**, *57* (38), 5497–5504. https://doi.org/10.1021/acs.biochem.8b00509.
(157)Siegbahn, P. E. M. The Mechanism for N_2 Activation in the E_4 – State of Nitrogenase. *Phys. Chem. Chem. Phys.* **2023**, *25* (35), 23602–23613. https://doi.org/10.1039/D3CP02851H.
(158)Pang, Y.; Bjornsson, R. Understanding the Electronic Structure Basis for N_2 Binding to FeMoco: A Systematic Quantum Mechanics/Molecular Mechanics Investigation. *Inorg. Chem.* **2023**, *62* (14), 5357–5375. https://doi.org/10.1021/acs.inorgchem.2c03967.

UNIVERSITÀ
DEGLI STUDI
DI TRIESTE

La borsa di dottorato è cofinanziata con risorse dell'Unione europea, NextGeneration EU - Piano Nazionale di Ripresa e Resilienza, Missione 4 – Componente 1 – Investimento 4.1 CUP J92B22000850007